Large-Scale Subject-Specific Finite Element Modelling of the Human Shoulder Complex

A thesis submitted to the University of Manchester for the degree of

Doctor of Philosophy

in the Faculty of Science and Engineering

2016

Manxu Zheng

School of Mechanical, Aerospace and Civil engineering

University of Manchester

Table of Contents

Final word count: 37,811 words

List of Tables

List of Figures

Title: Large-Scale Subject-Specific Finite Element Modelling of the Human Shoulder Complex

Degree: Doctor of Philosophy

Candidate: Manxu Zheng

University of Manchester

Date: 28 Dec 2016

Abstract

Shoulder problems such as anterior shoulder dislocation and rotator cuff tears are common shoulder musculoskeletal disorders. However, the cause of many shoulder disorders has not been studied adequately. The objective of this project is to develop and validate a large-scale subject-specific finite element (FE) model of the human shoulder complex to enhance our understanding of the biomechanical mechanism underlying joint motion and solve clinically related problems. It is hypothesised that a comprehensive subject-specific FE model of the human shoulder complex can represent the stability and mobility nature of the joint during normal movement *in-vivo*. The *in-vivo* shoulder motion measurement data of a young healthy male subject was collected first using a three-dimensional (3D) motion analysis system and subsequently used to construct a multi-body shoulder musculoskeletal model using OpenSim software to estimate the *in-vivo* subject-specific muscle activities. Driven by those derived muscle loadings, a subject-specific FE shoulder model with detailed representations of all the major musculoskeletal components was constructed based on high-resolution MR images scanned on the same subject. Quasi-static FE analysis was conducted to simulate the *in-vivo* subject-specific scapular abduction. Thereafter, the constructed FE model was used to perform a biomechanical study to investigate the effect of the rotator cuff tears on the glenohumeral joint stability during the propagation of the tears. A novel integrative stability index was proposed and used to quantitatively analyse the simulated results. In the quasi-static FE simulation of the scapular abduction of the healthy shoulder, the magnitude of the bone-on-bone forces of the simulation results at joint position 0, 10^o, 20^o and 30^o were found to be 8.18N, 91.45N, 146.14 and 408N, respectively. Whereas, the superior movement of the humeral head centre with respective to the scapula from 0 to 30^o was found to be 2.02mm. Both of the bone-on-bone force and humeral head superior movement of the FE simulation results were found to be in very good agreement with previous experimental and computational results in the literature. The biomechanical study simulating the propagation of the tears demonstrated that the stability of the glenohumeral joint decreased from 100% in intact condition to 0.18% in full rotator cuff tear condition. Important clinical findings were summarised as (1) the stability of the glenohumeral joint generally decreases with the increasing tear sizes; (2) smaller sizes of tears do not significantly affect the joint stability, in addition, the critical tear size in which the consequence of the rotator cuff tears becomes severe was determined as tear involved whole supraspinatus tendon and half of the infraspinatus tendon. The obtained results and findings could be used to improve the diagnostic and therapeutic strategies for clinicians when dealing with shoulder disorder patients. To sum up, in this study, a subject-specific finite element model of the human shoulder complex has been constructed and validated, and further used in investigating of the effect of the rotator cuff tears on the glenohumeral joint stability during the propagation of the tears.

Declaration

I declare that no portion of the work referred to in the thesis has been submitted in support of an application for another degree or qualification of this or any other university or other institute of learning.

Copyright Statement

Acknowledgements

I would like to use this opportunity to express my sincere gratitude to those who have made significant contributions to the completion of this thesis.

Firstly, I wish to thank my supervisors Dr. Lei Ren, Dr Zhenmin Zou, Dr. Chris Peach and Prof. Paulo jorge Da silva Bartolo for their supervisions during the four years of study. Especially, deep gratitude goes to Dr. Lei Ren for his kind supports and patient guidance. Many of his invaluable suggestions and shared experiences have made this thesis possible.

I would like to extend many thanks to my colleagues and friends, particularly to Dr. Dan Hu, Mr. Mohammad Akrami, Ms. Sivangi Raychoudhury, Dr. Yunhong Liang, Dr. Chunbo Liu, Dr. Guowu Wei and many others within and outside of the University of Manchester.

At last, I am extremely thankful to my parents for their unconditional love and support, which have always guided me and supported me through all the difficulties. To them, I dedicate this thesis.

Chapter 1 Introduction

1.1 Background

Shoulder pain is one of the most common pain syndromes nowadays. Population surveys demonstrated that 18-26% of adults are affected by shoulder pain [1, 2]. The symptoms can result in great discomfort and even loss of the ability to perform daily activities. However, the evaluation and diagnosis of shoulder disorders still remain challenging. The cause of many shoulder conditions has not been studied adequately [3]. The primary reason is due to the enormously complex structure of the shoulder anatomy. The human shoulder joint is considered a perfect compromise between mobility and stability [4]. As the major joint in shoulder complex, the glenohumeral joint permits the greatest range of motion of any joint in the human body. It is commonly referred to as the shoulder joint. The stability is mainly based on active muscle control with a minor contribution from the glenohumeral capsule, labrum and ligaments. Numerous experimental and computational studies had been conducted to investigate the glenohumeral joint stability and mobility features. However, the understanding of the *in-vivo* biomechanical function of the shoulder complex is still quite limited. Little is known about the contribution to the biomechanical system from each individual component including bone, muscle, ligament and cartilages structures as well as their interplay between each other.

Due to the ethical considerations and limitation by existing measuring techniques in traditional biomechanical measurements, computational simulation seems to be the most profound solution in the area of biomechanics [5]. In terms of the shoulder modelling, its complexity becomes the main disincentive to modellers [6]. A large number of experimental and computational studies have been conducted to improve our understanding of the functions and structures of the shoulder complex, including computer simulation studies using finite element (FE) method. However, so far, most of the FE shoulder models developed have been over-simplified due to the high complexity of the shoulder musculoskeletal system, and the *in-vivo* biomechanical functions of the shoulder complex have not been fully investigated.

Therefore, a comprehensive FE model with detailed representations of all the major biomechanical components of the shoulder complex is needed. Also, the subsequent FE simulations should be defined under the *in-vivo* physiological conditions where significant muscle activations are included. In addition, there is an increasing tendency in subject-specific or patient-specific computational modelling in computer-aided surgical planning where the FE model could be used for clinical application [7]. Subject-specific modelling can exclude individual differences and demonstrate accurate geometrical and kinematical data flow among different modelling and measuring techniques. Therefore, it is a desirable technique to investigate the intrinsic shoulder joint biomechanical functions.

Once validated, a subject-specific FE shoulder model could have numerous applications including but not limited to the following: (1) improving the understanding of the biomechanical mechanism underlying joint motion, (2) aetiology investigation of joint pathology, (3) clinical diagnoses of joint diseases, (4) surgical planning and pre-testing, (5) implant evaluation, design and optimisations and (6) rehabilitation devices design and consultation.

1.2 Hypothesis

It is hypothesised that a comprehensive subject-specific FE model of the human shoulder complex constructed by using a computational framework combining the two main computational biomechanics methods, i.e. multi-body musculoskeletal method and finite element method, informed by *in-vivo* measured anatomical and kinematics data of the subject can represent the stability and mobility nature of the joint during normal movement *in-vivo*. Further, the constructed FE model has the ability to serve as the basis for investigation of abnormal musculoskeletal conditions and derive clinical relevant findings.

1.3 Aims and objectives

The aim of this project is to develop and validate a large-scale subject-specific FE model of the human shoulder musculoskeletal complex. To improve our understanding of fundamental mechanisms underlying shoulder joint mobility and stability under *in-vivo* conditions. This primary aim is completed by accomplishing the following objectives.

1. To develop a profound understanding of the current shoulder biomechanics research and the state-of-the-art of the shoulder FE modelling.

2. To accurately measure the *in-vivo* subject-specific kinematics data of the human shoulder joint.

3. To predict the *in-vivo* subject-specific muscle loads under the experimental conditions.

4. To obtain an accurate subject-specific geometrical representation of the shoulder complex.

5. To construct the subject-specific FE model of the shoulder complex.

6. To conduct the *in-vivo* subject-specific quasi-static FE analysis of shoulder scapular plane abduction.

7. To investigate the influence of the rotator cuff tears on the glenohumeral joint stability during the propagation of the tears.

1.4 Methodology

To achieve the aim of this project, a computational framework combining the two main computational biomechanics methods, i.e. multi-body musculoskeletal method and finite element method was adopted. Each of the above specific objectives was achieved by the following methods.

1. A thorough literature review of the previous FE models of the human shoulder complex literature was conducted. Their major findings, limitations, potential clinical applications and modelling techniques were critically examined. The awareness and

understanding of the current limitation and challenges faced in this field have helped set the direction and objectives that this study should follow and pursue.

2. Stereophotogrammetry and surface electromyography (EMG) system was adopted. Specifically, Vicon infrared cameras and Delsys wireless surface EMG system with specially designed reflective marker fixation devices were used to measure the *in-vivo* subject-specific kinematics and the simultaneous muscle activities.

3. A subject-specific multi-body musculoskeletal model was constructed using OpenSim software. Based on the measured shoulder motion data, the *in-vivo* muscle forces were calculated by using inverse dynamics based force estimation method.

4. The same subject that participated in the motion measurements was chosen to perform medical scanning using advanced MR imaging techniques. The detailed 3D geometries of all major hard tissues and soft tissues around the glenohumeral joint and their relative positions were determined by segmentation and reconstruction of the scanned images in Mimic software. The reconstructed geometries were further constructed in CAD environment for solid 3D geometrical construction.

5. The construction of the FE model was performed by integrating all of the above modelling information. Specifically, the reconstructed geometries of the shoulder tissues were imported into Abaqus to define subject-specific tissue geometrical representation and were assembled together by carefully preserving their relative position relationships determined by MR images. Subsequently, their material properties and contacts were defined. Then, the measured kinematics and calculated muscle forces were imported into the FE model to define the *in-vivo* subject-specific loading and boundary conditions. Finally, the FE model was meshed using 3D quadratic tetrahedral element and the mesh sizes were verified.

6. The FE model was further constructed to reproduce different abduction angles defined by the measured motions. The further constructed models were used to perform this quasi-static FE analysis of the shoulder scapular abduction accordingly. The calculated muscle forces were imported into these models for the FE analysis.

Simulation results were validated against the *in-vivo* measured bone-on-bone contact force and humeral centre movement and also simulated stress distribution in literature.

7. The validated shoulder FE model was used to perform FE analysis with different sizes of tears. A novel integrative stability index was proposed and used to quantify the influences to joint stability due to rotator cuff tears.

1.5 Thesis overview

The thesis is divided into nine chapters. The first chapter briefly reviews the background of the analysis of human shoulder complex, introduces the objectives of this study and presents an outline of this study. The second chapter performed a thorough review of the background knowledge and previous works related to finite element modelling of the human shoulder complex. A summary of the review results i.e., current limitation and challenges in this field was conducted together with thusly determined directions and objectives that this study should follow and pursue for the whole project. The remaining seven chapters present the originally conducted work during this study. Each of these chapters started with a brief introduction that describes the objectives of the work presented in the particular chapter, and ended with a short discussion that summarises the major points from the chapter. Below is a breakdown of the thesis. A schematic diagram of these chapters can be found in Figure 1-1.

In Chapter 3, the *in-vivo* subject-specific shoulder motion with simultaneous muscle EMG signals of the subject was measured by advanced stereophotogrammetry and wireless surface EMG system. This measured kinematic data would be further implemented to construct the subject-specific multi-body musculoskeletal model and calculate the *in-vivo* muscle activations in Chapter 4. In addition, the measured joint positions during scapular abduction would be further used to define the loading and boundary conditions of the FE model in Chapter 6 and 7.

In Chapter 4, the prediction of the *in-vivo* muscle loads under experimental motions collected from the preceding chapter was presented. These predicted muscle forces and joint positions would be implemented to FE model as physiological the loading and boundary conditions condition in Chapter 6 and 7.

Chapter 5 provided the geometrical representations of the shoulder tissues as the foundation of the FE model construction, where the defined *in-vivo* subject-specific loading and boundary condition would be applied to. These constructed solid tissue structures would be imported to Abaqus for FE model construction and simulations in Chapter 6 and 7.

In Chapter 6, the detailed construction and verification process of the FE model of the human shoulder complex in Abaqus v6.13 were presented. This FE model is an integrated model containing all modelling information from Chapter 3 to 5. Specifically, Chapter 5 provided the anatomically accurate geometrical representations of the shoulder complex that served as the foundation of the FE model. Whereas Chapter 3 and 4 defined the *in-vivo* physiological boundary and loading conditions for the FE simulation. The constructed FE model in this chapter would be further developed for the simulation of the shoulder scapular abduction in Chapter 7 and rotator cuff tear propagation study in Chapter 8.

In Chapter 7, the subject-specific quasi-static FE analysis of the shoulder scapular plane abduction measured in Chapter 3 at a sequence of humerothoracic angles namely neutral, 10, 20 and 30 degrees was performed. Firstly, FE models at respective joint angles were generated through reproducing the scapular abduction motion using the initial model constructed in Chapter 6. Secondly, the quasi-static analyses of the scapular abduction at respective joint positions were performed using the calculated muscle forces at each relative joint position of the scapular abduction in Chapter 4. The simulation results were validated against *in-vivo* measured bone-on-bone contact force and the humeral head translation relative to the glenoid during shoulder abduction as well as other simulation results in the literature.

In Chapter 8, a biomechanical study on the rotator cuff tears was performed to investigate the influence and mechanism of the rotator cuff tears on the glenohumeral joint stability during the propagation of the tears, based on the FE model of the human shoulder complex constructed and validated in the preceding chapters. The simulation results on bone-on-bone force, stress distribution, and bone movement were presented. Subsequently, based on these simulation results, the glenohumeral joint stability study was conducted using a novel integrative stability index quantifying the joint stability proposed in this study. Several clinical related findings were revealed.

Finally, Chapter 9 drew the general conclusions by reviewing the main points of the work of each constituent chapter. In addition, the novel integrative methodologies used in the thesis were summarised which formed the whole computational framework that had been proven useful for clinical applications. Finally, future work was discussed and suggested.

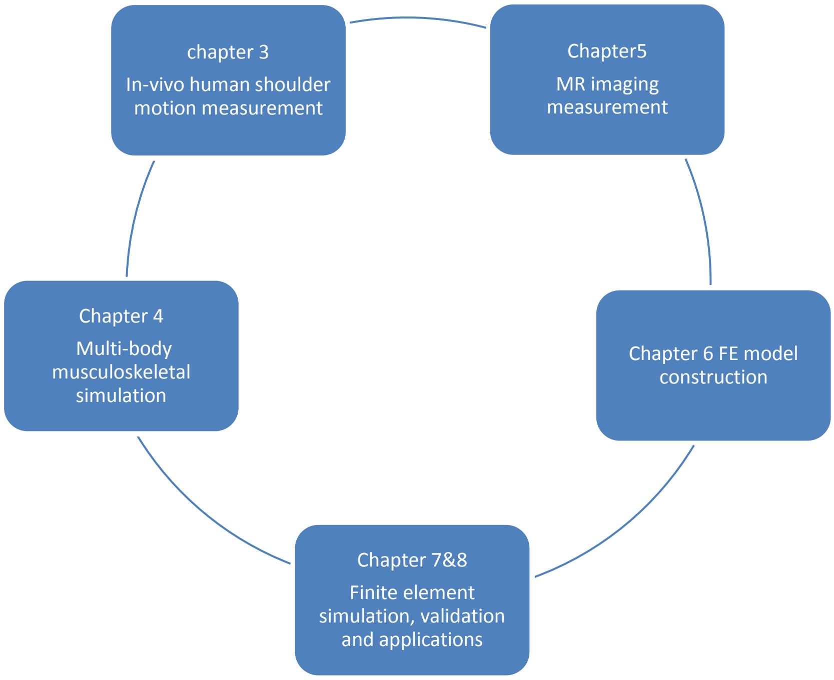

Figure 1-1 Schematic of the relationships of the chapters in this thesis

Chapter 2 Literature review

2.1 Introduction

This chapter presents the review of the background knowledge and previous works related to finite element modelling of the human shoulder complex. The review of the anatomy and biomechanical functions of shoulder joints is included in Section 2.2 which laid the foundation for the whole research. Subsequently, a thorough review of the previous published finite element studies of human shoulder complex is conducted in Section 2.3 which has been published in "International journal for numerical methods in biomedical engineering" in 2016 [8]. Finally, in Section 2.4, a summary of the review results i.e., current limitation and challenges in this field is presented together with thus determined directions and objectives that this study should follow and pursue for the whole project.

2.2 Anatomy and biomechanics of human shoulder complex

In order to construct accurate shoulder musculoskeletal models, a profound understanding of its anatomy and biomechanics is a necessity. The anatomy and biomechanics features of the major mechanical structures of the shoulder are critically discussed in the following sections including bones, joints and soft tissues.

2.2.1 Bones

"Hard tissue, mineralized tissue, and calcified tissue are often used as synonyms for bone when describing the structure and properties of bone or tooth" [9]. Bones have several major functions including supporting body, protecting organs, conducting body movement, mineral storage etc. [10]. The support and movement features are related to biomechanics. The geometry, location and orientation in the human body, and the relative motion defined by the joints are essential information for modelling which is critically reviewed in this section. Meanwhile, the bones themselves have complex substructures and have anisotropic, heterogeneous, inhomogeneous, nonlinear, thermorheologically complex viscoelastic material properties [9]. However, in the case of shoulder modelling, the active muscle control plays the major role in stability and mobility. The mechanical properties such as Young's modulus of the bones are relatively higher than those of the soft tissues. Therefore in most cases, the bone was assumed rigid due to its relatively small deformation. The shoulder skeletal morphology and muscle attachments are illustrated in Figure 2-1.

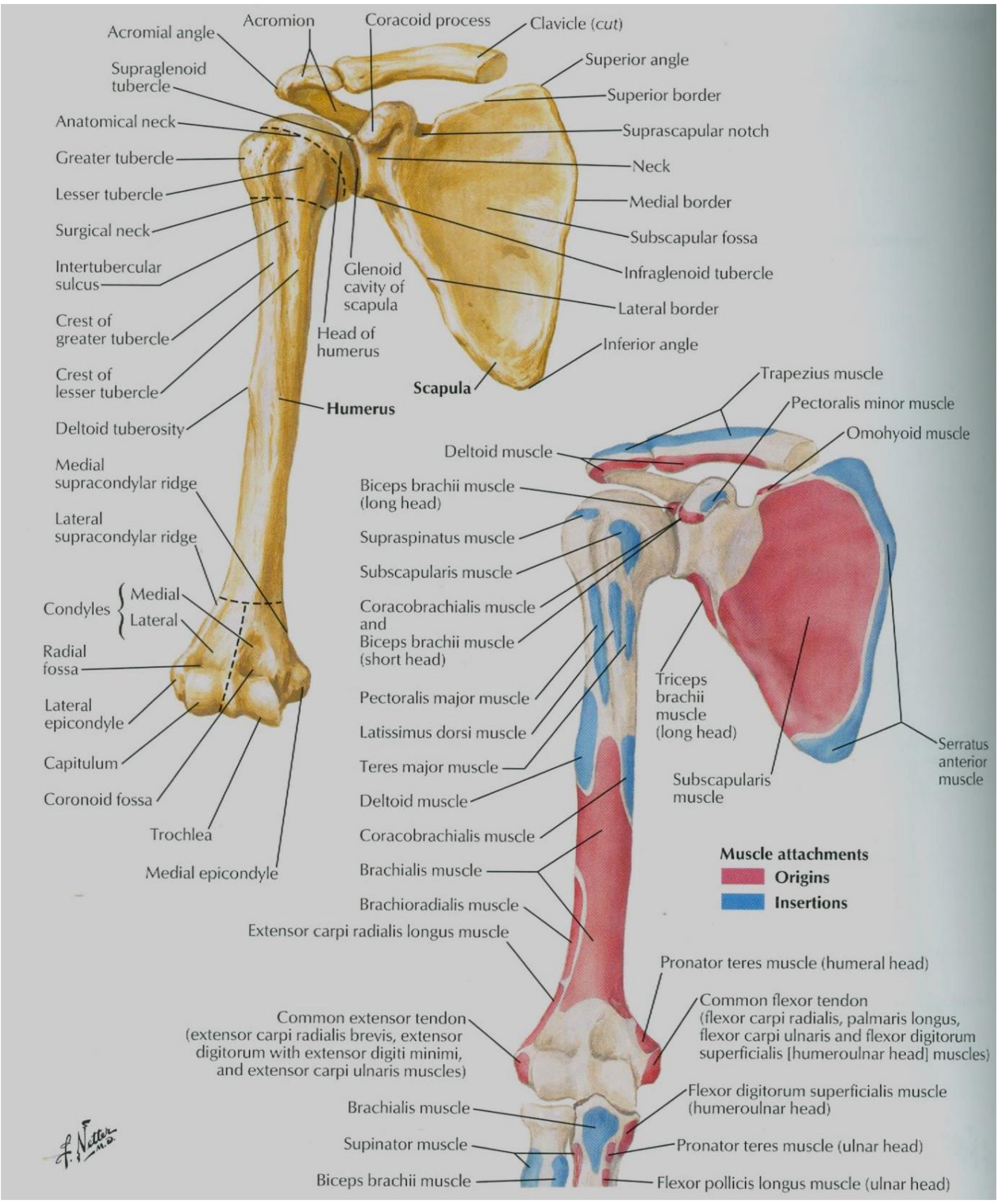

Figure 2-1 The shoulder skeletal [11]

2.2.1.1 Clavicle

The clavicles, or collarbones, are spindly, slightly curved long bones which are the sole connection between the pectoral girdle and axial skeleton (Figure 2-2). Each clavicle articulates with the trunk at the manubrium of the sternum by the sternal end, or medial end, which is a roughly pyramidal shaped end; the clavicle curves posteriorly and laterally until it articulates with the scapula at the acromial end by the acromion or the lateral end which is broader and flatter than the sternal end.

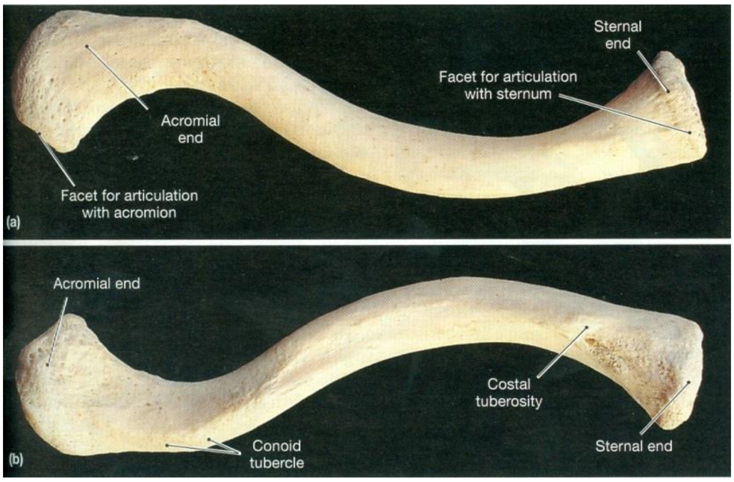

Figure 2-2 The clavicle bone (a) Superior and (b) inferior views of the right clavicle [12]

The superior surface which lies just deep to the skin is almost smooth whereas the inferior surface is rough and grooved for the attachment of the ligaments and muscles. For example, the conoid tuberosity and costal tuberosity are at the acromial end and the sternal end on the inferior surface respectively which provide the attachment sites for the ligaments of the shoulder. When one moves his / her shoulder, one can easily feel the clavicles change their positions. This is another function the clavicle performs beside providing attachments for the muscles, the limiting the position of the shoulder movements. This function is performed through two joints the sternoclavicular and the acromioclavicular joints (See Figure 2-3). The properties of these 2 joints will be discussed in Section 2.2.2.

2.2.1.2 Scapula and Humerus

“The scapulae, or shoulder blade, are thin, triangular flat bones. They lie on the dorsal surface of the rib cage, between rib 2 superiorly and rib 7 inferiorly” [10]. The scapula bone is connected to the thorax through the clavicle bone. It provides a mobile yet stable base for the motion of the humerus. The scapula also provides the insertion for a number of muscles and ligaments. Three borders, superior border, medial and lateral border, form the three sides of this scapular triangle (Figure 2-4). The superior border is the shortest and sharpest. The medial border, or vertebral border, parallels the vertebral column. The thick lateral border, or axillary border, abuts the axilla and ends superiorly in a shallow fossa, the glenoid cavity. This cavity articulating with the humerus forms the glenohumeral joint (see Section 2.2.2 for details).

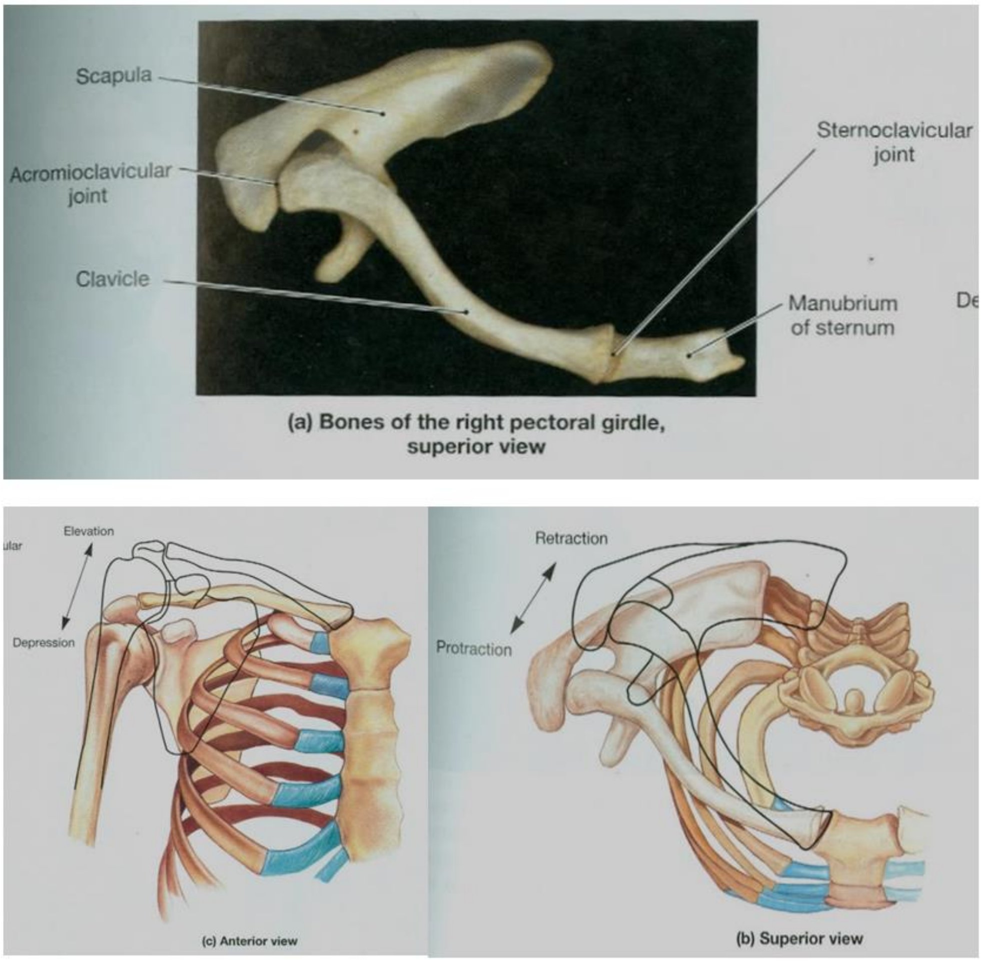

Figure 2-3 Bones of the right pectoral girdle and sternoclavicular and the acromioclavicular joints [12]

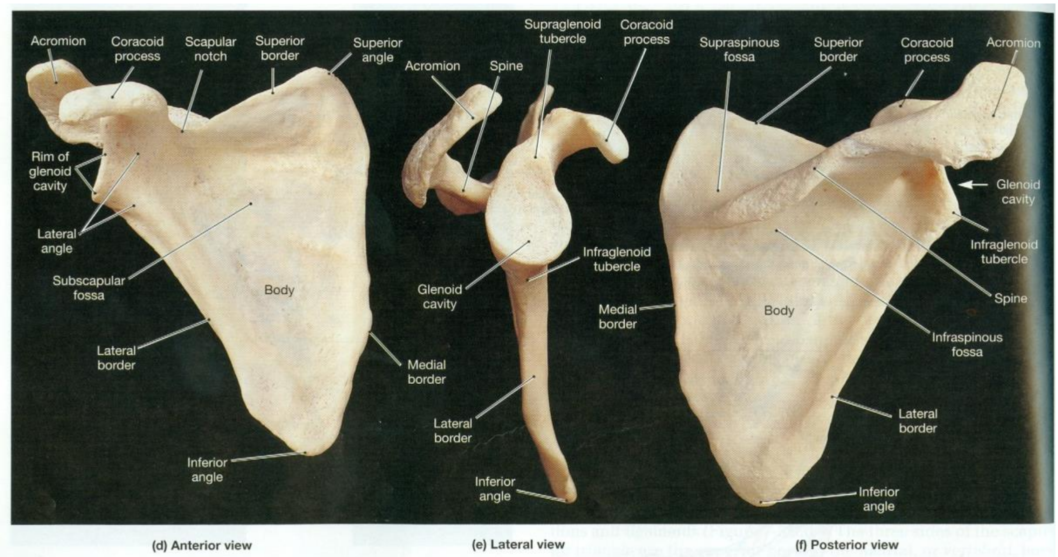

Figure 2-4 The scapula bone [12]

The humerus articulates with the scapula at the shoulder. The proximal end of the humerus is always considered as a hemispherical head which fits into the glenoid cavity [10] (See Figure 2-5). Humerus provides insertions of most of the muscles that cross the glenohumeral joint. Inferior to the head, at the lateral side is greater tubercle and more medial is lesser tubercle. These tubercles are sites where these muscles attach. Inferior to the tubercle is the surgical neck which is the most frequently fractured part of the humerus.

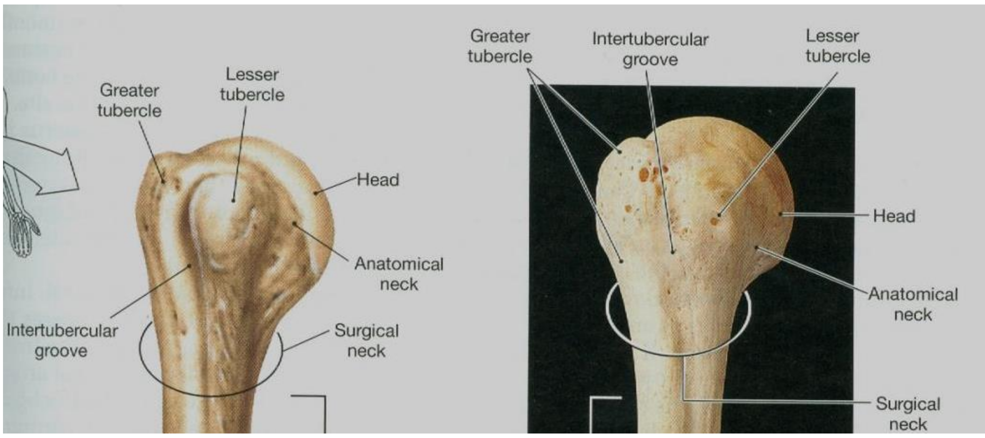

Figure 2-5 The humeral head [12]

2.2.2 Shoulder joint

The shoulder joint is comprised of five joints including three anatomical joints i.e., sternoclavicular, acromioclavicular, glenohumeral joints and two physiological joints i.e., scapulothoracic joint, subdeltoid joint [13]. The physiological joints are joints without usual anatomical features such as capsule or ligaments. Instead, they function as gliding structures to stabilise and position the shoulder [14]. All these joints are mechanically linked and move simultaneously to perform shoulder functions.

The sternoclavicular, acromioclavicular and glenohumeral joints work as a ball-socket joint which has 3 rotational degrees of freedom (DOF). Figure 2-6 takes glenohumeral joint as an example to illustrate the function of ball-socket joint.

The glenohumeral joint, or the shoulder joint as shown in Figure **2-7**, is a loose and shallow joint that provides the most freely moving joint of the body. This ball socket joint is formed by the humeral head and glenoid cavity. The articular surface of the cavity is relatively smaller than the humeral head articular surface. Even though the glenoid cavity was covered by a fibrocartilaginous glenoid labrum which deepens the joint slightly, the cavity contributes little to joint stability [10, 12]. The role of soft tissues in glenohumeral joint stability will be discussed in Section 2.2.3.

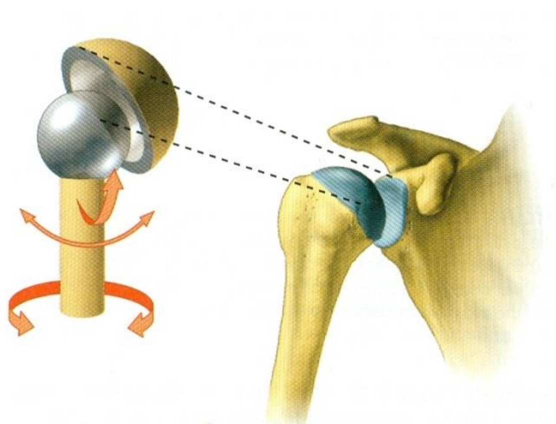

Figure 2-6 Ball-socket joint [10]

The scapulothoracic joint is predominantly made by muscles attached to the scapula (trapezius, rhomboids, levator scapulae, serratus anterior, and pectoralis minor). These muscles work simultaneously to orient the scapula in an optimal position for humeral head. "The scapula runs obliquely, mediolaterally, and posteroanteriorly, forming an angle of 30 ° open anterolaterally with the frontal plane" [13]. This plane is generally referred to as the scapulothoracic plane. Although it is not a true anatomic joint, it plays an important role in the biomechanics functions of the shoulder complex.

2.2.3 Soft tissues

Shoulder soft tissues can be divided into active and passive groups. Active soft tissues are the skeletal muscles and passive soft tissues mainly include the cartilage, ligaments, capsule and labrum. Soft tissues are the main stabiliser in shoulder mechanism.

2.2.3.1 Muscles

"Skeletal muscle tissue is packaged into skeletal muscles, discrete organs that attach to and moves the skeleton" [10]. Skeletal muscles have the vital functions in human locomotion such as movement, maintaining posture and stabilising joint. Commonly, muscles connect one bone to another across at least one joint by a rope-like tendon structure. Tendon is a tough band of fibrous connective tissues made from collagen. When muscles contract, they pull through tendons to bones which further cause one bone to move relative to another. In shoulder joint, most of the muscles have tendon structures except the deltoid muscle which is fleshly attached to the scapula and humerus bone. Most of the shoulder disorders occur in the muscle tendons attaching to the humerus bone, such as rotator cuff tears. Therefore, most previous studies focused

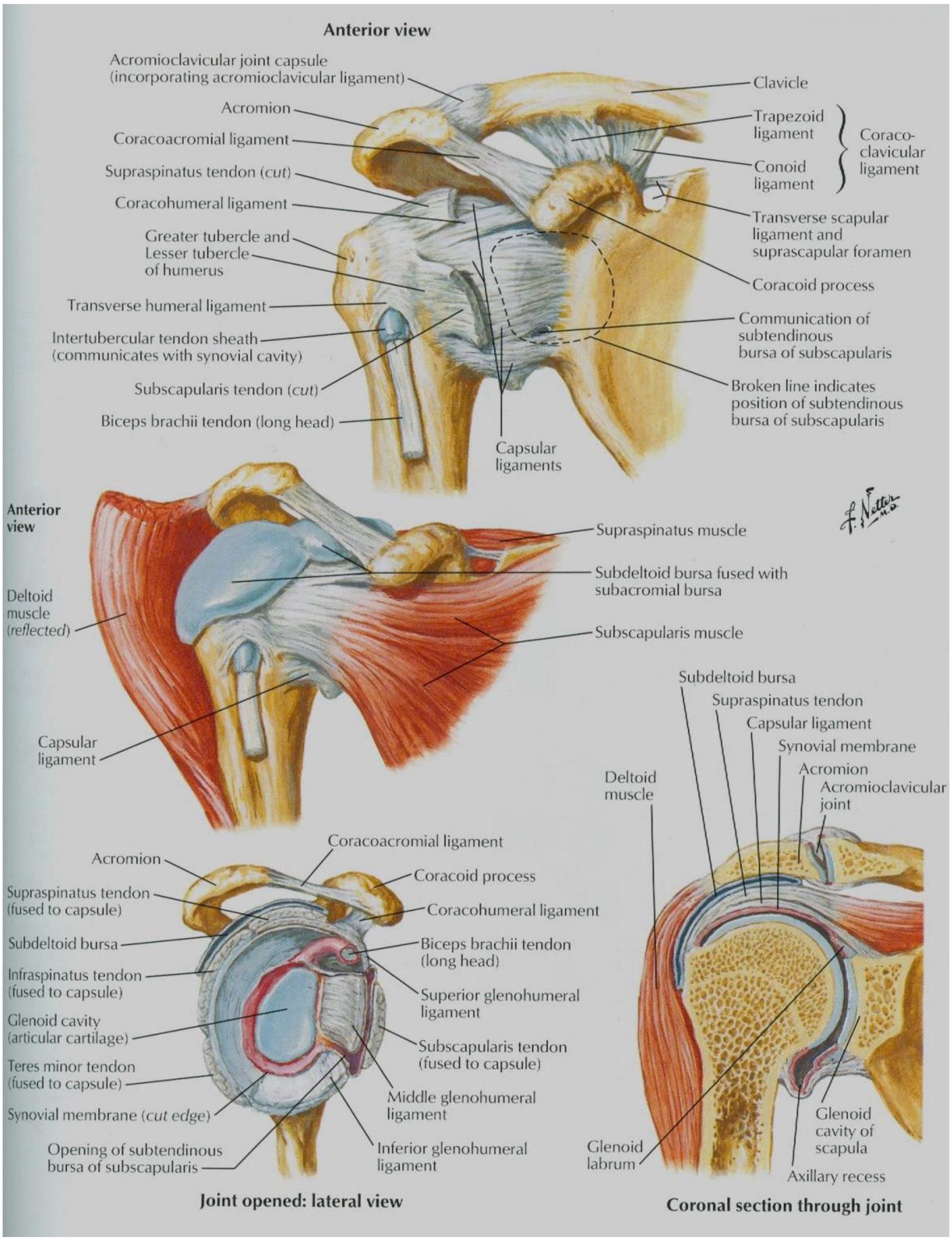

Figure 2-7 The glenohumeral joint [11]

on the tendon structures [15-17] or treated the whole muscle-tendon systems as tendons [18]. Similarly, since this study conducted the research on the large-scale joint mobility and stability analyses, the muscle-tendon system was treated all as the tendon as well. For simplicity, from this point onwards in this thesis, when the word “muscle” is mentioned, it is referred as the muscle-tendon system.

Muscle that cross the shoulder joint contribute most to the joint's stability [10]. For example, the biceps brachii long head attaches to the superior margin of the glenoid labrum, travels around the humeral head through the intertubercular groove of the humerus which secures the head of the humerus tightly against the glenoid cavity. Rotator cuff muscles including subscapularis, supraspinatus, infraspinatus, and teres minor provide substantial support for the joint and blend with joint capsule. The geometries of the muscles of the shoulder are critically reviewed and illustrated in Figure 2-8. These muscles of the shoulder can be divided into 2 groups: Muscles that position the pectoral girdle and Muscles that move the arm. Muscles that position the pectoral girdle: Levator scapulae, pectoralis minor, rhomboideus major, rhomboideus minor and serratus anterior trapezius; Muscles that move the arm: Coracobrachialis, deltoid, supraspinatus, infraspinatus, subscapularis, teres major, teres minor, triceps brachii, latissimus dorsi and pectoralis major.

2.2.3.2 Cartilage and labrum

Articular cartilage is a connective tissue that covers each end of the opposing bones. The cartilage can absorb compression and lubricate the joints. Cartilages in shoulder mechanism locate in glenohumeral joint (Figure **2-7**: Joint opened: lateral view) and sternoclavicular and the acromioclavicular joints. Functioning together with the fluid that fills the joint cavity, the friction coefficient of normal synovial joint such as the glenohumeral joint can be as low as 0.001 [19].

As mentioned in the glenohumeral joint section, the labrum is a fibrocartilage structure that covers the surface of the glenoid cavity which deepens the joint slightly (Figure **2-7**: Coronal section through joint). The labrum is general believed to provide slight stability by its geometrical form and conformity to the head of humerus [20]. In addition, the labrum serves as the attachment for biceps tendon and the glenohumeral ligaments.

2.2.3.3 Capsule and ligament

Similar to tendons, ligaments are band-like connective tissues made from collagen. In synovial joints, such as the glenohumeral joint, ligaments strengthened and reinforced the joint by holding bones together and prevent excessive or undesirable motions [10]. Ligaments are considered minor stabiliser in normal shoulder function comparing to the muscle. Ligaments normal only have limited stretchable ability. Therefore, in dislocated shoulders, the ligament tears such as humeral avulsion glenohumeral ligament (HAGL) tears are quite common. In glenohumeral joint, ligaments are blended with the joint articular capsule. The articular capsule is a thin and loose structure and extends from the margin of the glenoid cavity to the anatomical neck of the humerus. The only strongly thickened part of the capsule is the superior coracohumeral ligament and slightly thickened in the anterior part by rather weak glenohumeral ligaments [10]. Other than these ligaments, the rest of major ligaments that stabilise the glenohumeral joint are the acromioclavicular ligament, coracoclavicular ligaments and transverse humeral ligament. (Figure **2-7**: Anterior view)

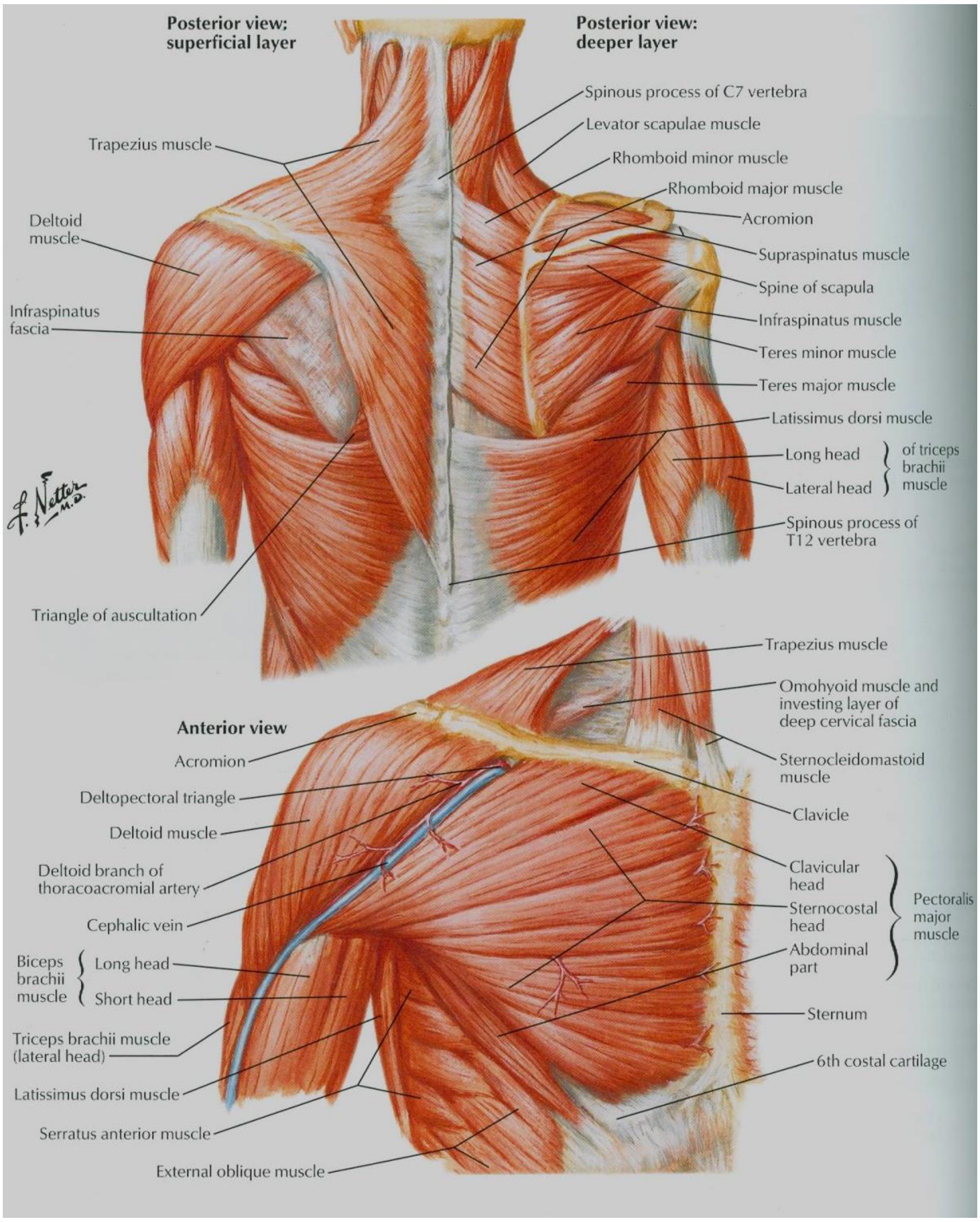

Figure 2-8 Muscles of shoulder [11]

2.3 Review of finite element models of the human shoulder complex

This section provides a thorough review of previous finite element (FE) studies in biomechanics of the human shoulder complex. The text in this part of the thesis i.e. section 2.3 has been published as part of the peer-reviewed journal paper by the author published in the International Journal for Numerical Methods in Biomedical Engineering [8] included in full in Appendix B.

Traditional biomechanical measurements are limited by the existing measuring techniques and ethical issues, and the *in-vivo* internal loading condition of the shoulder musculoskeletal complex is almost unmeasurable [21]. Most of the experimental studies to investigate the load transfer in the shoulder structure were limited to *in-vitro* conditions [22-26]. In this scenario, a computational method based on musculoskeletal models provides a valuable tool to estimate the biomechanical behaviour of the shoulder complex under different loading conditions. Computational shoulder models can be roughly classified as two major categories: multi-body models based on rigid body dynamics and finite element models based on continuum mechanics. In multi-body models, the body segments are assumed to be rigid bodies without deformations and muscles are simplified as single line actuators without 3D volume. In combination with muscle wrapping and muscle force estimation methods (optimisation-based or EMG-driven), these kinds of models are typically used for determining muscle forces *in-vivo* [27-32]. Through dynamic simulation analysis, multi-body models have the potential to investigate neuromuscular control strategies, musculoskeletal dynamics and simulated surgical interventions [33]. However, due to the major model simplification, the sophisticated deformations, stress distributions and interactions of different components of the shoulder musculoskeletal structure cannot be simulated by using multi-body models. Those are critical contributors to the *in-vivo* biomechanical and physiological functioning of the shoulder complex and therefore make it difficult to make any clinically useful conclusions from data provided by these methods. Moreover, measurement data used for driving multi-body models normally suffers from skin artefacts due to skin mounted markers used in motion analysis. Despite those limitations, multi-body models provide a valuable tool to improve our understanding of the *in-vivo* biomechanical functioning of the musculoskeletal system [34].

On the other hand, continuum mechanics models based on a finite element (FE) method offers a powerful tool to assess the internal loading conditions of the shoulder musculoskeletal structure [6]. They can provide valuable estimates of stress and strain distributions in the bones and soft tissues, which are usually not measurable *in-vivo*. The FE method was first developed to solve elasticity and structural analysis problems in 1940s [35]. Its basic concept is the discretisation (division) of complex mechanical structures into finite numbers of separate components with simple geometry called elements. In this way, complex nonlinear problems become solvable numerically. Nowadays, the FE method has been widely used in different engineering fields for system design and analysis [36]. Over the past decades, the FE method has also been increasingly used for investigating a large range of problems in biomechanics and orthopaedics [37]. According to a recent study, the number of articles using FE analysis in biomechanics appears to be increasing geometrically based on the PubMed database [38]. In FE shoulder modelling, the biggest challenge is how to properly represent the complicated structures and materials of the shoulder musculoskeletal system. This paper provides a critical review of the previous studies using FE models to investigate shoulder biomechanics, which are roughly categorised according to the physiological and clinical problems addressed: glenohumeral joint stability, rotator cuff tears, joint capsular and labral defects, and shoulder arthroplasty. The key modelling techniques used in each of those studies are listed in Table 2-1. The articles reviewed in this study were found based on the Web of Science and PubMed databases by using the keywords of "finite element", "numerical simulation", "glenohumeral joint" and "shoulder joint".

Table 2-1 Key modelling techniques and parameters used in the FE shoulder studies reviewed in this paper.

Clinical issue	Dimension	Geometric acquisition		Model components	Material properties		Boundary conditions	Loading conditions	Validation	Reference
		Bones	Soft tissues		Bones	Soft tissues				
Joint instability	3D	In vitro CT scans	In vitro measurement for muscle insertions; Cartilages filling the space between bones	Scapula and humerus; major abduction muscles: deltoid, supraspinatus, infraspinatus, subscapularis	Humerus is rigid; Scapula bone is linear elastic, nonhomogeneous material. $E(\rho) = E_0 (\rho/\rho_0)^2$, $\nu = \nu_0$, where E_0=15000, ν_0=0.3 ρ_0=1800.[39, 40]	Muscles were assumed exponential hyperelastic, incompressible $W = \alpha \exp(\beta(I_1-3)) - \alpha\beta/2(I_2-3)$ Where α=0.12MPa, β=1.0; [41-43] Cartilage was defined based on the Neo-Hookean incompressible constitutive law. $W = C_{10} (I_1 - 3)$ with $C_{10} = E/4(1+ \nu)$ where C_{10}=1.79 (E=10, ν=0.3). [44]	Humerus fixed in transverse plane, vertical translation supported by a spring; Scapula limited by spring elements fixed at spine; Muscles attached fixed with scapula	Initial pre-stress 1.5kPa on all muscles; Artificial gradual displacement on infraspinatus (external rotation) and subscapularis (internal rotation)	NO	Büchler P, et al.[45] (2002)

3D	Same as [45]	Same as [45]	Scapula and humerus; major abduction muscles and deltoid	Rigid	Cartilage was defined based on the Neo-Hookean incompressible constitutive law by W= $1.8(I_1-3)$; Muscle was modelled using parallel stiff fibres embedded along the principal direction of the muscle volume, which was described by a soft Neo-Hookean material with W = $0.5(I_1-3)$.	Estimated muscle forces based on literature data	Artificial rotation of scapula and humerus; A humerus weight of 37.5N applied on mass centre	Validate against literature[16] and in vitro study[46, 47]	Terrier A, et al.[48] (2007)
3D	Literature data		Humerus and scapula; ligaments	Rigid	Cartilages defined as Neo-Hookean hyperelastic, incompressible material.C_{10} = $E/4(1+\nu)$ $D_{10} = E/6(1-2\nu)$ Where E=10, ν=0.4 [45, 44]	Humerus fixed in sagittal plane, unconstrained laterally	Humerus moved 1.2mm to contact glenoid surface; 50N compressive load applied on humeral head laterally; [26, 22] Move humerus in anteroinferior direction about 17mm	Validated against cadaver studies [26, 22]	Walia P, et al.[49] (2013)

Clinical issue	Dimension	Geometric acquisition		Model components	Material properties		Boundary conditions	Loading conditions	Validation	Reference
		Bones	Soft tissues		Bones	Soft tissues				
	3D	In vitro CT scans for scapula Literature data for humerus	Published anatomical data (cartilage and labrum)	Humerus and glenoid; cartilage and labrum	Isotropic linear-elastic (E=18000, ν=0.35)	Cartilage and labrum are defined same as [45] Cartilage: C_{10}=1.79 (E=10, ν=0.4) and Labrum: C_{10}=12.5 (E=70, ν=0.4).	Estimated active muscle forces from multi-body model; Artificial glenohumeral elevation in scapular plane from 0º to 80º with arm weight 35N applied at arm centre of mass		Validated against in vitro[46, 50] and in vivo (EMG)[51, 30] studies	Favre P, et al.[52] (2012)
Rotator cuff tears	2D	In vitro MRI scans		Humerus and glenoid; supraspinatus, supraspinatus tendon	Rigid	Supraspinatus tendon was defined as biphasic, linear, fiber reinforced composite with longitudinally arranged collagen fibers (E=800) acting with an extrafibrillar matrix (plain stress element with E=8, ν=0.497).[53]	Humeral head fixed	Estimated theoretical load and angle on supraspinatus	No	Luo ZP, et al.[15] (1998)
	2D	In vivo MRI (humeral head)	In vivo MRI for supraspinatus In vitro measurement for cartilages	Humeral head; supraspinatus tendon and cartilages	Humeral head was divided to 3 regions: cortical bone (E=13800, ν=0.3); subchondral bone (E=2780, ν=0.3); cancellous bone (E=1380, ν=0.3)[54]	Supraspinatus tendon: E= 168, ν=0.497. Articular cartilage: E= 35, ν=0.450.[55, 53] Medium values between the tendon and the cancellous bone were defined for calcified fibrocartilage (E= 976, ν=0.366) and noncalcified	Humeral head fixed	Estimated theoretical load and angle on supraspinatus	Validated against literature data [15]	Wakabayashi I, et al.[16] (2003)

					fibrocartilage (E= 572, ν=0.432).				
2D	Same as [16]	Same as [16]	Humeral head; supraspinatus tendon and cartilages	Same as [16]	Same as [16]	Humeral head fixed	Estimated theoretical load and angle on supraspinatus	Validated against literature data [15]	Sano H, et al.[17] (2006)
3D	In vivo CT scans for humeral head	In vivo MRI for tendon; In vitro measurements for calcified and noncalcified cartilages;	Humerus head; supraspinatus tendon and cartilages	Same as [16]	Same as [16]	Humeral head fixed	Estimated theoretical load and angle on supraspinatus	No	Seki N, et al.[56] (2008)

Clinical issue	Dimension	Geometric acquisition		Model components	Material properties		Boundary conditions	Loading conditions	Validation	Reference
		Bones	Soft tissues		Bones	Soft tissues				
Rotator cuff tears	3D	In vitro CT scans for scapula and humerus	Cryosection photos for glenoid, humeral cartilages and rotator cuff tendons	Scapula and humerus; humeral articular cartilage and rotator cuff tendons	Rigid	Cartilage was modelled as a rigid body with a pressure-overclosure relationship;[57] Tendons were represented with a linear elastic orthotropic material model (E=140 ν=0.497). [15, 58]	Scapula fixed; Pre-defined kinematic boundary for humerus	Artificial rotation from 45° internal to 45° external about an axis parallel to the humeral shaft;	Validated against in vitro study	Adams C, et al.[59] (2007)
	3D	In vivo CT scans		Scapula and humerus; rotator cuff tendons and deltoid muscle	Solid E=15000, ν=0.3. [59, 48]	Muscle and tendons were defined as non-linear elastic material; Articular cartilage linear elastic E=15, ν=0.45.[60, 61]	Scapula fixed	Pre-defined loads on tendons based on cadaver studies [62, 23, 24]	Validated against in vitro study[61]	Inoue A, et al.[18] (2013)
Capsule and labrum defects	3D	In vitro CT scans		Scapula and humerus; anterior band of IGHL	Rigid	Anterior band of IGHL was represented using fiber-reinforced composites. (average material properties from literature)	Measured bone kinematics from the cadaver study		No	Debski R, et al.[63] (2005)
	3D	In vitro CT scans		Scapula and humerus; joint capsule and rotator cuff	Rigid	IGHL was defined as isotropic hypoelastic. (E=10.1, ν=0.4)[64]	Measured bone kinematics from the cadaver study[25]		Validated against in vitro study[65, 64]	Ellis B, et al.[66] (2007)

		tendon					
3D	In vitro CT scans	Scapula and humerus; capsule, ligaments and cartilages	Rigid	Capsular regions have the same ν=0.4995 but individual E: Anterior band of IGHL E=2.05 Posterior band of IGHL E=3.73 Anterosuperior E=2.12 Axillary pouch E=4.92 Posterior E=2.05	Measured bone kinematics from the cadaver study[67]	Validated against in vitro study	Moore S, et al. [68] (2008)
3D	Same as [68]	Scapula and humerus; capsule and cartilage	Same as [68]	Same as [68]	Measured bone kinematics from the cadaver study	Validated against in vitro study	Ellis B, et al.[69] (2010)
3D	In vitro CT scans	Scapula and humerus; capsule, humeral head cartilage	Rigid	Capsule tissues were represented using an isotropic hyperelastic constitutive model.	Measured bone kinematics from the cadaver study	Validated against specimen-specific in vitro study	Drury N, et al.[70] (2011)

Clinical issue	Dimension	Geometric acquisition		Model components	Material properties		Boundary conditions	Loading conditions	Validation	Reference
		Bones	Soft tissues		Bones	Soft tissues				
Capsule and labrum defects	3D	In vitro measurements		Glenoid labrum and biceps long head tendon	Glenoid defined as elastic isotropic material (E=1400)	Labrum and biceps defined as elastic isotropic material (E=241)	Glenoid fixed	Pre-defined loads on LHBT from muscle activities from literature[71]	No	Yeh ML, et al.[72] (2005)
	3D	In vitro CT scans		Glenoid; labrum, cartilages of humeral head and glenoid	Rigid	The humeral cartilage was assumed rigid; Glenoid cartilage was isotropic with properties of $E=1.7$, $\nu=0.018$, $\varphi_s=0.25$, $\rho=1075$; Labrum was transverse isotropic with properties of $E_p=0.24$, $E_\theta=22.8$, $^{v}{}_{p}=0.33$, $^{v}{}_{\theta p}=0.10$,$G_{\theta p}=2$ $\varphi_s=0.75$, $\rho=1225$ Subscripts define the transverse plane (p) and the circumferential direction (θ) of the labrum.[73-75]	Glenoid fixed Humeral cartilages constrained from all rotations and displacement along X-axis direction (anteroposterior oblique direction).	Move the humeral cartilage 1, 2, and 3 mm in +Y direction (superiorly) 50N applied in –Z direction (medial oblique direction)	Validated against in vitro study	Gatti C, et al.[20] (2010)

3D	In vitro CT scans	Glenoid, glenoid labrum, humeral head and glenoid cartilage.	Rigid	Estimated material coefficients of capsule.[63, 76]	Measured humerus motion from in vitro experiment	25N anterior load applied at 60^{o} of glenohumeral abduction and 0^{o}, 30^{o} and 60^{o} of external rotation	Validated against in vitro study	Drury N, et al. [77] (2011)

E: Young's Modulus (MPa); ν: Poison's ratio; ρ: density ($Kg{\cdot}m^{-3}$); I_1: first invariants of the Cauchy-Green tensor; G: shear modulus (MPa); φ_s solid volume fraction; W: strain energy density function; C_{10}, D_{10}: material property constants.

2.3.1 FE modelling of shoulder complex

2.3.1.1 FE models of glenohumeral joint stability

The low congruity of the articular joint surfaces in the shoulder affords its large range of motion, however it predisposes it to being the most commonly dislocated joint of the body. A number of studies have been conducted to investigate instability of the glenohumeral joint by using FE models considering the major components of the shoulder complex.

Buchler et al. [45] used a FE glenohumeral joint model, consisting of the major rotator cuff muscles and bones, to investigate the changes in joint contact stresses due to the changes of the shape of the humeral head and the glenoid contact shape and orientation in both healthy and pathological conditions. It was found that the changes in shape of the humeral head due to joint disorders (e.g. osteoarthritis) may reduce joint stability. However, one of the drawbacks of this study is lack of validation. This FE glenohumeral joint model was also used for analysing the biomechanical effect of the shapes of prosthetic humeral heads after shoulder arthroplasty [78]. Two prosthetic designs were examined against an intact shoulder: the second-generation (Neer II) and a patient-specific anatomical implant. Similar to the previous FE simulation, joint contact stresses (location and magnitude) were calculated and compared in three cases: intact shoulder, Neer II and patient-specific condition. The result showed that the patient-specific implant produced closer biomechanical conditions in both stress location and magnitude to the intact shoulder than the second generation implant. The Neer II implant moved the joint contact area eccentrically and led to bone contact stresses being up to 8 times higher than in the intact shoulder.

Terrier et al. [48] used a 3D FE model of the shoulder to investigate the biomechanical consequence of supraspinatus deficiency with a major focus on the reduction in glenohumeral joint stability that could lead to secondary osteoarthritis. The effect of supraspinatus deficiency was examined by FE model analyses in both healthy and pathological conditions (considered as a full supraspinatus tear). The result suggested that supraspinatus deficiency increases the upward migration of the humeral head resulting in increased eccentric loading, and thus decreases glenohumeral joint stability.

A similar FE shoulder model was used for investigating the effect of combined defects of the humeral head (Hill-Sachs) and of the glenoid (bony Bankart lesion) by Walia et al (see Figure 2-9) [49]. It was found that the glenohumeral joint stability (defined as the ratio of shear force to compressive force) was decreased from 43% to 0% for the combined presence of both lesions compared to the normal healthy shoulder.

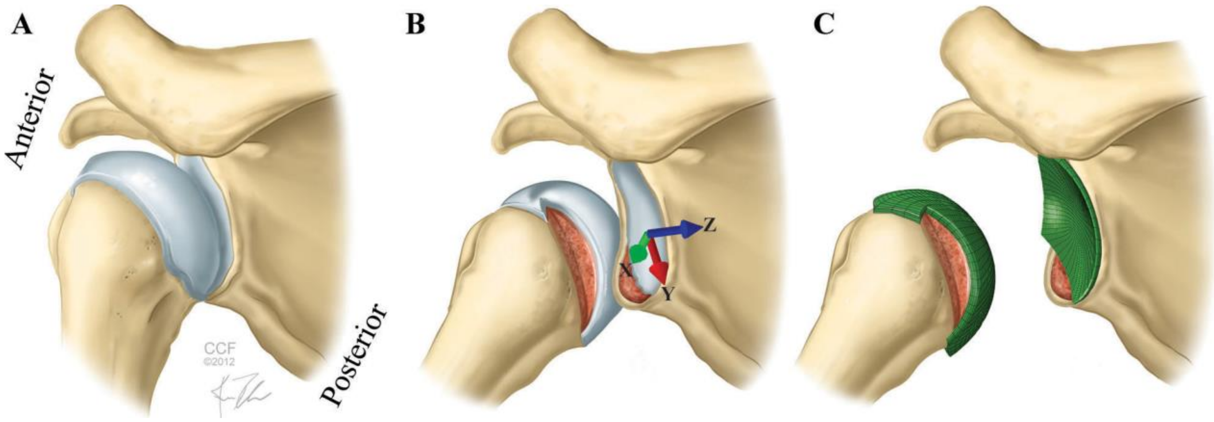

Figure 2-9 FE Simulation of the Hill-Sachs and bony Bankart lesion. (A) Intact shoulder at 0^{o} abduction; (B) Combination of Hill-sachs and bony Bankart lesion at 90^{o} abduction; (C) FE mesh in combined case [49]

A recent FE model of the glenohumeral joint used estimated muscle forces as the loading condition, and the humerus was allowed to move freely with six degrees of freedom [52]. These loading and boundary conditions enable the FE analyses to simulate motions of the shoulder complex closer to its realistic physiological condition than those with pre-described or artificially defined constraints. The FE analyses used tissue deformations, contact areas and contact pressures to evaluate glenohumeral joint stability. This study provides a useful framework for future FE studies of the shoulder complex. The major limitation of the study is that only the scapula and the humerus bones were considered, and the 3D geometry and structure of muscles and other soft tissues were neglected in the model. Their interactions with the bones and other musculoskeletal components could not be examined in the FE analyses.

In the studies discussed, different methods were used for quantifying glenohumeral joint stability. Buchler et al. [45] used an average of the contact area between the humeral head and the glenoid. Similarly, Terrier et al. [48] calculated the contact point on the glenoid to measure joint stability. Walia et al. [22] used a stability ratio (shear force over compressive force) defined in a cadaveric study. In a recent study by Favre et al.

[52], glenohumeral joint stability was defined as the shear force required to dislocate the joint under a 50N compressive load. The common feature of these methods is that glenohumeral joint stability is measured as the ability of the joint to keep the humeral head in the centre of the glenoid either through relative displacements or shear and compressive stresses. However, little is known about the relationships between those different methods. There is a lack of comparative studies as well a need to standardise how to quantify and report shoulder joint stability. Moreover, for simplification, most of the previous modelling studies considered only part of the shoulder musculoskeletal complex by neglecting some important factors that may have considerable effect on joint stability, e.g. muscle to muscle and/or muscle to bone contact forces. This leads to a poor understanding of the individual contribution of musculoskeletal components to shoulder stability. Joint stability is an overall performance that requires effective functioning of each part of the musculoskeletal structure [79]. Therefore, systematic investigations based on more comprehensive modelling with exchangeable evaluation results are needed for future studies.

2.3.1.2 FE models of rotator cuff tears

The shoulder complex is actively stabilised by contractions of the rotator cuff muscles. Rotator cuff tendon tears are one of the most common pathologies in the shoulder and the supraspinatus tendon is the most frequently affected. Tears can cause chronic shoulder pain, and may lead to secondary degenerative changes in the shoulder (e.g. cuff tear arthropathy). The aetiology of a rotator cuff tear is multi-factorial with genetic and environmental factors playing an important role. However, so far, the fundamental mechanism that initiates rotator cuff tears remains unclear. A number of studies have been conducted to explore the underlying biomechanical mechanisms which might cause rotator cuff tears using FE shoulder models.

In 1998, Luo et al. [15] used a simplified 2D FE shoulder model for the first time to investigate the initialisation mechanism of rotator cuff tears by analysing the stress environment in the supraspinatus tendon. The stress distribution was evaluated at the humeroscapular elevation angle of 0°, 30° and 60° respectively and also under two different acromial conditions (with and without subacromial impingement). It was found that the high stress concentration generated by subacromial impingement could initiate a tear. Moreover, the results showed that this tear may occur on the bursal side, the articular side, or within the tendon rather than only on the bursal side as the traditional mechanical models suggest. Two further studies based on improved Luo's model were conducted. Wakabayashi et al. [16] applied histological differences at the tendon insertion in their FE model to analyse the stress environment of the supraspinatus tendon. This study showed slightly different result from Luo's study and found that the maximum principle stress of the tendon occurs at the region in contact with the humeral head rather than at the insertion point. Whereas Sano et al. [17] examined the stress distribution in the pathological rotator cuff tendon and revealed potential partial thickness tears at three different locations: on the articular surface, on the bursal surface and in the mid-substance close to the insertion. It was found that high stress concentration occurs at the articular side of the insertion and the site of tear. The two studies used same modelling method and conditions as Luo's original model, but employed different histological parameters to simulate pathological conditions. Though those studies have improved our understanding of the initiation mechanism of rotator cuff tears, they were limited to 2D condition and lacked experimental validations.

The first 3D FE model of rotator cuff tears was reported by Seki et al. [56] in 2008 to analyse the 3D stress distribution in the supraspinatus tendon. It was found that the maximum stress occurs in the anterior portion of the articular side of the tendon insertion rather than at the tendon contact point with the humeral head as suggested by 2D analyses. This explains the frequent occurrence of rotator cuff tears at this site. This improvement was achieved due to the advantage of the 3D model analysis where the anteroposterior direction was investigated showing that the anterior part of the rotator cuff is not in contact with the superior surface of the humeral head. However, this study only analysed part of the shoulder complex at 0° abduction without experimental validation.

Adams et al. [59] used a 3D FE model of the glenohumeral joint to investigate the effect of morphological changes in the rotator cuff tendons following a tear. The result showed that the moment arms of infraspinatus and teres minor muscles were generally decreased. Consequently, the muscles attached to the torn tendons are required to generate more forces for the same motions, and the overall strength of the shoulder is decreased. This study revealed a potential relationship between shoulder strength reduction and sizes and locations of the rotator cuff tears. The magnitudes and general trends of the calculated moment arms were found in reasonably good agreements with the measured data. A limitation of this study is that tendons were divided along the force bearing direction, which only happens in massive cuff tears transverse to tendon collagen fibrils. Cuff tears along tendon collagen fibrils were neglected in the model analysis.

A most recent FE study of rotator cuff tears was conducted by Inoue et al. [18] A 3D FE model including the rotator cuff muscles and the middle fibres of the deltoid muscle was used for investigating the biomechanical mechanism of rotator cuff tears. Different stresses were found in the articular and bursal sides of the supraspinatus tendon resulting in shearing between the two layers, which was believed to initiate partial-thickness tears (see Figure 2-10). The limitation of this study is that the muscles and bones were reconstructed based on CT images, which are not very suitable for segmentation of soft tissues. Moreover, the simulated movement was limited to shoulder abduction and only three rotator cuff muscles and middle fibres of the deltoid were considered in the model.

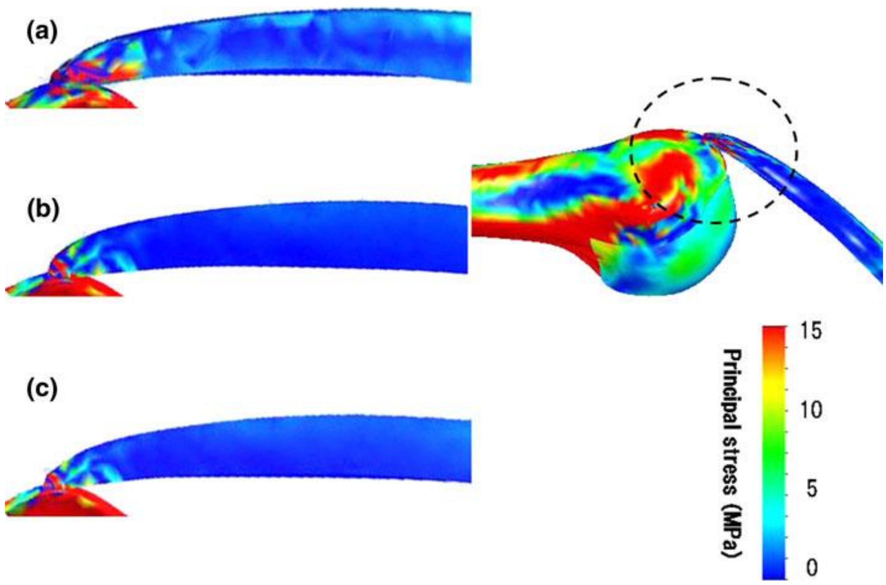

Figure 2-10 Distributions of tensile stress in the supraspinatus tendon at 90^{o} abduction View (a), (b) and (c) are anterior, middle and posterior section of the supraspinatus tendon in the sagittal plane respectively [18]

Those modelling studies investigated the aetiology of rotator cuff tears based on the hypothesis that mechanical stress concentration initiates tendon tissue tear. Although recent studies demonstrated some promising results, the underlying mechanism triggering the pathological process still remains unclear [18]. As the shoulder joint is actively stabilised by the rotator cuff muscles, the loading condition at the rotator cuff tendon may have a major effect on the simulation results. However, existing FE models either used in vitro data or were based on roughly estimated tendon force data. Therefore, more accurate *in-vivo* muscle force data is needed in order to provide more convincing results to reveal the fundamental mechanism underlying rotator cuff tears.

2.3.1.3 FE models of capsular and labral defects

The shoulder articular capsule and labrum are the major passive stabilisers of the glenohumeral joint. The capsule is a thin and loose structure reinforced by surrounding ligaments such as the inferior glenohumeral ligament (IGHL). The labrum is an integral component of the glenoid insertion of the IGHL, which increases the depth and concavity to the glenoid fossa to resist the humeral head translation [70]. Injuries, such as a Bankart lesion or HAGL lesion (humeral avulsion of the glenohumeral ligament), are common after an anterior shoulder dislocation. A number of FE studies have been conducted to understand the pathomechanics of the shoulder capsule and labrum. This may lead to new biomechanically oriented strategies to improve clinical diagnosis and surgical interventions to address capsular and labral defects [69].

The first FE study of the capsule was conducted by Debski et al. [63] in 2005, where a FE model of the glenohumeral joint with the anterior band of the IGHL was used for analysing the stress and strain distribution in the IGHL. Although the study revealed the continuous nature of the glenohumeral capsule, the FE model was limited by the fact that only the anterior band of the IGHL was considered and experimental validation was absent. Another FE model of the IGHL was constructed later to examine the strains and forces in the IGHL complex by Ellis et al.[66] It was found through a sensitivity analysis that the predicted strains were highly sensitive to the changes in the ratio of bulk to shear modulus of the IGHL complex. A further study suggested that it is more appropriate to consider the glenohumeral capsule as a sheet of fibrous tissue. This provides useful suggestions on better representation of ligaments in FE modelling [68].

Recently, Ellis et al. [69] constructed two subject-specific FE models of the IGHL to analyse the glenohumeral joint positions in clinical examinations by evaluating the strain distribution (see Figure 2-11). It was suggested that the isolated discrete capsule regions should not be used in analysing the function of the glenohumeral capsule. The study concluded that the positions of 30° and 60° of external rotation can be used for testing the glenoid side of the IGHL during clinical examinations, but are not useful for assessing the humeral side of the IGHL [69]. This provides useful suggestions to improvements in clinical evaluation of shoulder instability. The most recent FE study of the glenohumeral capsule was conducted by Drury et al. [77] with a more detailed model construction. The result showed that the glenoid side of the capsule undergoes the greatest deformation at the joint position under 60° abduction and at a mid-range (20°−40°) of external rotation. This suggested that standard glenohumeral joint positions could be used for the examination of pathology in the anterior inferior capsule caused by dislocations. FE studies have also been conducted to investigate defects of glenohumeral labrum, such as superior labrum anterior posterior (SLAP) tears, which are normally found among athletes involved in overhead sports [72]. Yeh et al. constructed 3D FE models of the superolabral complex with different biceps origins at four orientations during throwing, and the change of peak stress was examined. The maximum stress about 160Mpa was found in the deceleration phase of throwing, two times of that in the late cocking phase. This high stress in the deceleration phase may lead to tears at the superior glenohumeral labrum. However, no experimental validation was conducted in this study. A later FE study revealed that the superior humeral translation resulting in a shear force to the labrum could be a possible mechanism to the development of SLAP lesions [20].

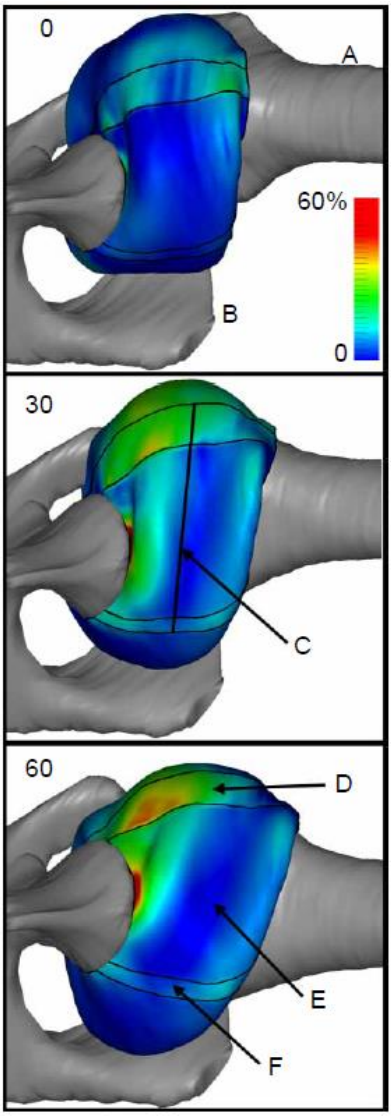

Figure 2-11 Inferior view of the first principal strain distribution in the left shoulder under 60^{o} of abduction at 0^{o}, 30^{o} and 60^{o} of external rotation. A, Humerus; B, glenoid; C, IGHL mid-line; D, Anterior band of IGHL; E, axillary pouch and F, posterior of IGHL [69]

Recent studies have attempted to consider both the capsule and labrum in FE glenohumeral joint models. Drury et al. [70] constructed a subject-specific FE model of the glenohumeral joint with the capsule and labrum components to investigate the effect of degenerating tissues on strains in the glenohumeral labrum and capsule by simulating varied labrum thickness and modulus. The results showed that decreasing the thickness of the labrum due to degeneration increases the average and peak strains in the labrum. This increase in strain provides a possible biomechanical mechanism by which the tissue degeneration results in glenohumeral labrum pathology with aging and also confirms the important, however minor static contribution of the labrum to shoulder stability.

In comparison to the rotator cuff muscles, the capsule and labrum are major passive stabilisers of the shoulder joint. They function to assist with stability when the shoulder joint reaches or exceeds the limit of the joint range of motion. In this scenario, material property might be more important than *in-vivo* loading for investigations of capsule and labrum defects. Although material property studies have been conducted for the capsule ligaments based on specimen-specific experiments [66, 68], more detailed studies are needed to quantify the complex material behaviour of the capsule and labrum *in-vivo*. Moreover, further studies may need to pay more attention to accurate representation of the glenoid insertion site which varies significantly between subjects [70].

2.3.1.4 FE models for shoulder arthroplasty

A total shoulder replacement includes the replacement of the humeral head and the glenoid with prostheses that perform as a new joint. Therefore, the prosthesis design is fundamental in shoulder arthroplasty. FE analysis has been widely used in the design of prosthesis especially in investigating the clinically important issue of glenoid component aseptic loosening. The FE studies conducted for shoulder arthroplasty assessment are critically reviewed in this section, and key design parameters and major findings of each study are detailed in Table 2-2.

The scapula is connected to the axial skeleton via the clavicle. It provides a mobile yet stable base for humeral movement. The scapula also provides the insertion for a number of shoulder muscles and ligaments. Several studies have been conducted to investigate the biomechanics of the scapula because bone remodelling of the scapula is considered as the first step towards the study of complications of shoulder arthroplasty [80]. According to a recent study, A typical bone modelling procedure for creating a patient-specific FE model involves four steps: (1) geometry acquisition using medical images (CT/MR), (2) segmentation of those images and creating FE meshes, (3) definition of patient-specific material properties, and (4) application of patient-specific multi-body loading and boundary conditions. The authors also examined the effect of three major modelling uncertainties, including bone density, musculoskeletal loads and material mapping relationship, on the predicted strain distribution. It was found that the number of uncertain components and the level of uncertainties determine the uncertainty of the results. The limitation of this study is that the material mapping relationship was determined based on cadaveric experiments conducted in vitro rather than from data measured *in-vivo* [81].

Glenoid component loosening is a critical clinical issue in total shoulder arthroplasty. Most of the FE studies of shoulder arthroplasty were designed to investigate this problem. Through FE simulation analyses, the biomechanical effects of different key design parameters, such as implant shape, positioning and orientation, prosthesis material, use of bone cement and articular conformity, were examined. A large number of those studies investigated the effect of the shape of the glenoid component. Different glenoid shapes: keel, stair-stepped, wedge and screw, were compared in an early study [82]. It suggested that the stair-stepped and wedge designs provided a more natural stress distribution compared to the keel design. However, this study was only limited to 2D condition. A later FE study found that the peg design is superior for normal bones, whereas the keel design is more suitable for rheumatoid bone [83]. Based on a failure model, the FE simulation predicted 94% and 86% of bone cement survival probability for the peg design for normal bone and rheumatoid bone conditions respectively. Whereas, the survival probabilities for the keel design are 68% and 99% respectively. Another study has concluded that a novel design with acromial fixation point for the glenoid component is unsuitable for shoulder arthroplasty due to the high stress resulted in the part of prosthesis attached to the acromion [84].

The conformity of the glenoid component with the humerus component has been investigated using FE analyses as well. It was found that a higher conformity has the advantage of moderating cement stress [85], and the effect of conformity is sensitive to the shoulder joint position [86]. For example, for the same conformity, the contact pressure, cement stress, shear stress, and micro-motions at the bone-cement interface were increased by more than 200% at 15° of retroversion compared to those at 0° of retroversion. Another FE study showed that the central alignment with the humerus component is the correct position for the glenoid component, and misalignment may lead to glenoid loosening [87].

Studies looking at the choice of prosthetic components did suggested that metal backed glenoid component might be best [82, 88, 85]. However, a recent study has shown that all-polyethylene cemented glenoid components are likely to be more resilient to aseptic loosening (see Figure 2-12) [89]. The use of bone cement is a controversial element to glenoid component implantation. A number of studies have been conducted to investigate this issue. An early 2D FE study analysed local stresses at the bone implant interface between two glenoid designs. This showed that the cemented all-polyethylene design produced more natural stress overall although extremely high stresses were found in the interface between the polyethylene and the metal [88]. A recent FE study using an integrated model suggested that the cementless, metal-back components are more likely to have stress shielding than the cemented all-polyethylene components regardless of bone quality [89]. Another study investigating the effect of cement thickness concluded that although a thin cement mantle weakens the cement, a thick mantle makes the implant rigid, and consequently increases the stress in the bone-cement interface [90]. The optimal cement thickness was found to be between 1.0 and 1.5 mm [90].

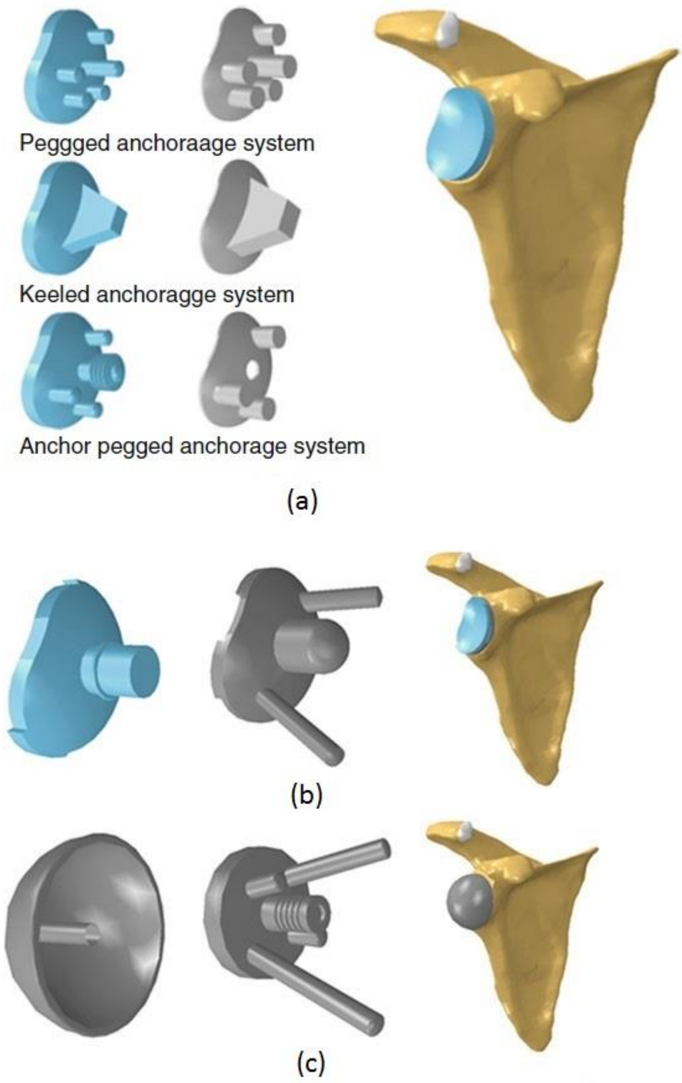

Figure 2-12 The FE study of shoulder arthroplasty (a) Three anatomical models of the cemented glenoid components (on the left) and their corresponding cement mantles (in the middle); (b) The cementless anatomical model of glenoid component; (c) The reversed glenoid component [89]

The previous studies of total shoulder arthroplasty using FE simulation analyses have greatly improved our understanding of the biomechanical effects of the key design parameters of shoulder implants, e.g. 3D shape, position and orientation, material and articular conformity etc. Future work should involve investigations of some unsolved problems, e.g. the mechanical degradation of the interfaces in cemented components [89], and bone loss in aseptic in both cemented and cementless components [89] as well as glenoid notching in reverse total shoulder arthroplasty. However, similar to the studies investigating shoulder joint instability, the major limitation here is still lack of detailed representation of all major shoulder musculoskeletal components and also physiologically realistic *in-vivo* loading and boundary conditions.

Table 2-2 The fundamental information and major findings of the FE shoulder arthroplasty studies reviewed in this paper

Implant geometry	Orientation and position	Cement	Prosthesis material	Glenohumeral conformity	Findings	Reference
Keel, stair-stepped, wedge and screw	N/A	Cemented	Cobalt-chromium metal for backing and polyethylene	N/A	1. An all-polyethylene implant could provide a more physiological stress distribution for nonaxial loads; 2. A soft tissue layer results in higher stresses; 3. Stair-stepped and wedge designs demonstrated a more natural stress distribution compared to keel design; 4. Screw orientation does not make much difference.	Friedman RJ, et al.[82] (1992)
Triangular keel	N/A	Cemented	Cobalt-chromium metal for backing and polyethylene	High and low conformity achieved by varying load distribution over contact area	Fatigue failure could originate from the high stresses in cement.	Lacroix D and Prendergast PJ.[85] (1997)
Keel	N/A	Cemented all-polyethylene component Uncemented metal-backed component		N/A	1. Cemented all-polyethylene design produced more natural stress overall. 2. Extremely high stress were found in the polyethylene in contact with metal surface	Stone KD, et al.[88] (1999)
Peg and Keel (DD 1134-96 and DD 1134-85 DePuy Inc.)	N/A	Cemented	All-polyethylene	N/A	A “pegged” anchorage system is superior for normal bone, whereas a “keeled” anchorage system is suitable for rheumatoid arthritis bone.	Lacroix D, et al.[83] (2000)

Implant geometry	Orientation and position	Cement	Prosthesis material	Glenohumeral conformity	Findings	Reference
Keel	N/A	Cemented and uncemented glenoid component	Polyethylene cup with a metal-backing	N/A	Uncemented design is a reasonable alternative to fixation with cement.	Gupta S, et al.[91] (2004)
Peg (Anatomica glenoid component Centerpulse Ltd.)	5 component alignments: central, anteverted, retroverted, inferiorly inclined, and superiorly inclined.	Cemented	Ultra-high molecular-weight polyethylene	N/A	Central alignment is the correct position. Misalignment of the glenoid prosthesis can lead to loosening. Joint replacement depends much on bone stiffness.	Hopkins, AR, et al.[87] (2004)
Acromion-fixation	N/A	Cemented	Polyethylene	N/A	High stresses were found in the part of prosthesis that attached to the acromion. The acromion-fixation design is not a good alternative.	Murphy LA and Prendergast J.[84] (2005)
Keel	N/A	Cement mantle thickness were examined from 0.5-2mm	All-polyethylene	N/A	The cement thinning weakens the cement, whereas the cement thickening makes the implant rigid, consequently increases the stress on bone cement interface. Optimal cement thickness is found to be between 1.0 to 1.5 mm.	Terrier A, et al.[90] (2005)

Implant geometry	Orientation and position	Cement	Prosthesis material	Glenohumeral conformity	Findings	Reference
Keel	Humeral and glenoid components were implanted based on manufacturer's recommendation	Cemented	All-polyethylene	Different values of conformity were tested (1-15 mm of radial mismatch)	Conformity had no influence at 0^{o} of retroversion, whereas, at 15^{o} of retroversion, the contact pressure, cement stress, shear stress, and micro motions at bone-cement interface increased by more than 200% and exceeded critical values above 10mm.	Terrier A, et al.[86] (2006)
Reversed and anatomical (Aequalis prosthesis, Tornier Inc)	N/A	N/A	All-polyethylene	N/A	Volumetric wear for the anatomical prosthesis and reversed version were 8.4 mm and 44.6mm respectively. Contact pressure for the anatomical prosthesis was about 20 times lower than that of the reversed. Anatomical prosthesis showed the consistency with the biomechanical and clinical data.	Terrier A, et al.[92] (2009)
Four anatomical and one reversed	N/A	3 anatomical models were Cemented 1 anatomical was Cementless	3 cemented anatomical model were all-polyethylene; 1 cementless anatomical model was metal-back; reversed model was all metal	N/A	Cementless, metal-back components are more likely to have stress shielding than cemented all-polyethylene components regardless of bone quality. The all-polyethylene components are better in treatment of the shoulder joint.	Quental C, et al.[89] (2014)

2.3.2 FE shoulder modelling techniques

For the FE studies reviewed in the preceding section, the key modelling techniques used in each shoulder FE model were listed in Table 1. To reduce the computational load, most of those FE models only considered part of the shoulder structure rather than modelling the whole shoulder complex. Therefore, major model simplifications and assumptions were normally involved in the modelling processes. Those simplifications and assumptions could greatly facilitate the computations when representing a complex musculoskeletal structure such as the human shoulder complex. However, this will inevitably lead to discrepancies between the simulated results and the realistic physiological functions. The limitations of those FE models are discussed in this section in terms of the key modelling techniques used: geometric data acquisition, material property representation, boundary and loading condition definition and experimental validation.

Normally, the first step in FE shoulder modelling is to reconstruct the 2D or 3D geometry of hard tissues and soft tissues of the musculoskeletal structure. Different approaches have been used for acquiring the dataset for the geometric construction varying from using literature data [82], average measured data [49] to subject-specific medical imaging data [45, 52, 15-17, 56, 59, 18, 70, 69, 63, 66, 68, 77, 72, 20, 93]. For geometric construction of bones, the most widely used approach is based on Computed Tomography (CT) imaging data, for example, the CT image databases for the modelling of the cervical spine and hip joint in our previous studies [94, 95]. While in some studies the bone geometry was measured directly in cadaveric dissections or used the datasets from literature [52, 16, 59, 66]. For geometric modelling of soft tissues, such as musculotendinous units and ligaments, datasets obtained from Magnetic Resonance (MR) imaging or colour cryosections were normally used [15-17, 56, 59]. However, the geometric reconstruction of articular cartilages still remains challenging. Assumptions are normally used for defining the geometry of articular cartilage, for example using the estimated average thickness for the whole bone surface [80] or filling the space between the humerus and the scapula with hyaline cartilage [45]. Some recent studies used the published anatomical datasets to determine the cartilage geometry [49, 52]. Subject-specific accurate geometric modelling of cartilage will assist a better understanding of the *in-vivo* cartilage mechanics in the glenohumeral joint. In many studies, the geometric data was obtained in vitro. However, to investigate the *in-vivo* functioning of the shoulder complex, the geometric data of the shoulder tissues is acquired preferentially *in-vivo* under unloaded conditions.

Due to the great complexity in the mechanical behaviours of biological materials, it has been proven very challenging to represent the realistic material properties of the shoulder tissues in FE modelling. Major assumptions were typically used in most of the FE shoulder studies. In most cases, bones were assumed to be rigid or isotropic linear elastic material with relatively large Young's modulus, because the deformation of bones is almost negligible compared to that of soft tissues. Muscles and tendons were modelled as isotropic linear elastic materials in many early studies [48, 15-17, 56, 59]. Some later FE studies considered the non-linearity in the material properties of muscles and tendons which is more accurate and closer to *in-vivo* condition [18]. However, only the passive behaviour of the musculotendinous units was represented in the modelling. A most recent shoulder FE study described the material property of muscles by using a constitutive relationship representing both the active and passive behaviour of muscles along the direction of muscle fibres [93, 96]. Conversely, tendons were modelled using different parameters to describe their along-fibre and cross-fibre properties [93]. These detailed properties have been shown to agree with *in-vivo* measurement of the biceps brachii [97]. In most cases, joint capsules were modelled as isotropic hyperelastic material [63, 66] and detailed parameters for each region were assigned in some studies which was validated through experimental strain measurements [68]. The labrum was normally assumed to be isotropic material [72]. Lately, detailed transverse isotropic material properties was applied in some recent studies which compared well to the experiment measurements [20]. For articular cartilages, they were modelled as homogeneous linear elastic material in most of the studies [48, 16, 17, 56, 18, 80]. However, in some cases, they were considered to be rigid same as bones by assuming that the material properties of cartilages do not have significant effect on simulation results [59, 20]. Biological materials normally have complicated mechanical property, which is anisotropic and nonhomogenous in nature with nonlinear and viscoelastic behaviours. However, depending on the research problem to be addressed, this material property might be simplified in some cases without compromising the quality of the analysis results. More sensitivity analysis studies are needed in the future to better understand the effect of different material properties [38].

The definition of boundary and loading conditions in previous shoulder FE studies vary dramatically due to the complexity in the joint motions and musculoskeletal loads of the shoulder complex. Many studies only considered part of the complex, and modelled the neglected parts using artificially imposed boundary or loading conditions [15-17, 56, 72, 45]. A number of studies defined their boundary and loading conditions according to the apparatus settings in the cadaveric experiments to facilitate model validations [59, 18, 98, 63, 68, 77, 20, 52]. Whereas, in some other studies, boundary conditions were defined by imposing artificially prescribed displacements or rotations of certain muscles or bones [93, 70, 69, 66]. However, none of the previously stated boundary and loading conditions are capable of describing the realistic physiological conditions of the shoulder complex where significant muscle activations are involved. Some studies have addressed this and have attempted to use previously determined muscle forces from multi-body models as boundary and loading conditions [48, 80, 90]. But, they either considered the scapula in isolation [80, 90] or performed a 2D analysis only [48]. The most appropriate implementation of boundary and loading conditions in shoulder FE modelling is to describe the natural shoulder joint and bone motions driven by physiologically realistic muscle forces without any artificial constraints imposed [52]. This kind of physiological boundary condition has been proven to be beneficial in FE modelling of the femur [99]. In addition, the FE simulation analyses in most of the studies were only limited to the static or quasi-static condition. We have applied dynamic FE simulation analysis to study cervical spine and foot biomechanics [100, 95], and have an ongoing study to use dynamic FE analysis to investigate the *in-vivo* functioning of the shoulder complex. Physiologically more realistic loading and boundary conditions are likely to provide the best way to predict the tissue stress environment *in-vivo*.

Experimental validation of FE models is essential because model simplifications and assumptions are normally employed in shoulder FE studies. Unfortunately, some of the studies were not validated or only simply compared to previously published results [15-17, 56, 82]. For in vitro measurement based studies, it is straightforward to validate the models against the specimen-specific experimental data [59, 18, 68, 20, 49], for example strain gauge data for surface strain [91, 98, 101] However, those validations were conducted based on the data collected in vitro, rather than *in-vivo* data describing the physiological functioning of the shoulder complex. The positions and motions of bones or joints captured from motion analysis systems could provide useful datasets to validate FE simulations *in-vivo*. Recently, we have successfully used this method to validate a FE model of cervical spine [95]. Moreover, recent advance in medical imaging domains (e.g. dynamic CT/MR scanning or ultrasound [102, 103] and force sensing [104] techniques provide promising methods to validate FE simulation results *in-vivo*.

It is evident that more comprehensive musculoskeletal FE modelling with physiologically realistic loading and boundary conditions is needed to further improve our understanding of the *in-vivo* functioning of the shoulder complex. To further this, subject-specific modelling is the most promising simulation solution. In musculoskeletal modelling, there are normally a large number of uncertainties involved in different components of the system, which is further confounded by inter-subject variations [38, 105]. To rigorously validate the modelling results *in-vivo*, personalised datasets and parameters are desirable. Subject-specific modelling studies have been successfully applied to other musculoskeletal complexes, such as pelvis [106] and femur [107], but very few to the shoulder joint. Future orthopaedic interventions and surgeries are likely to benefit from patient-specific biomechanical analyses and assessments before and/or after treatments. This approach has been successfully demonstrated in the total knee arthroplasty [108, 109] and periacetabular osteotomy surgery [94].

2.3.3 Review Findings

Previous FE studies to investigate shoulder biomechanics have been critically reviewed according to the clinical issues addressed. This confirms that FE modelling is a valuable tool to examine both physiological functions and clinical problems of the shoulder complex. Most of those modelling studies have improved our understanding of the biomechanical functioning of the shoulder joint. Specifically, they normally have one or more research focuses: biomechanical mechanism underlying joint motion, aetiology of joint pathology, clinical diagnoses of joint diseases and shoulder prosthetics design. It may be difficult to say which is the best model, but the most recent models using latest techniques tend to have more complicated configurations and provides more detailed databases than the models before. It is noticeable that more comprehensive model is needed to better understand the in the vivo functioning and also the interaction of different components of the shoulder joint. Recently there has been a tendency in shoulder FE studies to construct subject-specific or patient-specific FE models informed by muscle force and/or bone motion data from measurement based multi-body modelling. Despite the aforementioned limitations of multi-body modelling, this integration offers some promising solutions by providing more accurate boundary and loading conditions.

Fully validated shoulder FE models will greatly enhance our understanding of the fundamental mechanisms underlying shoulder mobility and stability, and the aetiology of shoulder disorders, and hence facilitate the development of more efficient clinical examinations and diagnoses, non-surgical and surgical interventions and treatments including prostheses. In author's opinion, the model validation may need to be conducted by interactively working with clinicians. Firstly, FE models could be carefully validated for healthy people by using the latest medical imaging and sensing techniques. Then, with some confidences built up, the models could be applied to individual clinical case by using the patient-specific database provided by clinicians. The models could be further improved based on prediction results and also feedbacks of doctors. Indeed, we still face many challenging problems before the realistic physiological functions of the shoulder mechanism can be accurately represented and analysed in FE simulations.

Future works and challenges involve:

1. Subject-specific representation of the non-linear anisotropic nonhomogenous material properties of the shoulder tissues in both healthy and pathological conditions, and also definition of boundary and loading conditions based on individualised physiological data. Special attention should be paid to the consistency between the FE models and the multi-body models used for muscle force estimation.

2. More comprehensive models describing the whole shoulder complex including appropriate 3D representations of all major shoulder hard tissues and soft tissues and their delicate interactions, are highly demanded to better understand the biomechanical functioning of the shoulder mechanism.

3. Dynamic FE simulations based on physiologically realistic boundary and loading conditions to better understand the *in-vivo* biomechanical functioning of the shoulder joint during our daily activities.

4. Advanced medical imaging, sensing techniques to quantify *in-vivo* strain and stress distributions of soft and hard tissues in both normal and pathological conditions so as to validate FE models more rigorously.

2.4 Summary

This chapter presented the literature review of the project. The review of the basic anatomy and biomechanical knowledge provided the foundation in shoulder study. Thereafter, the thorough review of all current state-of-the-art FE shoulder models had substantially enhanced the understanding of the implementation of the FE method in this field of shoulder research. The FE method had been widely used to investigate the shoulder biomechanics, such as aetiology study of joint instability, rotator cuff tears, capsule and labral defects and shoulder arthroplasty in addition to the numerous shoulder implants design and evaluation studies. However, there were plenty of limitations and challenges in this field among which are the lack of accurate comprehensive models that can be used to better understand the intrinsic joint functioning and also the interaction of different components of the shoulder joint under *in-vivo* conditions were the most urgent. Therefore, the main objective of this study was set to develop and validate an *in-vivo* subject-specific FE model of the human shoulder complex with anatomical accuracy.

The awareness and understanding of the current limitation and challenges faced in this field had helped set the direction and objectives that this study should follow and pursue. The main challenges faced in order to accurately represent the realistic physiological functions of the shoulder mechanism in FE simulations can be found in the above quoted abstract of the published review paper. The methods adopted to overcome several specific the limitation and challenges were summarised as following:

1. To define the comprehensive model describing the whole shoulder complex including appropriate three-dimensional (3D) representation of all major shoulder hard tissues and

soft tissues and their delicate interactions, MR imaging techniques were chosen. A minimum of two scanning protocols was designed including one with a large field of view covering the whole shoulder from most lateral deltoid muscle to the most medial sternum bone, and one with high image quality specific on the glenohumeral joint region. In addition, the reconstruction of these images was designed to cover all the above tissues; hence their interactions could be further defined based on the constructed tissues in the FE model.

2. In order to define boundary and loading conditions based on individualised physiological data in FE simulation, the same living healthy subject was used to perform both MRI scanning and 3D shoulder motion measurements. Furthermore, the *in-vivo* muscle activities and relative joint positions defined by the measured motions were planned to be determined using a multi-body musculoskeletal model to be constructed based on this same subject.

3. To assess the rationale for the integration of the two main computational biomechanics methods of the human shoulder complex, i.e. multi-body musculoskeletal method and finite element method, the finite element simulation was designed to conduct the quasi-static shoulder scapular abduction motion to be measured in 3D shoulder motion measurement implementing the muscle activations calculated from multi-body musculoskeletal simulation of the same motion.

4. To demonstrate the application of the FE model, a biomechanical study investigating the rotator cuff tears was performed. Special attention was planned to be paid for the accurate design of the bones and muscles around the rotator cuff insertion sites. In addition, a novel integrative stability index was planned to propose to define the comprehensive glenohumeral joint stability quantitatively.

Chapter 3 Three-dimensional measurement of human shoulder motions

3.1 Introduction

Accurate human shoulder kinematics measurement is a crucial step in obtaining physiological, *in-vivo* subject-specific muscle activities. The term “kinematics” is the term used for the description of human movement. It focuses on the motion itself, regardless of the force or momentum that causes this motion. In this chapter, an experiment was designed and performed to obtain the accurate 3D *in-vivo* kinematics of the subject under investigation. This measured kinematic data would be further implemented to construct the subject-specific multi-body musculoskeletal model and calculate the *in-vivo* muscle activations in Chapter 4. In addition, the measured joint positions during scapular abduction would be further used to define the loading and boundary conditions of the FE model in chapter 6 and 7.

Specifically, in this chapter, stereophotogrammetry was adopted for this kinematics measurement and simultaneous muscle activities were recorded by wireless surface muscle electromyography (EMG) system. These two advanced systems both use non-invasive methods, which were suitable for this study. In order to keep consistency with the FE model, the same subject had been chosen for this measurement as the subject under MR scanning. The experimental protocol and process for *in-vivo* 3D shoulder kinematics and muscle EMG measurement were presented. Specifically, for *in-vivo* 3D shoulder kinematics measurement, the specially designed marker fixation devices from our group [110] were used together with measurement apparatus designed and manufactured based on literature recommendations [111, 112]. The experiment was carefully conducted accordingly. Static motion trials were measured first with the subject remaining still for 5 seconds followed by dynamics trials when the subject performed frontal plane abduction, forward extension, scapular plane abduction and external rotation that aimed to cover normal shoulder motions. Finally, some of the measurement results were shown.

3.2 Background

The human motion measurement methods can be roughly categorised as direct measurement (goniometers and accelerometers) and imaging measurement techniques. Due to the complexity of most movements, the imaging system is considered as the system that can capture all the motion data [113]. The imaging measurement techniques, or to use the technical term "optoelectronic stereophotogrammetric", either use conventional photography or optoelectronic electrodes to capture the instantaneous position of markers located on the skin surface [114]. The Vicon motion capture camera system adopted in this study is a typical and widely used stereophotogrammetric system (See Figure 3-1). In Vicon system, there are normally six to twelve infrared cameras that use infrared light rather than visible light to exclude the influences from other light sources during motion capture measurements. In each frame, infrared light pulsed from the infrared lights mounted on these cameras is reflected from the reflective markers attached to the skin surface. This reflected infrared light is captured by the camera subsequently. The sampling frequency for the Vicon system in this study is 200 Hz.

Other two typical quantities measured during the above motion capture experiments are external forces using force plates, and electrical activity of muscles is recorded through electromyography [114]. As there are no external forces in this study, the simultaneous muscle activities are recorded by surface EMG system. Surface EMG signals were recorded by the Delsys Trigno™ Wireless EMG Systems and the trigger module with a sampling frequency of 2000 Hz. (See Figure 3-2.)

It should be noted that skin artefacts are the inherent source of errors in both of above measurements subject to the non-invasive *in-vivo* experimental conditions which should be listed as one of the limitations of this study. Skin artefacts

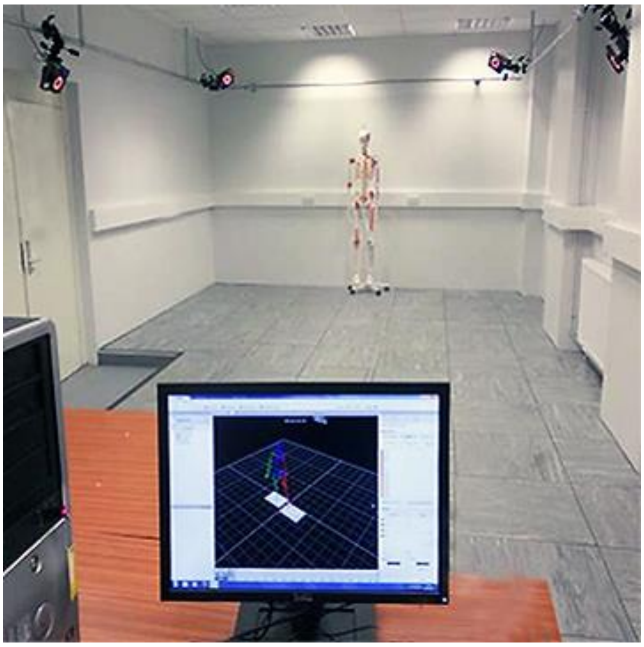

Figure 3-1 Vicon stereophotogrammetry system in the Biomechanics Lab

Figure 3-2 Delsys Trigno^{TM} wireless surface EMG system

3.3 Experimental protocol

The experiment protocol was designed to perform the motion capture and measure the simultaneous surface EMG signals. To ensure the subject-specific feature of this study, the same subject had to be chosen to keep the consistency between the kinematics measurements and MR imaging measurements. Therefore, one subject was chosen. Basic information on this subject was as follows: 26-year-old male, with height and weight of 172 cm and 65 Kg respectively, right-handed and no chronic or acute pain and injury to the right shoulder. This protocol was divided into two main parts, i.e. the surface EMG measurement protocol and the motion capture protocol. A pre-test of the

EMG electrode placement on each muscle of the subject was included in the surface EMG measurement protocol which was conducted prior to the main experiment.

3.3.1 Motion capture protocol

3.3.1.1 Global coordinate system

The global coordinate system adopted in this study was the commonly used conventional system. [113] Figure 3-3 illustrates the global coordinate system for 3D marker coordinates. The directions of the three Cartesian axes are as follows: the y-axis which is vertical and points upwards, the z-axis which is perpendicular to the y-axis and points right, and the x-axis pointing front and perpendicular to both y-axis and z-axis.

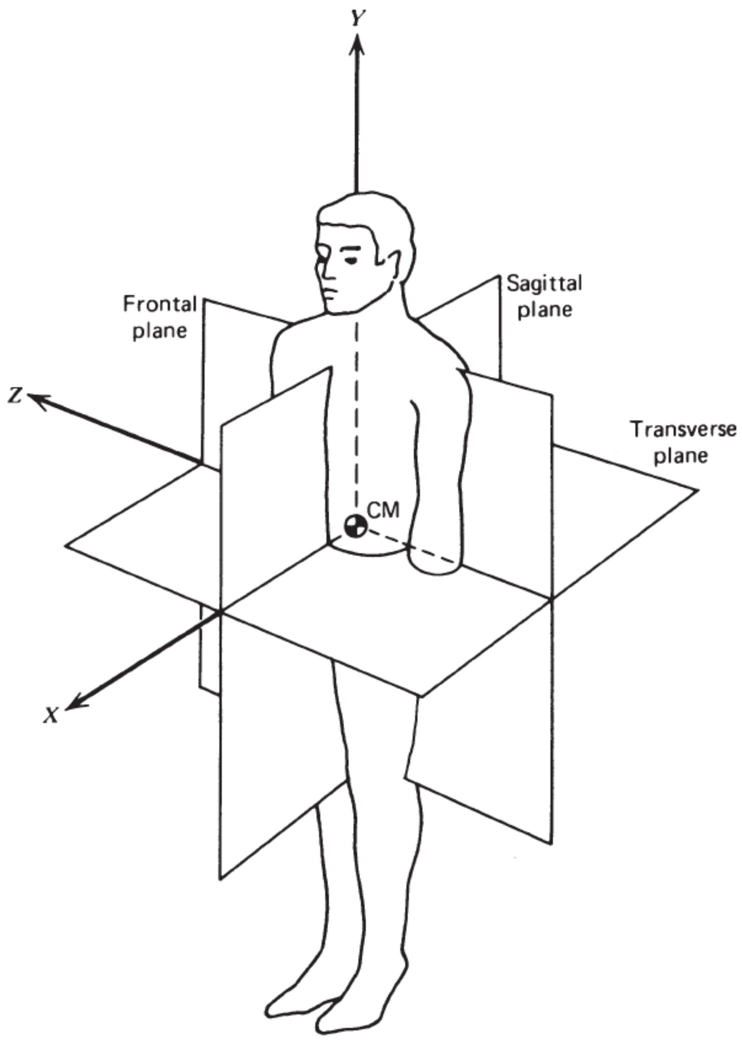

Figure 3-3 Global coordinate system adopted in this study [113]

3.3.1.2 Anatomical landmarks

Anthropometric information of the subject defined by a set of anatomical landmarks on each segment was determined based on ISB recommendation [115]. (See Figure 3-4 and Table 3-1 for details)

Table 3-1 Anatomical landmarks adopted in the study

Anatomical landmarks	Description
Thorax	
C7	Processus Spinosus of the 7th cervical vertebra
T8	Processus Spinosus of the 8th thoracic vertebra
IJ	Deepest point of Incisura Jugularis
PX	Processus Xiphoideus most caudal point on the sternum
Clavicle	
SC	Most central point on the sternoclavicular joint
AC	Most dorsal point on the acromioclavicular joint
Scapula	
TS	Trigomun Spinae Scapulae the midpoint of the triangular surface on the medial border of the scapula in line with the scapular spine
AI	Angulus Inferior most caudal point of the scapula
AA	Angulus Acromialis most laterodorsal point of the scapula
PC	Most ventral point of processus coracoideus
Humerus	
GH	Glenohumeral rotation centre
EL	Most caudal point on lateral epicondyle
EM	Most caudal point on medial epicondyle
Forearm	
RS	Most caudal-lateral point on the radial styloid
US	Most caudal-medial point on the ulnar styloid

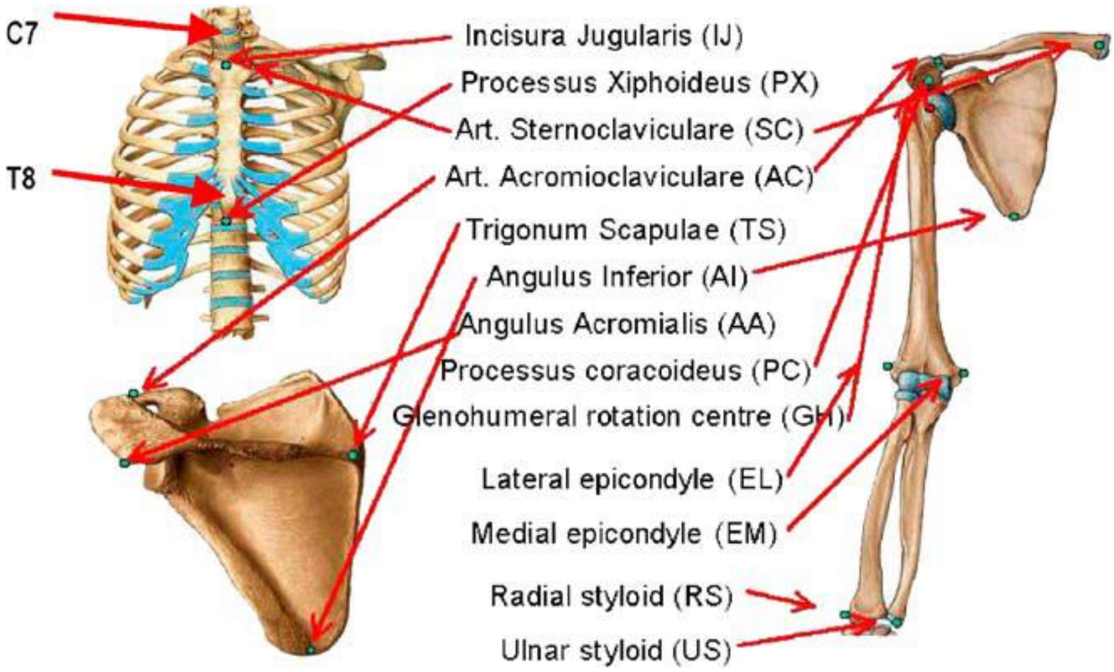

Figure 3-4 Bony landmarks from ISB recommendations [115]

3.3.1.3 Technical marker set

In order to track the 3D motion of the shoulder segments, a set of reflective marker clusters was designed to be attached to thorax, clavicle, scapula, humerus and forearm. In experimental trials, the 3D coordinates of the markers would be recorded by the cameras. Some of the technical makers are placed on anatomical landmarks where there are little artefacts during movement. The list of technical markers for each bone segments is presented as follows.

(1) Thorax: C7: 7th cervical vertebra

T8: 8th thoracic vertebra

IJ: suprasternal notch

PX: Xiphoid process most caudal point on the sternum

(2) Clavicle: SC: most central point on the sternoclavicular joint

AC: most dorsal point on the acromioclavicular joint

Mid-point on clavicle [111]

(3) Scapula: “Boomerang” shaped Acromion cluster[112]

(4) Humerus: Humeral cluster (Rectangular shape with 1 marker on each corner) [110]

(5) Forearm: Forearm cluster (Rectangular shape with 1 marker on each corner) [110]

A detailed naming system for all the technical markers is determined and presented in Table 3-2.

Table 3-2 The technical markers for each body

Body Segment	**Technical marker names**	**Support**
Thorax	‘STER1’, ‘STER2’, ‘STER3’, ‘STER4’	Rectangular plastic
Clavicle	‘SC’, ‘AC’, ‘MP’	N/A
Scapula	‘ACROM1’, ‘ACROM2’, ‘ACROM3’	Boomerang plastic
Humerus	‘HUM1’, ‘HUM2’, ‘HUM3’, ‘HUM4’	Rectangular plastic
Forearm	‘FARM1’, ‘FARM2’, ‘FARM3’, ‘FARM4’	Rectangular plastic

3.3.1.4 Shoulder motion design

A detailed experimental process was determined to conduct the shoulder motion analysis. Two experimental trials were presented involving calibration trials and shoulder motion trials.

(1) Calibration trials

(i). Anatomical landmark location with a technical wand

A technical stick with 2 reflective markers was used to determine the 3D coordinates of some anatomical landmarks, which were not conveniently determined by technical markers. 3 landmarks applied: AI, TS and AA.

(ii). Anatomical landmark calibration with technical markers

Reflective technical markers are directly used for the rest of the anatomical landmarks. Static trials were recorded without wand with the subject facing approximately four orthogonal directions, i.e., south, west, north and east respectively. Repeat recording of the static trials with a wand for AI, TS and AA individually.

(iii). Joint centre functional location trial

The functional method has been applied to determine the three-dimensional coordinates of shoulder joint centres. The subject is asked to perform a serial of continuously and sequential motions: flexion, return to neutral, extension, back to neutral, abduction, return to neutral and circumduction.

The calibration trial (i) was conducted to determine the position of some anatomical landmarks that were not suitable for directly applying skin marks on to such as the 3 anatomical landmarks of the scapular bone: AI, TS and AA. Thereafter, the calibration trial (ii) was performed to determine the relative positions between the anatomical landmarks and the technical markers. Both of the above trials are compulsory for measurement, while the calibration trial (iii) was not a compulsory. This trial was conducted as a backup measurement set for one of the methods for glenohumeral joint centre calculation in multi-body model construction [116].

(2) Shoulder motion trials

Each of the following motion trials is designed to be repeated 10 times for reliable and accurate data.

(i). Frontal plane abduction: 0-120^o (Humerothoracic angles)

(ii). Scapular plane abduction: 0-120^o (Humerothoracic angles)

The angle (30^o) between the scapular plane and the frontal plane was determined by the MRI scans of this subject.

(iii). Forward flexion: 0-120^o

(iv). External rotation: 0-45^o

The flexion of the glenohumeral joint is defined by lifting the arm at the shoulder in the anterior direction in the sagittal plane of the body; while the abduction of the glenohumeral joint is defined as raising the arm laterally in the coronal of plane of the body [10].

3.3.2 Electromyography measurement protocol

A list of muscles was chosen first for the EMG signals recording. Their relative surface EMG electrode placement position can be found first based on literature which can be found in Table 3-3. The EMG signals in this study were recorded merely for the use of qualitative observation to confirm that the muscles were active. They were not used for quantitative measurements.

As optimal placement of the EMG electrode for one muscle can vary between subjects, the position and orientation of the EMG electrode for each muscle were determined via test before performing the main experiment. Take the biceps muscle for example (see Figure 3-5). Position 1 Orientation 1 was defined as literature recommendations listed Table **3-3**. By performing the same motion as Position 1 Orientation 1, the surface EMG signal was recorded for other positions and orientation cases. Their respective EMG signal for biceps muscle during this movement can be found in Figure 3-6. By comparison, it was found that the signals yield similar patterns and Position 1 Orientation 1 demonstrated the optimal signal. Therefore Position 1 Orientation 1 was selected as the optimal placement for biceps muscle.

Table 3-3 EMG electrodes Placement for each muscle

Muscle	Position	Pennation Angle
Biceps	Biceps brachii proximal to the midpoint of the muscle belly [117]	45-50 [118]
Triceps Long head	Over the muscle belly parallel to the fibre orientation [119]	42 [118]
Deltoid Anterior	3.5 cm below the anterior angle of the acromion [120]	0
Deltoid Middle	Intersection of the midpoint between the anterior and posterior deltoid muscles and the midpoint between the acromion and deltoid tuberosity [120]	31 [118]
Deltoid Posterior	2 cm below the posterior angle of the acromion [120]	0

Infraspinatus	4 cm below the spine of the scapula, on the lateral aspect over the infrascapular fossa of the scapula [121, 122]	0
Pectoralis Major upper	3.5 cm medial to the anterior axillary line [120]	0
Trapezius Upper	Superomedial and inferolateral to a point 2 cm lateral to one-half the distance between the C7 spinous process and the lateral tip of the acromion [120]	0
Trapezius Middle	Parallel to the muscle fibres with one electrode placed medial and one lateral to a point 3 cm lateral to the second thoracic spinous process [123, 122]	0
Trapezius Lower	Electrodes were placed on an oblique vertical angle with one electrode superior and one inferior to a point 5 cm inferomedial from the root of the spine of the scapula [123, 122]	0
Latissimus dorsi	Caudally and laterally to the inferior scapular border at the T12 level, above the bulkiest portion of the muscle belly [124, 125]	0

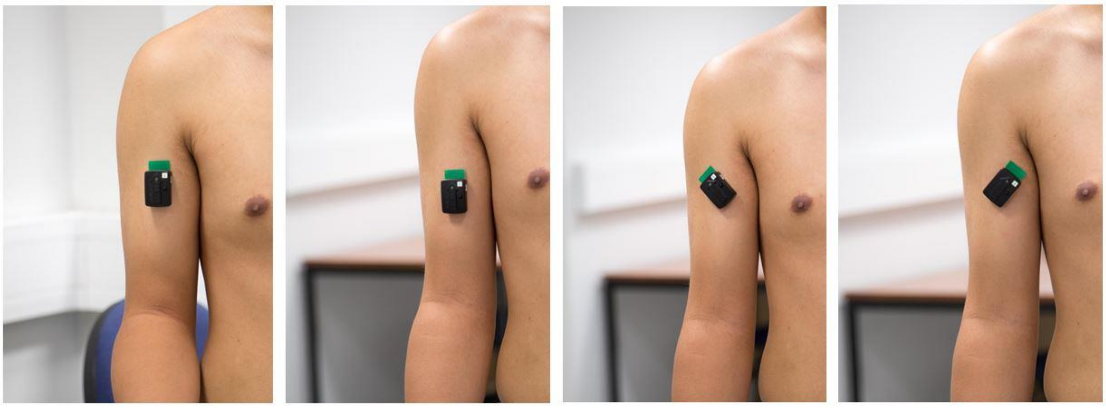

(a) (b) (c) (d)

Figure 3-5 EMG electrode placement test for biceps (a) Position 1 Orientation 1; (b) Position 2 Orientation 1; (c) Position 1 Orientation 2; (d) Position 1 Orientation 3

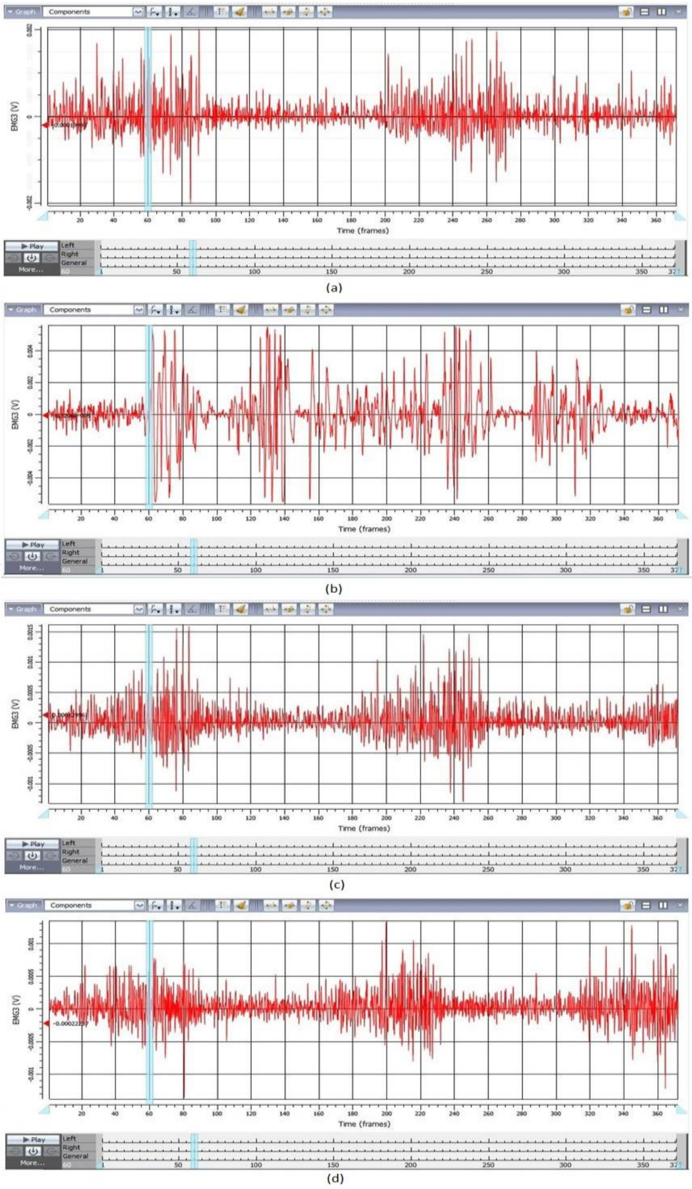

Figure 3-6 EMG signals comparison (a) Position 1 Orientation 1; (b) Position 1 Orientation 2; (c) Position 1 Orientation 3; (d) Position 2 Orientation 1

By repeating the same procedures for the rest of the listed muscles, their optimal electrode placement was determined and marked. See Figure 3-7.These marks were preserved till conducting the main experiments.

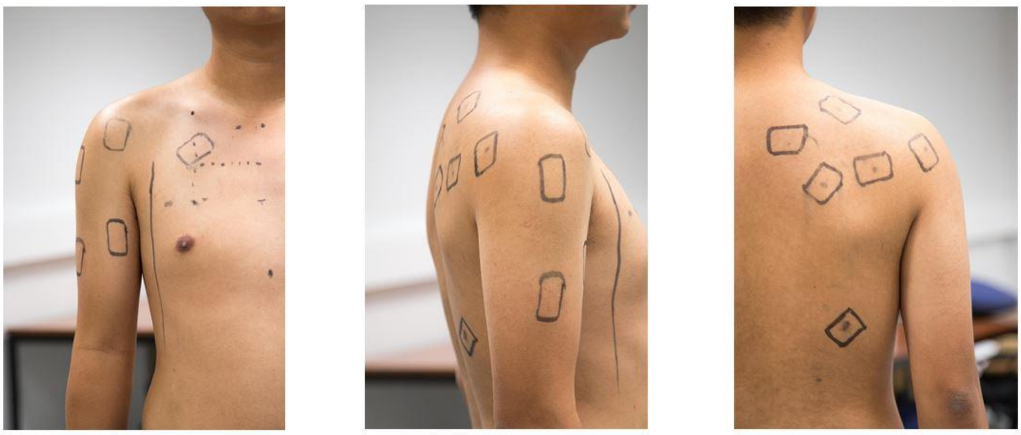

Figure 3-7 EMG electrode placement on each muscle around the shoulder joint

3.4 Measurement procedures

The main experiment was performed in early December 2015. It was carefully performed following the designed protocol. The experimental apparatus were examined and calibrated in the morning before starting the experiment. Experimental procedures were recorded by videos and notes. The subject was prepared by attaching the reflective markers according to the experimental protocol (See Figure 3-8).

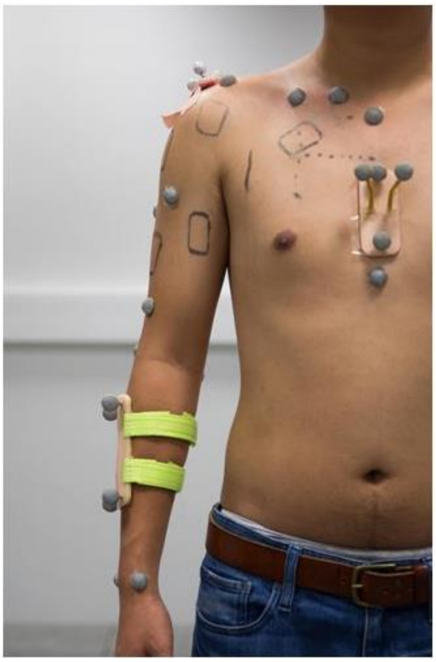

Figure 3-8 The subject attached with markers

3.4.1 Calibration trials

The Vicon system is recommended to be calibrated every day before use to ensure that any accidental changes (such as a camera being knocked accidentally) does not compromise the data quality. The calibration of the cameras was performed using a T-shaped calibration wand with five markers (See Figure 3-9)[126]. When calibrating the cameras, firstly, the threshold of the cameras on circularity was adjusted in an appropriate range, i.e. small enough so that the all five markers on the wand can be seen clearly while remaining relatively large to exclude noise. Secondly, the wand is required to move around the measuring volume for dynamic calibration of the cameras. With all the cameras set to calibration mode, the wand was moved around each individual camera and covered the whole working space. Certain number of wand frames count was captured and image errors were calculated by the system. Images errors were calculated for each camera by comparing the calculated 3D reconstruction marker set to its actually 2D view in each camera. All camera errors were found smaller than 0.2mm which was considered acceptable.

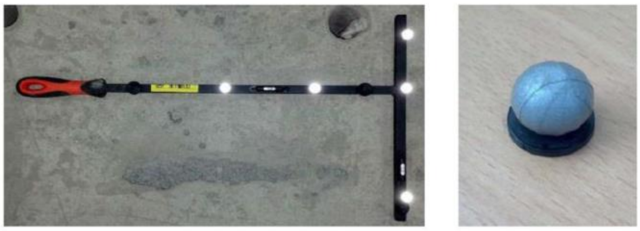

(a) (b)

Figure 3-9 Calibration wand used in Vicon system (a) Wand; (b) Marker [126]

3.4.1.1 Static calibration

The static calibration trial was performed to determine the relative position between the technical markers and the anatomical landmarks. The anatomical markers are markers that attached to the anatomical landmarks. Most of them were only used in the static trials for determining the positions of the anatomical landmarks. The technical markers were the markers that were used to track the human body in the motion trials. The relative positions between the technical markers and anatomical makers were determined in the calibration trials. Several less moveable markers, such as those attached to the thorax of the body, can also be used as technical markers.

A static trial was recorded when subject stayed still for 5 seconds. A technical stick with 2 reflective markers was used for 3 landmarks: AI, TS and AA respectively. Figure 3-10 is a demonstration of the application of the technical wand. Static trials without wand when the subject faced south, west, north and east respectively were recorded accordingly.

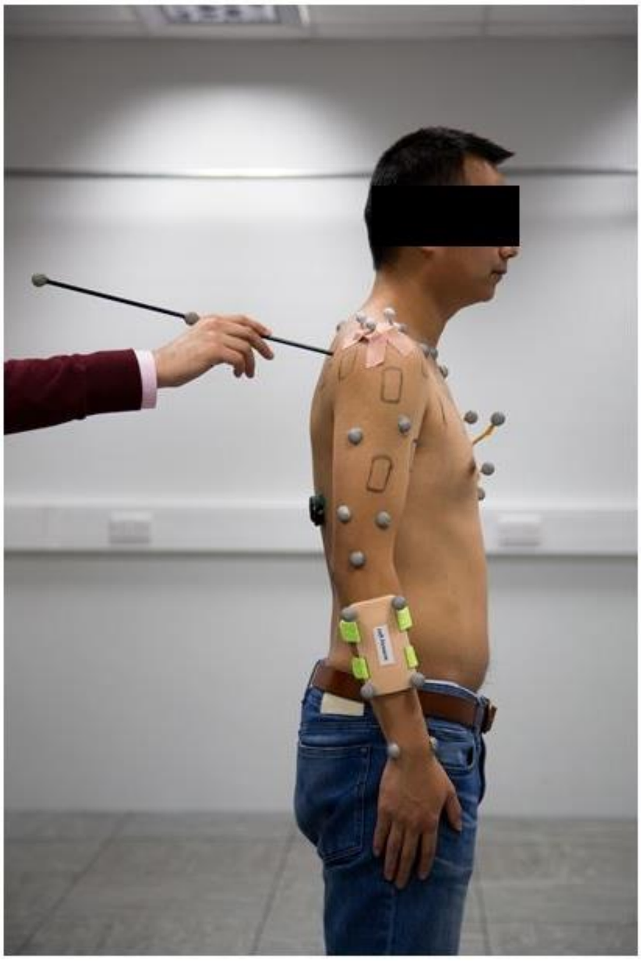

Figure 3-10 The application of technical wand for anatomical landmarks AI, TS and AA

3.4.1.2 Dynamic calibration

Dynamic calibration was conducted to work out the joint centre. The functional method has been applied to determine the three-dimensional coordinates of shoulder joint centres. Dynamic trials were recorded 3 times when the subject was performing a series of continuously and sequential motions: flexion, return to neutral, extension, back to neutral, abduction, return to neutral and circumduction.

3.4.2 Motion trials

When the calibrations procedures were finished, the EMG electrodes were attached to the subject according to the protocol. See Figure 3-11. Anterior, lateral and posterior view of the subjects with all makers and electrodes can be found.

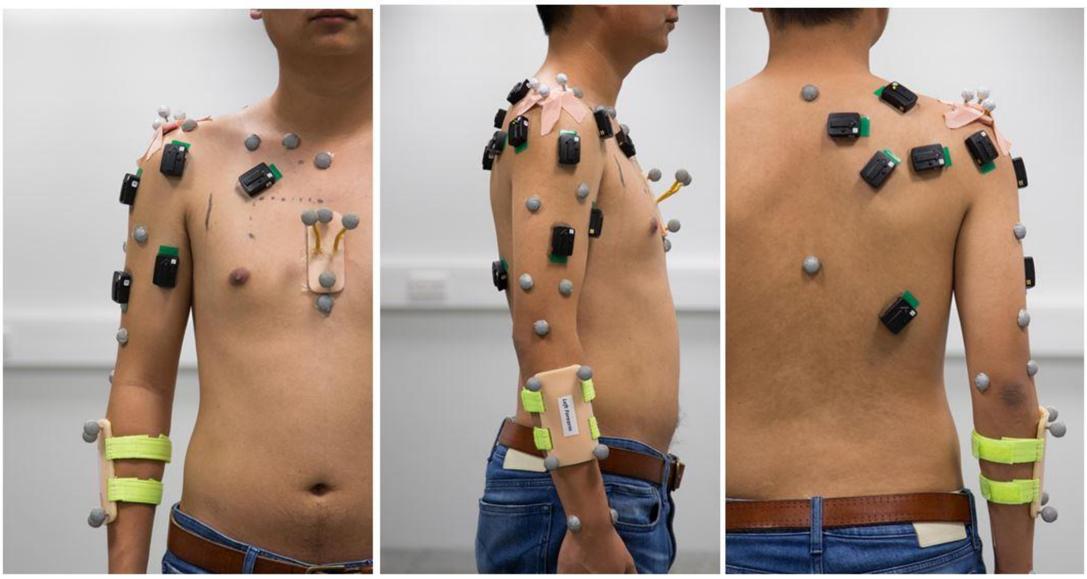

Figure 3-11 EMG electrodes attachment with markers

Motion data and EMG signals of the motion trials were recorded 10 times for each motion. Below are some screenshots from the videos when performing these motions. Figure 3-12 illustrated the abduction and adduction of the arm in the frontal plane of the body in a posterior view. Figure 3-13 demonstrated the abduction and adduction of the arm in the scapular plane (30^o from the frontal plane) of the body in an anterior view. Figure 3-14 showed the flexion and extension of the arm in the sagittal plane of the body in an anterior view. Figure 3-15 presented the external and internal rotation of the arm in an anterior view. During most of the measurements of these trials, markers were clearly seen in the system while several trials were a little noisy. Severely noisy trials would be excluded from calculations.

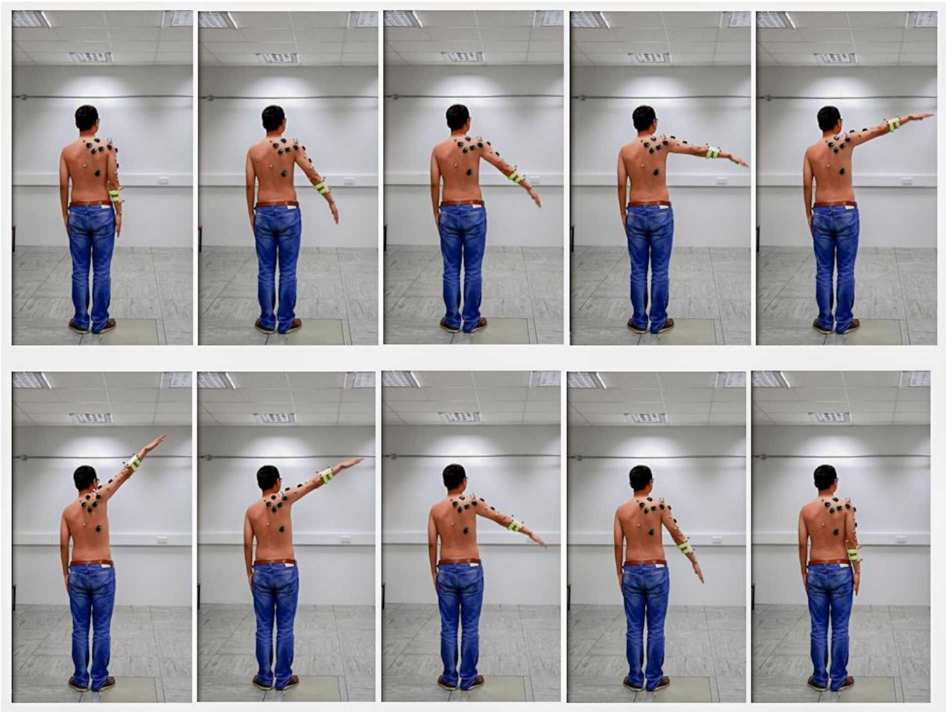

Figure 3-12 Frontal plane abduction animation photos

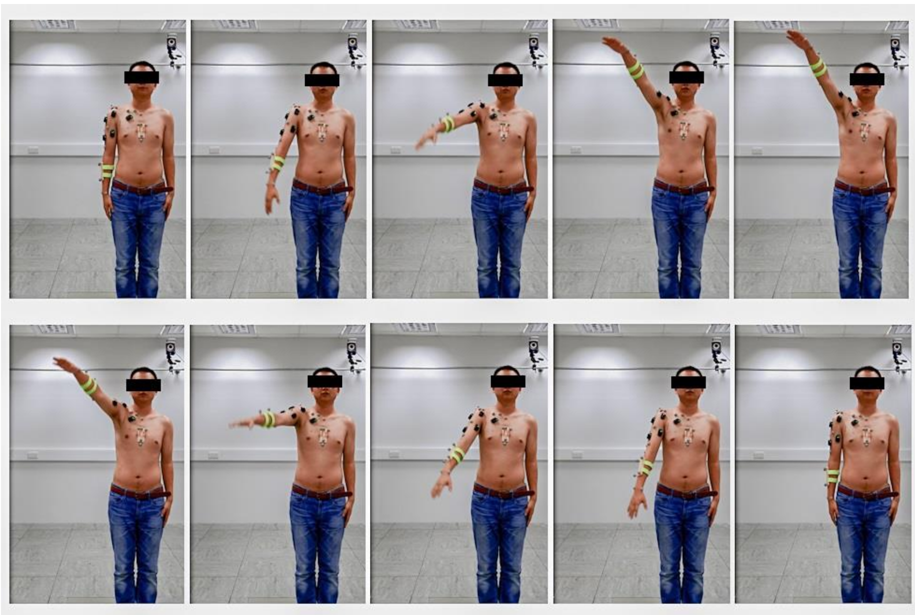

Figure 3-13 Scapular plane abduction animation photos

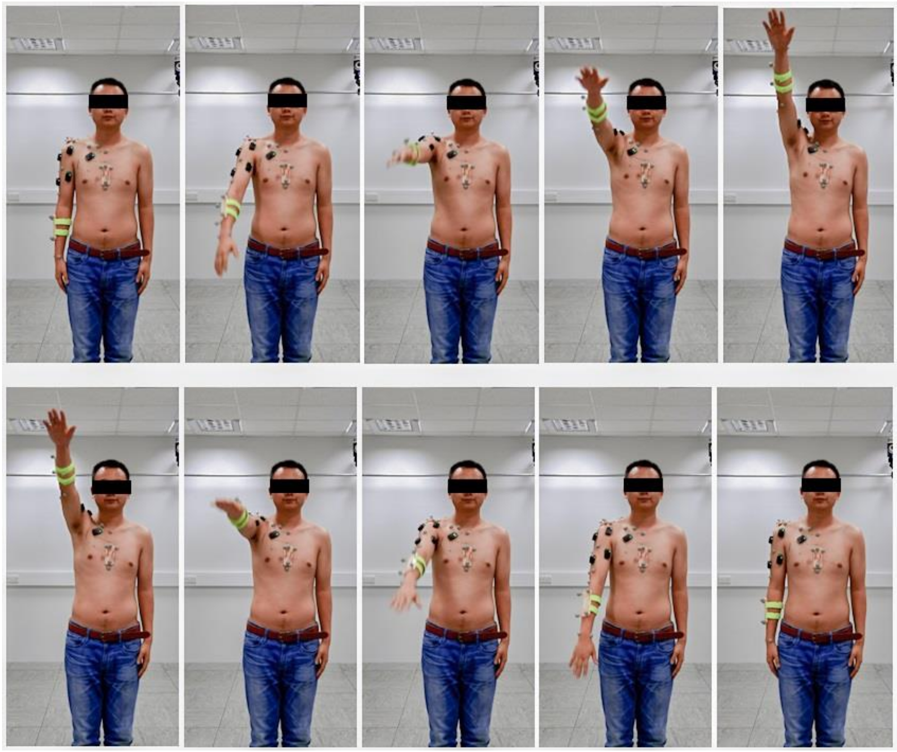

Figure 3-14 Forward extension animation photos

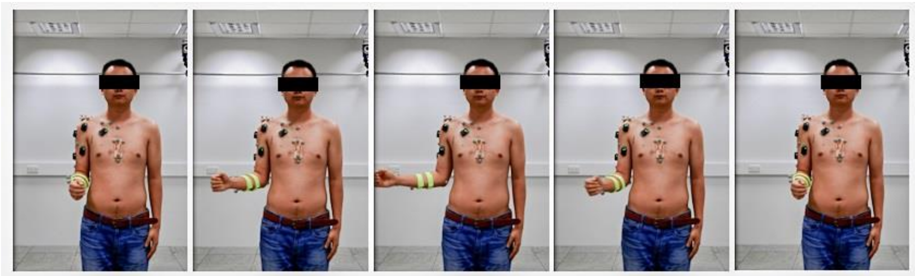

Figure 3-15 External rotation animation photos

3.5 Some measurement results

The recorded marker trajectories and EMG signals can be visualised directly in the Vicon software package Nexus. Figure 3-16 is a screenshot of the results of one frame in frontal plane abduction measurement. In this screenshot, 3D positions of all the markers of this instance time can be found in the middle upper view while the simultaneous EMG signal can be found in the middle lower view. By rough observations, all experimental data in each frame was displaced in the system. Full detailed result of the 3D marker positions and EMG signal could be found in the following parts in this section.

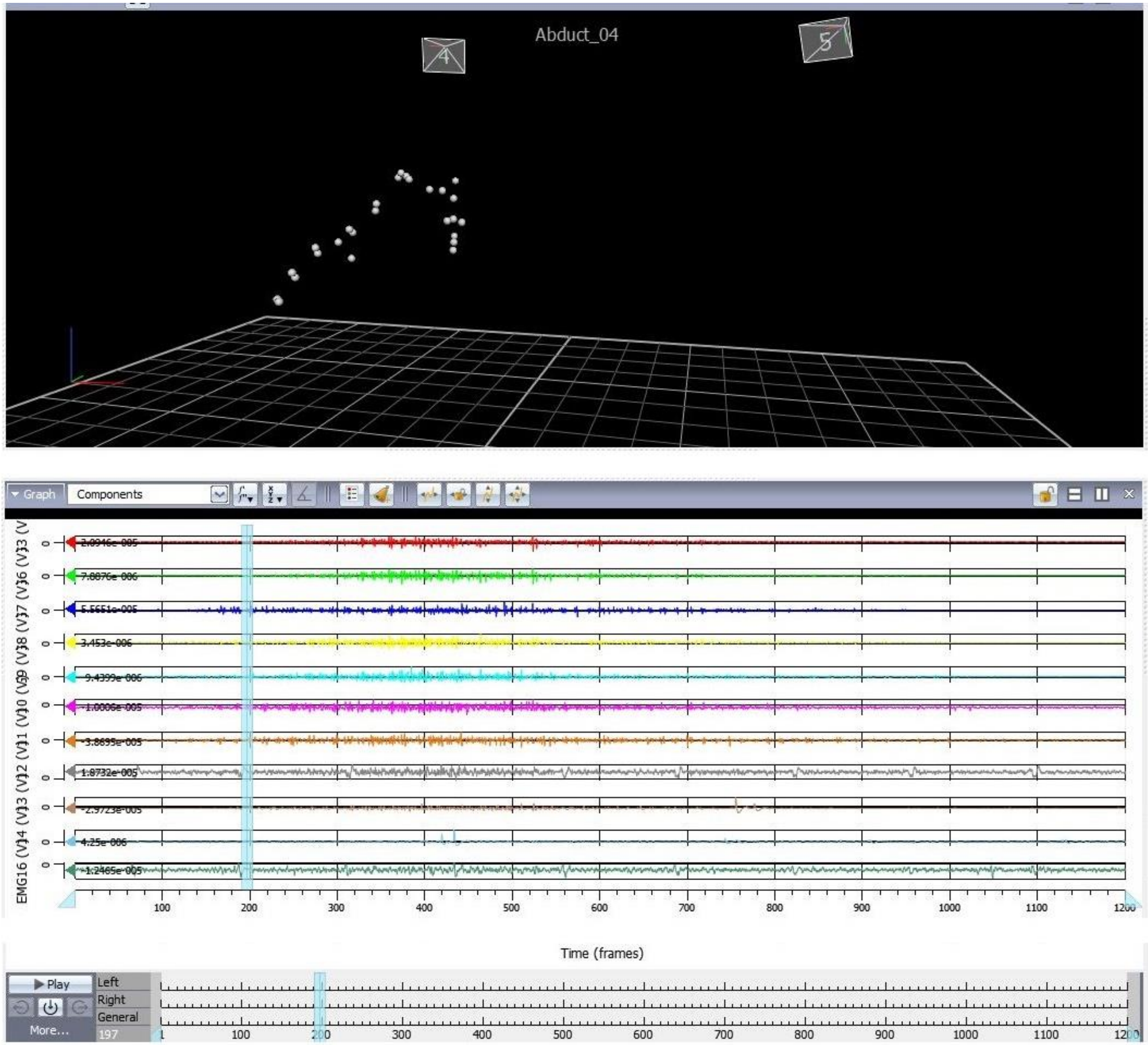

(a)

(b)

(c)

Figure 3-16 Example results in the Vicon system of (a) 3D marker positions and (b)EMG signals of all electrodes in one frame as shown in (c) (around 200s) in frontal plane abduction.

The raw data collected from the stereophotogrammetric systems contains noise and from many sources including electronic noise in optoelectric devices, image distortion errors and noise due to skin movement artefacts etc. [113]. In addition, markers could be missing in some frames due to the blocking of moving segments in some trials, which could result in gaps in trajectories. Therefore, the raw data was subjected to pre-processing procedures including gap filling and noise reduction before exporting. These pre-processing procedures were partially done by Vicon Nexus software packages auto-functions. However, a considerable amount of manual modification was conducted to finish including marker labelling, faulty marker fixation and manual gap filling etc. After pre-processing, the 3D motion data can be exported. Some example results can be found in Figure 3-17 to Figure 3-19. Figure 3-17 shows the trajectories of all the technical markers in one static trial. It was found that all markers remained in their X, Y and Z coordinates steadily. As the origin of Vicon system was on the ground and the Z axis was perpendicular to the ground, which was in parallel with the y-axis of the body (See Figure 3-3). Therefore, some of the markers such as the acromion markers (light blue lines on top of all lines) can be found with the maximum values, i.e., about 1500mm which is about 1.5m. Considering the height of the subject is 1.72m, we can say this 1.5m from the shoulder to the ground was acceptable. Figure 3-18 demonstrated the trajectories of all the technical markers in abduction (one of the dynamic trials). In basic interpretation, the largest variation in marker trajectories can be found in markers on the forearm. The Z coordinates of these several markers (in purple lines) started from around 900mm in the beginning and gradually increased until maximum of 1720mm at 2.4s and gradually decreased until reach its original position in 5s. At the beginning of the measurement, the forearm rest by the side of the body when the Z coordinates of the markers was found with the height of less than 1000mm (1m). In the middle of the measurement, the arm abducted to the about 120^{o} (Humerothoracic angles) when these several markers approximately had the same height with the head of the subject. And the Z coordinates of these markers were found to have the height of the head, i.e., 1728mm (1.72m). Therefore, the trajectories of these several markers were found agree with experimental observations. Figure 3-19 demonstrated the EMG signals of all the electrodes in the same abduction trial in Figure 3-18. By rough interpretation of the EMG signals, all the muscles were found functional.

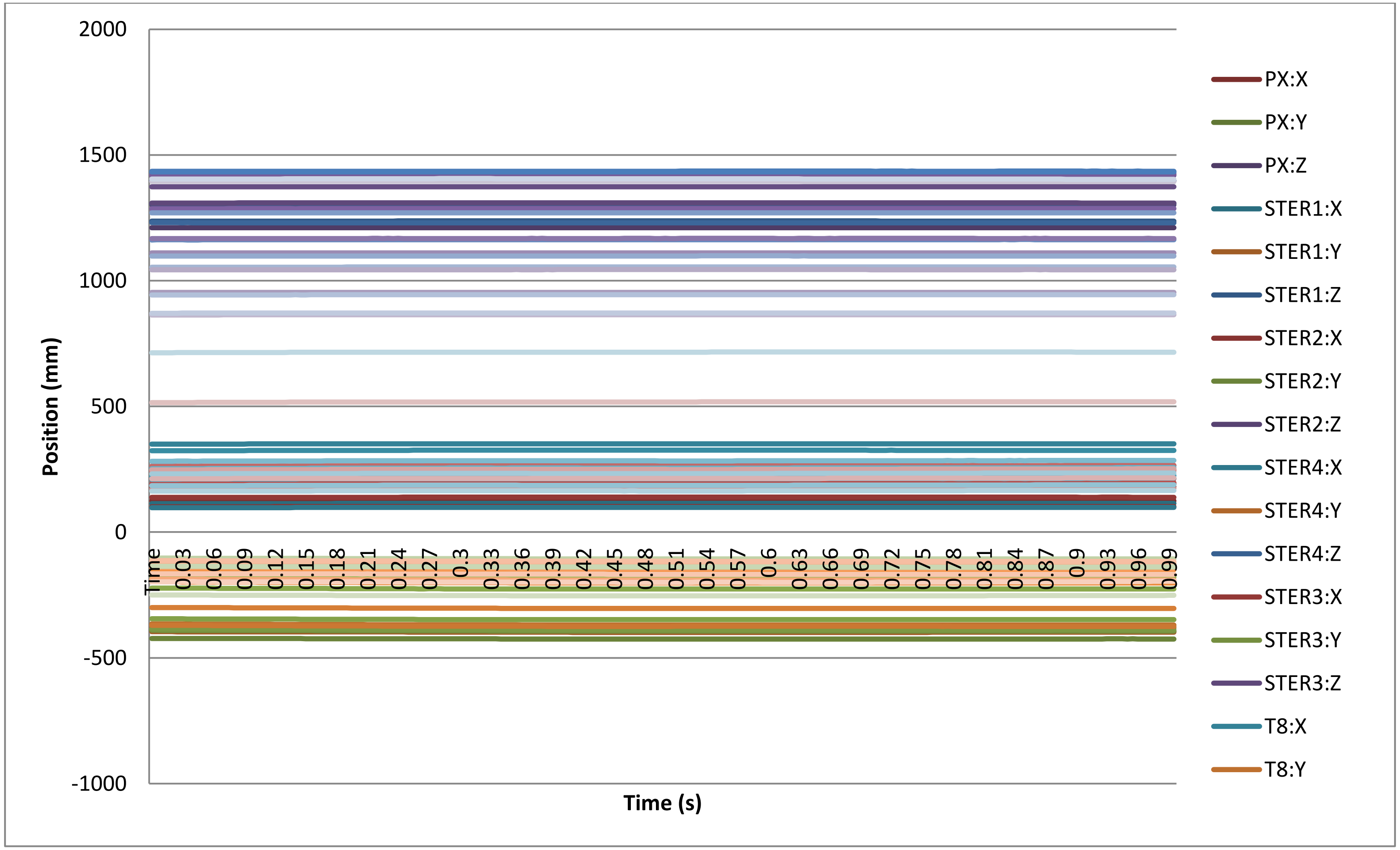

Figure 3-17 Marker trajectories in one static trial

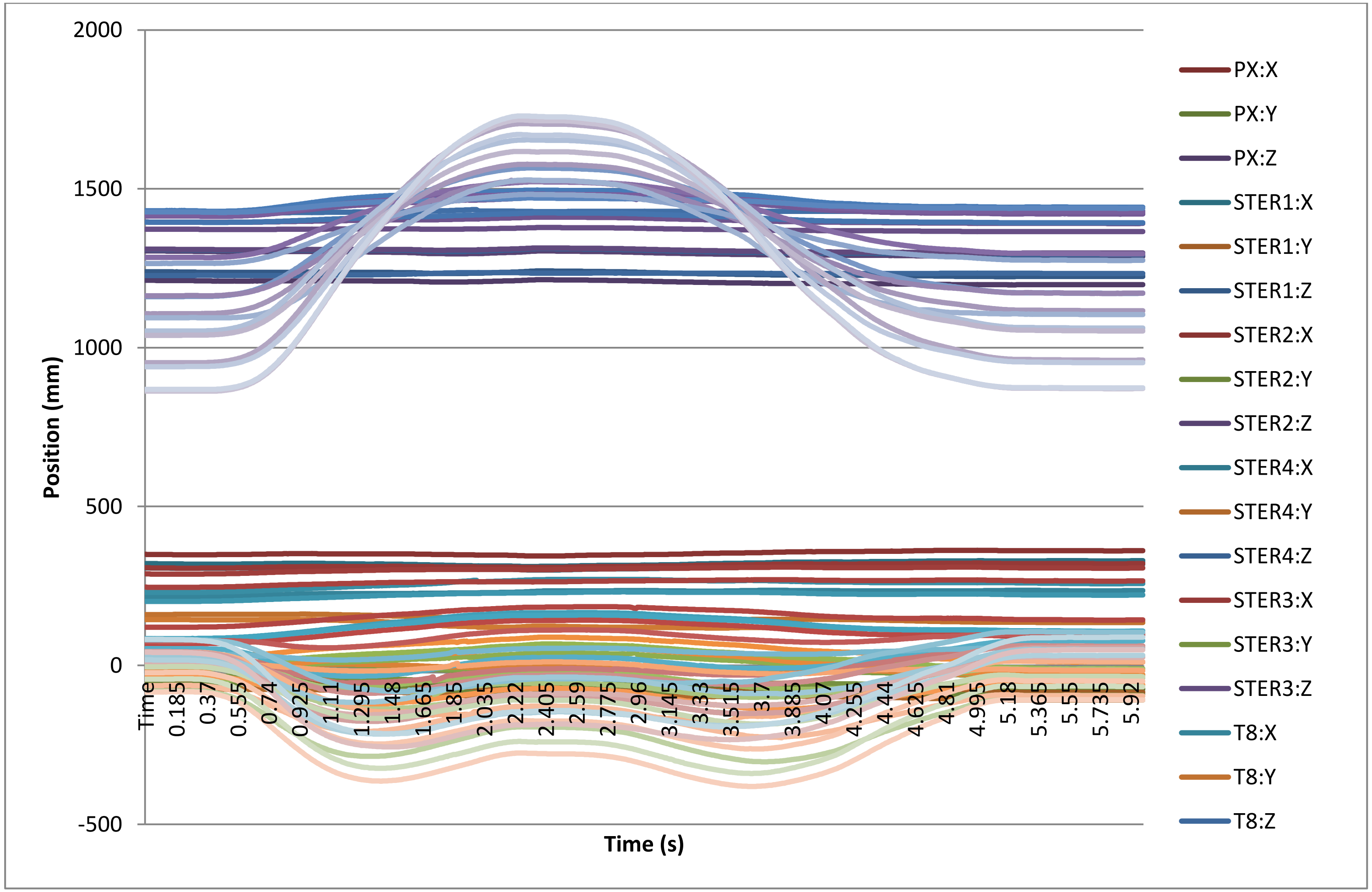

Figure 3-18 Marker trajectories in one dynamic trial

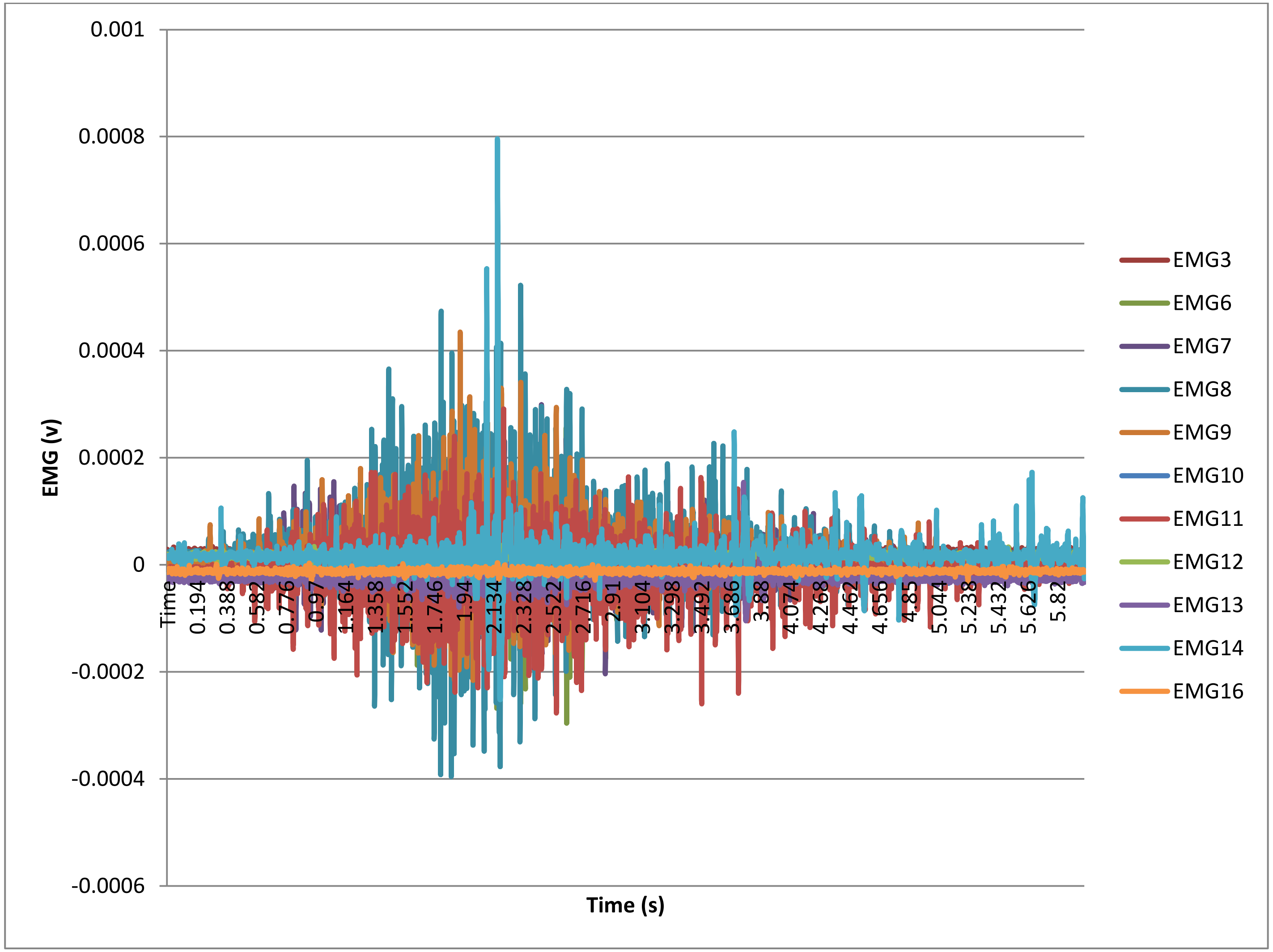

Figure 3-19 Simultaneous EMG signals of the biceps muscle in the above dynamic trial

3.6 Summary

This chapter presented the in-vivo 3D subject-specific shoulder motion with simultaneous muscle EMG signals of the subject that was measured by advanced stereophotogrammetry and wireless surface EMG system. A detailed experimental protocol was designed to use Vicon infrared cameras and Delsys wireless surface EMG systems based on literature recommendations and practical pre-test for the reflective markers attachment and EMG electrode placement on the body of the subject. The experiment was carefully conducted accordingly. Static motion trials were conducted first with the subject remaining still for 5 seconds followed by dynamics trials when the subject performed frontal plane abduction, forward extension, scapular plane abduction and external rotation that aimed to cover normal shoulder motions. All motion trials were performed multiple times to exclude random errors. Some of the raw experimental data were presented subject to pre-processing. The data contained trajectories of all technical markers and simultaneous EMG signals. Rough interpretations of these data indicated that the measurements cohered with relative experimental observations. The EMG signals measured in this chapter were merely used for qualitative observations, while the measured kinematics data would be further implemented to construct the subject-specific multi-body musculoskeletal model and calculate the *in-vivo* muscle activations in Chapter 4. In addition, the measured joint positions during scapular abduction would be further used to define the loading and boundary conditions of the FE model in Chapter 6 and 7.

Chapter 4 Musculoskeletal modelling of the human shoulder complex using OpenSim

4.1 Introduction

This chapter presents the prediction of the *in-vivo* muscle loads under experimental motions collected from the preceding chapter. As briefly discussed in Chapter 2, the multi-body model is the other computational biomechanical shoulder model type besides FE model. This category of models is mainly designed to estimate the internal loadings (e.g. muscle loads) of the musculoskeletal system during motion. In the field of musculoskeletal biomechanics study, it is stated that the multi-body models offer the macromechanics of the skeleton whereas the FE models the micromechanics of the articulating surface [34]. The specialised software package OpenSim was adopted to construct the subject-specific multi-body musculoskeletal model based on a generic model from published work. The construction of the subject-specific model was conducted by scaling the generic model using the measured static data of four markers on the thorax and four markers on the humerus during the experiment. The constructed musculoskeletal model contains 3 degrees of freedom in the glenohumeral joint (a general ball-socket joint). A total number of 25 muscles were defined by 29 bundles around the shoulder and elbow joints. The same marker system used in the experimental measurements was adopted to drive the model so to calculate the glenohumeral joint angles during the scapular plane abduction during the motion capture experiment using inverse kinematics method. Subsequently, joint torques were calculated to match the above joint motions by inverse dynamics method. Finally, the individual muscle loads in each instant time during motion were estimated by further decomposing the calculated joint torques among the muscles using the static optimisation method. The above inverse dynamic based force estimation method had been widely used for decades. In this study, this method was mainly executed using the available toolbox modulus in OpenSim software, while partially processed manually using MATLAB. A brief overview of the background of the muscle force prediction techniques and the OpenSim software were presented in section 4.2. While, the detailed process using OpenSim for muscle force estimations and the final results were presented starting from section 4.3, followed by a discussion in section 4.4. The motion under analysis was limited to the scapular plane abduction in the range of 0-30^{o} intercepting from the whole range motion data obtained from the experiment so as to keep consistency with the FE simulation.

4.2 Background

The musculoskeletal system is a mathematically redundant force system which means that there are more unknown muscle forces than equilibrium equations. In order to get a unique set of solution for individual muscles forces, optimisation method was introduced. Optimisation theory is believed to give good indications of the physiological basis underlying muscular force-sharing function in many musculoskeletal structures [127]. Optimisation of muscle forces can be conducted in both static and dynamic configurations and based on different standard mathematical methods and criteria. Although the human body and muscles are dynamic motors, it is shown that static optimisation can give equivalent satisfactory results as dynamic optimisation depending on desired evaluation [128]. There are two strategies when applying static optimisation i.e. inverse and forward dynamics. The inverse dynamics based static optimisation method has been commonly used for decades, due to the availability of the joint kinematics data and ground reaction forces [129]. Figure 4-1 illustrates how the inverse dynamic based optimisation works in general. The individual muscle forces F_{MT} are estimated by minimizing this objective function $J(F_{MT})$ subject to the rest of the equations/inequations in the figure which represents the physiological constrains.

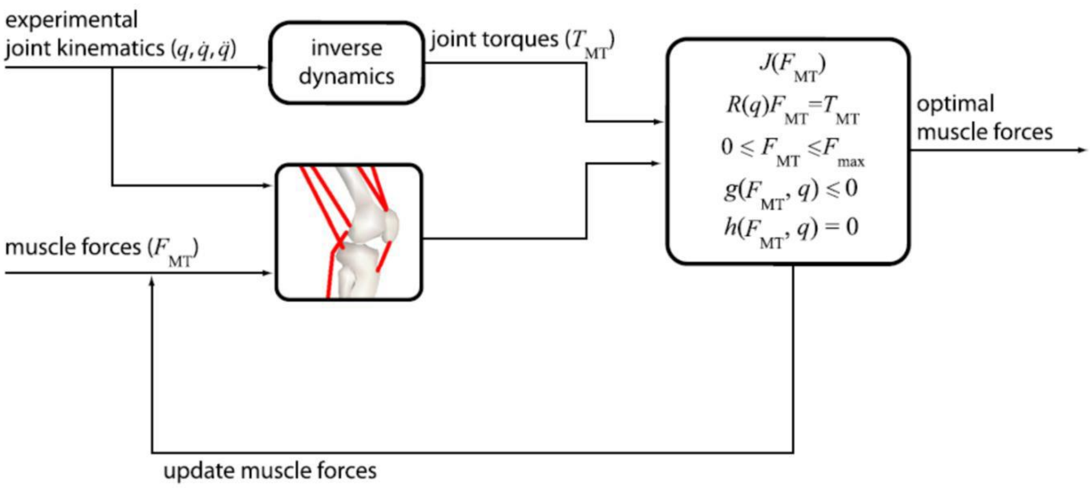

Figure 4-1 Schematic diagram of inverse dynamic based static optimisation [129]

The OpenSim is open-source software that enables individual investigators to develop subject-specific musculoskeletal modelling, simulations and analyses. Furthermore, it has built up a platform where the biomechanics community can contribute, exchange, test and improve each other's models and simulations into a library [130, 131]. The scale toolbox allows users to conduct subject-specific simulations by scaling the generic model to fit the subject in their own experiments. Thereafter, to perform the standard inverse based-static optimization on the scaled generic model, a set of toolboxes is also available in OpenSim including inverse kinematics toolbox to resolve joint position, velocity and accelerations from experimental marker positions corresponding to the landmarks of the segment; inverse dynamics toolbox to determine a set of generalized joint torques to match this estimated acceleration and static optimisation toolbox to decompose the generalized joint torques among the redundant muscles [132]. Comparing to Figure 4-1, the inverse kinematics toolbox takes the raw experimental marker trajectories as input and outputs the "experimental joint kinematics ($q, \dot{q}, \ddot{q}$)" in the figure; the inverse dynamics toolbox is the "inverse dynamics" block and the static optimisation toolbox is equivalent to the block that contains the objective function $J(F_{MT})$. It should be noted that there are plenty of objective functions used in different studies and the objective function used in OpenSim is the sum of the squared muscle activations.

4.3 Construction of the subject-specific multibody musculoskeletal model and motion simulation

The construction of the subject-specific multibody musculoskeletal model was performed using the experimental data from static trials in Chapter 3 based on the generic model from literature. In order to keep consistency with the finite element model, when selecting the generic model, its muscle configuration was primarily monitored. Specifically, the muscle configuration of the model needed to include all rotator cuff and deltoid muscles. In addition, the ability to describe the overall performance of individual muscle was favoured. Therefore, the optimal model among the few shoulder musculoskeletal models in OpenSim library that facilitate this study was the Dynamic Arm model as shown in Figure 4-2 [133, 96]. This model is the shoulder model in OpenSim built by the founders of OpenSim, which had been widely used in published works [134, 135]. In this model, the shoulder joint contains 3 degrees of freedom (a general ball-socket joint simulating the glenohumeral joint). A total number of 25 muscles were defined by 29 bundles around the shoulder and elbow joints. Muscle configurations of the rotator cuff muscles were each represented by one bundle, which can provide the overall performance of individual muscle as favoured. The deltoid muscle was divided into three bundles which were also acceptable. Considering this study is conducting some exploratory research on integrating different computational biomechanical methods of the shoulder joints, the scapulothoracic and sternoclavicular motions could be too complicated to be duplicated in the FE model. Hence, the FE simulations were constrained in 0-30 ° humerothoracic abduction in the scapular plane, in which this chosen multi-body model could demonstrate accurate muscle loading results with efficiency and little computational cost since scapulohumeral rhythm would cause no problem in this range of motion [136].

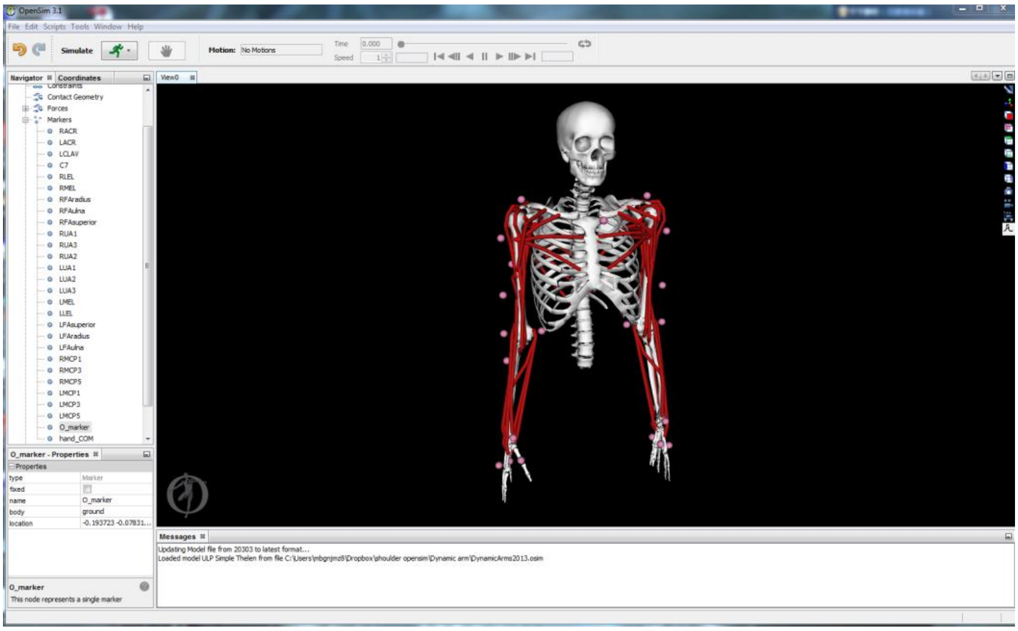

Figure 4-2 The Dynamic Arm model [133]

To keep the consistency of the coordinate system in OpenSim with the experimental configuration, all the experimental data were subject to coordinate transformation. In addition, the raw experimental data was smoothed using a fourth-order, zero-lag, low-pass Butterworth filter with a cuff-off frequency of 3 Hz [51]. The MATLAB codes conducting these procedures can be found in Appendix A (1) raw experiment data transformation and smoothing.

4.3.1 Subject-specific scaling of the generic model

The scaling step is conducted by scaling the multi-body model so that the virtual markers on the model match the experimental markers, provided that both of the virtual and experimental markers are refering to the same anatomical landmarks of the subject. Overview of the scale step can be found in Figure 4-3. The .osim file represents the multibody model; the .trc file contains the experimental data from static trials and the virtual marker data is included in the .xml file.

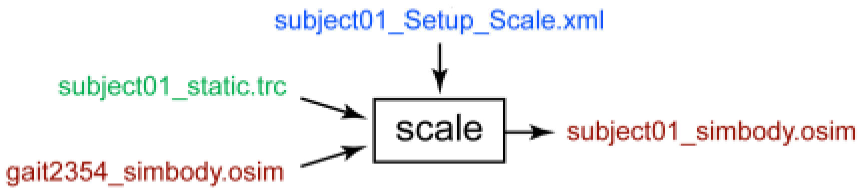

Figure 4-3 Schematics of scale toolbox in OpenSim [132]

To apply scaling to the generic model, firstly, the experimental data were converted to OpenSim file format using Excel where the number of frames (200), markers (8) and time (0.79s) were defined. The 8 markers were selected 4 on the thorax: PX, IJ, C7 and T8, while the other 4 were on the humerus: HUM1, HUM2, HUM3 and HUM4. (See Table 3-1 and Table 3-2 for details, these 8 markers were used for all the procedures in this chapter) Subsequently, the virtual marker set on the model was defined according to the experimental settings. To ensure the accuracy of the scaling, the marker names and positions were carefully defined based on the experimental markers. (See Figure 4-4)

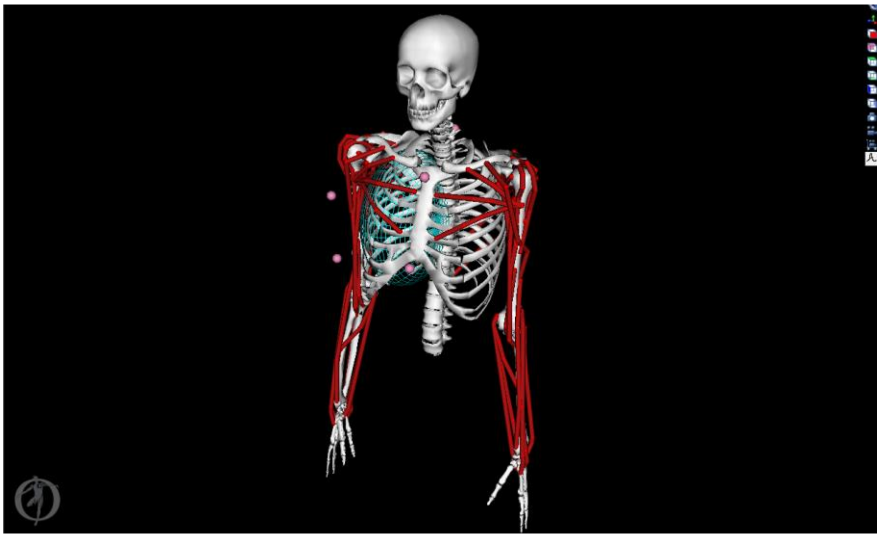

Figure 4-4 Virtual marker definition on the generic model

The generic model with defined virtual marker set was then used in the scale toolbox. The comparison between the scaled model and the generic model can be found in Figure 4-5. The accuracy of the scaling procedure can be found in the message prompt "Frame at (t=0): total squared error = 3.13e-4, marker error: RMS=6.26e-3, max=8.70e-3 (T8)". The total squared error and marker errors were found significantly small. The generic model was considered scaled to the fit the experimental subject successfully.

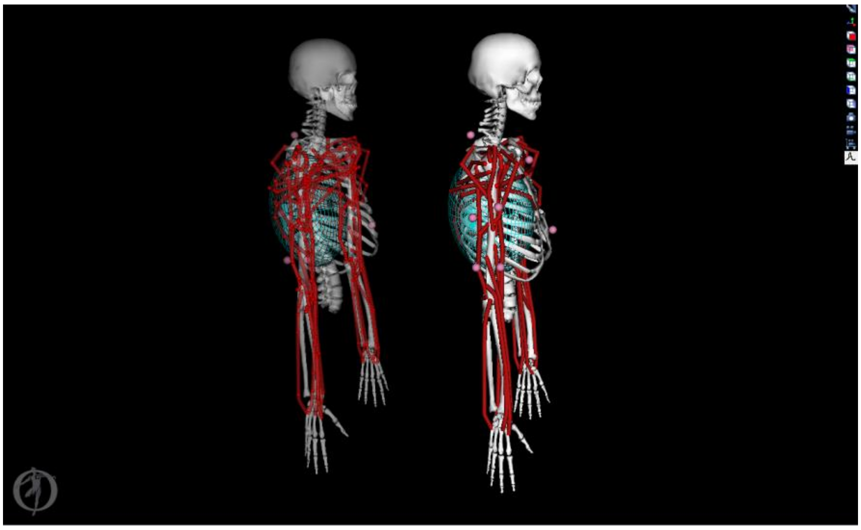

Figure 4-5 Subject-specific scaled model (right) versus generic model (left) after scaling

4.3.2 Joint angles calculation by Inverse kinematics

The scaled model was then used for the calculation of the joint angles by inverse kinematics under experimental humerothoracic abduction motion trials. Similar to the scaling step, the inverse kinematics step is performed through moving the model segments so that the virtual markers match with experimental ones. This movement of the model segment is conducted by computing the joint angles of the model needed on each instant time during the motion to match the model to the corresponding experimental subject. The overview of the inverse kinematics toolbox can be found in Figure 4-6.

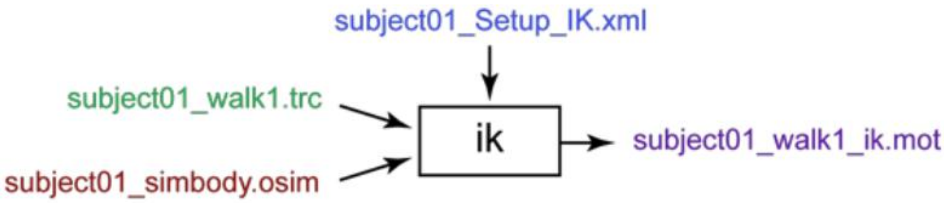

Figure 4-6 Schematics of inverse kinematics toolbox in OpenSim [132]

Similar to the scale step, the experimental data of the abduction trials was converted to OpenSim format in Excel where the frames (1200), markers (8) and time (5.99s) was included. The inverse kinematics step was driven by the experiment data. The 3 Euler angles for the ball-socket type glenohumeral joint, namely “shoulder_elv”, “shoulder_rot” and “elv_angle” were computed in each frame to adjust the model predictions to match the experimental makers. This match was computed by minimising a sum of squared errors of maker’s coordinates with the experimental makers’. During the calculation, the joint angles were computed in each instant of time and the model moved accordingly (See Figure 4-7).

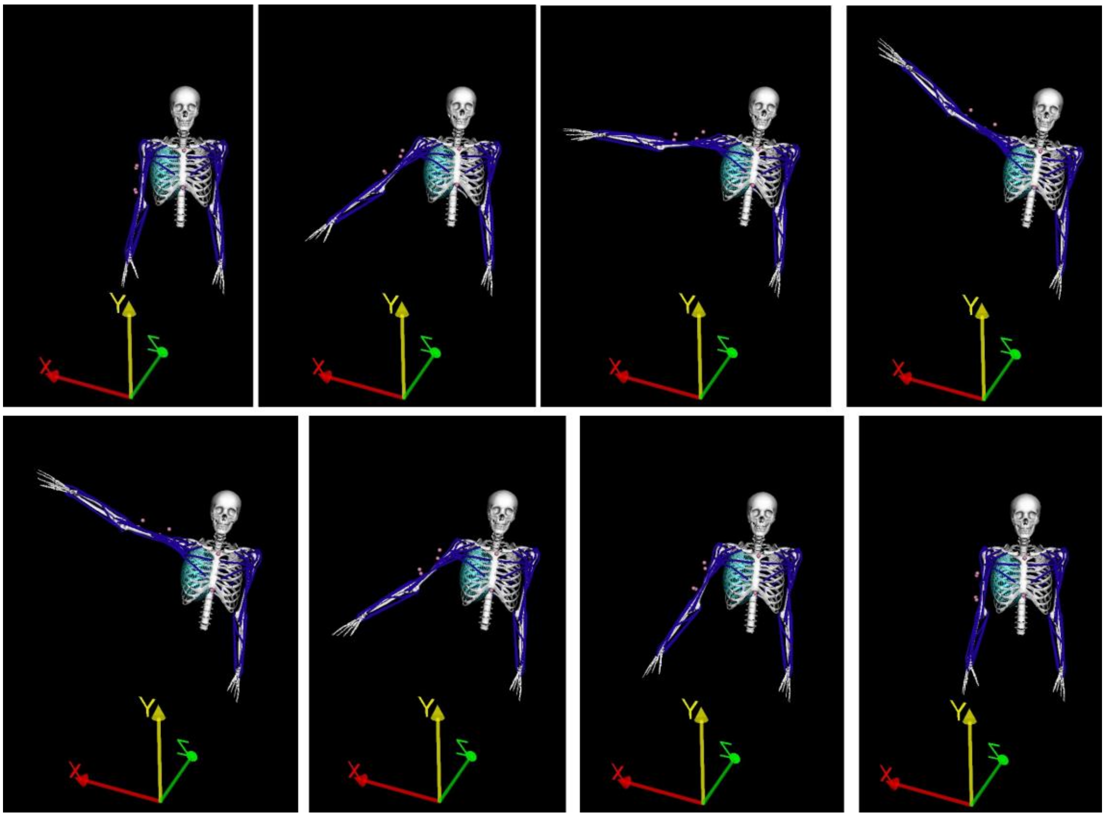

Figure 4-7 Animation screenshots in inverse kinematics step

By rough observation, the calculated motion can be found to be well following the experimental motion. More significantly, the accuracy of the inverse kinematics calculation of each instant time (1200 in total) could be found on the message prompt:

> "Frame 1 (t=0.005): total squared error = 4.55e-4, marker error: RMS=7.54e-3, max=9.66e-3 (HUM2)
>
> Frame 2 (t=0.01): total squared error = 4.54e-4, marker error: RMS=7.53e-3, max=9.60e-3 (HUM2)
>
> ……
>
> Frame 1198 (t=5.99): total squared error = 0.30e-4, marker error: RMS=6.14e-3, max=7.42e-3 (C7)
>
> Frame 1199 (t=5.995): total squared error = 0.30e-4, marker error: RMS=6.13e-3, max=7.38e-3 (C7)"

All the calculation errors can be found considerably small. The maximum total squared error and the maximum marker error were 1.85e-3 and 1.52e-2 (root mean square) in frame 616 (t=2.61), where we can also find the maximum single marker error 0.02 of the maker HUM3. The calculated joint angles of the glenohumeral joint can be found in Figure 4-8. This figure demonstrated the computed three Euler angles for the ball-socket type glenohumeral joint during the experimental measured motion, namely shoulder_elv, shoulder_rot and elv_angle. The variations of these three angles were the reason that caused the motion of the model in Figure 4-7 which had been found to agree with the experiment observations. The shoulder_elv angle represented the humerothoracic abduction of the subject. This joint angle started at around 5^{o} in the beginning and gradually increased to maximum of above 100^{o} in around 450s. Afterwards, it decreased gradually until its original position in around 850s. The total variation is about 95^{o} which was found close to our experimental trials.

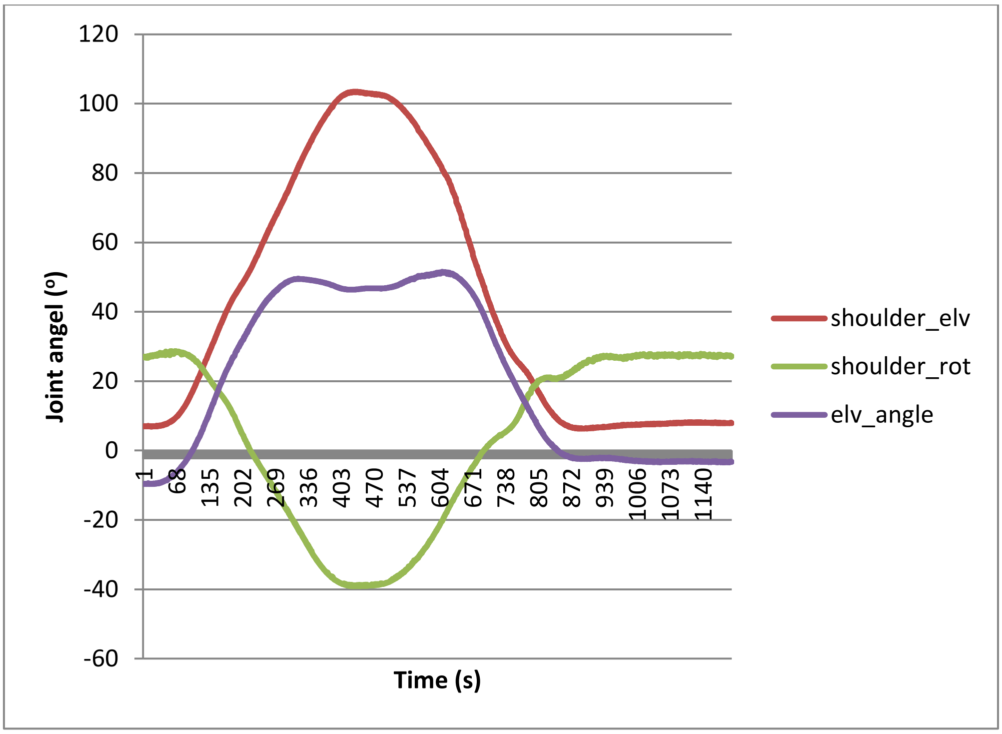

Figure 4-8 Joint angles calculated in the inverse kinematics step for one whole cycle

4.3.3 Muscle forces prediction by inverse dynamic based static optimisation

In OpenSim, the inverse dynamics is included in the static optimisation. The calculated joint angles from inverse kinematics step were implemented first to determine the joint torques which were further resolved to individual muscle forces. The overview of the static optimisation toolbox can be found in Figure 4-9.

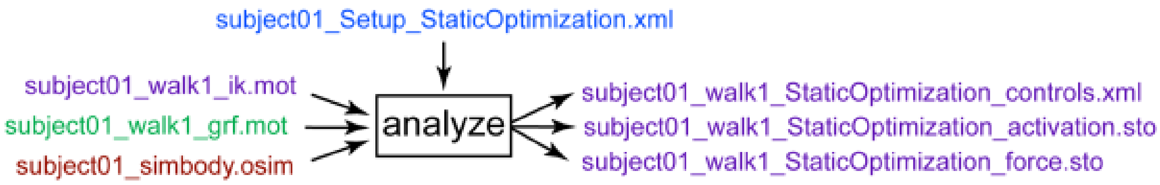

Figure 4-9 Schematics of static optimisation toolbox in OpenSim [132]

As there were no external forces in this experiment, only the calculated joint angles served as the input to the model in this step. The calculation for one trial took about

8mins during which the movement of the model in OpenSim was found to be the same as the movement in inverse kinematics calculation (Figure 4-7). No error messages were found during the whole calculation. The constraint violations for all the frames were found to be considerably small in which the largest constraint violation was found in time 2.89s with a value of 2.69e-013. This indicates that the static optimisation was accurately performed in decomposing the joint torques into muscle forces.

By repeating both of the inverse kinematics and static optimisation steps, the muscle forces were resolved for all trials of scapular plane abduction. All the results normalised using MATLAB (See Appendix A (2): Muscle forces normalisation). By deleting one trial data that was obviously laid far off from all the rest of the trials, the results of the predicted muscles forces of all the trials for each muscle and their mean values and standard deviations can be found from Figure 4-10 to Figure 4-16. In these figures, individual patterns of the muscle force variation in each of the 6 trials in scapular abduction were presented on top, while the means and standard deviations for all 6 trials were computed and illustrated in the bottom of the figure. The results for teres minor and deltoid posterior muscle forces were found significantly small (less than 3N over the whole range). The rest of the muscle forces were found to increase monotonically, including deltoid anterior (0.75N to 37.88N), deltoid middle (42.73N to 108.40N), supraspinatus (6.90N to 21.61N), infraspinatus muscle (21.29N to 120.62N) and subscapularis (26.21N to 54.23N). This increasing trend general agrees with reality that one requires to use more muscle effort to raise his/her arm.

As a summary, the muscle forces of above muscles at the neutral, 10, 20 and 30 degrees of scapular abduction were listed in Table 4-1.

Table 4-1 Muscle forces of rotator cuff muscles and deltoid muscle in 0 (neutral), 10, 20 and 30 degrees scapular plane abduction

Abduction angle (°)	**muscle forces (N)**						
	Del-ant	Del-mid	Del-post	Supras	Infras	Subscap	T-minor
0	0.75	42.73	2.77	6.90	21.29	26.21	1.55
10	18.69	74.36	0.96	12.89	44.46	38.43	0.83
20	30.50	90.56	0.91	16.86	71.75	46.54	0.86
30	37.88	108.40	1.05	21.61	120.62	54.23	1.29

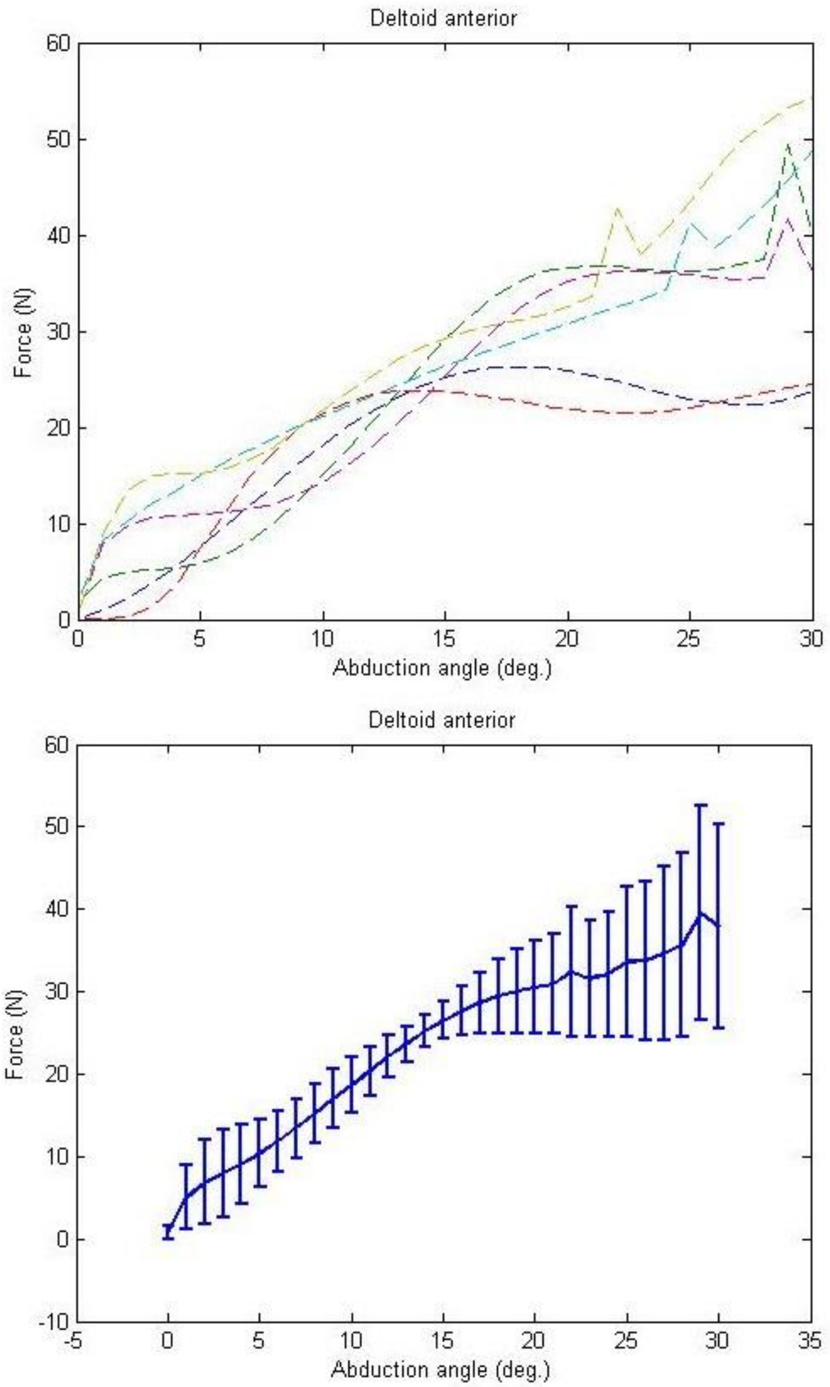

Figure 4-10 Predicted muscle forces for deltoid anterior muscle during shoulder scapular plane abduction. Top: individual pattern of each trial; bottom: means and standard deviations for all 6 trials

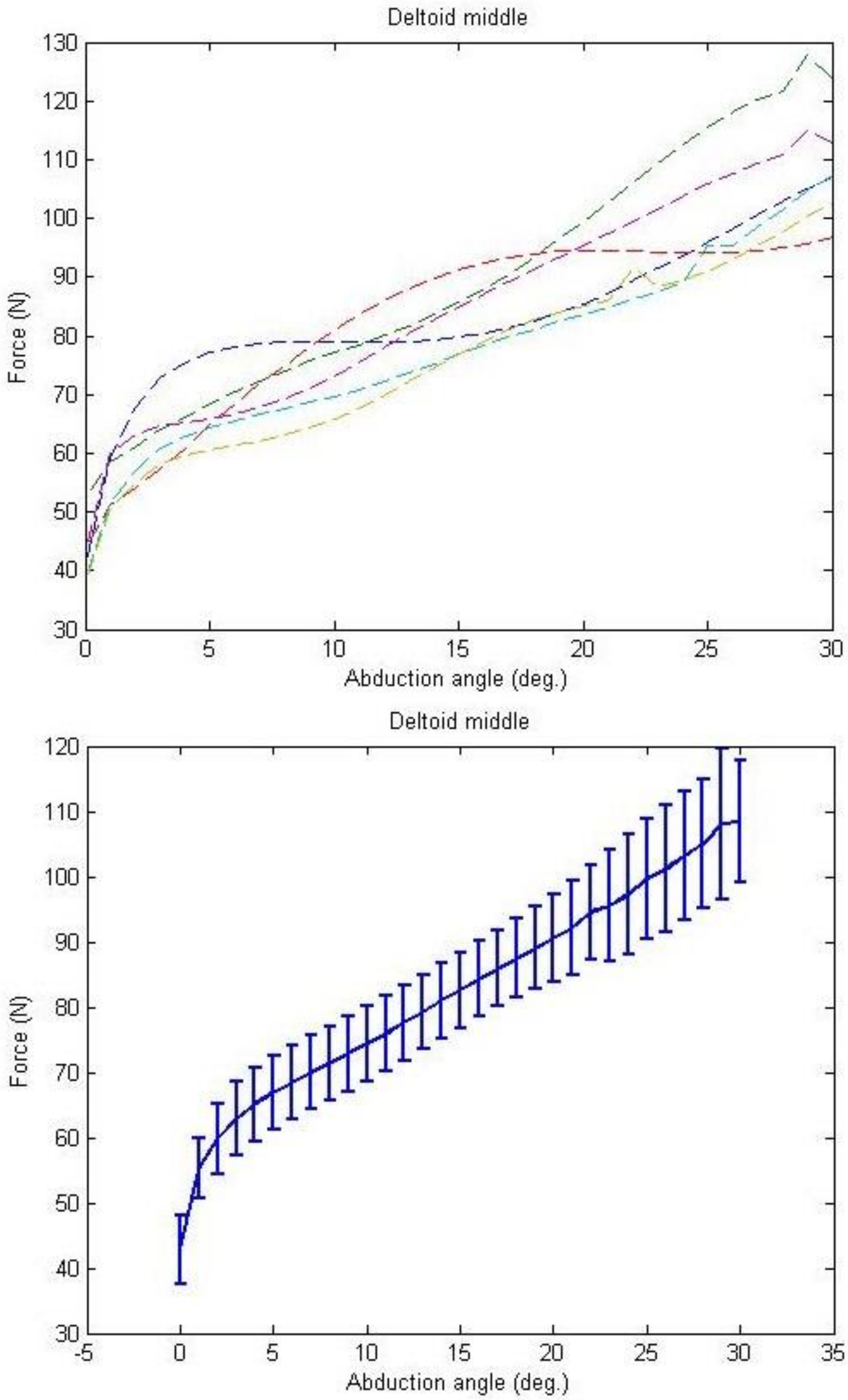

Figure 4-11 Predicted muscle forces for deltoid middle muscle during shoulder scapular plane abduction. Top: individual pattern of each trial; bottom: means and standard deviations for all 6 trials

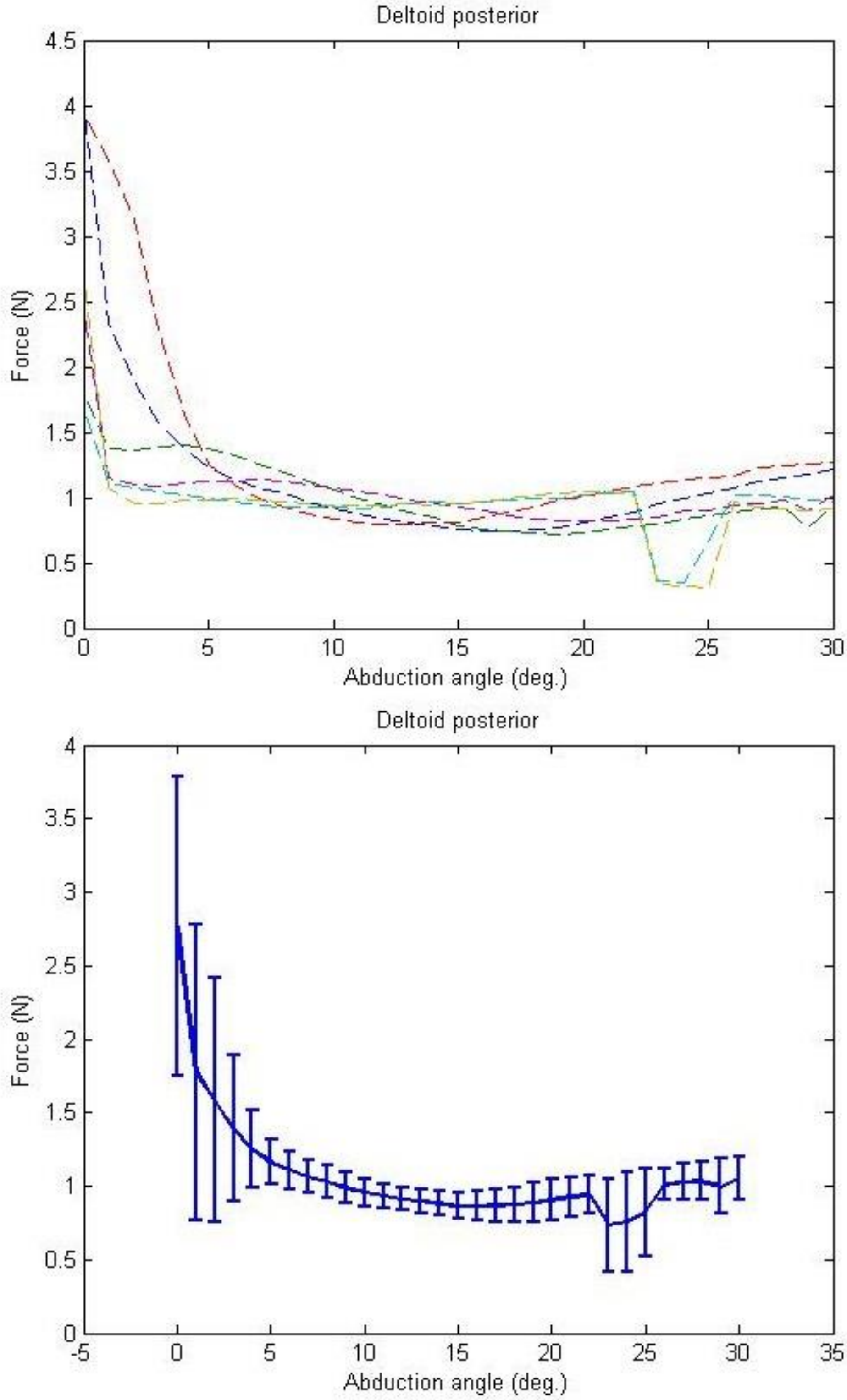

Figure 4-12 Predicted muscle forces for deltoid posterior muscle during shoulder scapular plane abduction. Top: individual pattern of each trial; bottom: means and standard deviations for all 6 trials

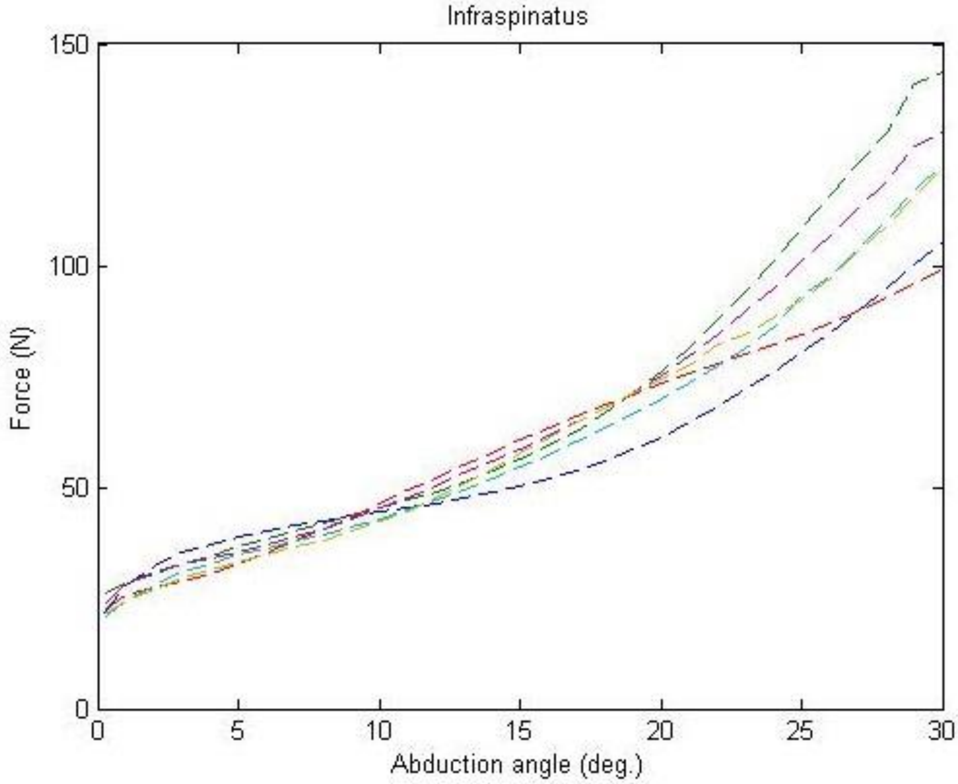

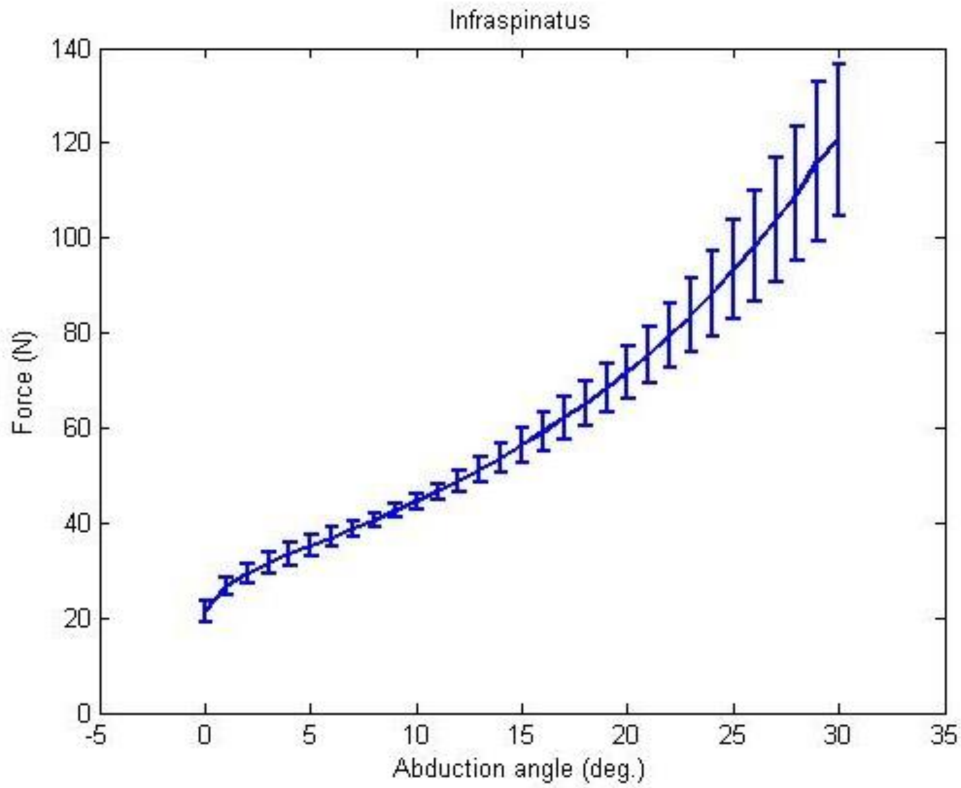

Figure 4-13 Predicted muscle forces for infraspinatus muscle during shoulder scapular plane abduction. Top: individual pattern of each trial; bottom: means and standard deviations for all 6 trials

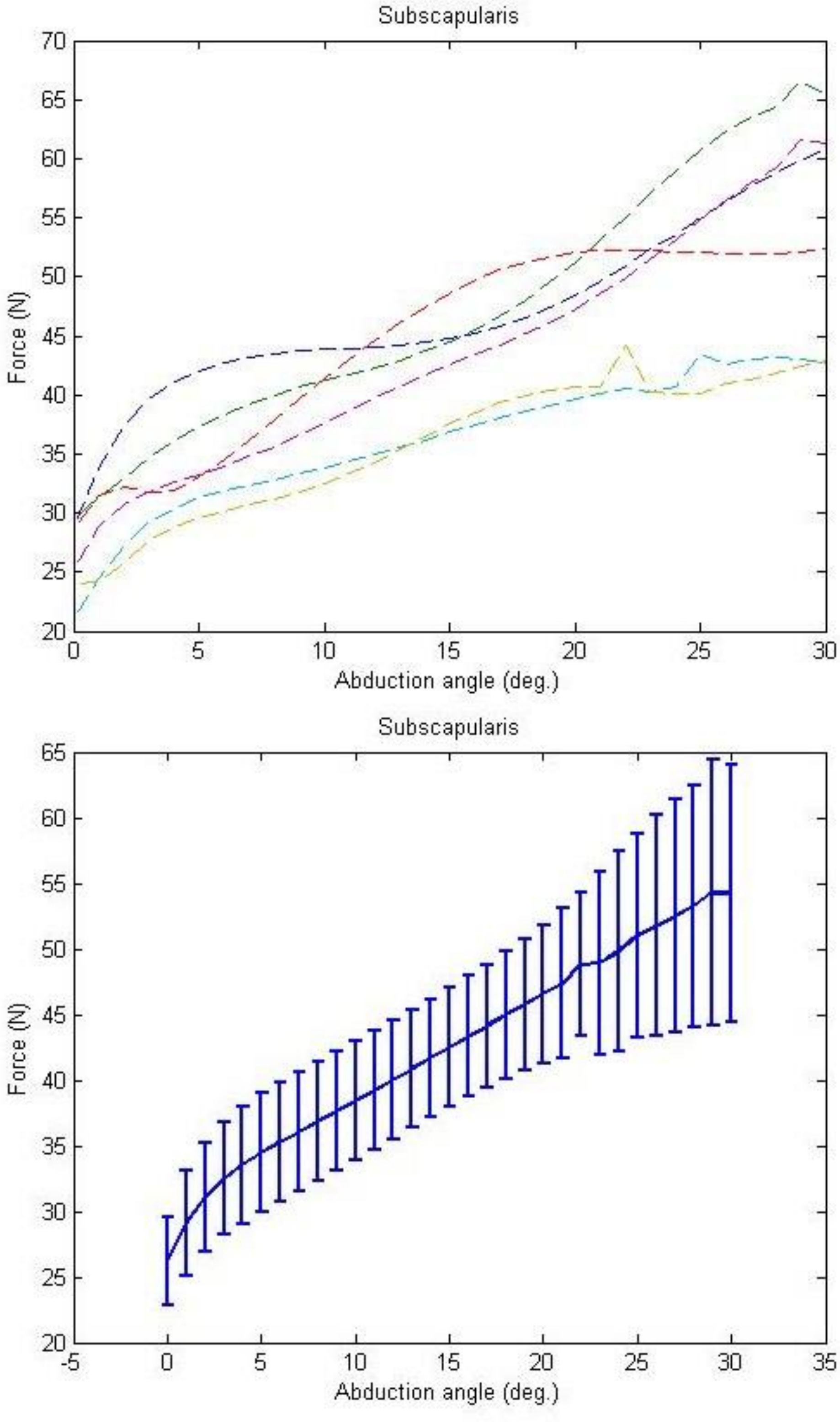

Figure 4-14 Predicted muscle forces for subscapularis muscle during shoulder scapular plane abduction. Top: individual pattern of each trial; bottom: means and standard deviations for all 6 trials

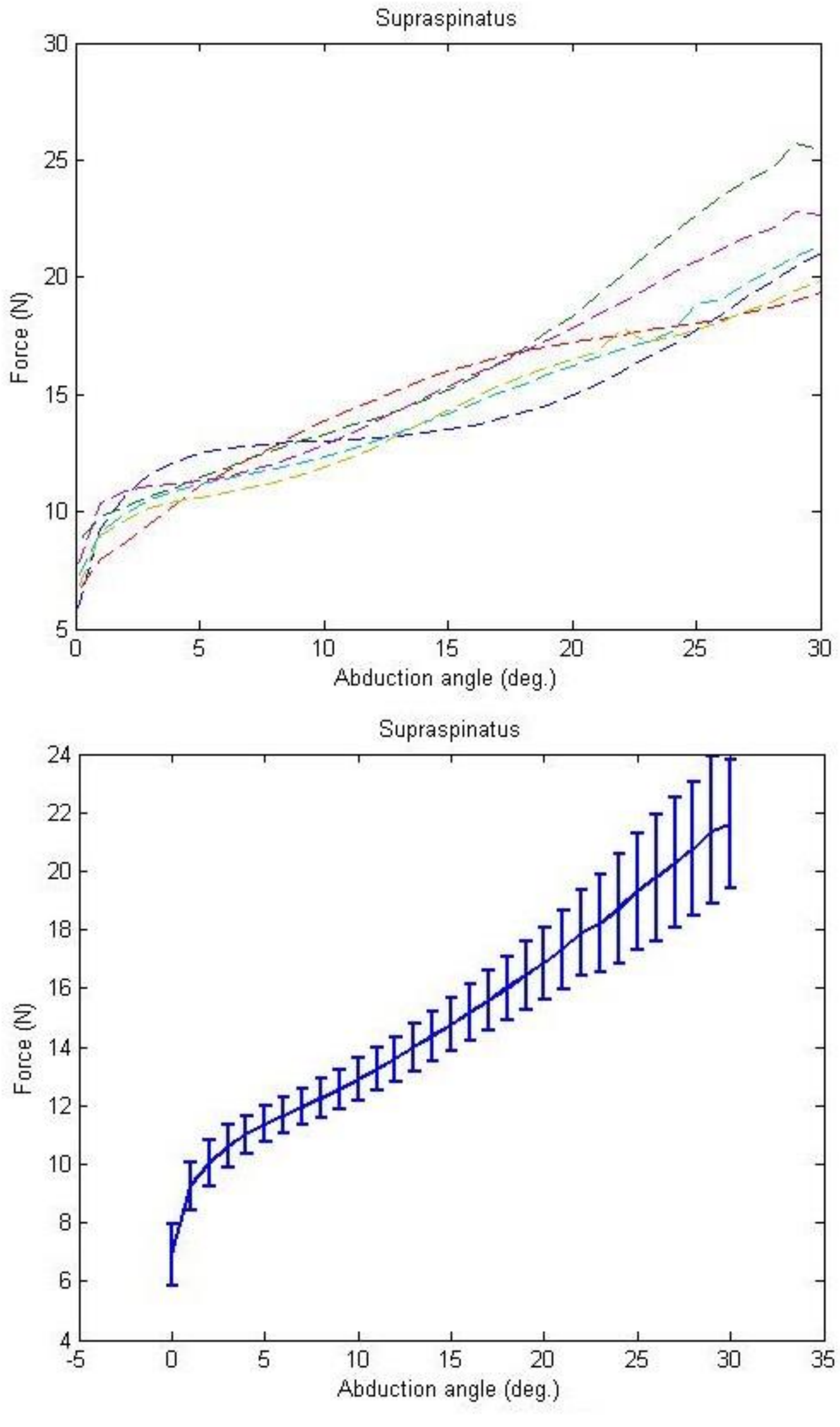

Figure 4-15 Predicted muscle forces for supraspinatus muscle during shoulder scapular plane abduction. Top: individual pattern of each trial; bottom: means and standard deviations for all 6 trials

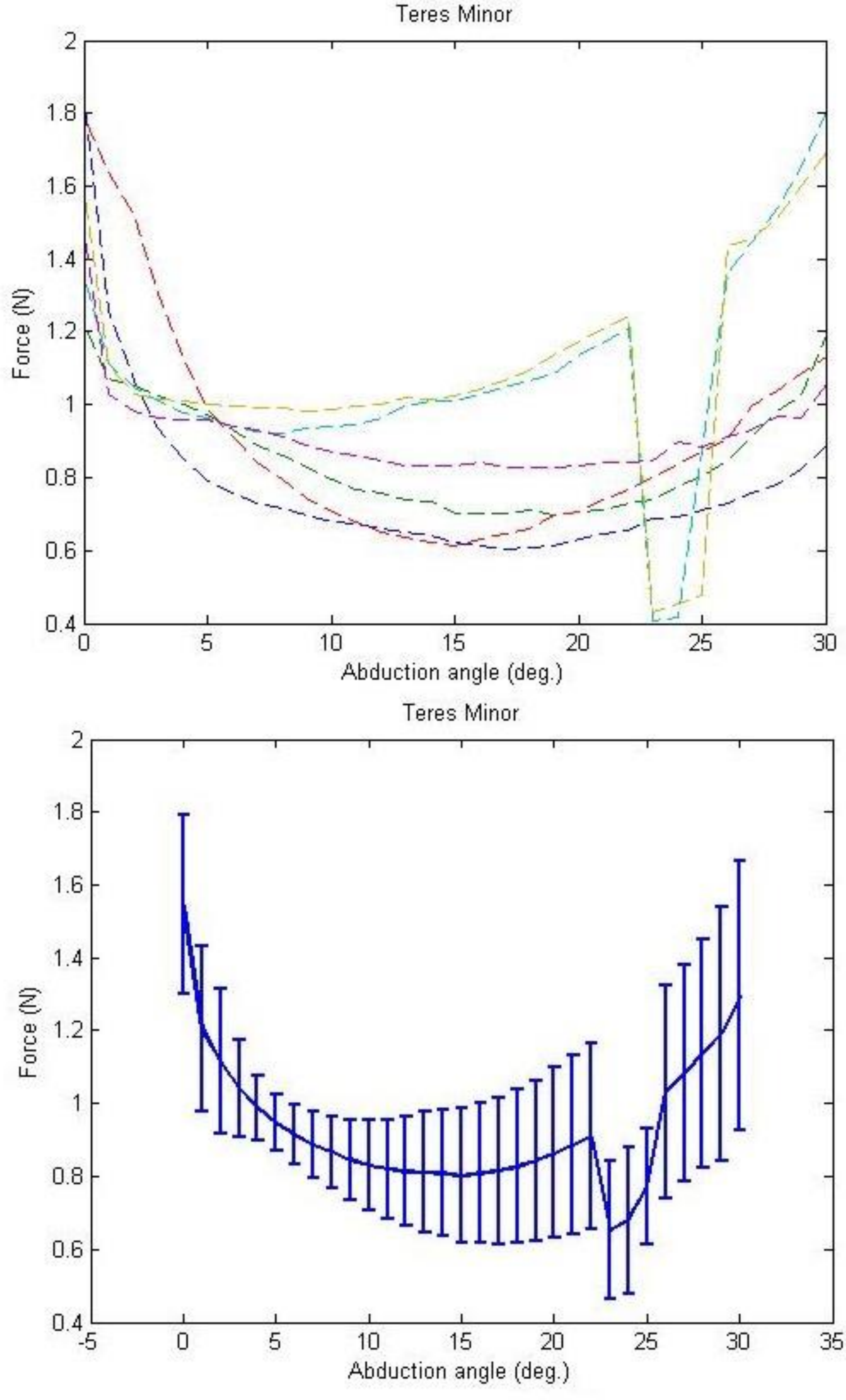

Figure 4-16 Predicted muscle forces for teres minor muscle during shoulder scapular plane abduction. Top: individual pattern of each trial; bottom: means and standard deviations for all 6 trials

4.4 Discussion

In the field of muscle force prediction study, *in-vivo* measurements are challenging both technically and ethically. Therefore, computational methods such as the multi-body musculoskeletal method used in this study were generally used. Particularly, this method had the ability to provide insight into predicting the mechanics of the system and neurological control in addition to the muscle force prediction. It was the state-of-the-art technologies in this field. Although muscle EMG cannot directly measure the muscle forces, it has been proven to demonstrate well the muscle activities signals [30, 33]. Therefore, the muscle EMG is often performed for observing the muscle stimulation qualitatively. However, due to the limited range of motion (0-30 degrees) in this study, it was not a necessity to process the EMG data for verification. Instead, the calculated muscle force results were compared to literature data. The predicted muscle forces were compared with literature data including three multibody studies [51, 52, 137] and one *in-vitro* study [138].

Among all the results of predicted muscle forces, the results for teres minor and deltoid posterior were found significantly small (less than 3N over the whole range) which were comparable to the results in the literature [52, 137] (maximum 6N), while the forces for these two muscles were either unavailable in some study [51] or combined with other muscles such as infraspinatus [138]. There were some sudden jumps on the calculated muscle forces in deltoid posterior and teres minor muscle in two trials , this should have come from the computation perturbations of the muscle wrapping, fortunately, the magnitude of the jump or even the whole muscle force for these two muscles were rather small, which would not cause significant problems in further calculations. The predicted muscle forces of the rest of the abductor muscles, namely the deltoid anterior, deltoid middle, supraspinatus, infraspinatus and subscapularis muscle were illustrated together with the relative literature data from Figure 4-17 to Figure 4-21 respectively.

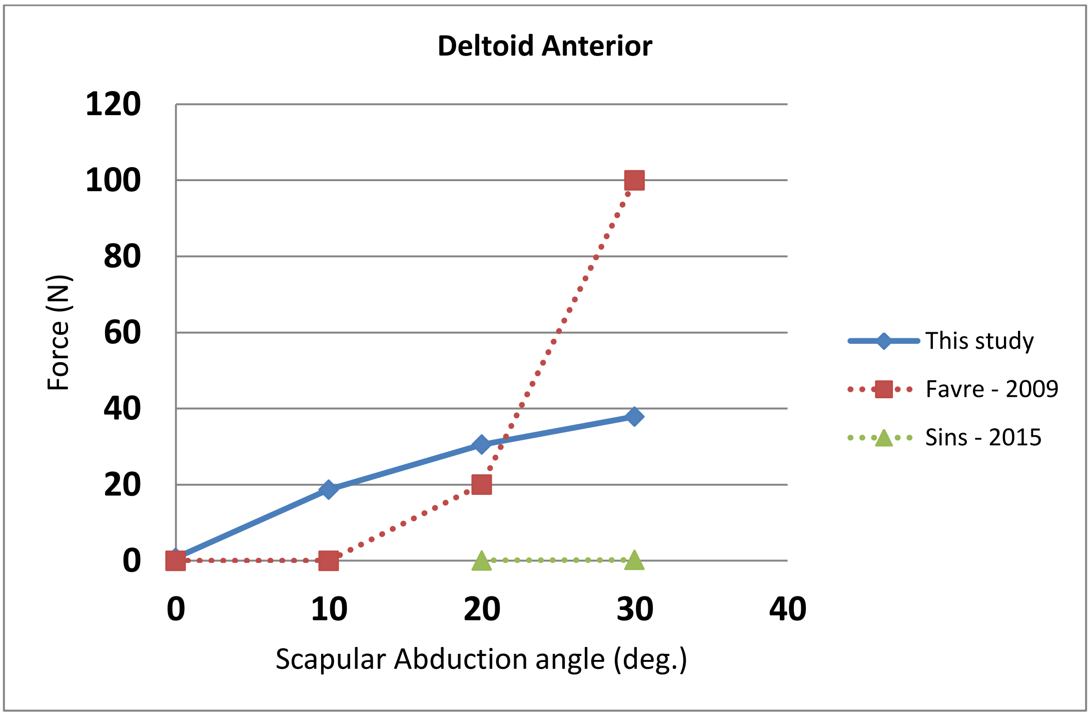

Figure 4-17 Deltoid anterior muscle forces results and comparison with other studies

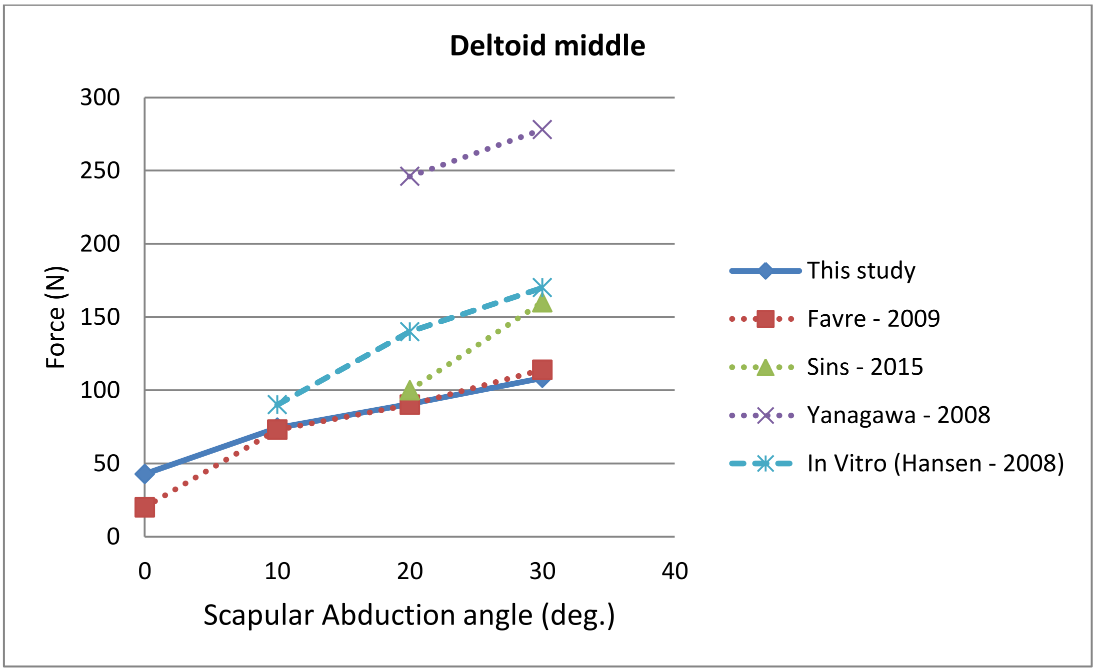

Figure 4-18 Deltoid middle muscle forces results and comparison with other studies

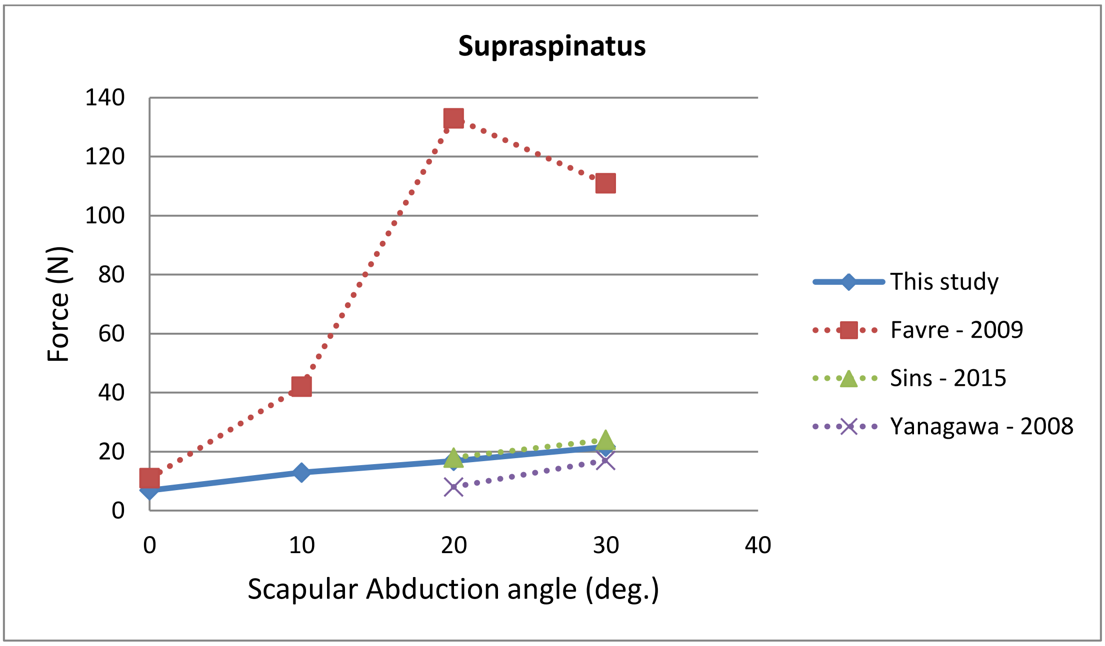

Figure 4-19 Supraspinatus muscle forces results and comparison with other studies

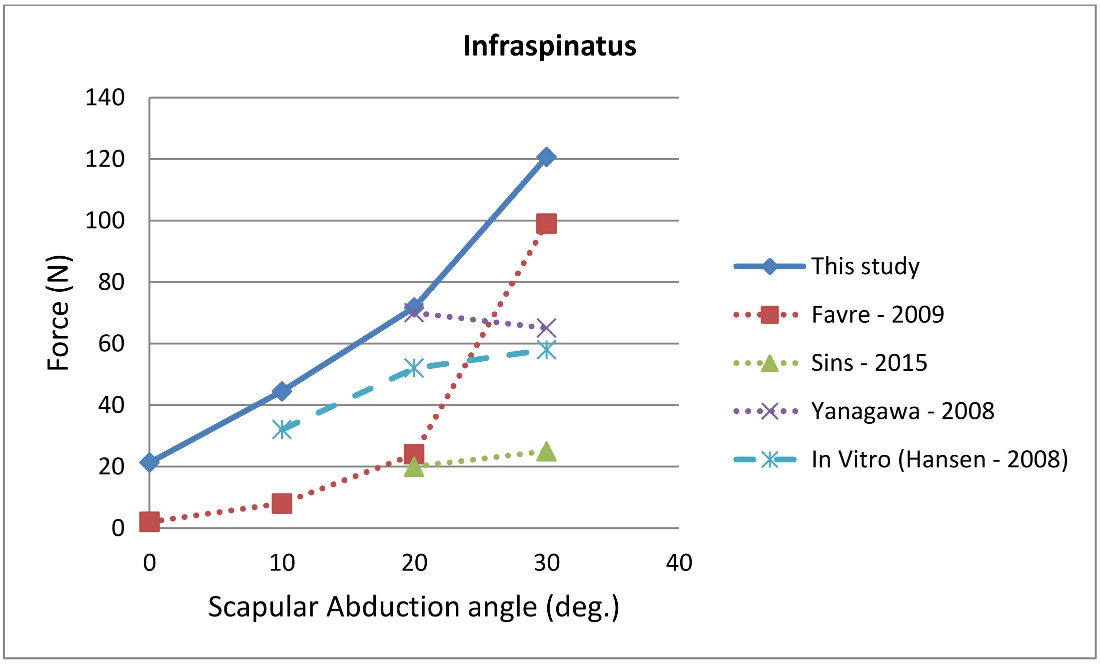

Figure 4-20 Infraspinatus muscle forces results and comparison with other studies

The figures showed that the muscle loads in scapular plane abduction have various results among literature. Besides, muscle results of the neutral position and 10^{o} abduction are not available in some literature. This is probably due to the fact that, unlike the abduction in the frontal plane which is a standard motion of the upper limb, the abduction in the scapular plane is subjected to individual difference. In addition, the scapular abduction motion itself is difficult for one subject to accurately perform repeatedly. Despite these differences, the general trend and magnitude of the predicted

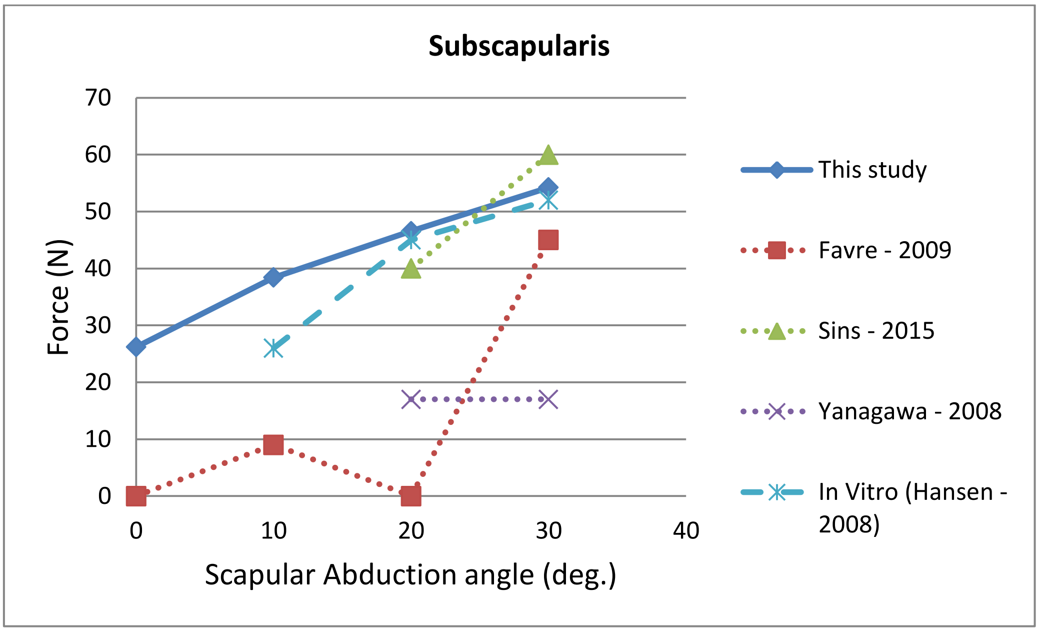

Figure 4-21 Subscapularis muscle forces results and comparison with other studies

muscle forces in this study had demonstrated generally good agreement with the literature predictions. The only notable difference was found in the predicted muscle forces in infraspinatus muscle where relatively large force was found in general. This was probably due to the fact that the muscle was divided into few numbers of bundles in the model adopted in this study. Similar patterns can be found in infraspinatus muscle in a study comparing the influence of the number of muscle bundles and paths on the muscle force predictions during the frontal plane abduction and forward flexion, "The infraspinatus stands out by showing a large amount of force that increases to compensate the decrease of its moment arm" in a model with fewer muscle bundle divisions i.e. 21 muscles defined by 37 bundles which is similar to the model used in this study [139]. This should be noted as one limitation of this study.

Due to the methodology in replicating the muscle contraction in FE model (pre-defined stress method in chapter 6), the goal of this chapter was set to obtain an overall performance of the main abductor muscles with relatively high accuracy. Even though some differences exist between the predicted muscles forces in this study and literature data, the results showed an overall good agreement with literature in trend and magnitude. Therefore, it can be concluded that the predicted muscle forces in this chapter are acceptable.

4.5 Summary

In this chapter, a brief introduction was presented for multi-body musculoskeletal simulation and the OpenSim software at first. The measurement kinematic data from previous chapter were further processed for use in OpenSim. The processed measured static data of four markers on the thorax and four markers on the humerus during the experiment were used to construct a subject-specific multi-body musculoskeletal model by scaling the generic model. The constructed musculoskeletal model contains 3 degrees of freedom in the glenohumeral joint (a general ball-socket joint). A total number of 25 muscles were defined by 29 bundles around the shoulder and elbow joints. The same marker system was used to implement the measured scapular abduction motion trials to drive the model so as to calculate the glenohumeral joint angles during the scapular plane abduction during the motion capture experiment using inverse kinematics method. The motion of the multi-body model that was caused by the predicted joint angles were found to agree well with experimental observations. These predicted joint angles were then used to calculate the joint torques which were further decomposed into individual muscle forces by static optimisation method. The predicted muscle forces were well validated against literature results. Some of the possible reasons for difference of the muscles forces from literature were discussed. Further, these muscle forces and joint positions were used to define the physiological loading and boundary conditions in FE simulations in Chapter 6 and 7.

Chapter 5 Medical image processing and three-dimensional geometrical construction

5.1 Introduction

The preceding two chapters presented the *in-vivo* subject-specific motion analyses and muscle activities prediction. Thereafter, these measured kinematics data in Chapter 3 and the calculated muscle loadings in Chapter 4 would be used to define the physiological loading and boundary conditions in FE analysis. This chapter provided the geometrical representations of the shoulder tissues as the foundation of the FE model construction, where these physiological loading and boundary conditions would be defined on. Starting from this chapter, the detailed process of constructing the *in-vivo* subject-specific FE model of the shoulder complex is presented. The whole process basically follows the framework of developing CAD-based anatomical modelling as shown in Figure 5-1 similar to previous literature [140]. This chapter presents the process of this study from the medical scanning to the generation of 3D solid model. Firstly, MR images of the same subject in the above motion studies was scanned and segmented for 3D contour-based geometrical reconstruction in Mimics software. The MR imaging measurements and image qualities were presented in section 5.2. Several sequences of the MR images were obtained including a sequence of the whole right-side upper body and another two sequences of the detailed view of the glenohumeral joint with high resolution. Subsequently, in section 5.3, a detailed description of the geometrical reconstruction of all the major components of the shoulder was conducted with an emphasis on the parts around the glenohumeral joint. In order to keep the accuracy of the anatomical model, segmentation and 3D reconstruction of all the MR imaging were conducted manually. Finally, the reconstructed geometry was subjected to further processing such as smoothing and surface generating in Catia V5 software for solid model construction in Section 5.4. A total of 16 tissues structures were constructed, including 3 bones, 2 cartilages, 6 ligaments and 5 muscles. In the following chapters, this solid model was imported to Abaqus for FE model construction and simulations.

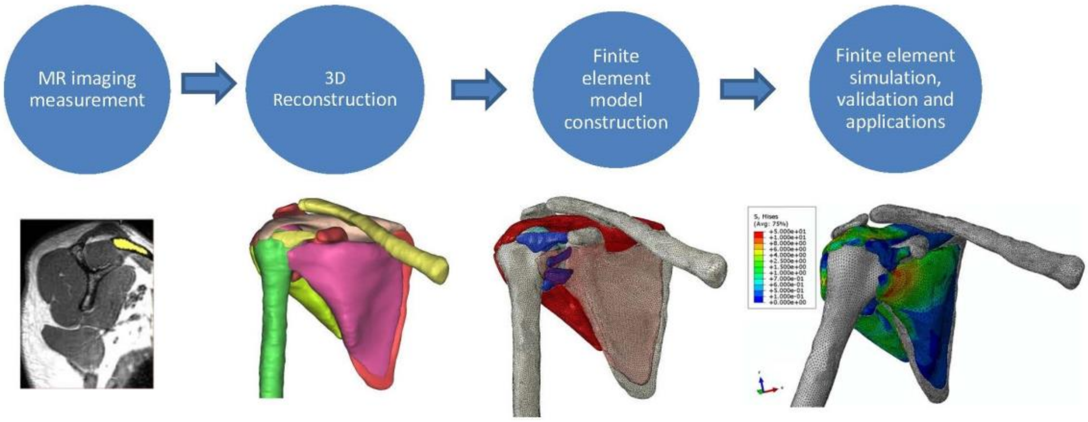

Figure 5-1 Framework of developing CAD-based anatomical modelling

5.2 MR imaging measurement

As discussed in the review of the FE modelling techniques in Chapter 2, the most appropriate shoulder tissue geometry acquisition method that facilities the research objectives of this study was the MR image scanning of the subject under unloaded conditions in supine position with the arm in neutral rotation and adducted position. Although the MR image of the subject was originally scanned did not have enough field of view, the segmentation method was able to be pretested on these images. As illustrated in Figure 5-2, parts of the scapula and clavicle cannot be recognised. Therefore it was rescanned twice. The segmentation and reconstruction process was conducted mainly based on the second scanning which had a larger field of view that almost contained the whole right-side upper body. However, the quality of the images had to be compromised with this enlarged field of view. Therefore, as a supplement to the second scanning, the third scanning that focused on the glenohumeral joint parts for determining the boundaries of the tissues was performed. Table 5-1 presents the image quality summary about the second and third scanning which was obtained from the technicians of the MR scanner. Selected parameters were determined by published papers [141, 142]. It shoulder be noted that the subject was required to remain motionless during scanning for about 50 mins. The unavoidable movement of the subject was an inherent source of error that affected the imaging quality.

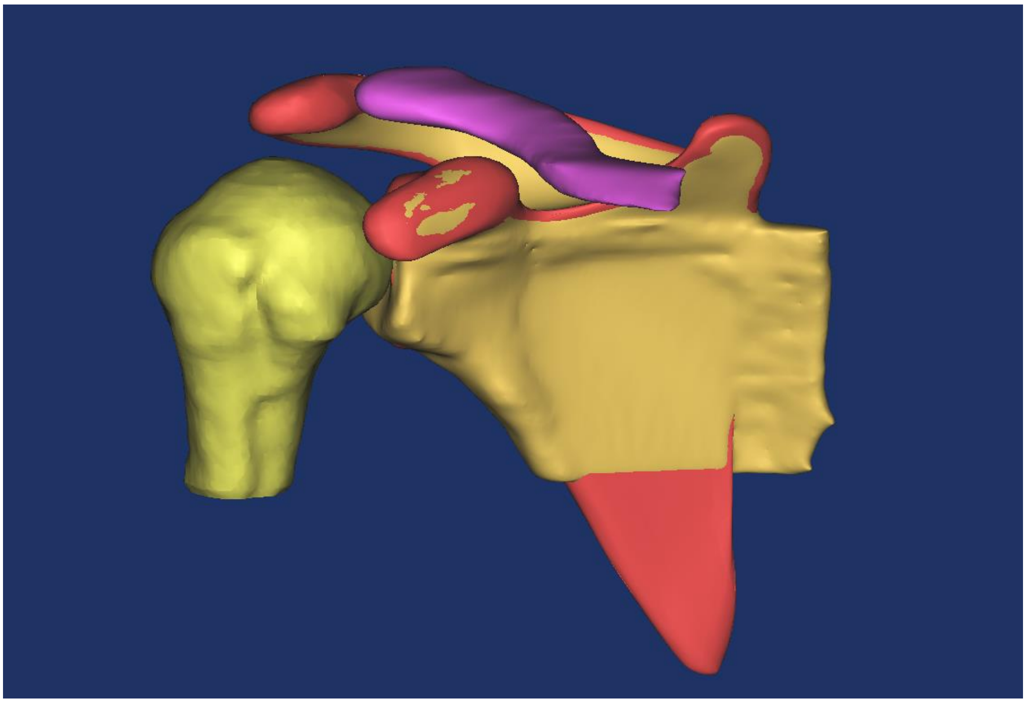

Figure 5-2 Bony structures reconstruction from initial scans

5.3 MR imaging segmentation and 3D reconstruction

This section took the segmentation and 3D reconstruction of the clavicle bone as an example to demonstrate in details the process. The reconstructed geometries of other parts of the shoulder complex were illustrated accordingly. Mimics 17.0 software was used for the segmentation and 3D reconstruction of all the MR images.

5.3.1 Bones

According to the anatomy review in Chapter 2, the clavicles, or collarbones, are spindly, slightly curved long bone which is the solo direct connection between the pectoral girdle and axial skeleton. () The best view when segmenting the clavicle is the sagittal oblique view as shown in Figure 5-3 (a). In this view, the clavicle bone of the subject can be recognised in each slice of the images which lies on top of the shoulder. A mask (in yellow) was created and used to segment the clavicle bone in this slice as shown in Figure 5-3 (b). This segmentation was performed for the clavicle in each slice manually. See some examples in Figure 5-4. When the segmentation of the clavicle bone was done in all the slices, the 3D region growth was conducted to get the 3D reconstruction (See Figure **5-5**). Comparing to the anatomy review in Figure 2-2 and Figure 2-3, it can be found that the reconstructed geometry matches well with the literature illustration.

Table 5-1 MR Imaging quality summary

MRI Scanner Information	**Achieva Philips Medical System**	
Parameters	Scan sequences	
	T1W_3D_FFE	PD_VISTA_SPAIR
Study Date	2nd July 2014	17th November 2014
Patient	MD113_MZ_V2	MD113_SHOULDER
Matrix		312x268
Slice thickness/Gap	1.4/0.7	0.82/0.41
Number of slices	343	219
Row/Columns	352/352	400/400
Pixel Spacing		0.48/0.56

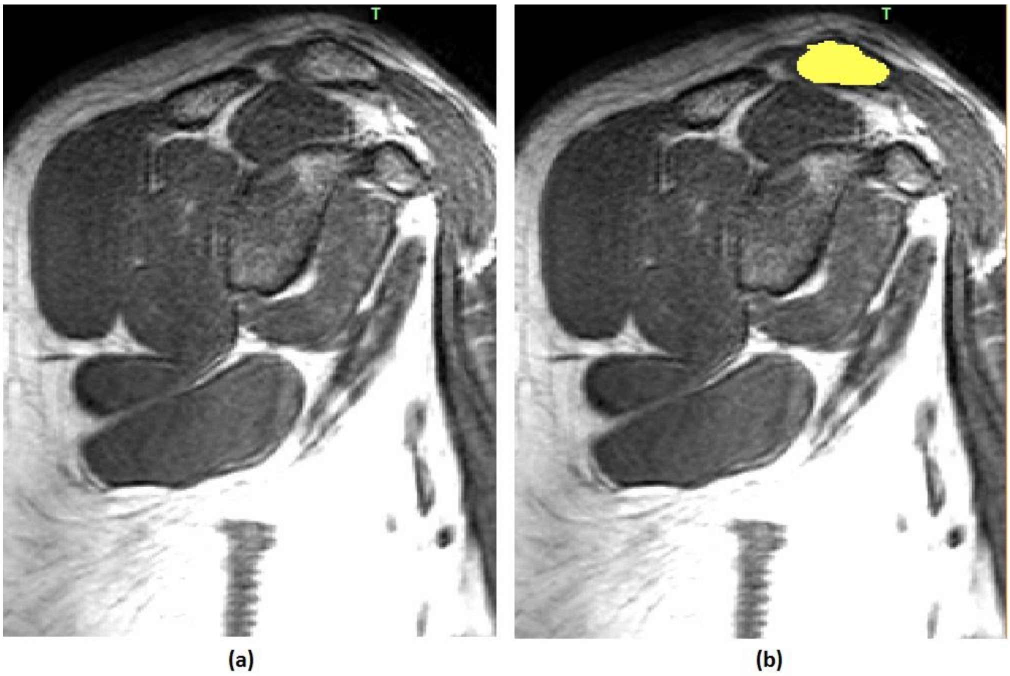

Figure 5-3 Mask creation for clavicle in one slice of the MR images

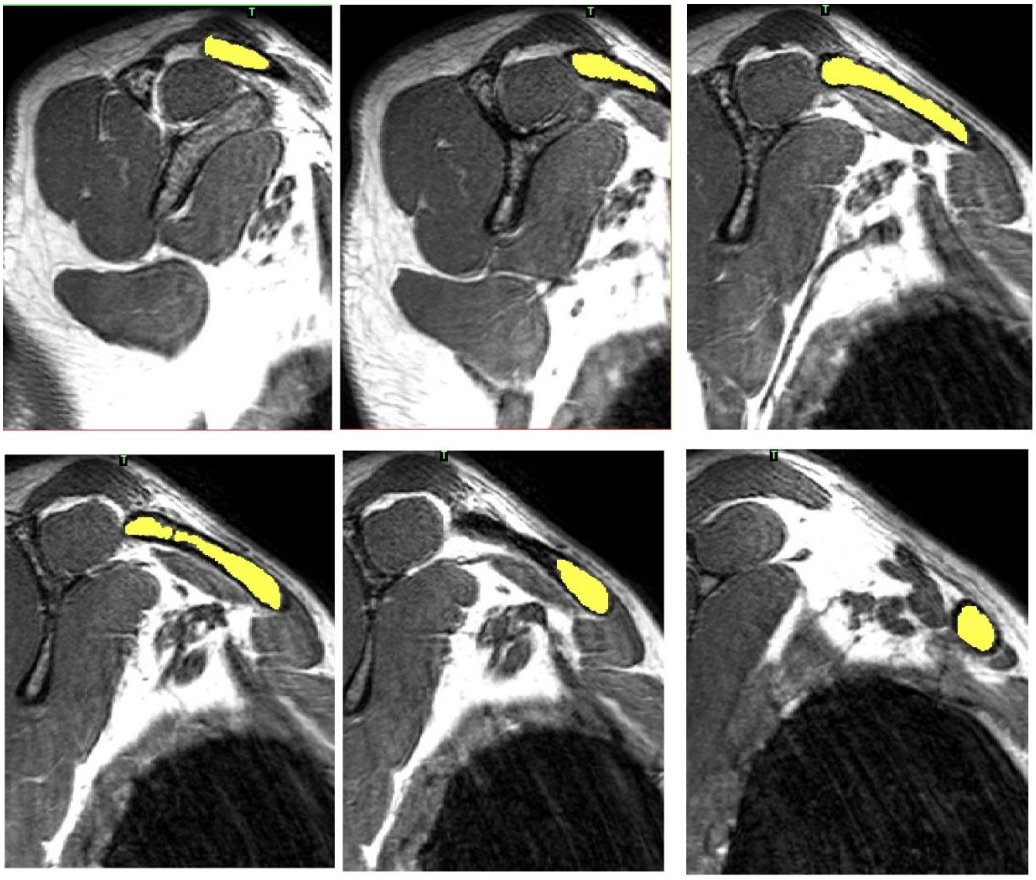

Figure 5-4 Example segmentation results for clavicle in some slices

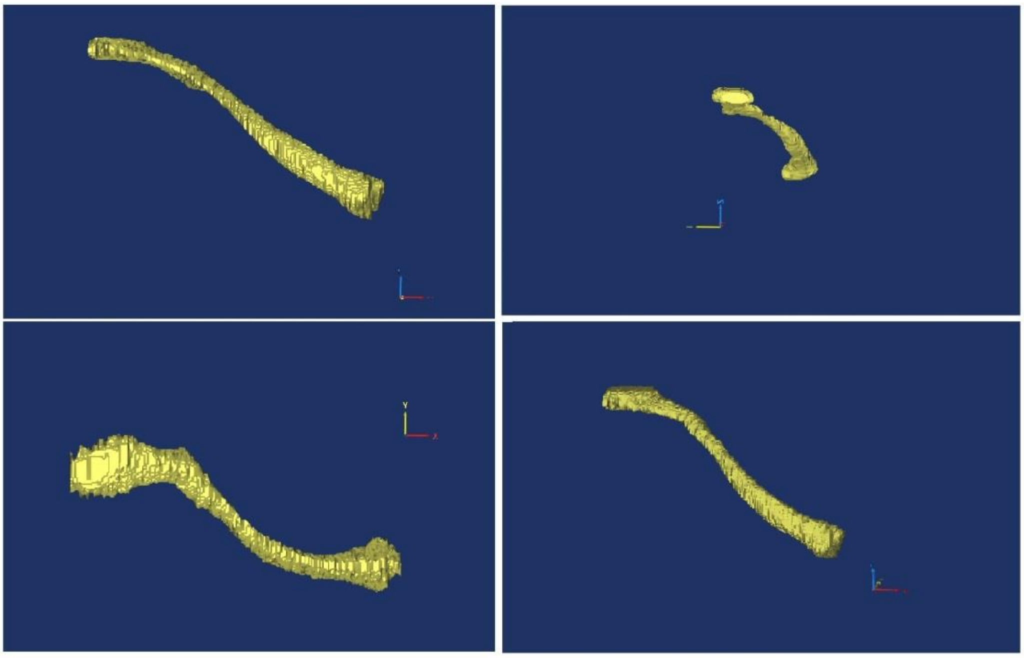

Figure 5-5 3D reconstruction of the clavicle from segmentation

The same process was repeated for scapula and humerus bone. The scapula was segmented in both sagittal and axial views due to its geometrical complicity, while the humerus bone was mainly segmented in axial view. The reconstructed geometries for these two bones can be found in Figure 5-6 and Figure 5-7. Figure 5-6 was illustrated with the same layout as the scapula anatomy review in Chapter 2 (see Figure 2-4). From left to right, the (a) anterior, (b) lateral and (c) posterior view of this bone can be found similar to the literature illustration. In the anterior view, the coracoid process can be seen clearly; in the lateral view, the glenoid cavity can be found easily; while in the posterior view, the spine and acromion could be found. In Figure 5-7, the reconstructed humeral bone was demonstrated with an emphasis on the humeral head. Comparing to the Figure 2-5, the featured structures such as the great and lesser tubercle, intertubercular groove where biceps tendon lies in can be found in (a) anterior and (b) lateral view. The relative positions between the reconstructed bone tissues including clavicle (in yellow), scapula (in cyan) and humerus (in green) were shown in Figure 5-8 which compares well with the shoulder anatomical skeletal structure illustration in Figure 2-1. These relative positions of the bones were carefully preserved before being imported and assembled together in Chapter 6.

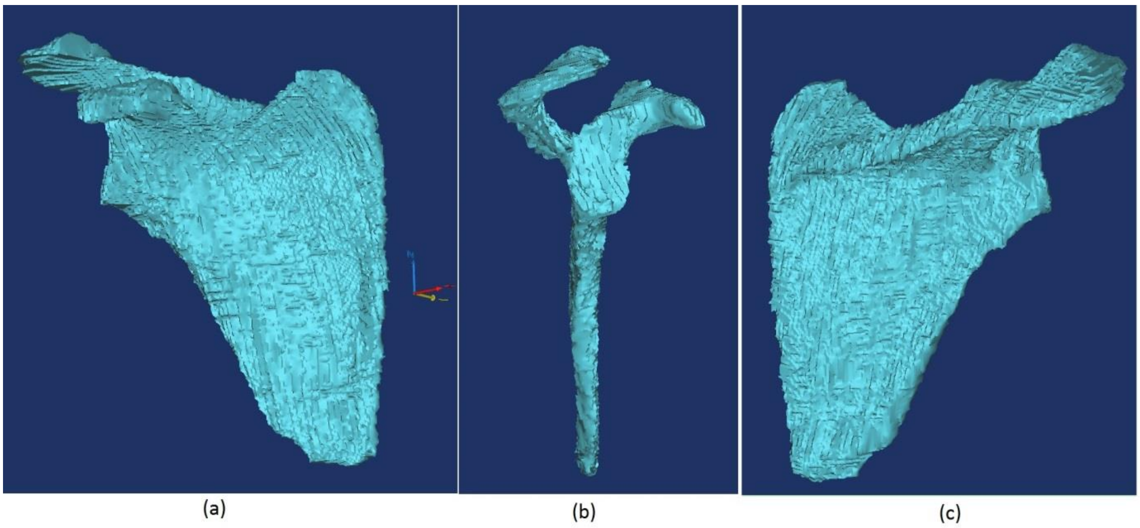

Figure 5-6 3D reconstruction of the scapula from segmentation. (a) Anterior View; (b) Lateral view; (c) Posterior view

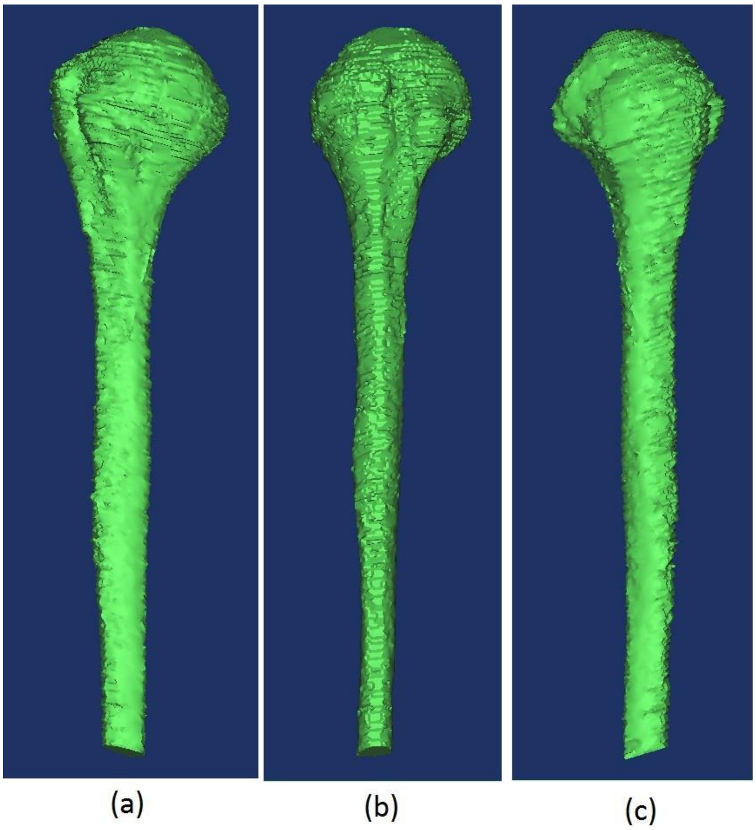

Figure 5-7 3D reconstruction of the humerus from segmentation. (a) Anterior View; (b) Lateral view; (c) Posterior view

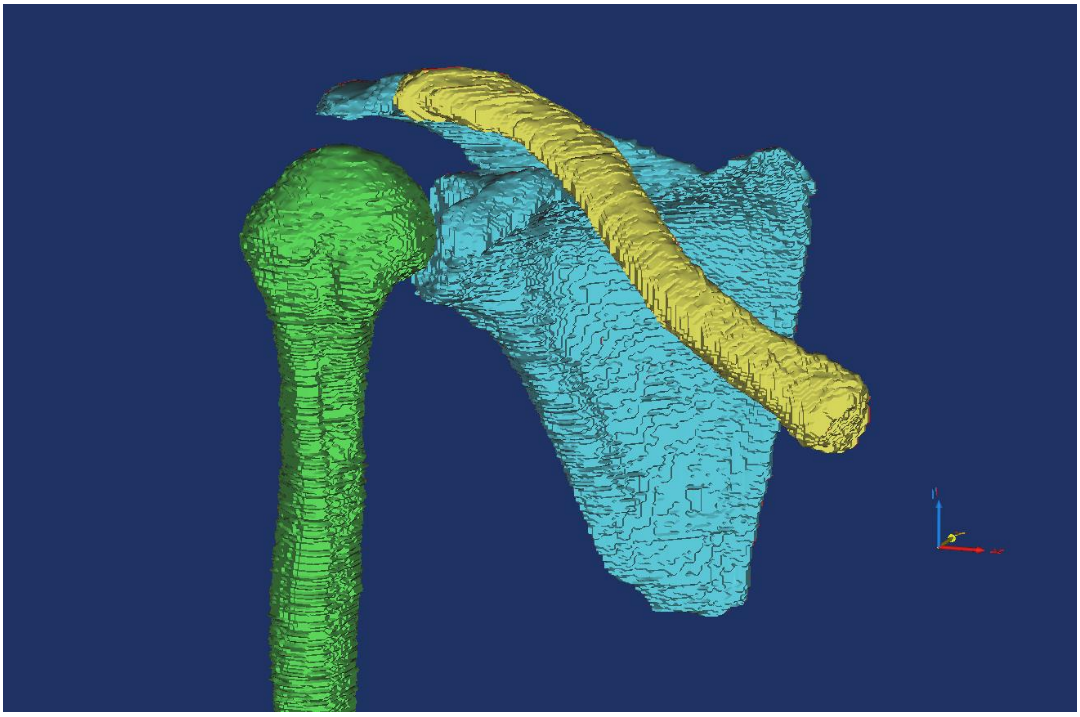

Figure 5-8 Overview of the 3D reconstructed bone tissues

5.3.2 Muscles

As discussed in Chapter 2, the muscle-tendon system was treated all as the tendon. Therefore, the muscles and tendons were constructed as a whole. As all the muscles are attached to the bone, the establishment of the bony structures provides the foundation for the shoulder muscle reconstruction. The process used to reconstruct muscles is the same as the bony structures. However, the muscles are soft tissues. In some parts such as the axillary region, the muscles wrap around each other which made the recognition of the boundary among multiple parts difficult. The third scanning was used to assist this process. The rotator cuff muscles including supraspinatus, infraspinatus, teres minor and subscapularis are considered the main stabiliser in shoulder joint is of the region of interest of this project. These four muscles were segmented carefully together with the deltoid muscle which was believed as an important muscle in the abduction. The 3D reconstructed rotator cuff muscles and the deltoid muscle can be found in Figure 5-9 and Figure 5-10. In Figure 5-9, the shape of the rotator cuff muscles can be found in (a) anterior view for subscapularis (in pink) and (c) posterior view for supraspinatus (in peach), infraspinatus (in read) and teres minor (in brighter yellow) on top of the skeletal structure of the shoulder. A good view of the rotator cuff tendons which merged in the humeral head can be found in (b) lateral view. Whereas in Figure 5-10, the complex geometry of the deltoid muscle (in purple) on top of precious skeletal and rotator cuff muscles can be viewed from (a) anterior View, (b) lateral view, (c) posterior view. All muscle geometries and origin and insertion sites were found to be similar to anatomy review in Chapter 2 (see Figure 2-8).

When the initial reconstruction of the bone and muscle structures was completed, a meeting was arranged with our collaborative surgeons during which the bony structures and important muscles were checked. As a result, the 3D reconstruction of all the structures was histologically correct in general. Except that the rotator cuff muscle tendons should merge as a whole part surrounding the humeral head. Therefore, special efforts were made to the insertion of rotator cuff muscle insertion site. As it was not possible to determine the boundaries of the tendons in MR images, the insertions of the supraspinatus tendon and infraspinatus tendon were determined following a state-of-the-art anatomy study [143]. The improved insertion site of the tendons comparing with the finding in the anatomy study can be found in Figure 5-11.

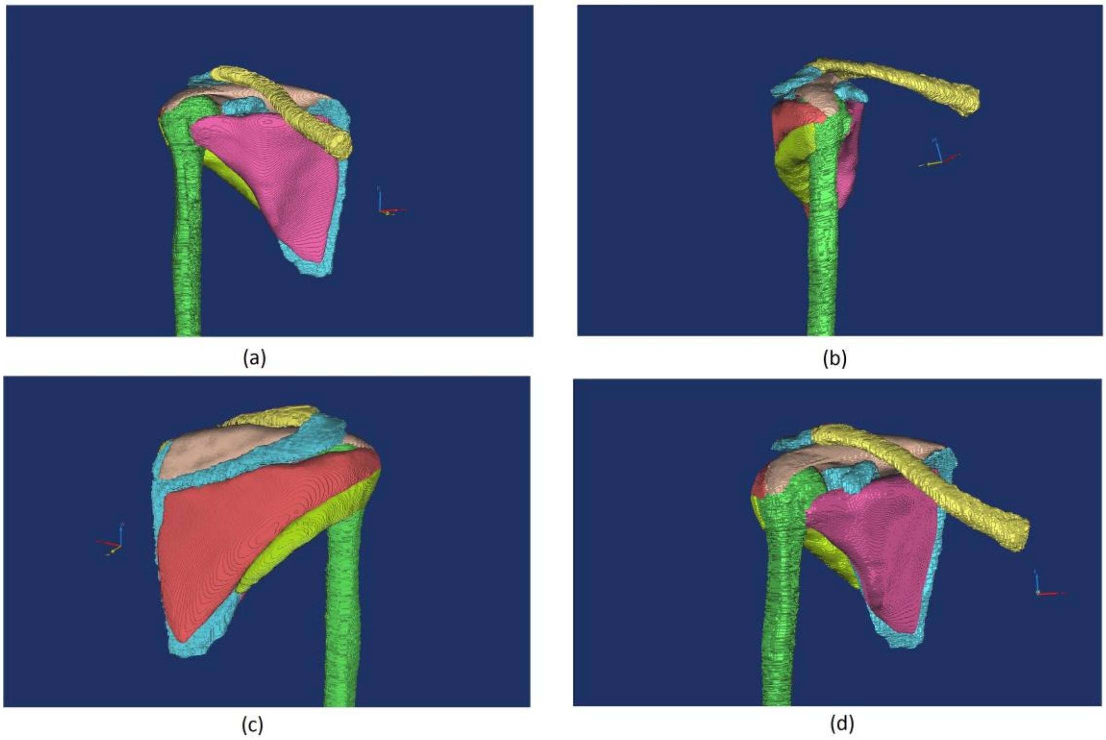

Figure 5-9 3D reconstruction of the rotator cuff muscles from segmentation in which subscapularis in magenta; supraspinatus in peach; infraspinatus in red and teres minor in yellow. (a) Anterior View; (b) Lateral view; (c) Posterior view; (d) Overview

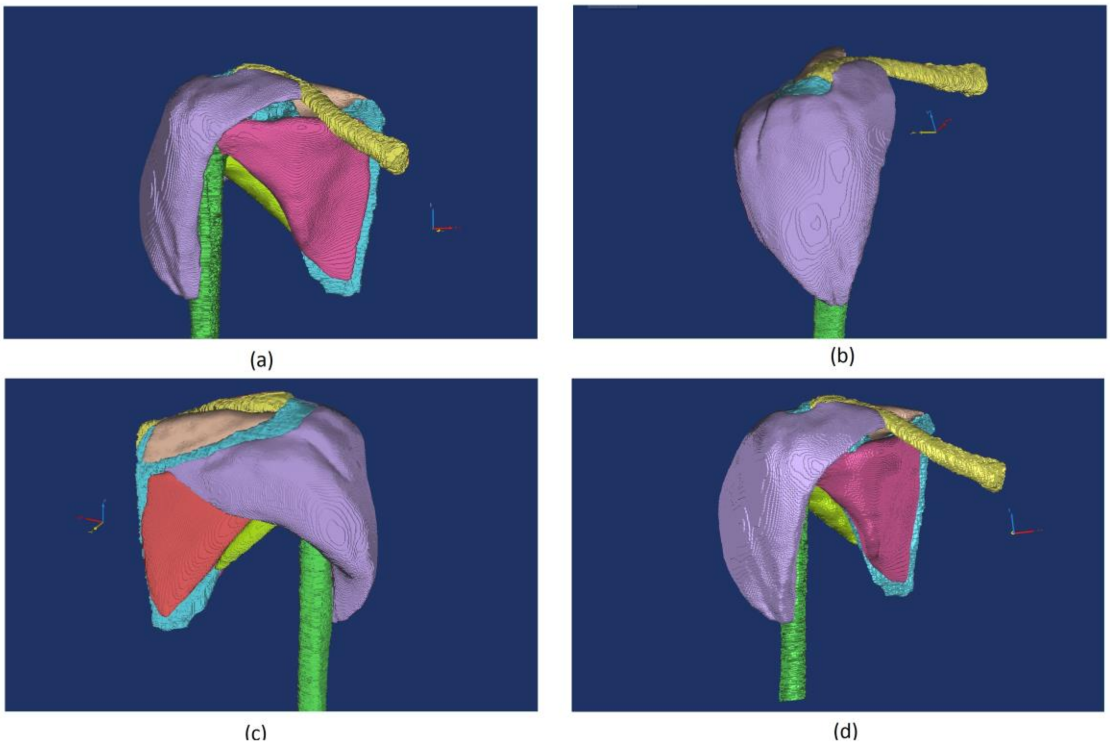

Figure 5-10 3D reconstruction of the deltoid muscle from segmentation. (a) Anterior View; (b) Lateral view; (c) Posterior view; (d) Overview

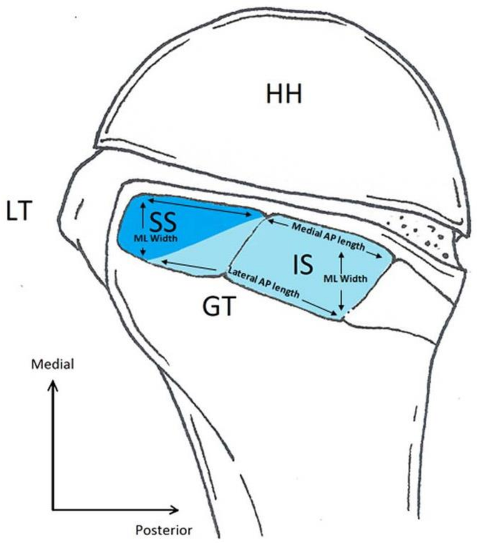

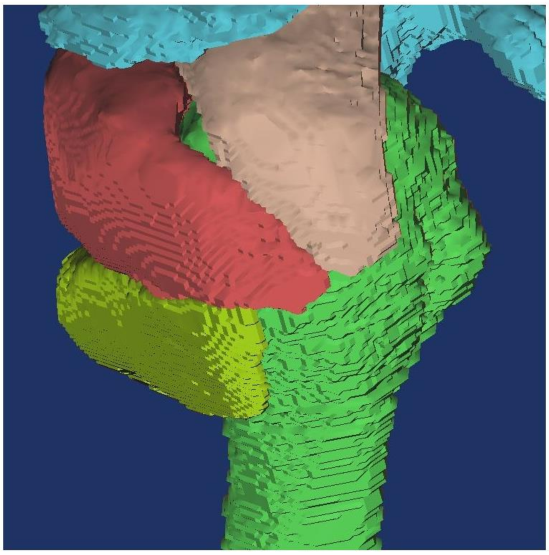

Figure 5-11 Comparison of the (a) anatomy findings of the rotator cuff insertion site [143] with (b) the improved design in this study

N.B. (a) illustrates the left shoulder while (b) in this study is the right shoulder.

5.3.3 Ligaments

The ligaments around the glenohumeral joint were mainly segmented and reconstructed in the third scan and imported to the main model. Even with the best imaging, the ligaments were difficult to be recognised especially the middle glenohumeral ligament which has several different forms between normal individuals. The segmentation was also guided by anatomy study [144] (See Figure 5-12). With the consultation from the surgeon, the middle glenohumeral ligament was recognised as the type (A) in Figure 5-12 which was the normal shoulder. There were in total 4 ligaments including coracohumeral ligament (CHL), Superior glenohumeral ligament (SGHL), middle glenohumeral ligament (MGHL), and inferior glenohumeral ligament (IGHL) presented in Figure 5-13. The IGHL was divided into 3 parts including an anterior band of IGHL (AB-IGHL), axillary pouch of IGHL (AP-IGHL) and a posterior band of IGHL (PB-IGHL). It can be found that the reconstructed geometries of these ligaments can be found in well agreement with the anatomy review of the ligaments as shown the anterior view of Figure **2-7**.

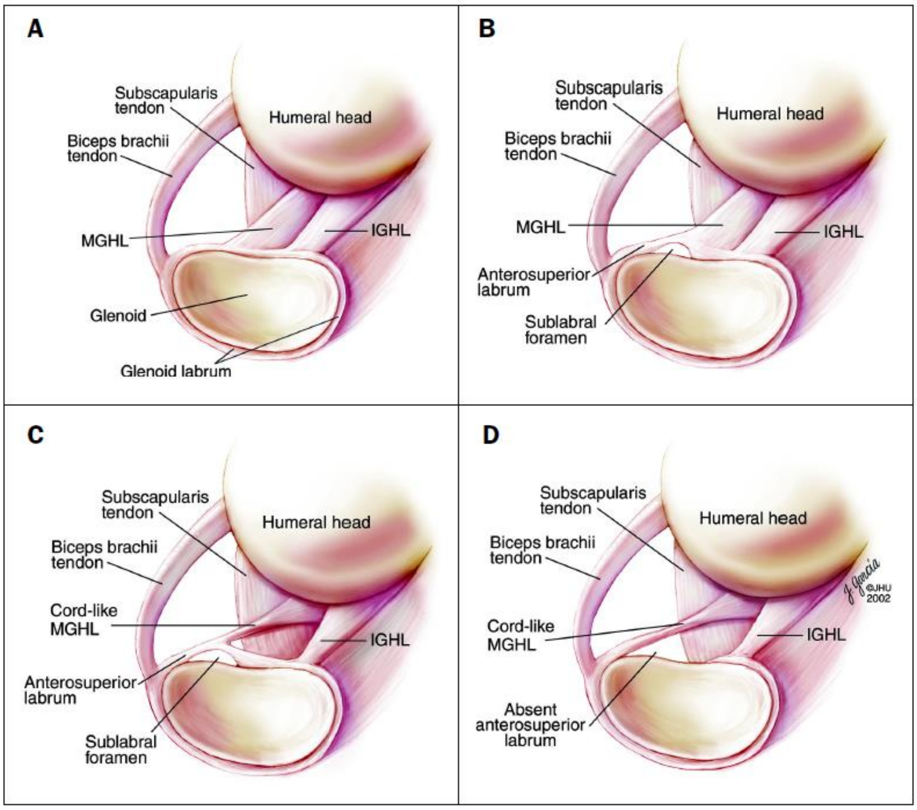

Figure 5-12 Schematic drawings demonstrating the anterosuperior labral anatomy of a right shoulder in four forms [144]

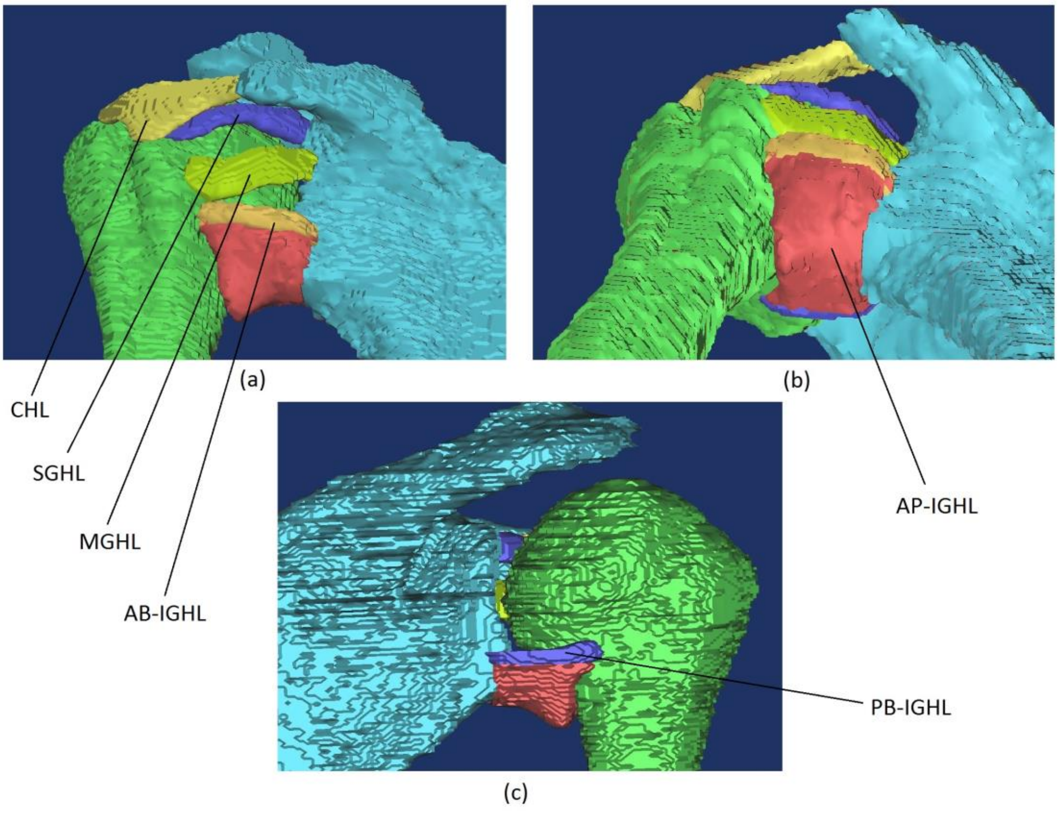

Figure 5-13 3D reconstruction of the ligaments around the glenohumeral joint from segmentation. (a) Anterior-inferior View; (b) inferior view; (c) Posterior view

5.4 Three-dimensional geometrical construction

5.4.1 Three-dimensional geometrical construction of the MR reconstructed tissues

The above MR reconstructed model had produced a realistic 3D anatomical appearance of the shoulder tissues. However, this voxel-base anatomical representation cannot be used in biomechanical engineering. To perform the FE simulation and analysis, this voxel-based anatomic representation had to be converted to vector-based model using CAD-based solid modelling [140]. In this study, we name it 3D geometrical construction. Catia V5 was used for this process. Similar to the previous section, the clavicle was used as an example to demonstrate the process. The reconstructed clavicle was subjected to basic smoothing before exported in STL format. The smoothed clavicle geometry was subsequently imported into Catia. Figure 5-14 illustrated the process in the construction of this vector-based solid model. Figure 5-14 (a) illustrated the import of the voxel-based anatomic representation of the clavicle bone in Catia. Subsequently, the imported reconstructed 3D clavicle was used in the surface generation which contains the geometric topological relation of the model as shown in Figure 5-14 (b). Thereafter, the solid model was constructed by closing the newly generated surfaces in. The final 3D geometrical constructed vector-based solid model of the clavicle was completed (see Figure 5-14 (c)) and ready to be imported to Abaqus for further simulations.

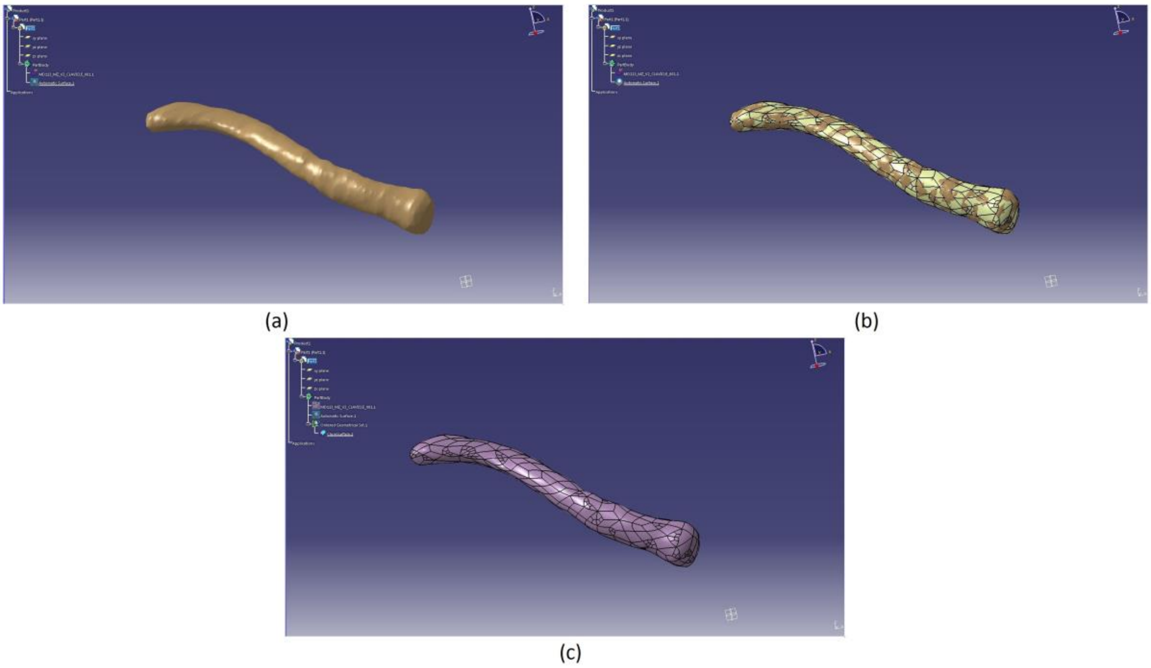

Figure 5-14 3D geometrical construction process. (a) MR reconstructed geometrical representation of the clavicle; (b) surface generation; (c) 3D solid model construction

This process was conducted for all the MR reconstructed structures from the previous section. The complex geometries such as scapula and deltoid muscle had difficulties when performing surface generation due to some void, shape edges or rough surfaces which were generated during segmentation. They were further fixed in Catia until the surface generation can be performed successfully. The constructed CAD-based solid models for all these structures can be viewed from Figure 5-15 to Figure 5-18. The 3D geometrical construction of the skeletal structures can be found in Figure 5-15. It can be found that the relative positions of the bones were well preserved as they were in Figure 5-8. The four rotator cuff muscles and deltoid muscle are shown in Figure 5-16 and Figure 5-17 both from anterior-lateral view. Noted that all the muscles were in individual geometries which would be subject to further process when assembled in Chapter 6. Same procedures were applied to ligaments as shown in Figure 5-18 from anterior-medial view see (Figure 5-13 (a)). In Figure 5-18, from top to bottom, ligaments were coracohumeral ligament (CHL), Superior glenohumeral ligament (SGHL), middle glenohumeral ligament (MGHL), and inferior glenohumeral ligament (IGHL).

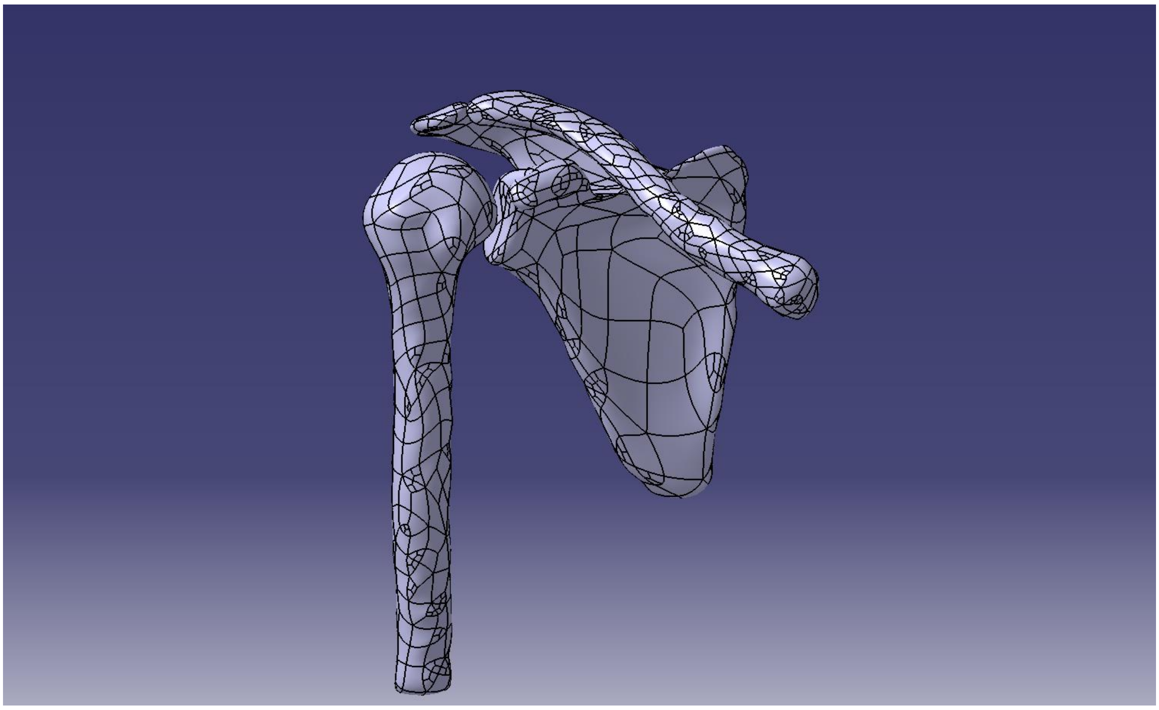

Figure 5-15 3D geometrical construction of the bones

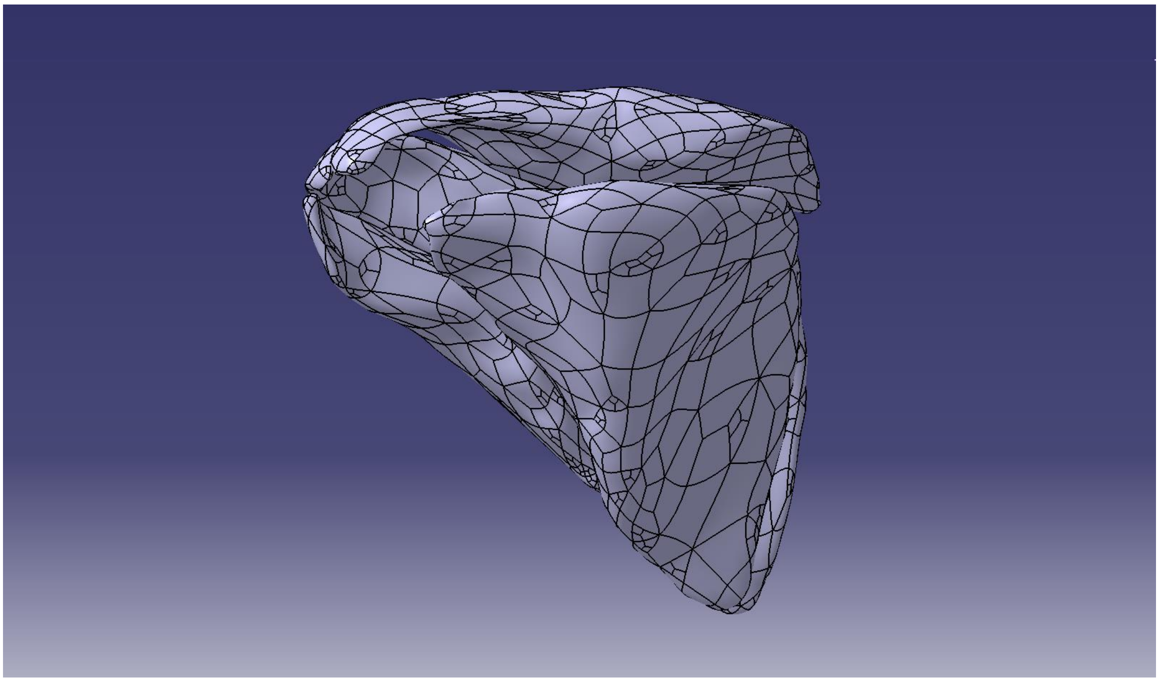

Figure 5-16 3D geometrical construction of the rotator cuff muscles

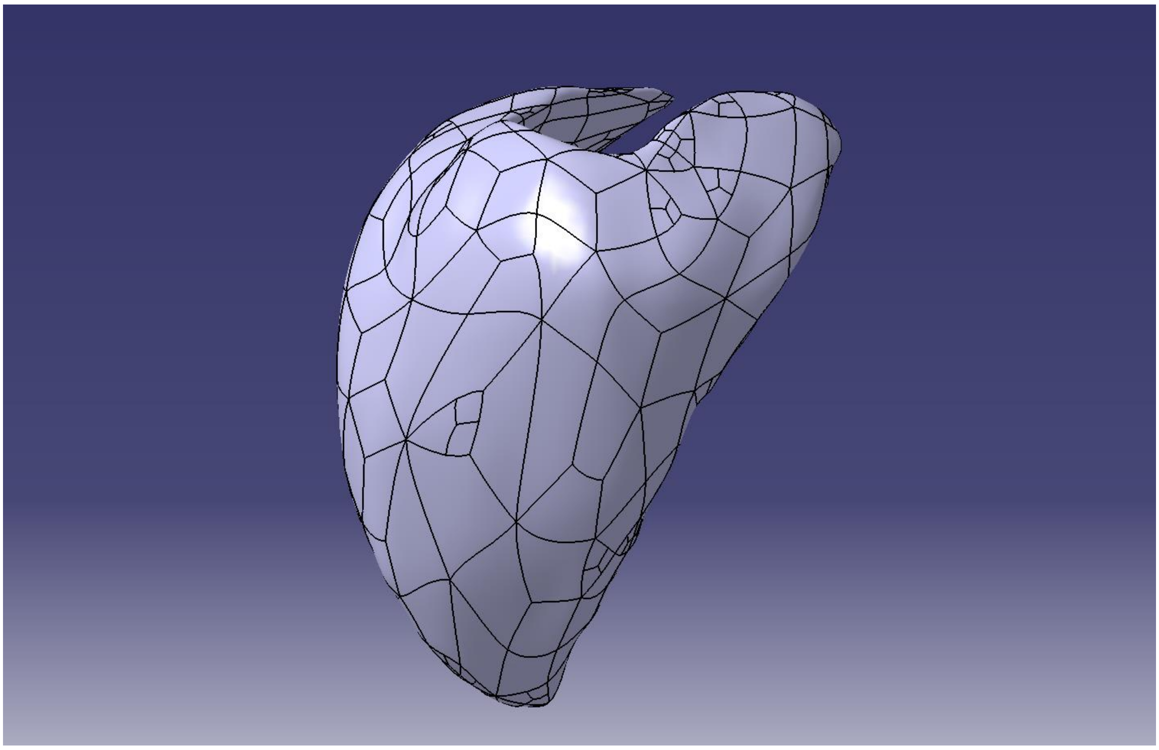

Figure 5-17 3D geometrical construction of the deltoid muscle

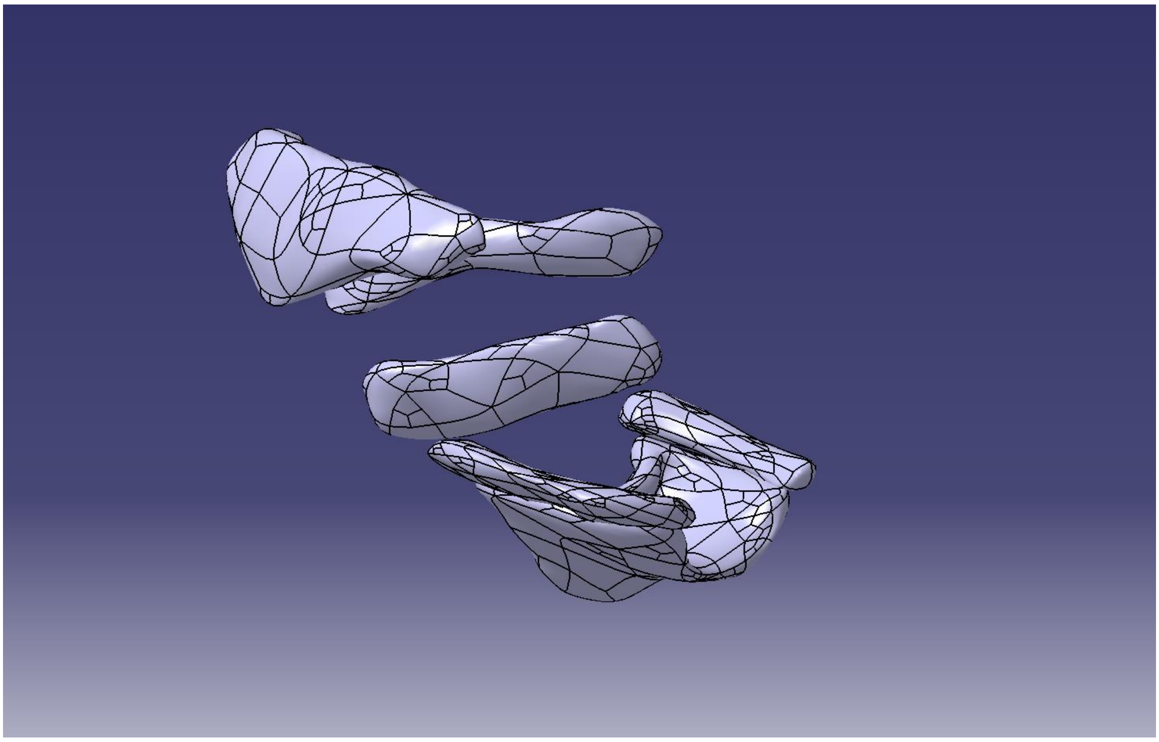

Figure 5-18 3D geometrical construction of the ligaments

5.4.2 Three-dimensional geometrical construction of the glenohumeral cartilages

The cartilages of the glenohumeral joint were initially reconstructed in MR images by Mimics using the same method as the rest of the components. However, the thickness of the cartilages was too small to be reconstructed to a continuous surface. Therefore the cartilages of the glenohumeral joint were designed in Catia by thickening the surfaces of the respective bones i.e. humeral head and the glenoid fossa. Figure 5-19 illustrated the thickening process when designing the humeral cartilage. The thickening values for both cartilages were determined by a cadaveric study which is 0.6mm for humeral cartilage and 1mm for glenoid cartilage [145]. The thickened surfaces were merged as one part before they were exported back to Mimics to determine the boundaries through Boolean operation by the initially reconstructed realistic geometry of the cartilage. Figure 5-20 (a) showed the merged one-part humeral cartilage, while Figure 5-20 (b) showed the humeral cartilage with realistic boundaries. The glenoid cartilages were designed in the same way as shown in Figure 5-21. The relative position with respect to the humerus and scapula can be seen in Figure 5-22. The bones were set to be transparent for better view of the cartilages. Anatomy of the cartilages can be found in Figure **2-7** (Joint opened: lateral view and Coronal section through joint view).

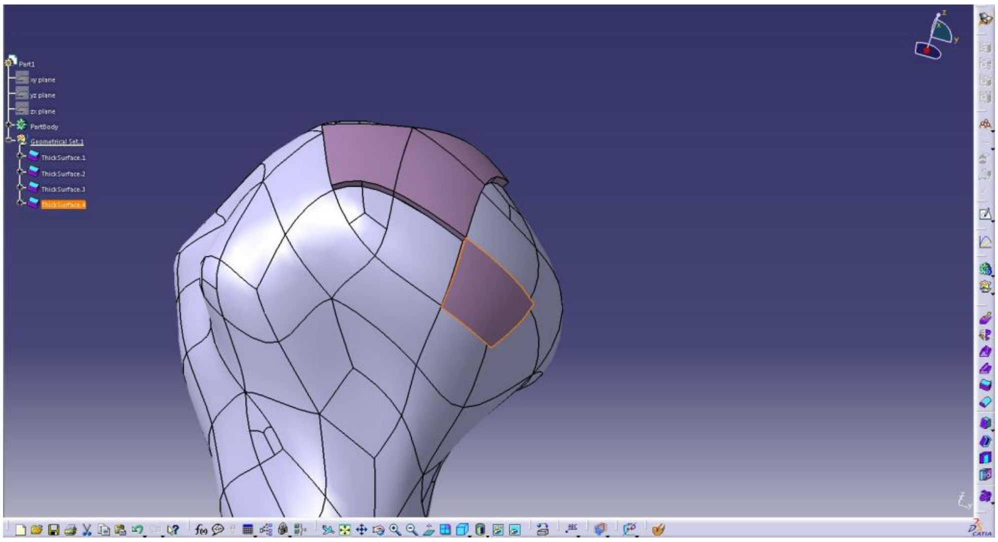

Figure 5-19 Thickening surfaces of the humeral head for designing humeral cartilage

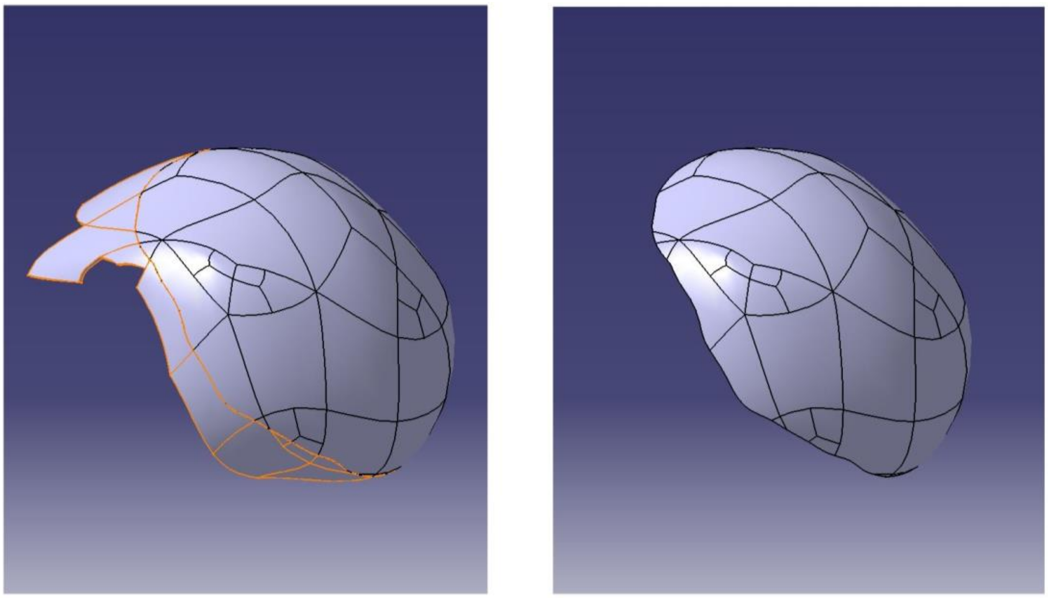

(a) (b)

Figure 5-20 Designed humeral cartilage before (a) and after (b) the Boolean operation with the MR reconstructed humeral cartilage

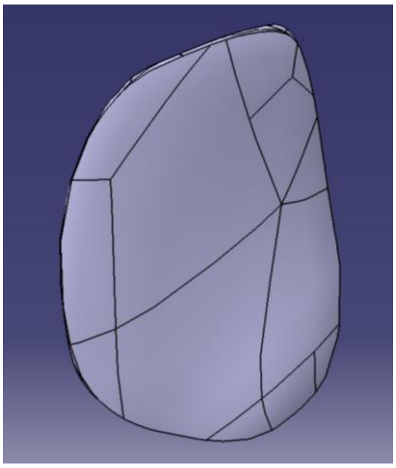

Figure 5-21 Designed glenoid cartilage

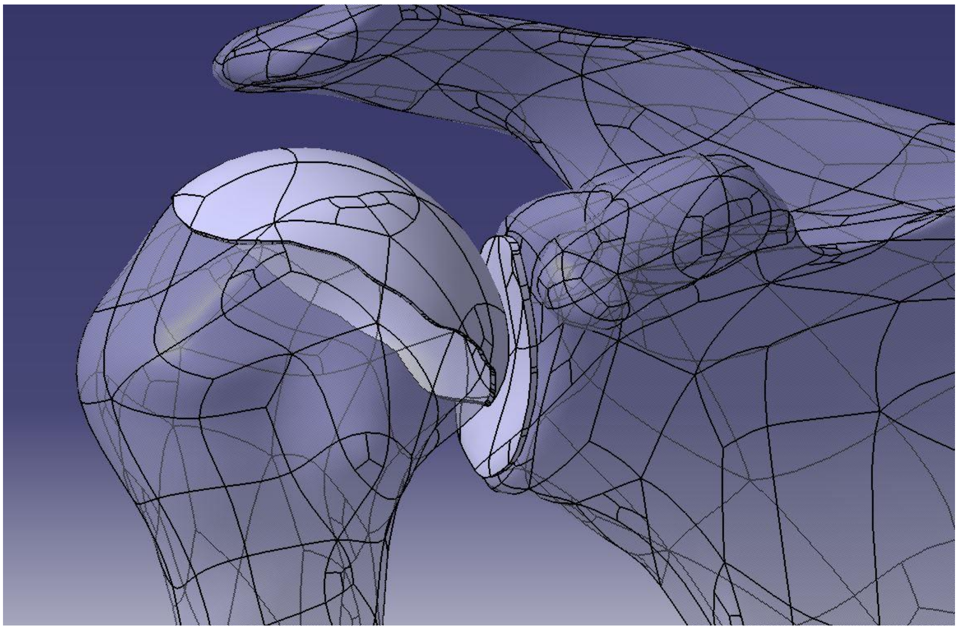

Figure 5-22 The relative position of the designed cartilages with respect to the bones

5.5 Summary

This chapter presented the process in constructing the anatomical model of the shoulder complex based on MR imaging. The same subject under *in-vivo* kinematics measurement and muscle loading calculation in Chapter 3 and 4 was scanned multiple times with the advanced MR imaging technologies. The scanned images were subjected to segmentation and 3D reconstruction before importing to CAD environment for 3D geometrical construction where the solid anatomical models were constructed. In the next chapter, these constructed anatomical models would be imported to Abaqus environment as the foundation of FE model construction and simulation.

All possible efforts had been made in every stage of geometrical construction intended to get the highest possible accuracy of the model, including multiple scanning, manual segmentation and integrating the state-of-the-art anatomy studies. Furthermore, the reconstructed geometries were confirmed by the medical partners i.e. a surgeon and a senior radiologist. It can be concluded that a novel, anatomically accurate, subject-specific geometrical model of the human shoulder complex had been constructed based on the state-of-the-art technologies.

To sum up, a musculoskeletal shoulder complex with accurate representations of all the major bones, muscles, ligaments and cartilages around the glenohumeral joint had been successfully constructed. All 16 parts of the constructed solid anatomical models were listed in Table 5-2.

Table 5-2 Summary of the 3D constructed geometries

Anatomical category	Part name
Bones	Humerus
	Scapula
	Clavicle
Cartilages	Humeral cartilage
	Glenoid cartilage
Ligaments	Coracohumeral ligament (CHL)
	Superior glenohumeral ligament (SGHL)
	Middle glenohumeral ligament (MGHL)
	Inferior glenohumeral ligament anterior band (AB-IGHL)
	Inferior glenohumeral ligament axillary pouch (AP-IGHL)
	Inferior glenohumeral ligament posterior band (PB-IGHL)
Muscles	Subscapularis
	Supraspinatus
	Infraspinatus
	Teres minor
	Deltoid

Chapter 6 Construction of the finite element model of the human shoulder complex

6.1 Introduction

This chapter presents the detailed construction and verification process of the FE model of the human shoulder complex in Abaqus v6.13. This FE model is an integrated model containing all modelling information from chapter 3 to 5. Specifically, Chapter 5 provided the anatomically accurate geometrical representations of the shoulder complex that served as the foundation of the FE model. The reconstructed bone, muscle, ligament and cartilage geometries of the subject were imported into Abaqus as individual parts before assembly. Especially, their relative positions from MR reconstruction were carefully preserved. Whereas chapter 3 and 4 defined the *in-vivo* physiological subject-specific boundary and loading conditions for the FE simulation. Specifically, the measured scapula and clavicle bone kinematic data were defined as the boundary conditions. The calculated muscles forces from Chapter 4 were used to define the muscle loadings that dynamically stabilise the humerus which was left free of any prescribed constraints. The constructed FE model in this chapter would be further developed for the simulation of the shoulder scapular abduction in Chapter 7 and rotator cuff tear propagation study in Chapter 8.

In this chapter, Section 6.2 describes in details the definitions of the main aspects of the shoulder FE model construction, including assembly, material property, mesh, interaction and loading and boundary condition. In Section 6.3, a preliminary simulation was conducted to test the above model definitions. Subsequently, the mesh size sensitivity study was conducted independent of the validation which would be presented in Chapter 7. Finally, a summary was presented in Section 6.4.

6.2 Finite element model construction

6.2.1 Model assembly

The beginning of the FE construction was the import and assembly of the solid anatomical models of the shoulder components from Chapter 5. At first, they were imported as independent parts. Thereafter, instances were created in assembly module based on these independent parts. During assembly, their relative positions from MR reconstruction were carefully preserved. To simulate their physiological relationships and facilitate the requirements when defining contacts, several Boolean operations were performed between these parts.

The first Boolean operation was conducted between the ligaments and bones. To simulate their firmly bonded relationship and ensure stability through the whole analysis, the ligaments were merged with the humerus and scapula bone by retaining boundaries which allowed different material properties assignment to individual tissue. Similarly, the glenoid cartilage was merged with the glenoid fossa by retaining boundaries. A new part was generated named as Bone-ligaments (See Figure 6-1). In fact, the merge Boolean operation served as a firmly attached interaction such as tie constraint [146]. The benefit was the reduced computational cost and modelling efforts; whereas the drawback was that the relative interaction was omitted.

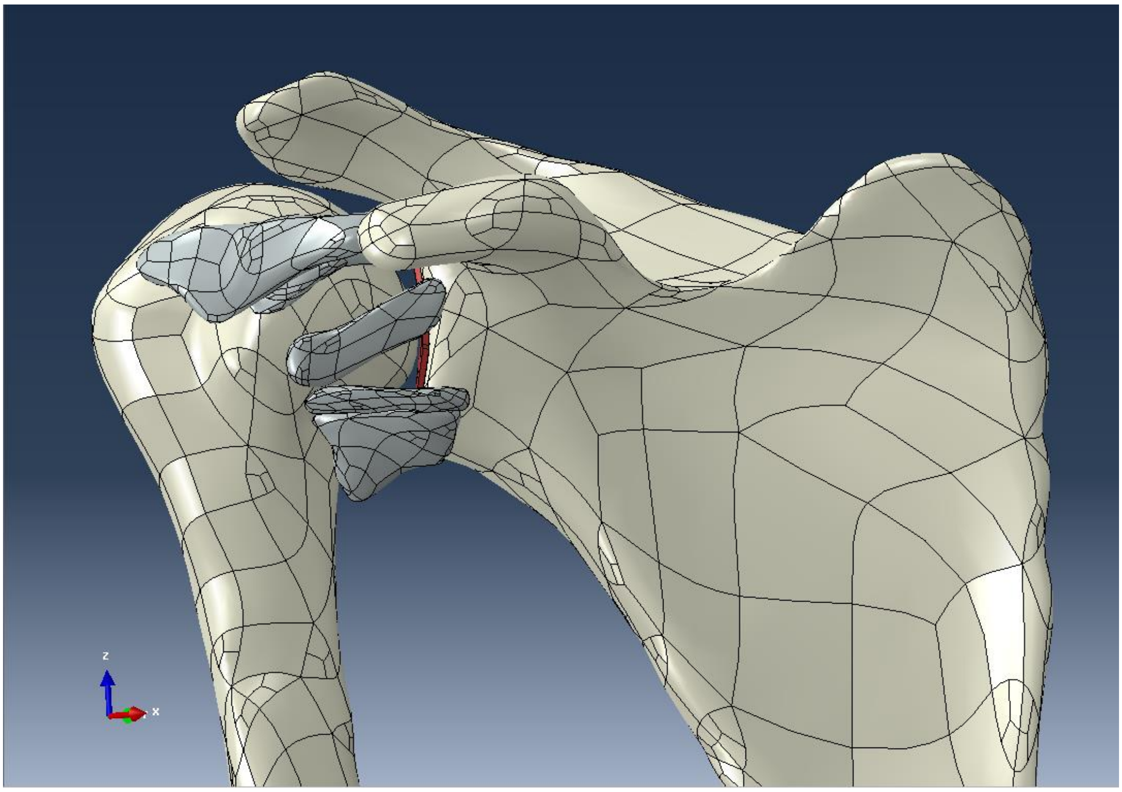

Figure 6-1 Merged bones, glenoid cartilage and ligaments

The second Boolean operation was conducted between muscle and bones. To generate the adjacent but no overlapping surfaces between the bones and muscles, a cut Boolean operation was conducted on the rotator-cuff muscles. The muscle was designed to have some overlapping geometry with respect to the bones in the MR segmentation step. Figure 6-2 showed the cut operation on the infraspinatus muscle by the scapula for the generation of the infraspinatus origin area as an example of this process. Similarly, the infraspinatus muscle was cut by the humerus head to generate the insertion area. The generated surface had positional adjacent relationships with the scapula bone which would be convenient to define contacts and avoid potential errors. Subsequently, this cutting Boolean operation was conducted for all the rotator cuff muscles. New generated parts were named cut-infraspinatus, cut-supraspinatus, cut-teres and cut-subscapularis.

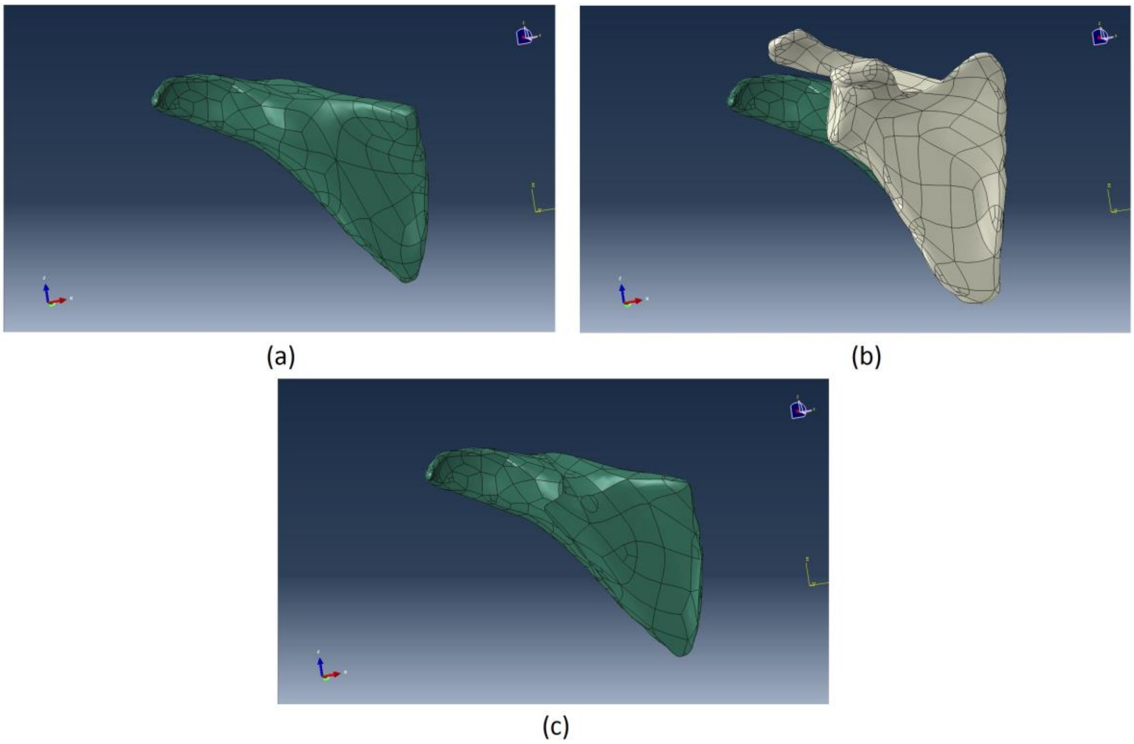

Figure 6-2 Muscle-bone contact surface generation on the infraspinatus muscle by Boolean operation (a) Before cutting; (b) during cutting; (c) after cutting

The third Boolean operation was conducted to generate the rotator cuff structure. The cut-supraspinatus, cut-infraspinatus and cut-teres muscle were merged as a whole instance with boundaries removed since they consisted of the same tissue. (See Figure 6-3) The merged part was designed to replicate the connective nature of the rotator cuff tendons.

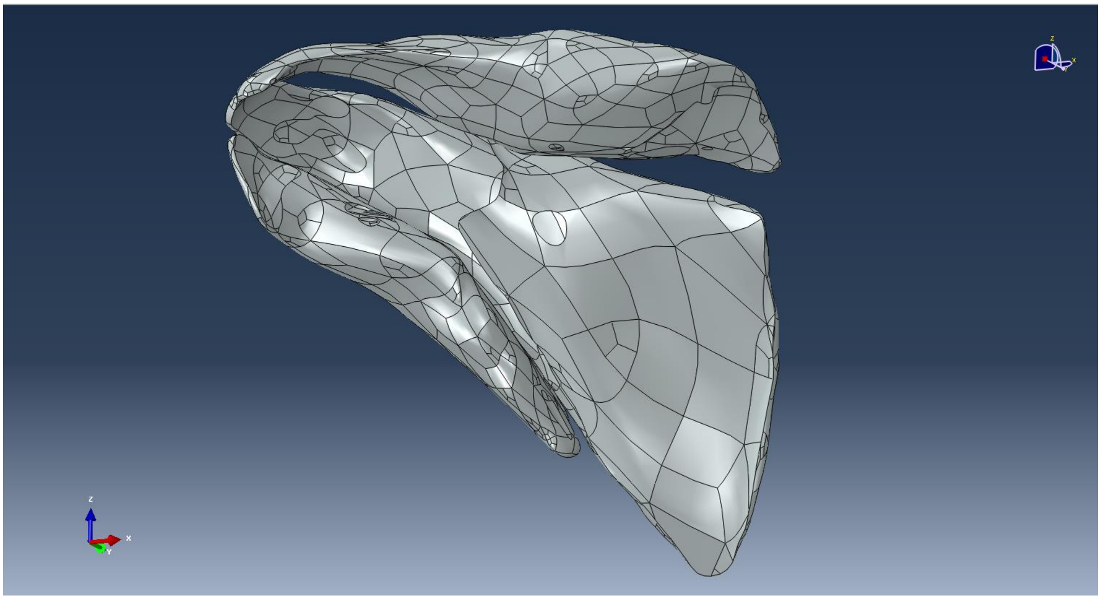

Figure 6-3 The merged rotator cuff muscles

The names of the instances and anatomical structure contained in the new assembly were listed in Table 6-1. Figure 6-4 showed all the parts in the assembly in the anterior view.

Table 6-1 Instances in the new assembly.

Instance name	Anatomical structures contained
Bone-ligaments	Scapula, humerus, glenoid cartilage and all ligaments
Humeral-cartilage	Humeral cartilage
Clavicle	Clavicle
Rotator-cuff	Supraspinatus, infraspinatus and teres minor muscle
Subscapularis	Subscapularis muscle

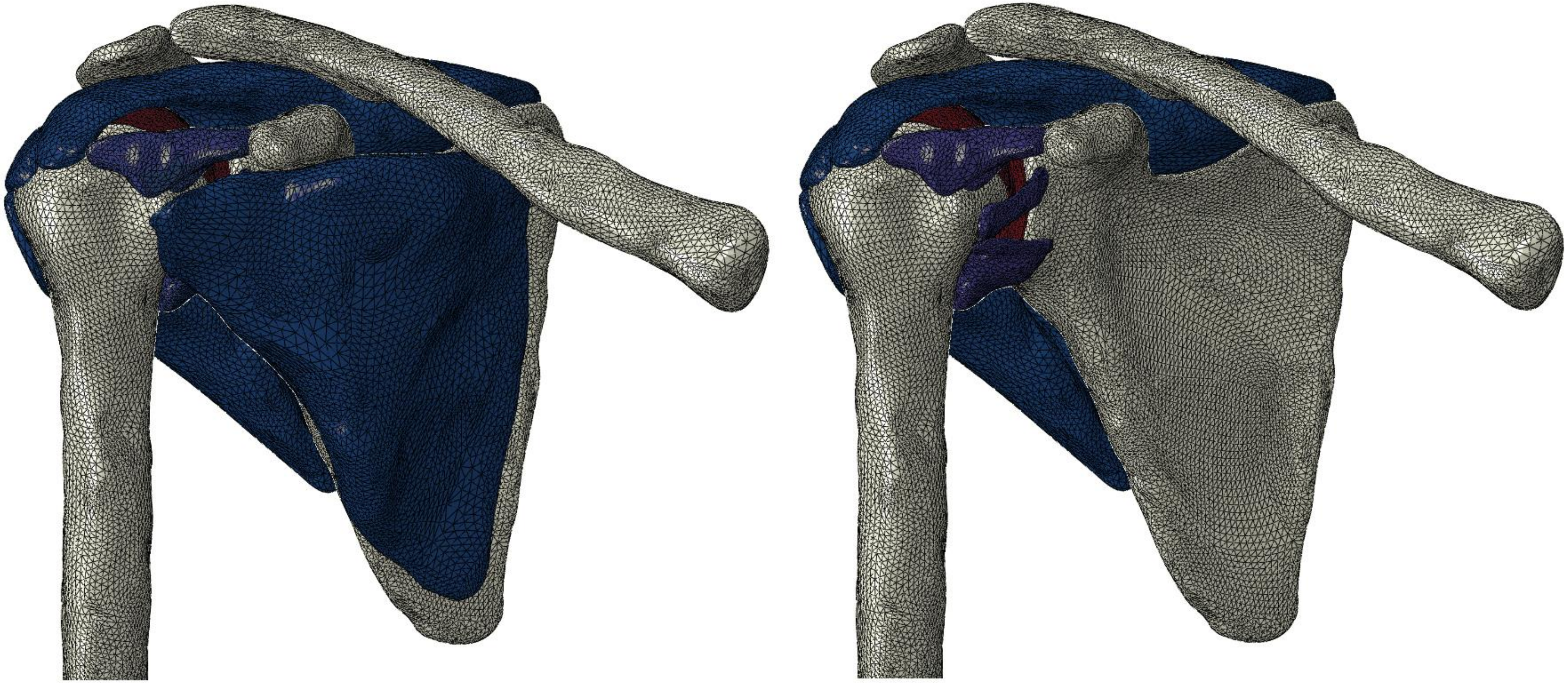

Figure 6-4 Assembly overview (The left is the plot of the right by hiding subscapularis muscle)

6.2.2 Material property definitions

The material properties were assigned to the newly generated parts from the Boolean operations. The values of the material properties of the anatomical tissues in this study were determined based on literature. (See Table 6-2) As this study focused on the large-scale joint stability investigation, the amount of components involved were substantial. The benefit was that this complexity allowed overall joint performance and force transmitting mechanism evaluation, whereas the drawback is obviously the considerably large computational cost and efficiency. Therefore, the material properties were selected based on the basic rule: to use optimal material definitions that were sufficient enough to solve the problems under investigation while keeping the least complexity of the whole model. Hence, for most of the tissues involved, the type of the material property was selected as linear elastic. To evaluate the accuracy of the material property definitions, a detailed sensitivity study was conducted to investigate the influence of these definitions of the soft tissues on these results of the simulations which would be presented in the next chapter. In addition, rigid body definitions on the bones were assigned and tested later in a preliminary simulation.

Table 6-2 Material properties of the anatomical components adopted in this study

Tissue types	**Material types**	**Properties**	
		E (MPa)	v
Bones	linear elastic [52]	18000	0.35
Cartilages	linear elastic [18]	15	0.45
Muscles	linear elastic [16]	168	0.497
Ligaments	hypoelastic [66]	10.1	0.4

(E: Young’ modulus; v Poisson’s ratio)

6.2.3 Mesh generation

3D quadratic tetrahedral element type (C3D10: A 10-node quadratic tetrahedron)was adopted in this study. The tetrahedral element was most commonly used for constructing computational grids for biomechanical models of the living tissues and has been used in numerous studies [7, 147-149]. In this study, all parts were meshed with tetrahedral elements. Specifically, the tetrahedral meshes were generated automatically with by manually applying seed sizes. The mesh sizes and numbers summary can be found in Table 6-3. The meshed parts and assembly were shown in Figure 6-5 to Figure 6-7.

Table 6-3 Mesh summary

Parts	Mesh size (mm)	Number of elements
Bone-ligaments	1.5	337075
Humeral-cartilage	1.2	10842
Clavicle	1.5	55188
Rotator-cuff	2	166473
Subscapularis	2	97009
	Total number of elements	666587

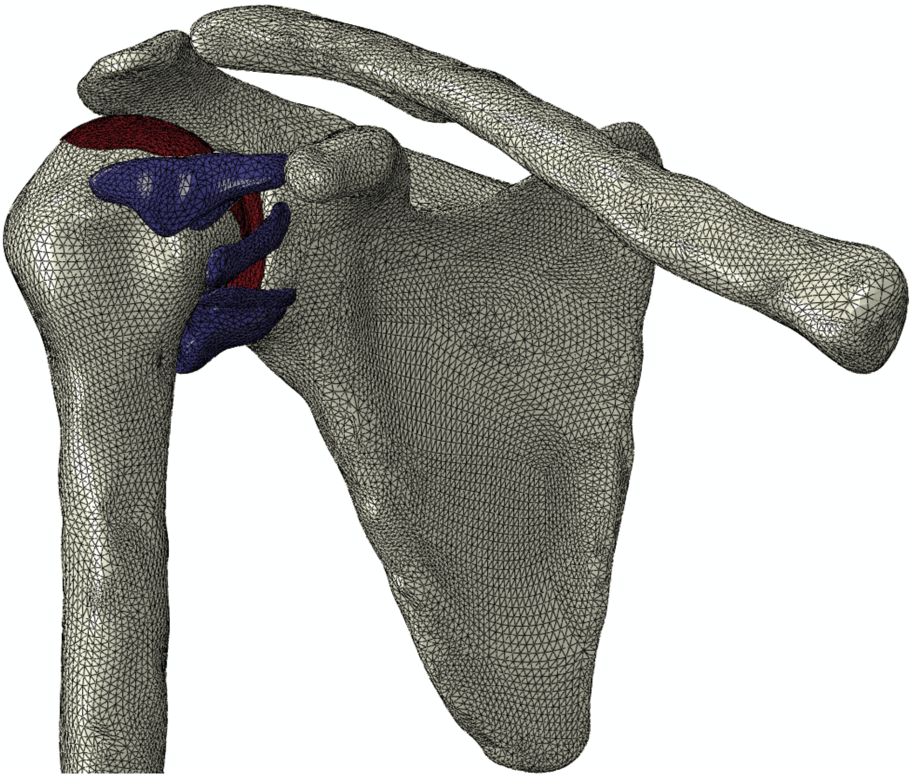

Figure 6-5 Meshed bone-ligaments-cartilages parts

Figure 6-6 Meshed muscle parts

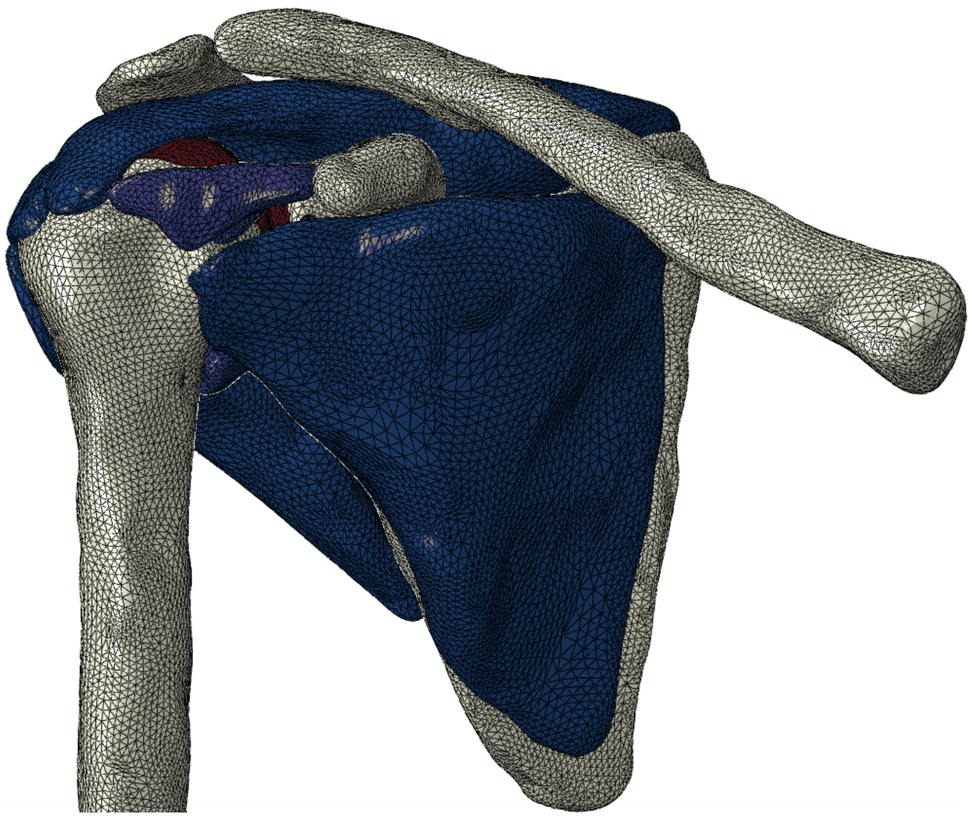

Figure 6-7 Meshed assembly

6.2.4 Contact definitions

The contacts were defined on the meshed parts to simulate the physiological relationships between the segments of interest. There were mainly two types of surface-surface based contact properties defined in this model, namely frictionless sliding and firmly bonding contacts.

The first contact property i.e., the frictionless sliding property, was defined to simulate the natural function of the cartilages which they slide on top of each other almost frictionless (friction coefficient of normal synovial joint such as the glenohumeral joint can be as low as 0.001) [19]. This property was defined by the basic default “hard contact” normal behaviour and “frictionless” tangential behaviour. The “hard contact” indicates that the contact pressure dramatically changes when the contact clearance (distance separating two surfaces) becomes zero [146]. The “frictionless” tangential behaviour is as its literal meaning that the friction coefficient equals zero. As a result, the contact pressure causes no friction during analysis. This property was assigned to the cartilages by selecting the master surface “glenoid cartilage” and the slave surface “humeral cartilage”. (See Figure 6-8) Similarly, the physiological wrapping functions between the rotator cuff muscles and the humeral head were defined by this property as well. Figure 6-9 used that teres minor vs humeral head contact definition as an example to illustrate the contact definitions between the teres minor and the humeral head. The contacts for other rotator cuff muscle were defined by the same method.

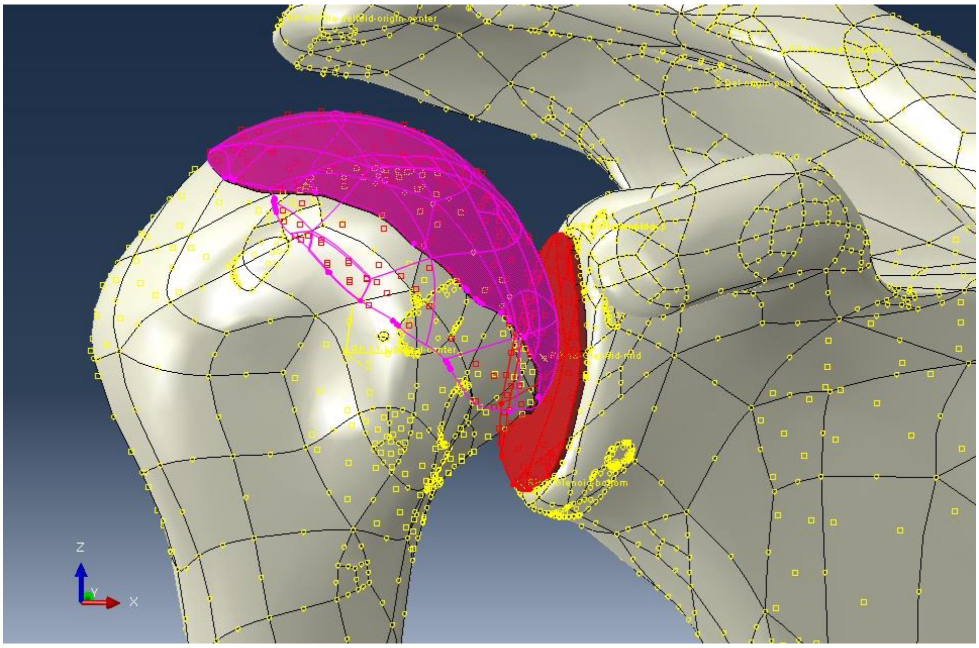

Figure 6-8 Contact definition between the cartilage surfaces in which master surface (glenoid cartilage) in red and slave surface (humeral cartilage) in purple

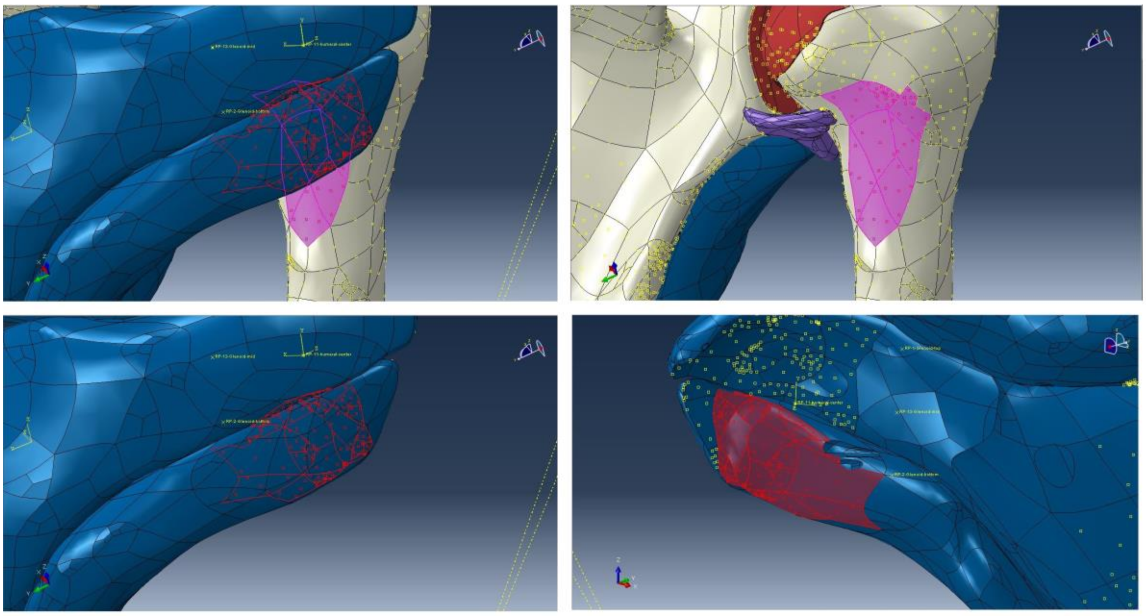

Figure 6-9 Demonstration of the definition of the wrapping function by the frictionless sliding property between the rotator cuff muscles and the humeral head

The second contact property, i.e. the firmly bonding property, was defined to simulate the tightly bonded connection between the bone and muscle at the origin and insertion surfaces. Several property definitions were tried to simulate this behaviour including "tie", "kinematics constraint" and "MPC controls" in Abaqus. However, probably because of the complexity of the geometries or software constraints, none of these definitions could work properly (error messages showed up) in this model. Instead, the surface-based cohesive behaviour was defined to solve this problem. This behaviour can be used to model "sticky" contact which suits the case in this study [146]. An elastic traction-separation law was assumed in this behaviour:

$$\begin{bmatrix} t_n \\ t_s \\ t_t \end{bmatrix} = \begin{bmatrix} K_{nn} & 0 & 0 \\ 0 & K_{ss} & 0 \\ 0 & 0 & K_{tt} \end{bmatrix} \begin{bmatrix} \varepsilon_n \\ \varepsilon_s \\ \varepsilon_t \end{bmatrix}$$

Where quantities t_n, t_s and t_t represent the nominal tractions in the normal and two local shear directions; K_{nn}, K_{ss} and K_{tt} represent corresponding stiffness components while ε_n, ε_s and ε_t represent the separation between bonded surfaces. A typical traction-separation response can be found in Figure 6-10. The tip of the curve is where the failure of the bonding occurs. This failure is useful for the definition of the fracture studies, while damage definition is required in addition to the cohesive behaviour. However, in this model, the failure of the bonding was not expected and the separation value was desired to be as low as possible. Therefore, damage was not defined and the value of the stiffness components K_{nn}, K_{ss} and K_{tt} was set to be relatively high (1e10 N/m). While the magnitude of the muscle forces was no higher than 200 N, hence the separation of the cohesive surfaces can be considered negligible. Two surfaces were bonded tightly as desired by the cohesive definition. Figure 6-11 takes this contact property definition on the subscapularis-scapula interaction surfaces as an example.

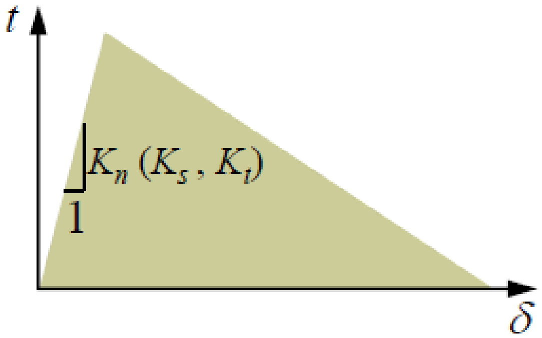

Figure 6-10 Traction-separation response in cohesive surface definition [146]

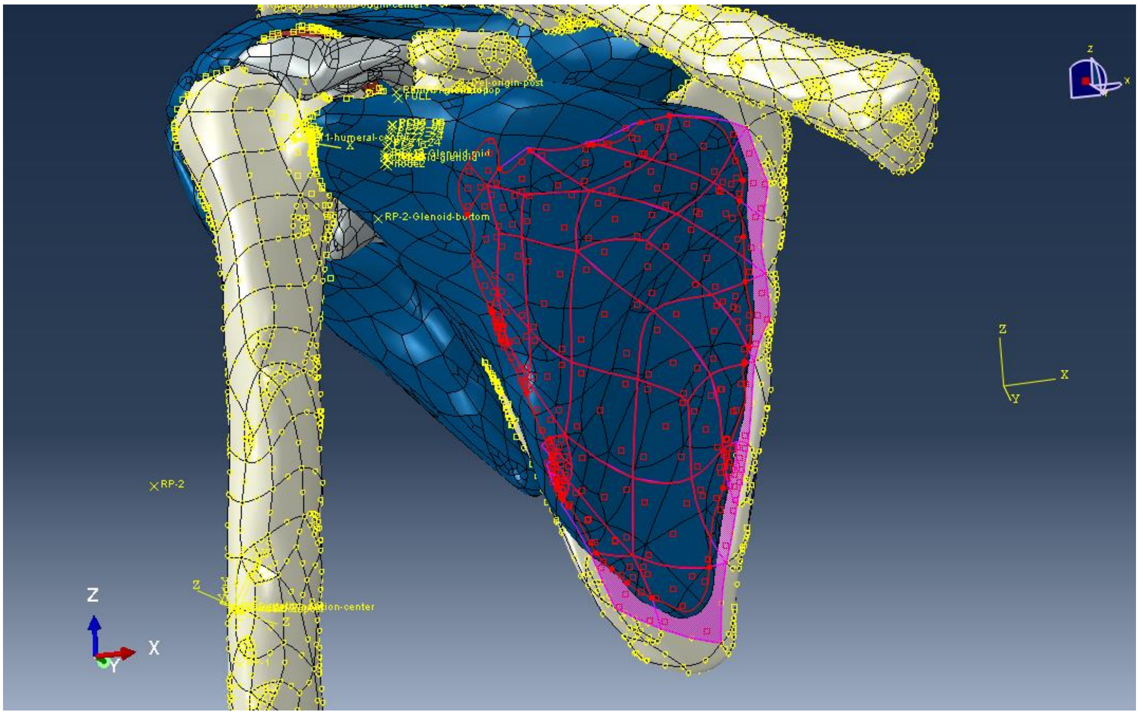

Figure 6-11 The contact definition between the bone (scapula) and muscle (subscapularis) surfaces at the origin site

6.2.5 Loading and boundary conditions

The loading and boundary conditions were one of the key components when performing FE analysis. As one of the major novelties of this study, the realistic loading and boundary conditions were completely determined by the *in-vivo* subject-specific measurement and force calculation in chapter 3 and 4. No artificial loading or boundary conditions were assumed in this study. The boundary conditions were designed to replicate the *in-vivo* kinematics testing in Chapter 3 for the scapular plane abduction from neutral to thirty degrees. The loading conditions were determined by the muscle loads calculated based on *in-vivo* experimental measurements in Chapter 4.

6.2.5.1 Boundary conditions

To define the boundary conditions on the bones, several reference points were assigned to the bones with the rigid constraint definition on the bone geometries. Coordinates of the reference points of the bone segments can be found in Table 6-4. The constraint bone segments were illustrated from Figure 6-12 to Figure 6-14. The reference point of the clavicle bone was selected as the origin centre of the deltoid anterior muscle; the reference point of the scapula was selected as the glenoid centre which was the middle point of the glenoid top and glenoid bottom. (See Figure 6-13) The reference point of the humeral head was defined as the assumed spherical centre of the humeral head. This spherical centre was calculated by selecting four approximate centres by roughly dividing into four main regions on the humeral head. The calculation process and MATLAB coding can be found in Appendix A (3): Humeral centre estimation.

Table 6-4 Reference points of the bone segments

Reference Point of rigid constraint	Bone segment	Coordinates in global frame (X, Y, Z)
Origin centre of deltoid anterior	Clavicle	(-99.92, -21.67, 101.72)
Glenoid centre	Scapula	(-130.55, -5.58, 70.1)
Humeral centre	Humerus	(-148, -20, 71.6)

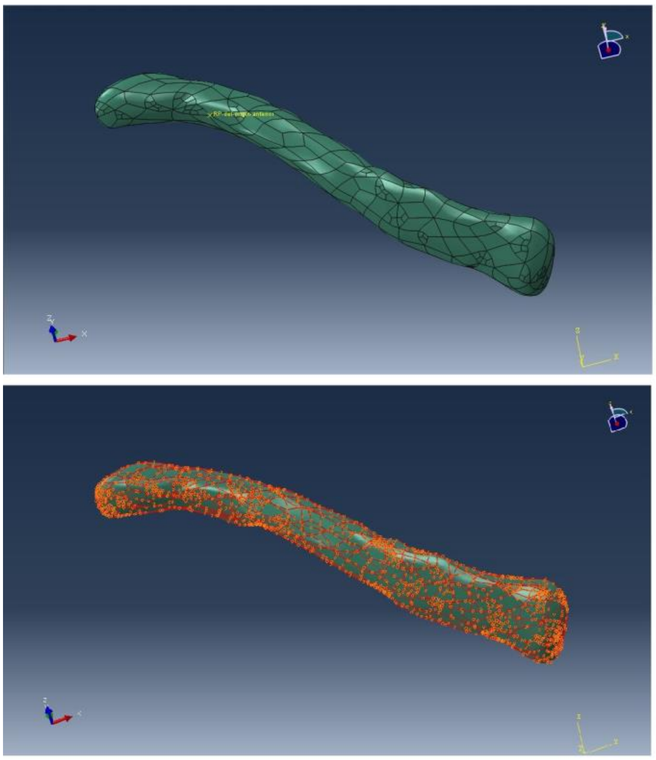

Figure 6-12 Rigid body constraint definition of the clavicle

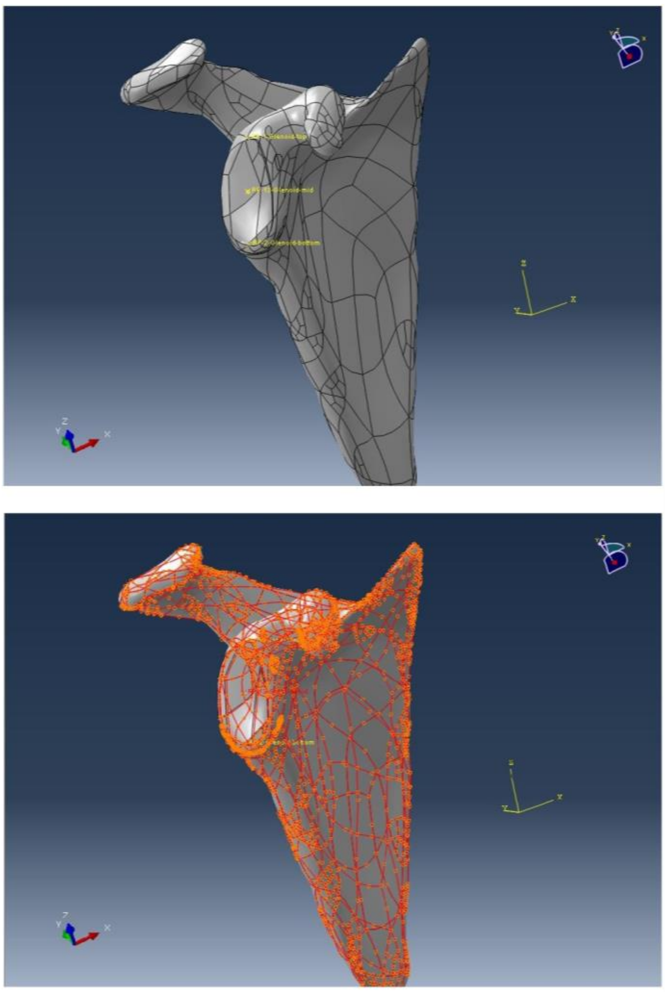

Figure 6-13 Rigid body constraint definition of the scapula

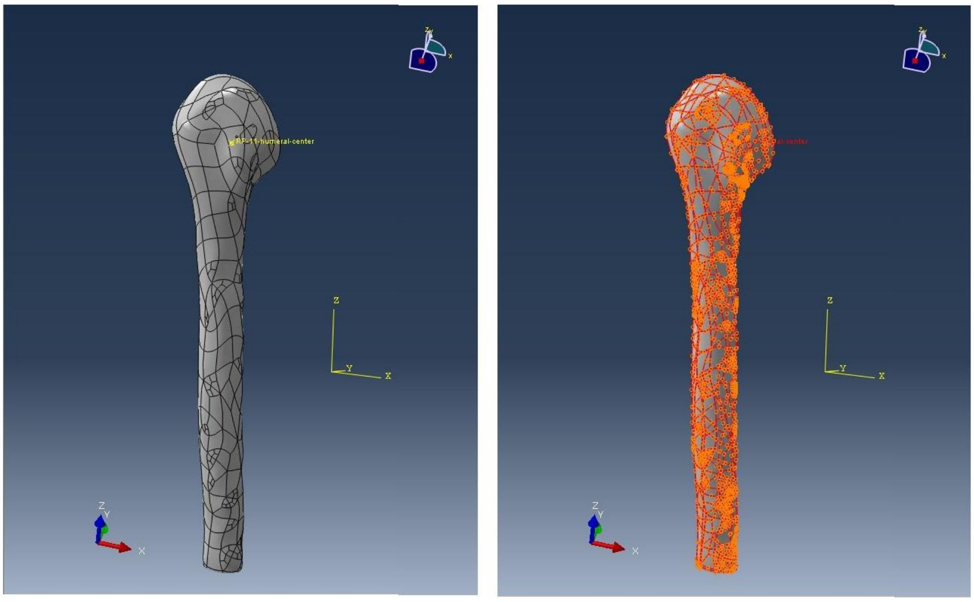

Figure 6-14 Rigid body constraint definition of the humerus

To replicate the *in-vivo* kinematics testing in Chapter 3 for the scapular plane abduction from neutral to thirty degrees, the scapula and clavicle bone were set to be completely fixed, while the humerus bone was free to move. Specifically, to apply this boundary condition, the clavicle and scapula bone were fixed by constraining the 6 degrees of freedom of their reference points named “origin centre of deltoid anterior” and “glenoid middle”. (See Figure 6-15)

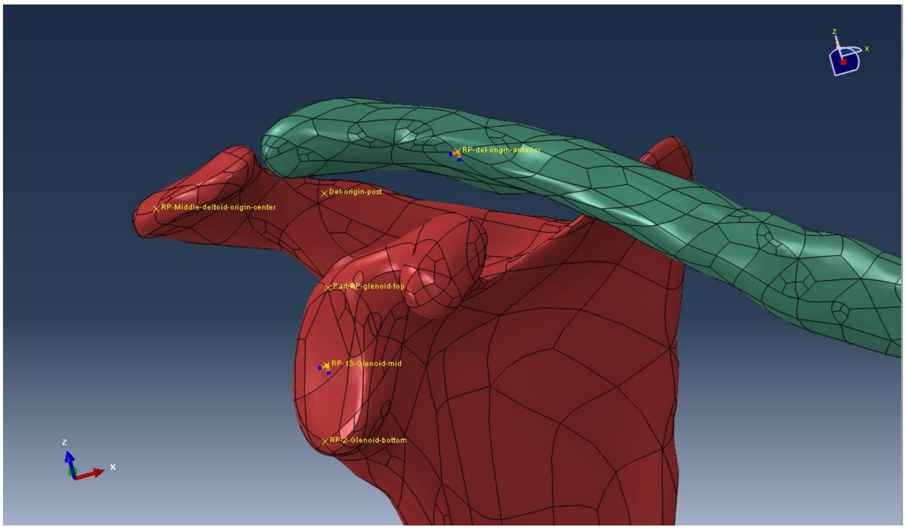

Figure 6-15 Boundary conditions: fix clavicle and scapula bone completely

6.2.5.2 Loading conditions

As mentioned, the loading conditions of this model were completely determined by the calculated muscle forces in Chapter 4. Magnitudes of the muscle force of the neutral position can be found in Table 4-1. To accurately implement these muscle forces in the FE model, two methods were adopted. The first method is applying predefined stress to the muscle belly portion to simulate the muscle contraction. This method was applied to the rotator cuff muscles. In the second method, the concentrated forces were applied to the deltoid insertion centre and pointing the muscle insertion centre. This applied to deltoid anterior, middle and posterior muscles. The second method was quite straightforward and commonly used since the volume of the deltoid muscle was not included in this model. However, the first method was actually a novel invention in this field of research. In this FE model, muscles were attached to both sides of the bones which are realistic representations of the physiological conditions. However, every coin has two sides, this definition makes load applying difficult. Because of this definition, there were no free ends or surfaces for applying muscle loads as previous works did [15, 16, 56, 18]. Therefore, we proposed the predefined stress method for this muscle load implementation which also represented the muscle contractions in realistic scenarios.

Specifically, in the first method, the muscle forces were applied by evenly distributed predefined stress on every node of the muscle belly portion. (See Figure 6-16)

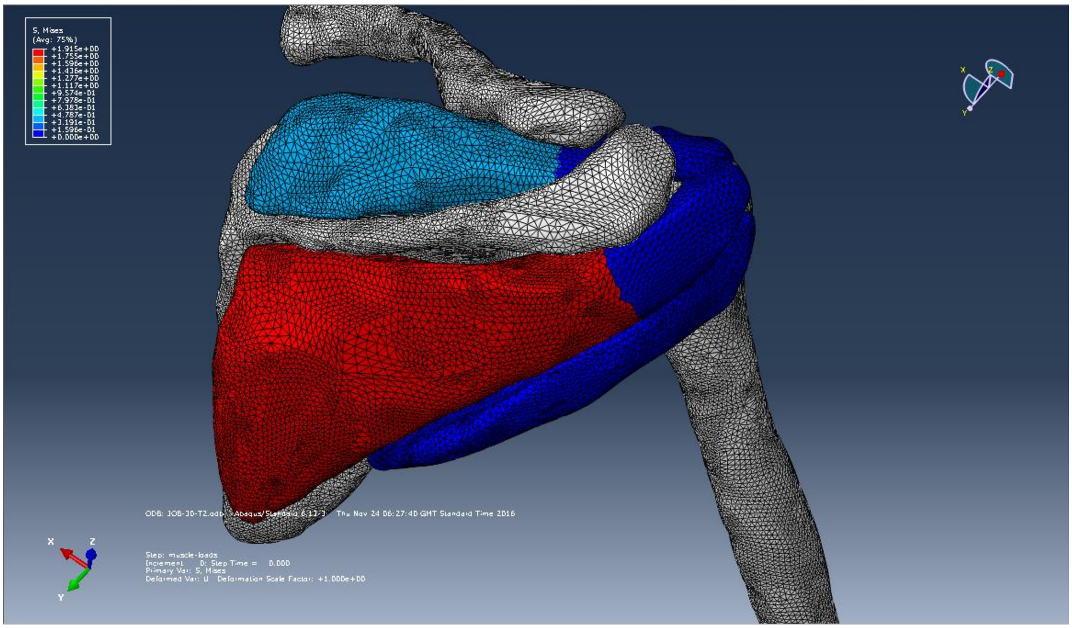

Figure 6-16 Predefined stress applied on muscle bellies (e.g. infraspinatus muscle belly in red; supraspinatus muscle belly in light blue)

To simulate the contraction of the muscle to the bones, the stress applied on the muscle was defined to be in one-dimensional stress state where the one-dimension is defined to be along the direction of the line connecting the centroids of origin and insertion sites. Figure 6-17 takes subscapularis muscle as an example to illustrate the one-dimensional stress state in one slice of the elements of the muscle belly portion. (N.B. The slice of the muscle belly was chosen only to get a better view of the stress state of the applied one-dimensional stress. The predefined stress was applied to the whole belly portion as demonstrated in Figure 6-16.)

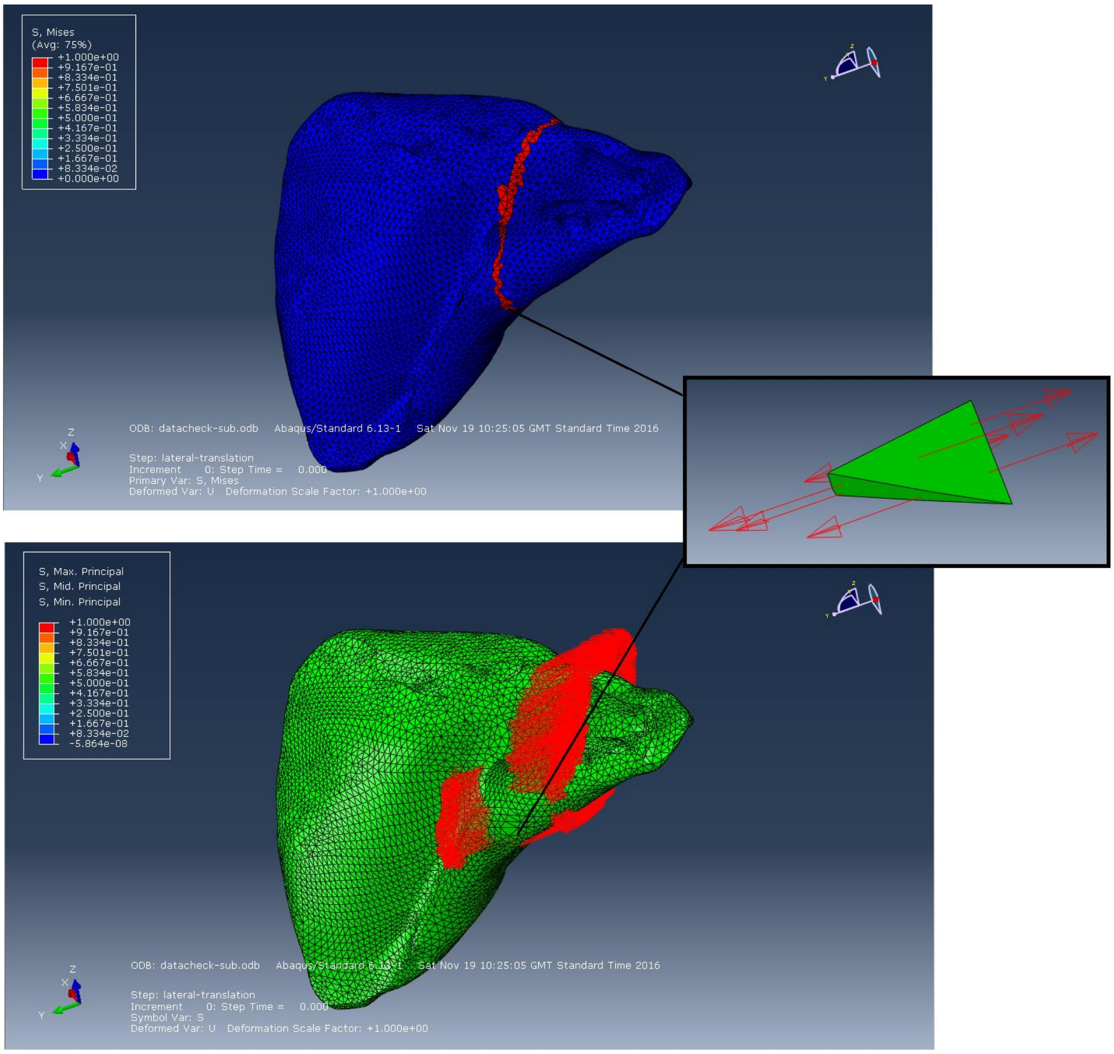

Figure 6-17 One-dimensional stress state of the predefined stress on one slice of the muscle belly of the subscapularis

N.B. The double sided arrows pointing outside of the element represent the principal stress in tension while the colour of the arrow (red) represents the magnitude of this principal stress.

Specifically, when defining the one-dimensional stress state, these stress states had to be defined in global coordinates. (Abaqus 6.13 only allows the predefined stress definition in the global coordinates.) Local coordinates of the rotator cuff muscles were established firstly where the X-axis was defined to be along the direction of the line connecting centroids of origin and insertion sites. (See Figure 6-18) Each of their X-Y-

Z axis angular positions with respect to the global coordinates' was measured to determine the rotation matrices. (See Figure 6-18 and Table 6-5)

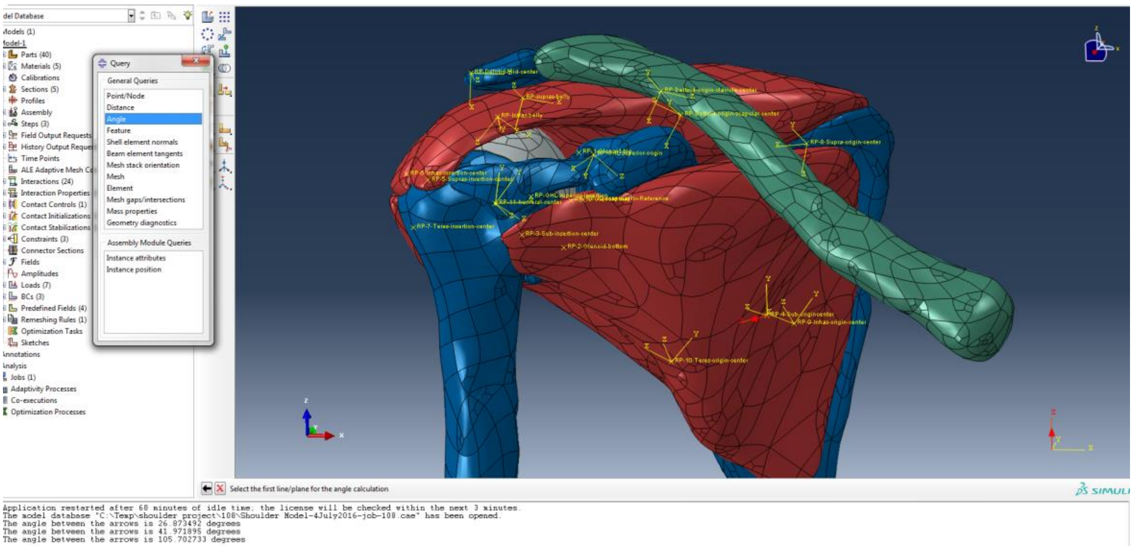

Figure 6-18 Definition of the local coordinates of the rotator cuff muscle

Table 6-5 Relative angular positions between the local muscle coordinates and the global coordinate

	Global\local	x	y	z
Subscapularis	x*	116.7	144.76	68.77
	y*	95.02	63.67	26.87
	z*	152.76	68.34	105.7
Supraspinatus	x*	140.05	129.94	89.35
	y*	126.24	44.56	67.79
	z*	104.52	73.56	157.78
Infraspinatus	x*	129.12	130.61	65.02
	y*	53.38	93.37	36.83
	z*	119.75	40.81	64.83
Teres minor	x*	127.04	127.42	58.83
	y*	48.08	91.67	41.97
	z*	115.89	37.47	64.94

The rotation matrices R_i of each local-global coordinates were determined by the direct cosine matrix of the angles in Table 6-5. As the X-axis in local coordinate was defined in the muscle fibre direction, the normalised local stress tensor can be defined as T_L=

$\begin{bmatrix} 1 & 0 & 0 \\ 0 & 0 & 0 \\ 0 & 0 & 0 \end{bmatrix}$ in every local coordinate. Subsequently, the local stress tensors were converted to the global coordinates by the equation: $T_{Gi} = R_i^T * T_L * R_i$, [150] where T_{Gi} represents the converted stress tensor in global coordinate for each muscle. See results as follows.

Subscapularis: $T_{Gsub} = \begin{bmatrix} 0.2019 & 0.3670 & -0.1627 \\ 0.3670 & 0.6671 & -0.2958 \\ -0.1627 & -0.2958 & 0.1311 \end{bmatrix}$

Supraspinatus: $T_{Gsup} = \begin{bmatrix} 0.5877 & 0.4921 & -0.0087 \\ 0.4921 & 0.4121 & -0.0073 \\ -0.0087 & -0.0073 & 0.0001 \end{bmatrix}$

Infraspinatus: $T_{Ginf} = \begin{bmatrix} 0.3981 & 0.4107 & -0.2664 \\ 0.4107 & 0.4237 & -0.2749 \\ -0.2664 & -0.2749 & 0.1783 \end{bmatrix}$

Teres minor: $T_{Gter} = \begin{bmatrix} 0.3629 & 0.3660 & -0.3118 \\ 0.3660 & 0.3692 & -0.3145 \\ -0.3118 & -0.3145 & 0.2679 \end{bmatrix}$

In terms of the determination of the magnitude of the stress tensor in the above-designed state, a supplement FE muscle model was established which contained only the rotator cuff muscles. (See Figure 6-19) All definitions of the new model were designed the same as the main model including mesh, material definition, and loading conditions, except the boundary conditions. The muscle origin and insertion sites were set to be fixed in each muscle. The standout difference was the fixation definition in the insertion sites. While in the main model, they were bonded to the humerus bone surface. An assumption was made that the muscle forces due to the muscle contraction of the prescribed stress state were the same between these two models. Specifically, the origin sites were fixed directly, while the insertion sites were fixed through coupling constraint (insertion site was constrained to one reference point) so that the reaction forces due to muscle contractions can be read directly from the results. According to Newton's third law, the magnitude of the forces due to muscle contraction is equal to the reaction force and the direction is opposite. The above converted normalised stress tensor in global coordinate was applied to respective muscle at first. The simulations were successfully conducted on each muscle at a time. The reaction force for each rotator cuff muscles was recorded, specifically, subscapularis, supraspinatus, infraspinatus and teres minor muscle with the reaction force of 205.68N, 29.58N, 53.9N and 41.67N respectively.

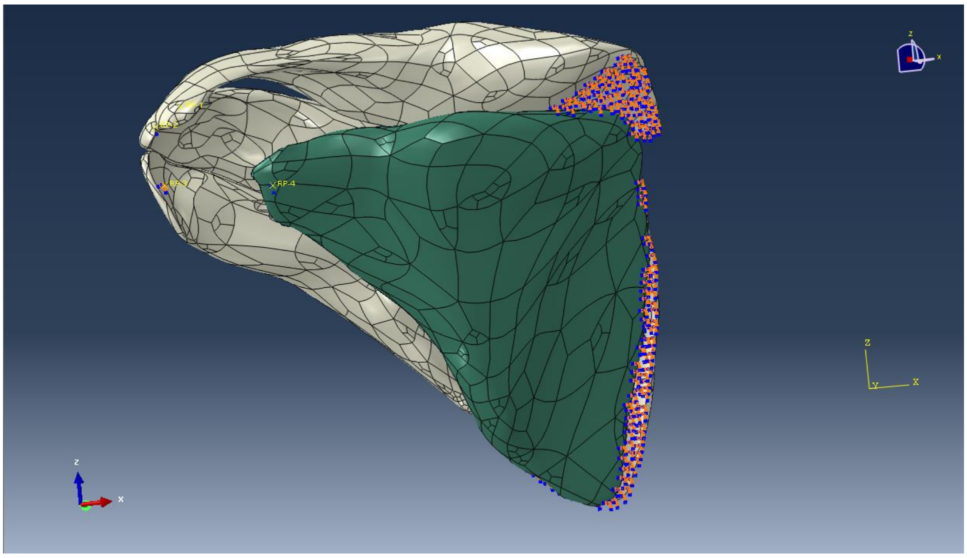

Figure 6-19 Supplement muscle model for the determination of the magnitude of the stress state that can generate desired muscle forces.

Through testing, it was found that the magnitude of the reaction force was proportional to the magnitude of the stress tensor. Rotator cuff muscle forces calculated in Chapter 4 for the neutral position were 26.21N, 6.9N, 21N and 1.54N for subscapularis, supraspinatus, infraspinatus and teres minor muscle respectively. Therefore, the magnitude of the respective magnitude was estimated as 0.1274, 0.2334, 0.3949 and 0.0371 of the normalised magnitude. Hence, the stress tensors of rotator cuff muscles for the neutral position were calculated as follows:

Subscapularis:

$$T_{Gsub0}=\begin{bmatrix} 0.2019 & 0.3670 & -0.1627 \\ 0.3670 & 0.6671 & -0.2958 \\ -0.1627 & -0.2958 & 0.1311 \end{bmatrix} * 0.1274 = \begin{bmatrix} 0.0257 & 0.0467 & -0.0207 \\ 0.0467 & 0.085 & -0.0377 \\ -0.0207 & -0.0377 & 0.0167 \end{bmatrix}$$

Supraspinatus:

$$T_{Gsup0}=\begin{bmatrix} 0.5877 & 0.4921 & -0.0087 \\ 0.4921 & 0.4121 & -0.0073 \\ -0.0087 & -0.0073 & 0.0001 \end{bmatrix} * 0.2334 = \begin{bmatrix} 0.1372 & 0.1149 & -0.002 \\ 0.1149 & 0.0962 & -0.0017 \\ -0.002 & -0.0017 & 0.00003 \end{bmatrix}$$

Infraspinatus:

$$T_{Ginf0}=\begin{bmatrix} 0.3981 & 0.4107 & -0.2664 \\ 0.4107 & 0.4237 & -0.2749 \\ -0.2664 & -0.2749 & 0.1783 \end{bmatrix} * 0.3949 = \begin{bmatrix} 0.1572 & 0.1621 & -0.1052 \\ 0.1621 & 0.1673 & -0.1086 \\ -0.1052 & -0.1086 & 0.0704 \end{bmatrix}$$

Teres minor:

$$T_{Gter0}=\begin{bmatrix} 0.3629 & 0.3660 & -0.3118 \\ 0.3660 & 0.3692 & -0.3145 \\ -0.3118 & -0.3145 & 0.2679 \end{bmatrix} * 0.0371 = \begin{bmatrix} 0.0135 & 0.0136 & -0.0116 \\ 0.0136 & 0.0137 & -0.0118 \\ -0.0116 & -0.0118 & 0.0099 \end{bmatrix}$$

Subsequently, the estimated stress tenors were verified by implementing to the supplement model. For convenience, the above stress state was written in the format as

$[\sigma_{11}, \sigma_{22}, \sigma_{33}, \sigma_{12}, \sigma_{13}, \sigma_{23}]$, where, σ_{11}, σ_{22} and σ_{33} represent its 3 normal stresses where σ_{12}, σ_{13} and σ_{23} represent its 3 shear stresses in the global coordinate. T_{Gsub0} was taken as an example to show the relationship between this shortened format with the previous matrix format:

$$T_{Gsub0} = \begin{bmatrix} 0.0257 & 0.0467 & -0.0207 \\ 0.0467 & 0.085 & -0.0377 \\ -0.0207 & -0.0377 & 0.0167 \end{bmatrix} = \begin{bmatrix} \sigma_{11} & \sigma_{12} & \sigma_{13} \\ \sigma_{21} & \sigma_{22} & \sigma_{23} \\ \sigma_{31} & \sigma_{32} & \sigma_{33} \end{bmatrix}$$

N.B. $\sigma_{12} = \sigma_{21}$, $\sigma_{13} = \sigma_{31}$, $\sigma_{23} = \sigma_{32}$;

Hence, T_{Gsub0} can be expressed as T_{Gsub0} = [0.0257, 0.085, 0.0167, 0.0467, -0.0207, -0.0377].

Results can be found in Figure 6-20 and Figure 6-21. In this figure, the direction of the arrow represents the direction of the reaction forces to the muscles; whereas, the colour of the arrow represents the magnitude of these forces. It was found that the directions of forces were the muscle contraction directions. While the magnitudes (in red) can be read on top of the legend as 26.22N, 21.29N, 6.904N and 1.546N for subscapularis, supraspinatus, infraspinatus and teres minor muscle respectively, which were almost exactly the same as the recalculated values as expected above.

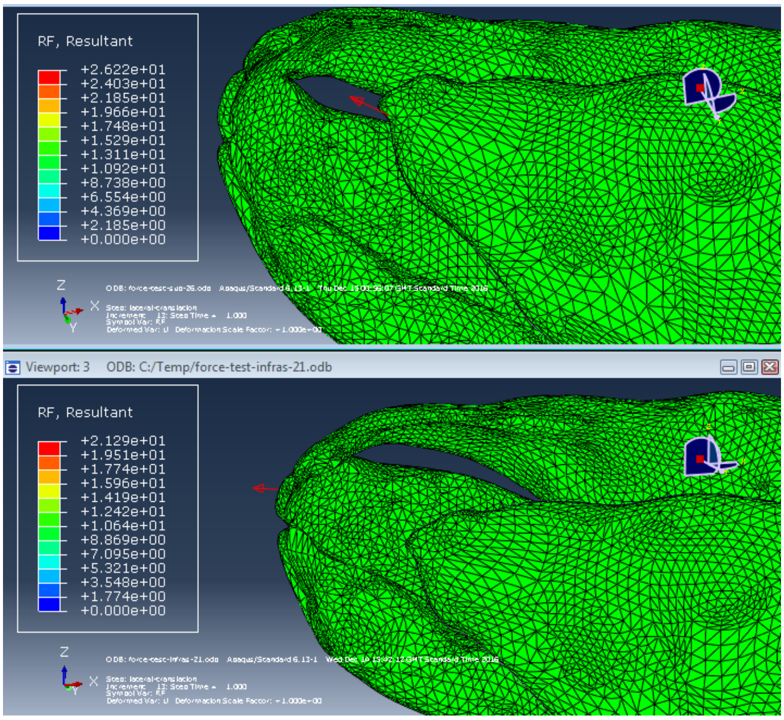

Figure 6-20 Verification of the reaction forces of the one-dimensional stress state of the subscapularis (top) and infraspinatus (bottom) muscle

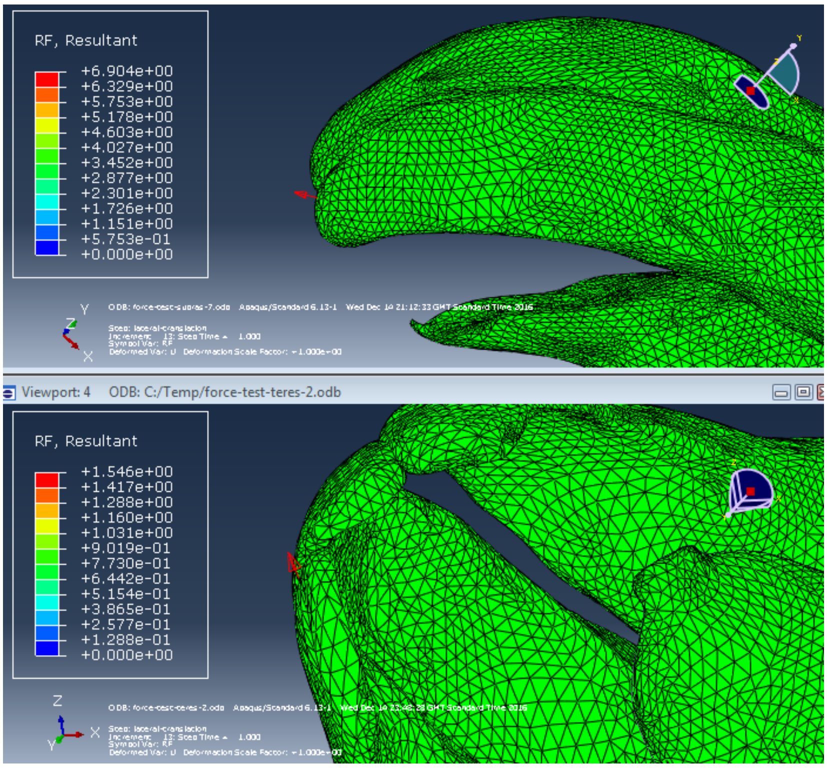

Figure 6-21 Verification of the reaction forces of the one-dimensional stress state of the supraspinatus (top) and teres minor (bottom) muscle

The second method was designed for the implementation of the deltoid muscle forces. The concentrated forces were applied to the deltoid insertion centre with force direction pointing to the muscle insertion centre. Local coordinates for anterior, middle and posterior portion were defined with the X-axis to be the line through insertion centre with direction pointing to the insertion centre. (See Figure 6-22) The magnitude of these forces was found in Table 4-1 as 0.75N, 42.73N and 2.76N in anterior, middle and posterior portions respectively.

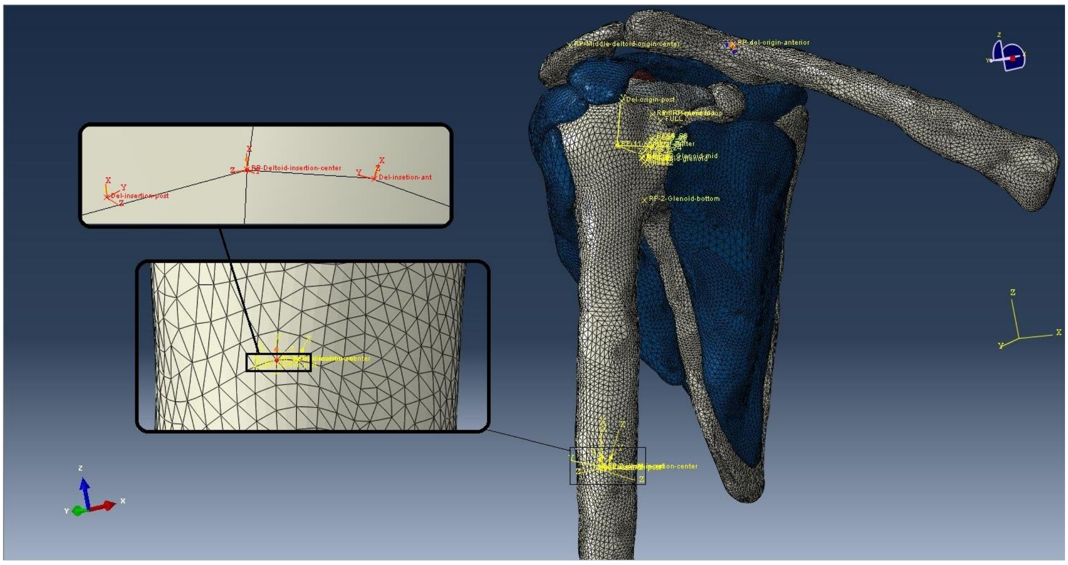

Figure 6-22 Implementation of the deltoid muscle forces in the model

6.2.6 Preliminary simulation

A preliminary simulation was conducted mainly to confirm that all the above definitions were working as expected while the secondary purpose was to test the influence of the rigid bone definitions. As the model was constructed to simulate the static condition, Abaqus/Standard solver was used for the analysis which solves stress analysis problems iteratively (i.e., Newton-Raphson method). A static analysis step was defined in the step module. Due to the complexity of the model, the control of the iterative solver was set manually to improve the convergence of the Newton-Raphson method. Initial and minimum increment size were set to be relatively small, specifically 0.005 and 1E-12 respectively. A history output was requested to view CFN (total force due to contact pressure) and CAREA (total area in contact) in the results; the field output was requested as default.

A test force was applied on the deltoid insertion site by surface pressure with total force 200N. Another comparison simulation was conducted with the same definitions except that the definition of scapula bone was revised from rigid to deformable (linear elastic E=18000MPa, v=0.3). Both of the simulations were completed successfully. All definitions were working as expected. Figure 6-23 illustrated the overview of the Von Mises stress distribution of these two models. It was found that these two simulations demonstrated almost the exactly the same results. The top of the legend showed the maximum Von Mises stress over the whole model. In both of the two models, this value 29.36 was found exactly the same. In addition, the same value 3.106e-2 of the peak stress value on the glenoid cartilage was found in both cases. Despite that no difference was found in results, the computational time increased significantly from 4.6 hours to 7 hours when the scapula was set to be deformable. Therefore, it can be concluded that the rigid body definition of the bones had no significant influence on the simulation conducted by this FE model.

6.3 Model verification: the mesh size sensitivity study

Verification of the computational model was defined as the process of determining if the discretisation of a mathematical model of a physical event can be used to represent the mathematical model of the event with sufficient accuracy [151].

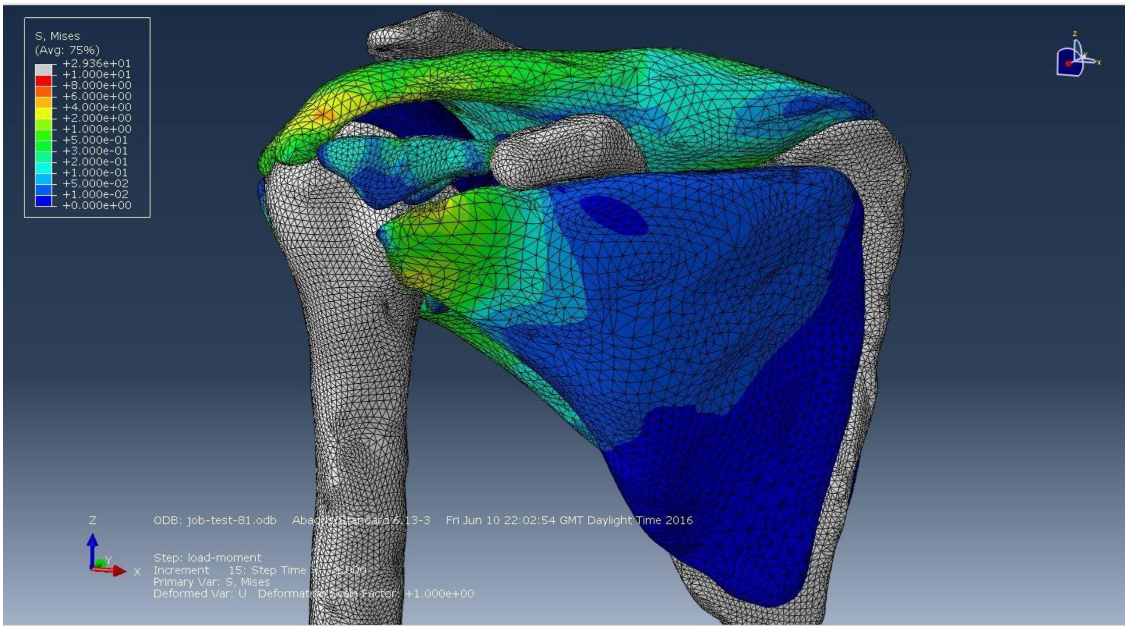

(a)

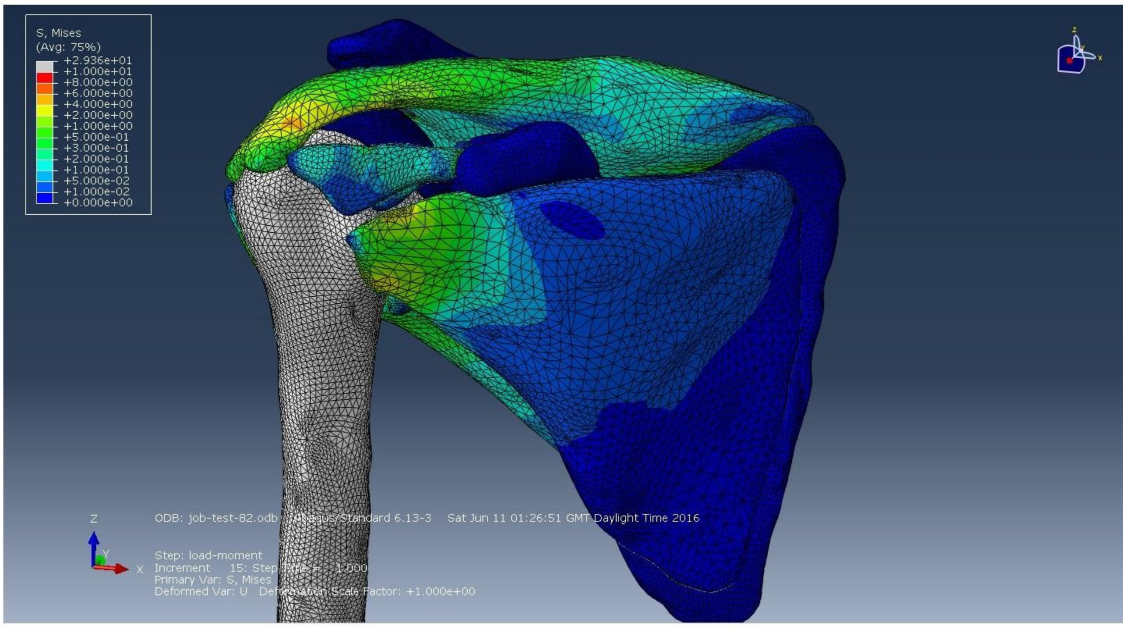

(b)

Figure 6-23 Comparison of the simulation results between the scapula bone (a) rigid and (b) deformable definitions

In this study, a mesh size sensitivity study was conducted to verify the mesh of this FE model were sufficiently dense i.e. the mesh sizes were small enough to solve the problem under investigation. It was also advised that the verification should be conducted before and independently of the validation phase to distinguish the potential modelling error from the discretization error [151]. Hence, for this mesh size sensitivity study, instead of muscle forces in scapular plane abduction, a set of muscle forces in frontal plane abduction were determined from the literature as follows: 53.52N for deltoid middle, while 5.12N, 19.42N, 38.32N and 2.55N for rotator cuff muscles namely supraspinatus, infraspinatus, subscapularis and teres minor, respectively [152, 52]. The magnitude of the stress state was determined via testing in supplement model as above before entering to the model as loading conditions.

The simulation was firstly conducted by the model with original mesh using the research computing facility CSF (24 cores and 48GB memory). The calculation converged smoothly with 16 increments and a total of 2541 seconds. The results of Von Mises stress distribution can be found in Figure 6-24. All contacts and interactions were working as expected. The joint bone-on-bone contact force can be found in the history output to be 14.61N which was also in the realistic magnitude [153]. The forces due to muscle wrapping contact definitions on the rotator cuff muscles were also found in history output to be 57.31N, 50.51N and 0N for infraspinatus, supraspinatus and teres minor.

Subsequently, the denser mesh was regenerated on the main components of the model, namely the Rotator cuff, Subscapularis and Bone-ligament parts. A sequence of smaller mesh sizes was assigned to regenerate the mesh comparing to the original mesh sizes of 1.5mm and 2 mm for muscles and bone-ligaments respectively. However, due to the complexity of the geometry, the mesh can only be generated with certain specific sizes for the part. Specifically, the only denser mesh size that can discretise part “Rotator-cuff” was 0.9mm while for “bone-ligament” was 1mm. Therefore, the model with denser mesh was generated with these two mesh sizes. A total mesh number of 2758946 was generated which was 4.14 times the original mesh number. Other than the mesh, all the rest of the definitions remained unchanged for the simulation. The model with denser mesh was submitted to CSF with the same computational resources (24 cores and 48GB memory). Similarly, the simulation converged smoothly with 13 increments, however, the total computational time was 356274s (99 hours). The result can be seen in Figure 6-25. Key results including bone-on-bone force, rotator cuff wrapping forces and peak stress on glenoid cartilage were monitored for comparison. (See Table 6-6)

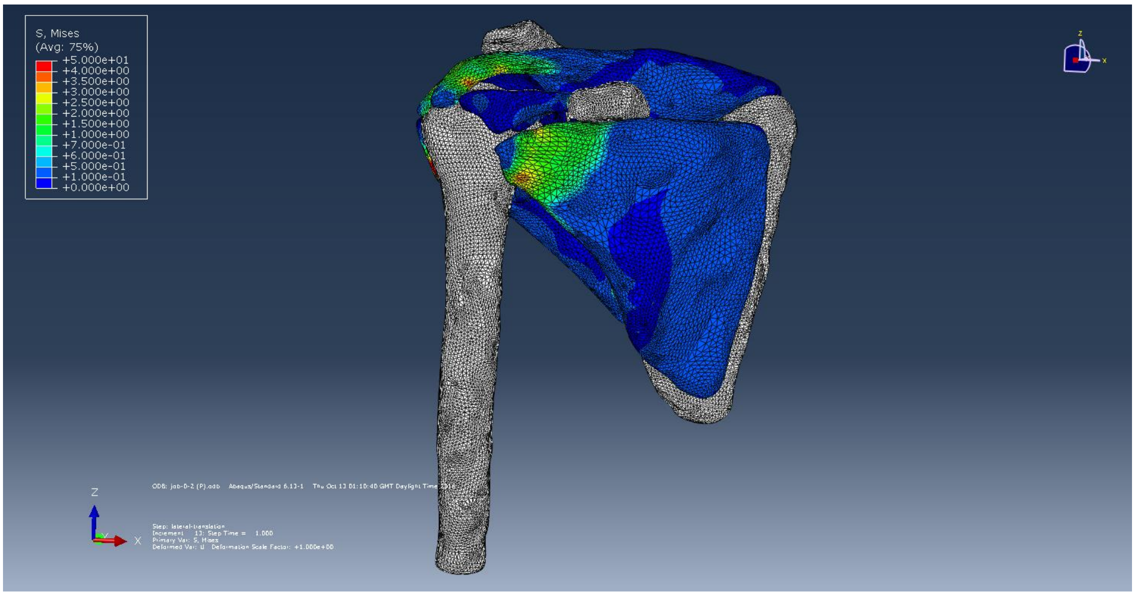

Figure 6-24 Overview of the Von Mises stress distribution of the simulation using the model with original mesh

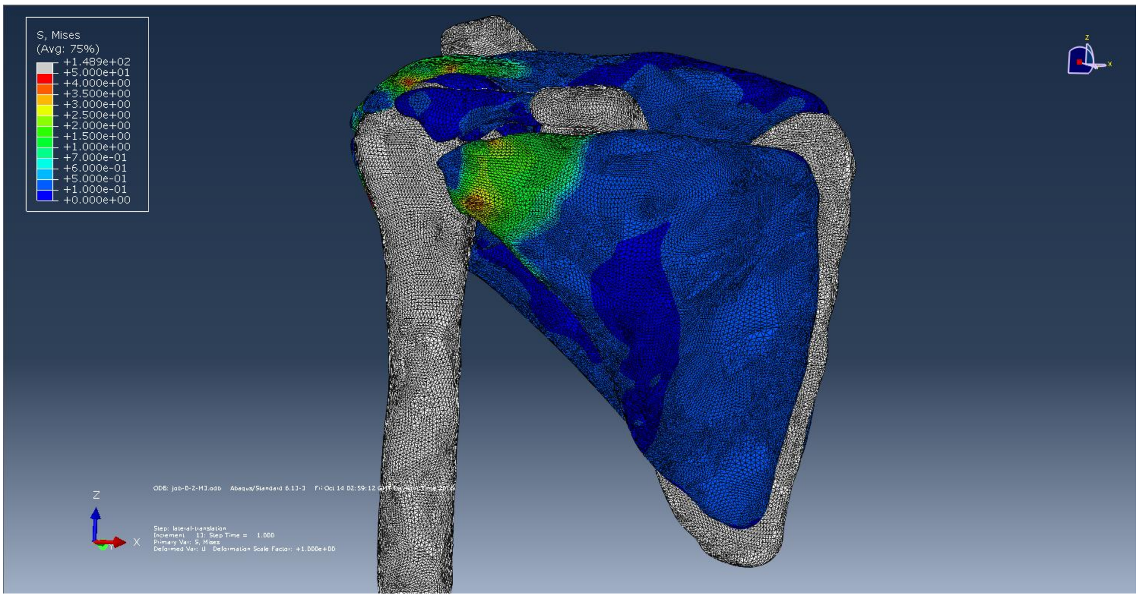

Figure 6-25 Overview of the Von Mises stress distribution of the simulation using the model with denser mesh

Based on the comparison of the results of the two models, it can be found that the performance of the simulation increased insignificantly (average of 3.08%), however, the computational time dramatically increased (154 times larger). Therefore, it can be concluded that the original mesh sizes already demonstrated accurate results. The FE model was verified.

Table 6-6 Comparison of the key results between original model and denser mesh model

	Bone-on-bone force	Peak stress on glenoid cartilage	Infras-wrapping	Supras-wrapping	Teres-wrapping	Computational time
original mesh	14.61	1.369	57.31	50.51	0	2284 (38 mins)
denser mesh	15.8	1.455	59.17	50.97	0	356274 (99 hours)
difference (in percentage)	8.15%	6.28%	3.25%	0.91%	0.00%	15498.69%
				Average	3.72%	

6.4 Summary

In this chapter, the detailed construction process of the FE model had been presented. Firstly, all 16 of the reconstructed geometrical models from Chapter 5 were imported as individual parts to Abaqus. Subsequently, they were assembled with several Boolean operations. The merge Boolean operation was performed between bone and ligament parts, and among the three adjacent rotator cuff muscles to simulate their firmly bonded physiological relationship; the cut Boolean operation was conducted on the muscles by the bones to create the contact definition surfaces. Especially, the merged rotator cuff is a replicate of the connective nature of the rotator cuff tendons which has not been conducted in any previous studies.

Thereafter, material properties were assigned to relative sections of the model based on literature data. Then the 5 parts were meshed with the quadratic tetrahedral element (C3D10) one by one with manually specified global seed sizes. Specifically, mesh sizes of 1.5, 1.2 and 2 were seeded for bone-ligament parts, humeral cartilage and muscle parts. A total number of 666587 elements were generated.

Subsequently, contacts among or within these parts were defined. The muscle-bone connective contacts were bonded together with cohesive surface based behaviour definition; whereas the cartilages interactions and muscle wrapping functions were simulated by frictionless sliding behaviour definition.

Then, the boundary and loading conditions were completely determined by the *in-vivo* measurements and muscle forces calculation from chapter 3 and 4. This physiological definition of the boundary and loadings was one of the major novelt of this project. Specifically, the clavicle and scapula bone were constrained in all six degrees of freedom, while the humerus was actively positioned and stabilised by the calculated *in-vivo* muscle loading in Chapter 4 and passively by the glenoid and the ligament structures without any prescribed artificial control. In terms of the implementation of the muscle forces in the model, the deltoid muscle forces were directly applied by concentrated forces acting on the insertion centre pointing to the origin; whereas muscle forces of the rotator cuff muscles were applied through defining one-dimensional stress state in the muscle belly portion where the one-dimension was set to be along the muscle fiber orientation to simulate the large-scale muscle contraction. In addition, a supplement muscle model was constructed to determine the magnitudes of these stress states.

Finally, a preliminary simulation was performed to pre-test the model before the main simulation and excluded the potential errors from the rigid definition of the bone structures. Then, model verification was conducted with a mesh size sensitivity study. To perform the verification independent of the validation, instead of scapular plane abduction, a set of muscle forces in the neutral position of frontal plane abduction were selected based on literature. With denser mesh, the model did not yield significantly accurate results, however, computational time increased dramatically. The model with original mesh was verified.

To sum up, a large-scale subject-specific FE model of the human shoulder complex with all detailed representation of all the major bones, muscles, tendons, ligaments, and cartilages etc. had been successfully constructed with verified mesh sizes.

Chapter 7 Finite element simulation of shoulder scapular plane abduction

7.1 Introduction

The FE model constructed in Chapter 6 was generated based on the reconstructed geometries of MR images which were measured when the subject was in neutral shoulder joint position as described in Chapter 5. Therefore, this model was the FE model of the subject in the neutral position; we named it as Model-0. However, to perform the subject-specific quasi-static FE analysis of the shoulder scapular plane abduction measured in Chapter 3 at a sequence of humerothoracic angles namely neutral, 10, 20 and 30 degrees, the FE models of the other respective joint positions were needed. We named these models as Model-10, Model-20, and Model-30. In this chapter, Model-10, Model-20, and Model-30, were generated through reproducing the scapular abduction motion using Model-0. A detailed construction process was presented in Section 7.2. Subsequently, in Section 7.3, the newly generated models together with Model-0 were used to perform the quasi-static analysis of the scapular abduction at respective joint positions. Muscle forces at each relative instant time of the scapular abduction calculated in Chapter 4 were implemented to the respective models. Simulation results were presented followed by a material property sensitivity study of the bones, muscles and ligaments. The validation of the simulation results was conducted in Section 7.4. Finally, a summary of this chapter was conducted in Section 7.5.

7.2 Further construction of the FE models and the scapular abduction simulation

7.2.1 Construction of the FE models at 10, 20 and 30 degrees scapular abduction

As discussed, the FE model in neutral shoulder position had been constructed in the Chapter 6 which was named as Model-0. The construction of the FE models in other abduction angles namely Model-10, Model-20, and Model-30, were generated through reproducing the scapular abduction motion using Model-0. This construction process was completed in three steps. The first step was performed to obtain the deformed geometries of the soft tissues by reproducing the scapular abduction to respective joint angles in Model-0. Subsequently, in the next step, the obtained deformed geometries (in orphan mesh formation) were extracted from the results of the previous simulation results to construct the models by the same definitions as Model-0 including material properties, interactions and analysis control etc. Finally, the respectively calculated muscle forces at each relative instant of the scapular abduction from Chapter 4 were implemented to respective models for each model. For the accurate implementation of the muscle forces in each joint angle, supplement muscle models of each model were constructed.

In the first step, Model-0 was revised in the boundary and loading conditions definitions to perform this motion. Local coordinate for the humerus bone was defined first. The humeral head spherical centre (reference point of the humerus) was defined as the origin; the line through the origin and pointing to the glenoid middle (reference point of the scapular) was defined as the X-axis. The X-Y plane was defined by selecting the glenoid top point. The Z-axis was subsequently generated as normal to the X-Y plane through the origin. (See Figure 7-1) The X-Y plane was considered as the scapular plane. Therefore the rotation of the humerus in the scapular plane abduction was defined by the rotation of the humerus bone around the Z-axis with the value of -0.1744, -0.3488 and -0.5232 in radians for Model-10, 20 and 30 respectively.

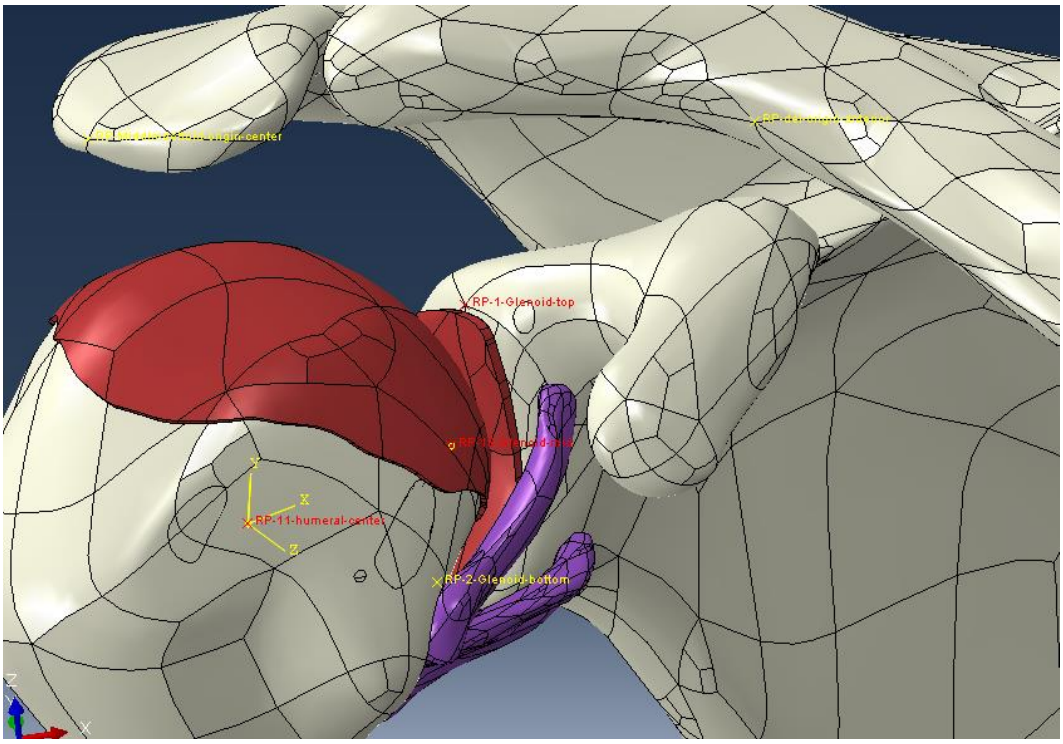

Figure 7-1 Local coordinate definition of the humeral head

However, the geometry of the humeral head was actually a spherical-like shape. The first several simulations results in enormously large bone-on-bone force which prevented the simulation from converging i.e. the bones were stuck with each other. Therefore, a translational displacement was added to the humeral centre in the –X direction to release this influence. The magnitude of this displacement was determined through testing. Multiple simulations were conducted with a sequence of displacement magnitude when the output bone-on-bone force was monitored. The desired displacement was defined by the bone-on-bone force just reaching 0, i.e. the joint cartilages just left contact. The abduction simulation for Model-30 was presented for example. Four simulations using the displacement magnitude of -1mm, -2mm, -3mm and -4mm were performed in which simulation in -1mm could not converge due to large bone-on-bone force. The bone-on-bone forces for simulations in -2mm, -3mm and -4mm were 1177N, 0, and 0. It can be found that the cartilages left contact between -2mm and -3mm. Subsequently, more simulations were conducted with the refined displacement range set to be -2.5mm, -2.75mm and -3mm. the bone-on-bone results were found to be 150N, 4N and 0. In this way, the optimal displacement magnitude for the scapula abduction simulation was determined as -2.8mm. Similarly, some of the abnormally deformed soft tissues were corrected. The results can be found in Figure 7-2. The results (equilibrium condition) was considered as the geometrical model of the subject in 30 degrees scapular abduction which would be further used to construct the FE model namely Model-30. Similarly, the motion reproducing simulations for 10 and 20 degrees scapular abduction were conducted. The results can be found in Figure 7-3 and Figure 7-4.

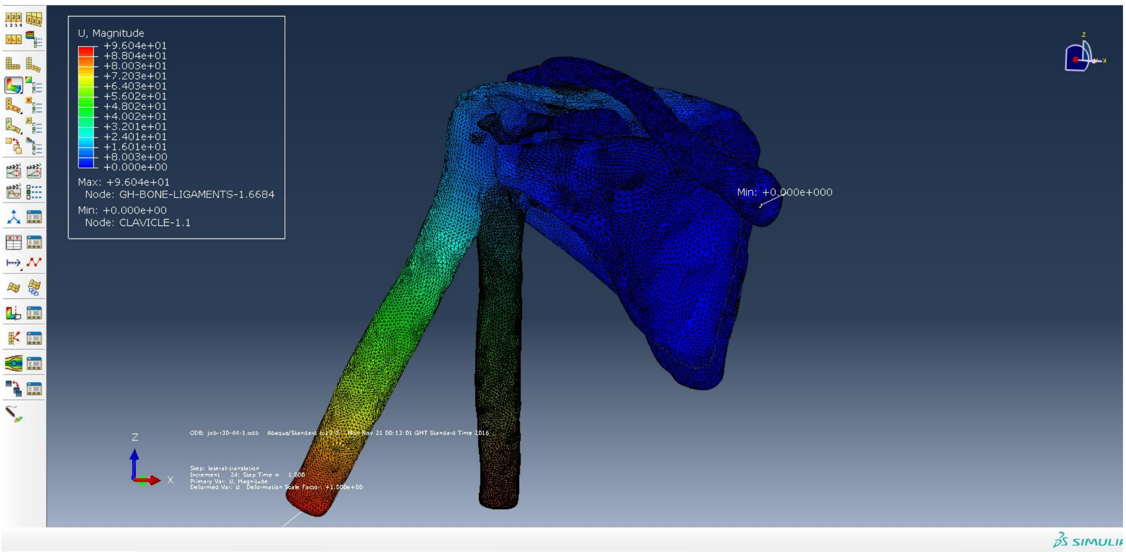

Figure 7-2 Motion reproducing of Model-0 from 0 to 30 degrees scapular abduction

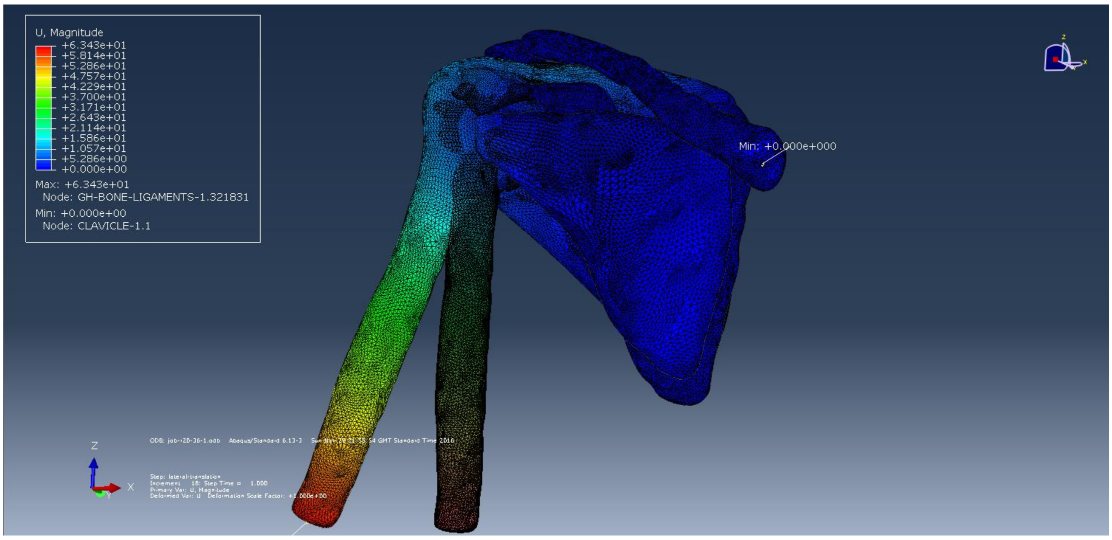

Figure 7-3 Motion reproducing of Model-0 from 0 to 20 degrees scapular abduction

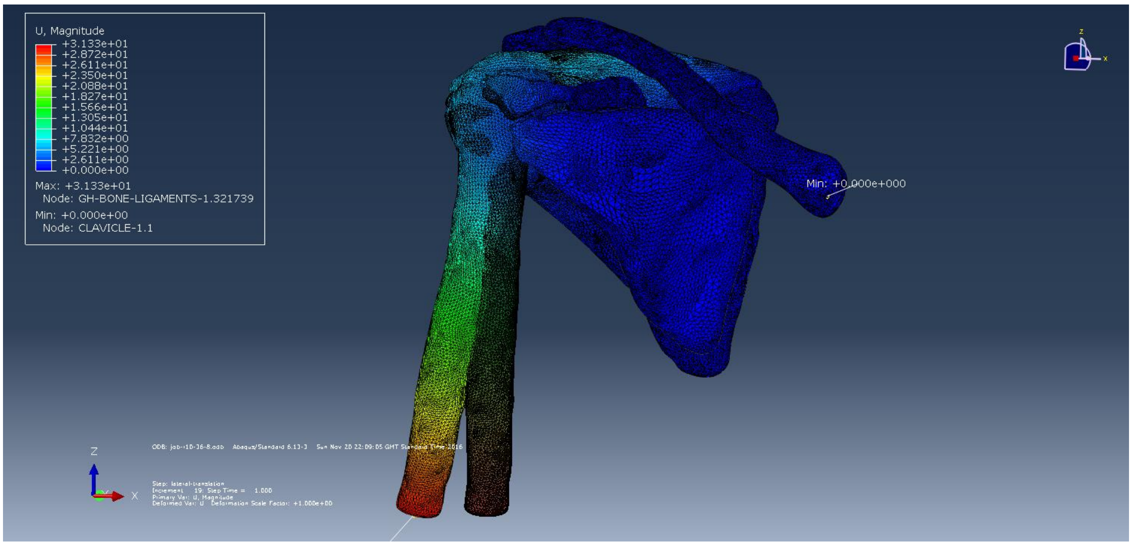

Figure 7-4 Motion reproducing of Model-0 from 0 to 10 degrees scapular abduction

In the previous step, the geometrical models of Model-10, 20 and 30 had been determined by the results of the reproduced scapular abduction. In the second step, these results were re-imported into Abaqus as orphan meshed geometries. Their relative positions in the results were carefully preserved. Other than muscle loadings magnitudes, all of the FE definitions including material properties assigning, interaction definitions, boundary conditions and analysis controls etc. were implemented to construct Model-10, 20 and 30 consistent with Model-0. All three models were successfully construed. Figure 7-5 illustrated Model-30 as an example.

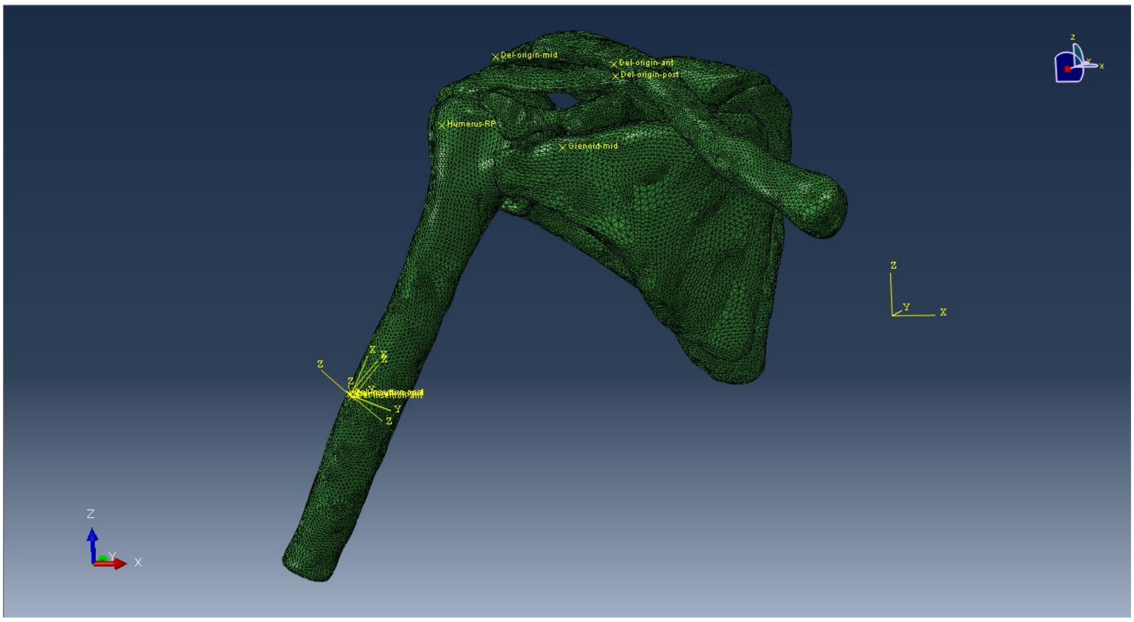

Figure 7-5 Constructed FE model at 30 degrees scapular abduction

In the final step, supplement muscle models were constructed based on the same reproduced deformed muscle geometries as above. Similarly, these models were defined by the same methods as the supplement muscle model of Model-0. Figure 7-6 illustrated the supplement muscle model of Model-30 as an example.

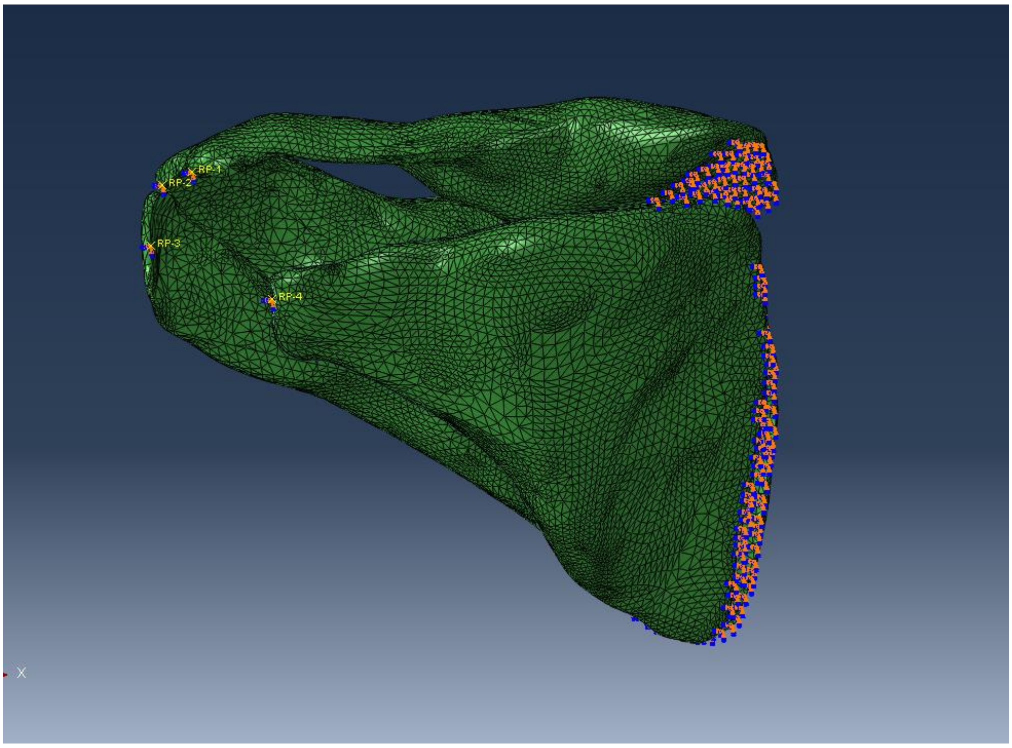

Figure 7-6 Supplement muscle model for Model-30

7.2.2 Simulation of the scapular abduction

Together with Model-0, the above constructed FE models namely, Model-10, 20 and 30 were used for the simulation of the scapular plane abduction. Firstly, physiological subject-specific muscle forces for each joint position were obtained from Table 4-1 in Chapter 4. The magnitude of the one-dimensional stress state for the rotator cuff muscles was determined via testing in each supplement muscle model using the same method as demonstrated in Chapter 6. Results of the one-dimensional stress states can be found in

Table **7-1**.

Table 7-1 One-dimensional stress states for rotator cuff muscle forces for Model-0 to 30

Model-0						
	σ_{11}	σ_{22}	σ_{33}	σ_{12}	σ_{13}	σ_{23}
$\mathbf{T_{Gsub0}}$	0.02617	0.08646	0.01700	0.04756	-0.02109	-0.03833
$\mathbf{T_{Gsup0}}$	0.13719	0.09621	0.00003	0.11488	-0.00203	-0.00170
$\mathbf{T_{Ginf0}}$	0.15721	0.16731	0.07043	0.16218	-0.10522	-0.10855
$\mathbf{T_{Gter0}}$	0.01346	0.01370	0.00994	0.01358	-0.01157	-0.01167
Model-10						
	σ_{11}	σ_{22}	σ_{33}	σ_{12}	σ_{13}	σ_{23}
$\mathbf{T_{Gsub10}}$	0.03864	0.12767	0.02510	0.07023	-0.03114	-0.05660
$\mathbf{T_{Gsup10}}$	0.21235	0.14892	0.00005	0.17783	-0.00314	-0.00263
$\mathbf{T_{Ginf10}}$	0.30249	0.32193	0.13551	0.31206	-0.20246	-0.20887
$\mathbf{T_{Gter10}}$	0.00773	0.00787	0.00571	0.00780	-0.00665	-0.00670
Model-20						
	σ_{11}	σ_{22}	σ_{33}	σ_{12}	σ_{13}	σ_{23}
$\mathbf{T_{Gsub20}}$	0.04682	0.15468	0.03041	0.08510	-0.03773	-0.06858
$\mathbf{T_{Gsup20}}$	0.22678	0.15905	0.00005	0.18992	-0.00336	-0.00281
$\mathbf{T_{Ginf20}}$	0.47608	0.50667	0.21327	0.49114	-0.31864	-0.32872
$\mathbf{T_{Gter20}}$	0.00775	0.00789	0.00572	0.00782	-0.00666	-0.00672
Model-30						

	σ_{11}	σ_{22}	σ_{33}	σ_{12}	σ_{13}	σ_{23}
$\mathbf{T_{Gsub30}}$	0.05685	0.18782	0.03692	0.10333	-0.04581	-0.08327
$\mathbf{T_{Gsup30}}$	0.25231	0.17695	0.00006	0.21130	-0.00373	-0.00313
$\mathbf{T_{Ginf30}}$	0.76219	0.81118	0.34145	0.78630	-0.51015	-0.52628
$\mathbf{T_{Gter30}}$	0.01199	0.01220	0.00885	0.01210	-0.01030	-0.01039

Subsequently, the determined one-dimensional stress states were implemented in relative FE models for the *in-vivo* subject-specific scapular plane abduction quasi-static simulations. All models converged well. Results can be found in the next section.

7.3 Simulation results and analysis

7.3.1 Results

The overview of the Von Mises stress results of the *in-vivo* subject-specific scapular plane abduction quasi-static simulations in joint position 0, 10^o, 20^o and 30^o can be found in Figure 7-7 to Figure 7-10, respectively. In the anterior view (a) of each of the four figures, relative high stresses in subscapularis tendon on the insertion site were found increasing in both magnitude and regions. The same trend was found in the rest of the rotator cuff tendons in view (b), (c) and (d). The maximum stresses in each tendon were found in the contact surface or some of the sharp corners of the structure due to stress concentration. Figure 7-11 illustrated penetrated view of the Von Mises stress distribution inside the glenohumeral joint in joint position 30^o to show the relative position of the joint contact during the movement of the arm. A detailed contact pressure distribution on the glenoid cartilage in each of the joint positions can be found in Figure 7-12. As a result, the bone-on-bone forces and glenohumeral contact area for each joint position can be found in Table 7-2. The area in contact and the peak pressure on the cartilage as well as the magnitude of the bone-on-bone forces can be found to increase monotonically. The magnitude of the bone-on-bone in joint position 0, 10^o, 20^o and 30^o were found to be 8.18N, 91.45N, 146.14 and 408N respectively. The contact area increased from 7.6mm^2 to 88.04mm^2; while the peak pressure was found to increase from 1.45MPa to 7.67MPa (the maximum values in the legends of Figure 7-12) Interestingly, the location of joint contact areas in joint position 0 and 10^o were found approximately in the centre of the cartilage; while it moved posteriorly slightly in joint position 20^{o} and more obviously in the joint position 30^{o}. Discussion and validation of these results would be conducted after the material sensitivity study in the next section.

Table 7-2 Bone-on-bone contact force and total area in contact in the glenohumeral cartilages contact

Scapular abduction angle (degrees)	FE model	Bone-on-bone force (N)	Area in contact (mm^2)
0 (neutral)	Model-0	8.18	7.6
10	Model-10	91.45	31.89
20	Model-20	146.14	46.13
30	Model-30	408	88.04

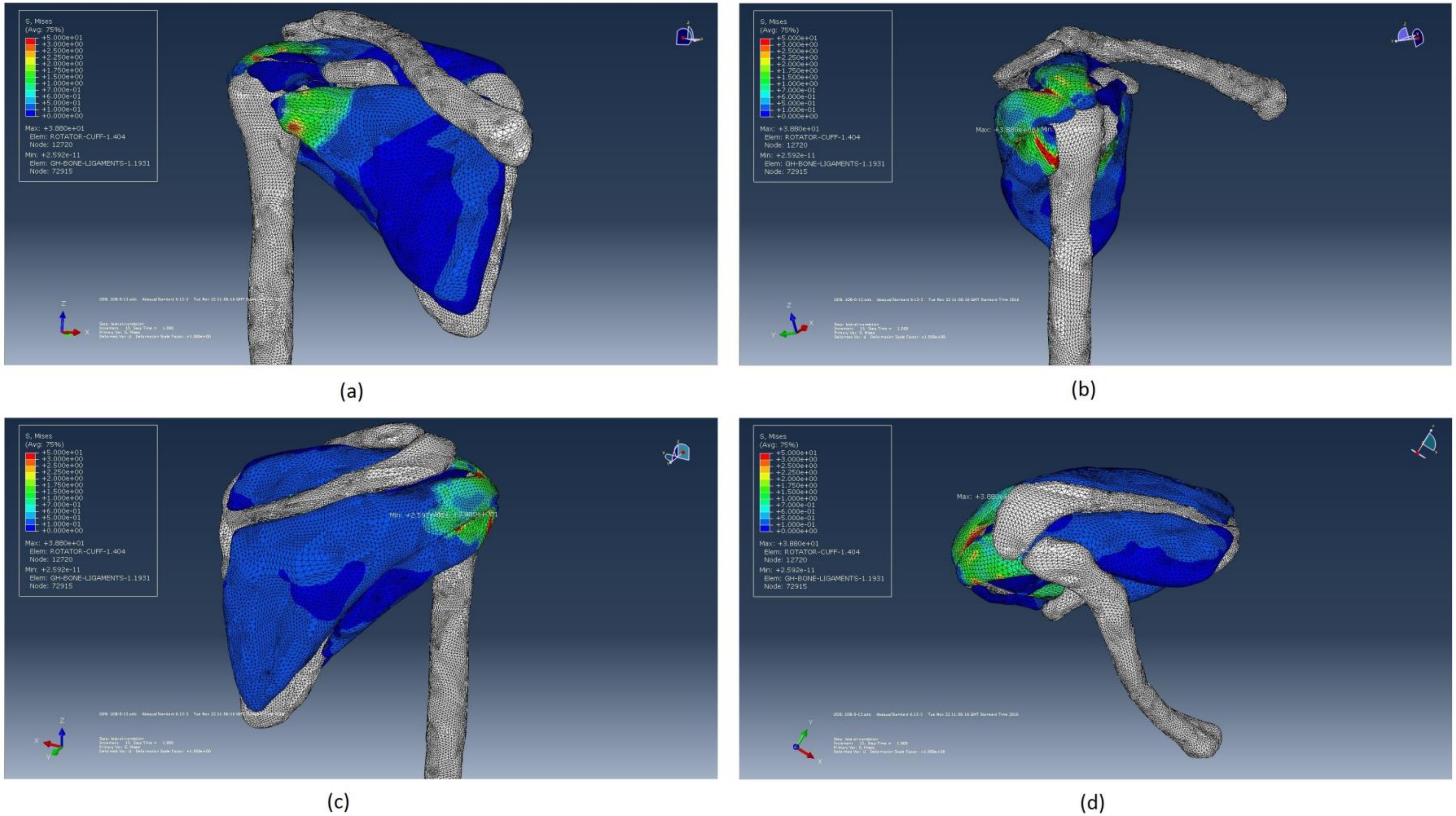

Figure 7-7 Overview of the results of the Von Mises stress distribution of the FE simulation in 0 degrees (neutral position) of scapular abduction. (a) posterior view; (b) sagittal oblique view; (c) posterior view; (d) superior view

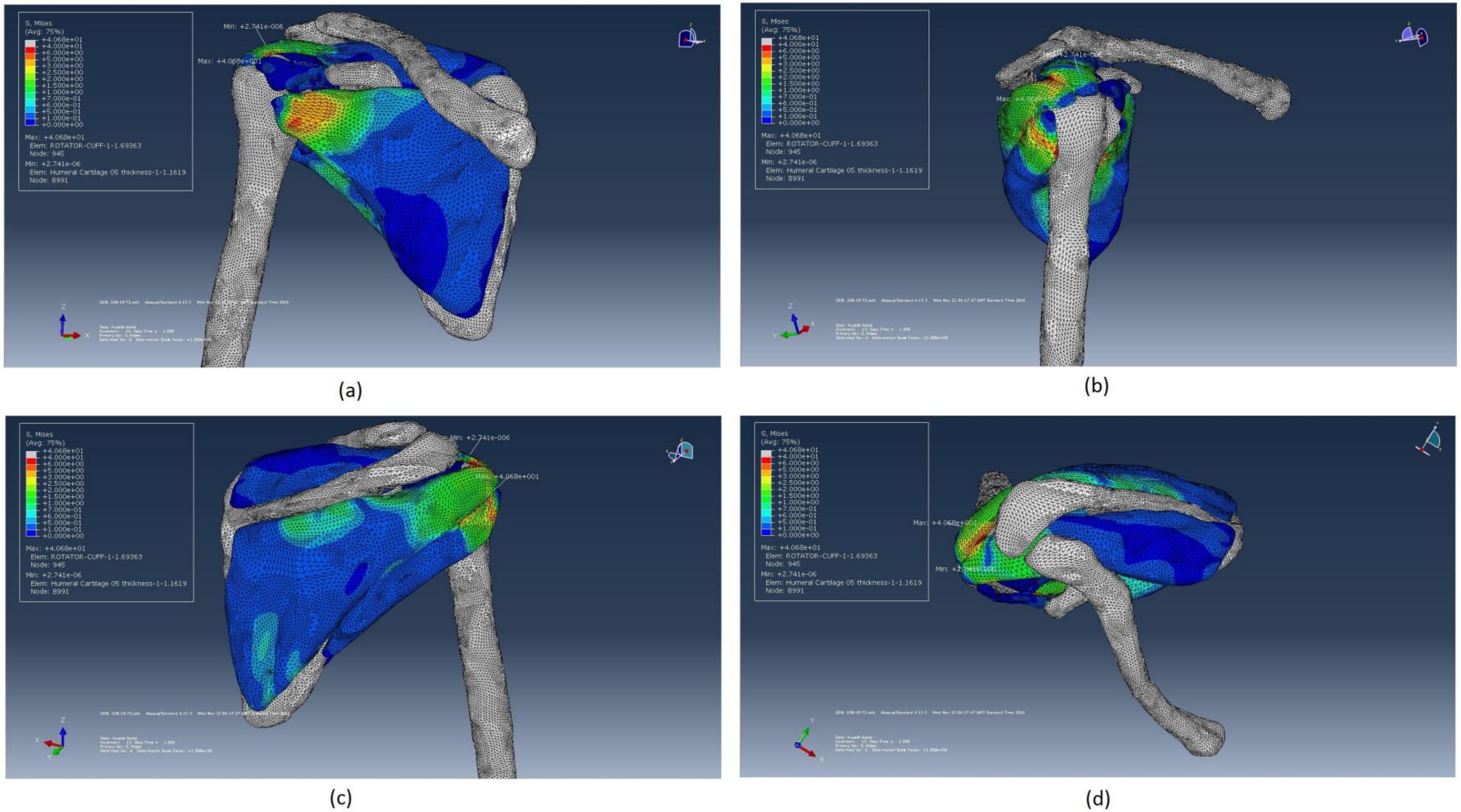

Figure 7-8 Overview of the results of the Von Mises stress distribution of the FE simulation in 10 degrees scapular abduction. (a) posterior view; (b) sagittal oblique view; (c) posterior view; (d) superior view

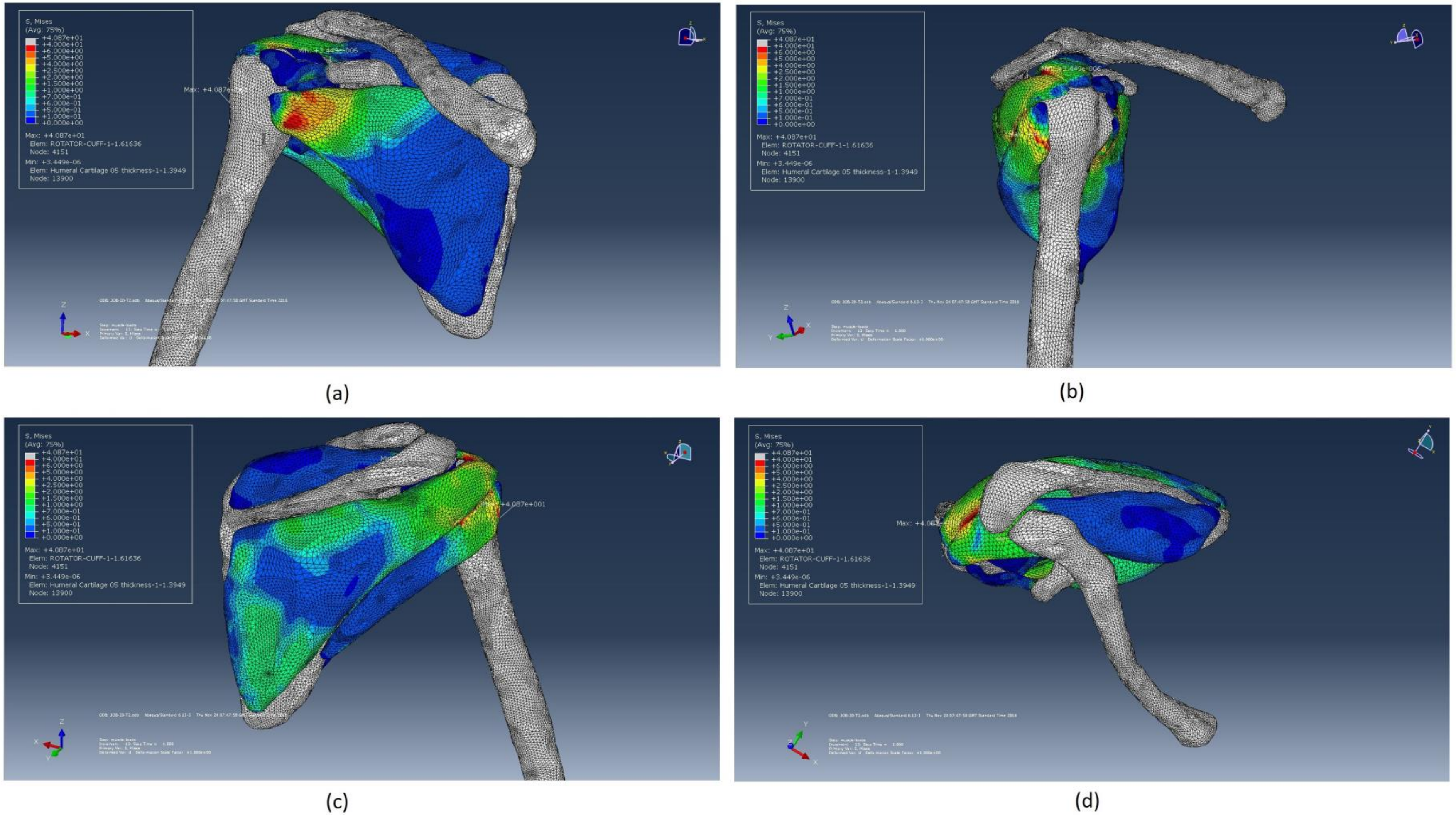

Figure 7-9 Overview of the results of the Von Mises stress distribution of the FE simulation in 20 degrees scapular abduction. (a) posterior view; (b) sagittal oblique view; (c) posterior view; (d) superior view

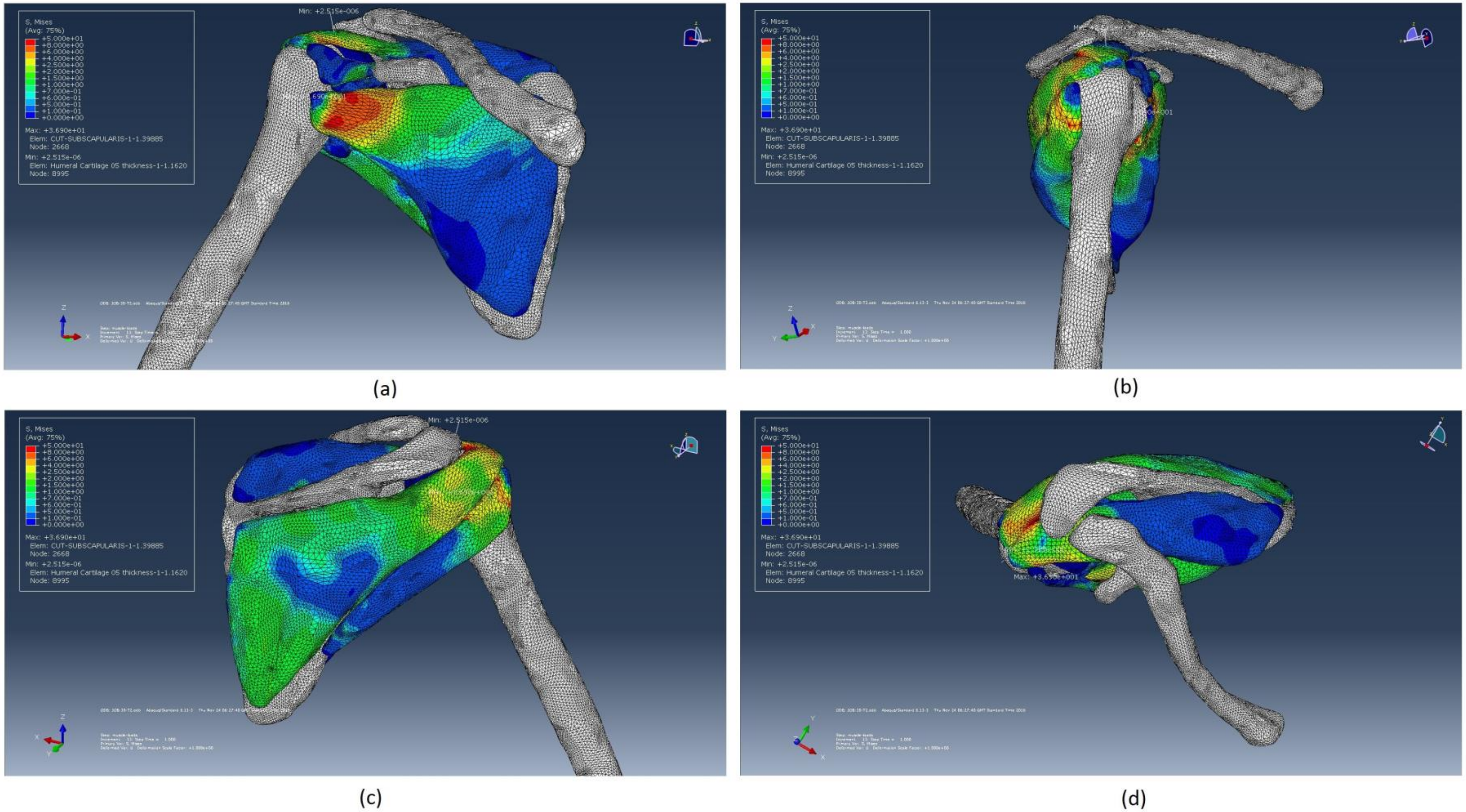

Figure 7-10 Overview of the results of the Von Mises stress distribution of the FE simulation in 30 degrees scapular abduction. (a) posterior view; (b) sagittal oblique view; (c) posterior view; (d) superior view

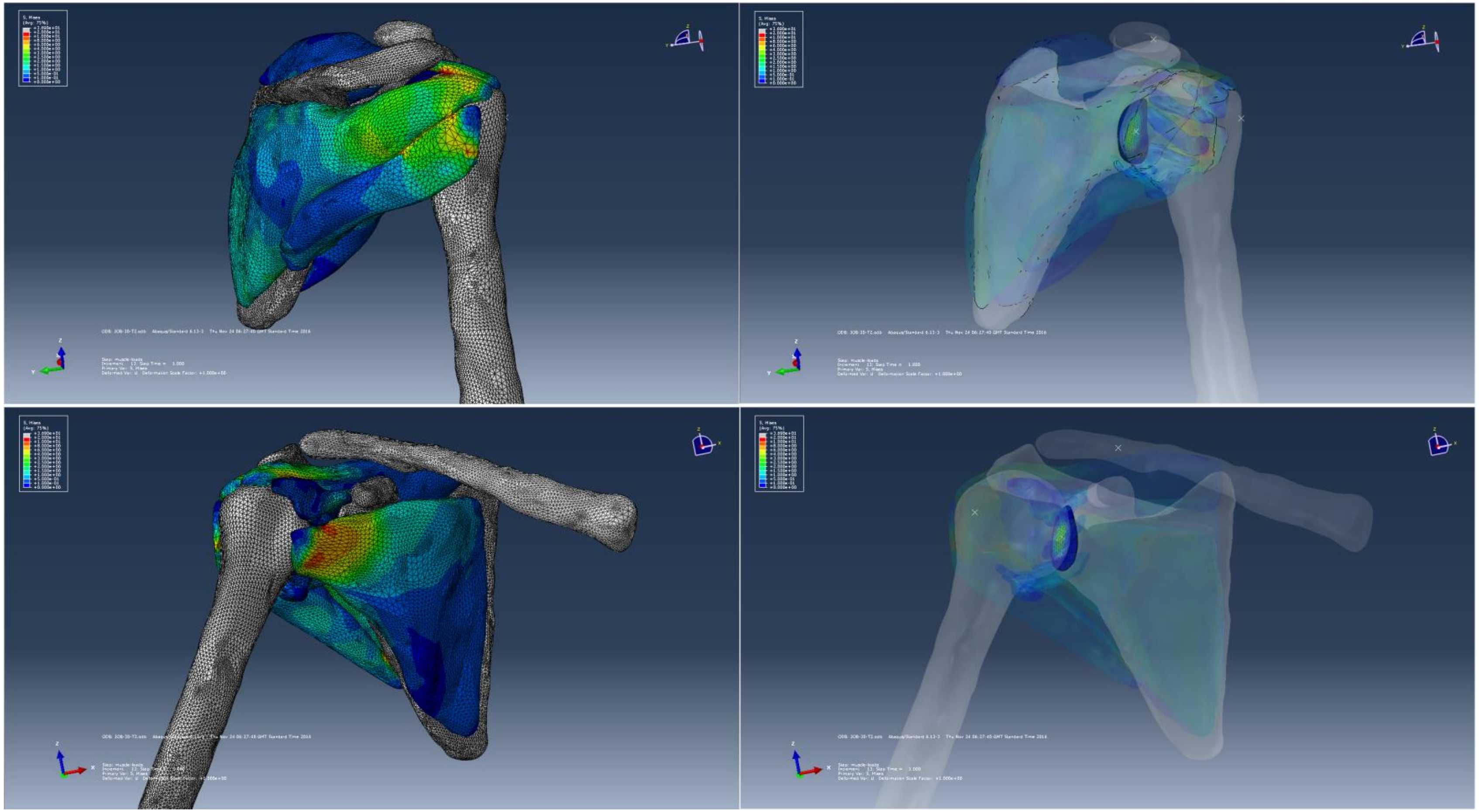

Figure 7-11 The exterior and respective penetrated view of the Von Mises stress distribution of the ligaments and glenoid cartilage inside the glenohumeral joint in 30 degrees scapular abduction

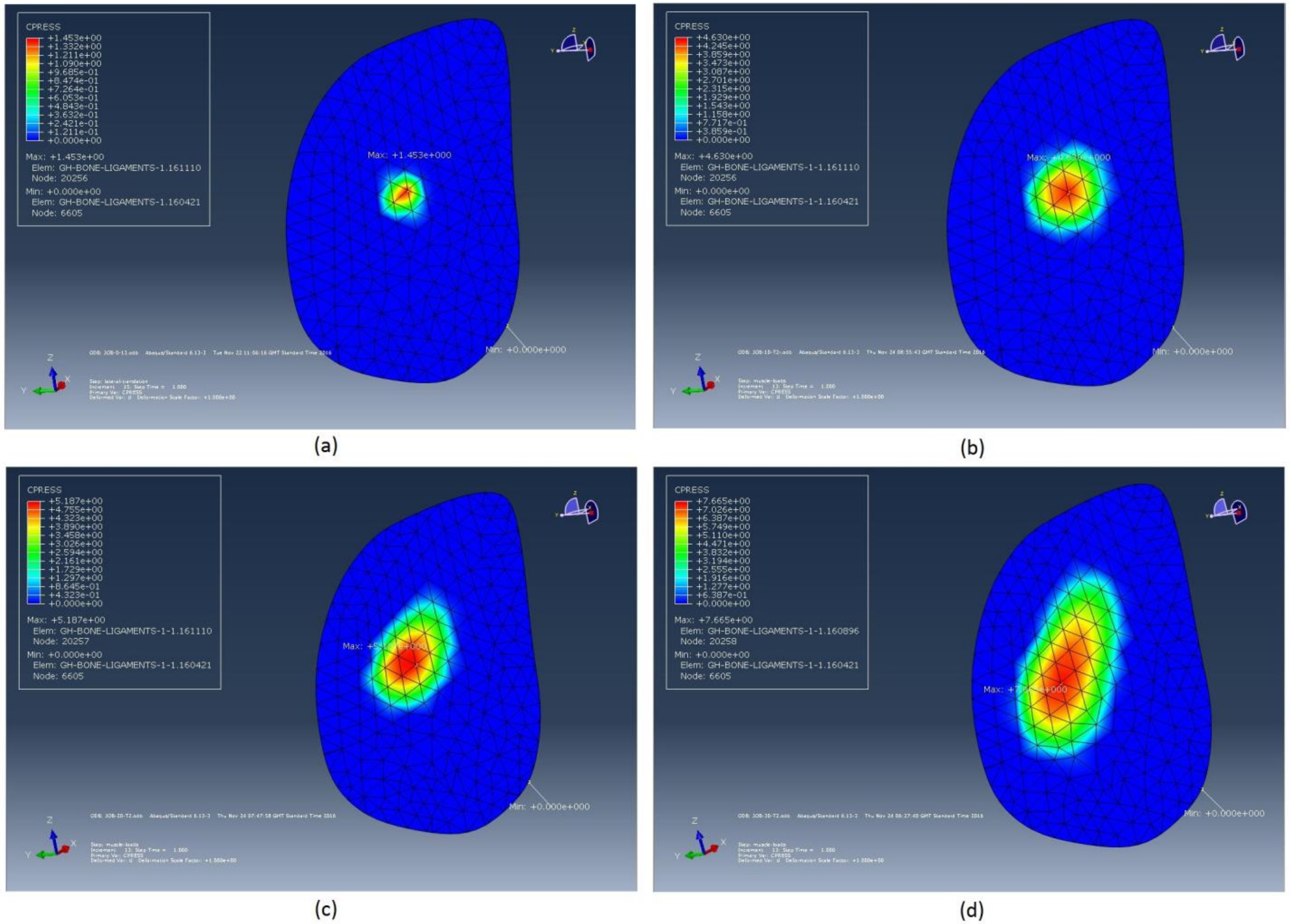

Figure 7-12 The contract pressure distribution on the glenoid cartilage in (a) 0 (neutral), (b) 10, (c) 20, and (d) 30 degrees scapular abduction

7.3.2 Material property sensitivity study of the soft tissues

The sensitivity study of material property definitions of the muscles and ligaments was conducted on Model-30. The Young's moduli of the values used in material definitions of the muscles and ligaments were tested with varying ±5%, ±10% and ±20%. While keeping all other FE definitions unchanged, a total of 6 models with new material definitions was generated and submitted for analysis. All of these simulations converged well same as the original model. Glenohumeral bone-on-bone force and peak stress was monitored in their results. The results and differences compared to original Model-30 can be found in Table 7-3. The simulation results of the GH bone-on-bone contact force and the peak stress on the glenoid by FE models showed negative linear response to the variation of elastic modulus of the respective soft tissues, i.e., the increase of the elastic modulus caused both of the two results to decrease and vice versa. Specifically, the increase of the muscle's elastic modulus by 5%, 10% and 20% caused the bone-on-bone force and peak stress to decrease by 2.3%, 4.52%, 8.66% and 2.02%, 4.11%, 7.80%, respectively; whereas the decrease of the muscle's elastic modulus by 5%, 10% and 20% caused the bone-on-bone force and peak stress to increase by 2.33%, 4.70%, 9.59% and 1.83%, 3.24%, 8.47% respectively. Similarly patterns were found in ligaments but relatively small. The maximum variations (0.48%) were found when the Young's moduli of the ligaments increased 10%.

It can be found that the model was not sensitive to the material property definition of the ligaments (maximum variation -0.48% in peak stress when increase 20% of ligament young's property). Although relatively larger sensitivity was shown on the muscle material property definitions, the magnitude still remained in a relatively small range which was around 1:2 i.e. where 1% change of the results requires the material property to change 2%. In addition, the results of the bone-on-bone force and peak stress on the glenoid cartilages were in a linear response to the variation of Young's modulus of the muscle. In the author's opinion, this was an accurate reflection of the FE model. Considering that Model-30 was constructed when the glenohumeral cartilages were in a small amount of clearance, i.e., not in contact in the initial condition. Then, muscle forces were implemented to the model during simulation when the humerus was displaced and stabilised. As a result, the bone-on-bone force and peak stress on the glenoid were generated due to the displacement of the humerus relative to the glenoid. Noted that the muscles were firmly attached to the humerus, hence this displacement also equalled the deformation of the muscles in the fibre muscle fibre direction. Therefore, the variation of Young's modulus of the muscle could cause the above linear influences on the results.

Table 7-3 The results of bone-on-bone force and peak stress on glenoid cartilage with respect to the variation of Young's modulus of muscle/ligaments material property definition

	Bone-on-bone force	**Peak stress on glenoid cartilage**	**Differences compared to original**	
Original Model-30: Muscle E=168 v=0.479 Ligament E=10.1 v=0.4	408.70	3.768	Bone-on-bone force	Peak stress on glenoid
Muscle E=134.4 (-20%)	447.90	4.087	9.59%	8.47%
Muscle E=151.2 (-10%)	427.92	3.890	4.70%	3.24%
Muscle E=159.6 (-5%)	418.23	3.837	2.33%	1.83%
Muscle E=176.4 (5%)	399.30	3.692	-2.30%	-2.02%
Muscle E=184.8 (10%)	390.23	3.613	-4.52%	-4.11%
Muscle E=201.6 (20%)	373.32	3.474	-8.66%	-7.80%
Ligament E=8.08 (-20%)	409.65	3.784	0.23%	0.42%
Ligament E= 9.09 (-10%)	409.22	3.776	0.13%	0.21%
Ligament E= 9.595 (-5%)	408.94	3.772	0.06%	0.11%
Ligament E= 10.605 (5%)	408.46	3.764	-0.06%	-0.11%
Ligament E=11.11 (10%)	408.20	3.760	-0.12%	-0.21%
Ligament E=12.12 (20%)	407.79	3.750	-0.22%	-0.48%

7.4 Validation

The results of the FE simulation of this study were mainly validated in three ways. The bone-on-bone forces in each abduction angle were validated against the *in-vivo* and *in-vitro* measurements as well as other simulation studies. The superior translation of the humeral head was validated against a recent *in-vivo* measurement. Finally, the stress distribution of the muscle tendon was compared with literature data.

7.4.1 Bone-on-bone contact forces during shoulder abduction

The bone-on-bone forces for each abduction angle was compared with a list of literature including one *in-vivo* study [153], one *in-vitro* study [138] and several simulation studies [154, 30, 6, 155, 137]. (See Figure 7-13) Good agreement of the magnitude and tendency was found.

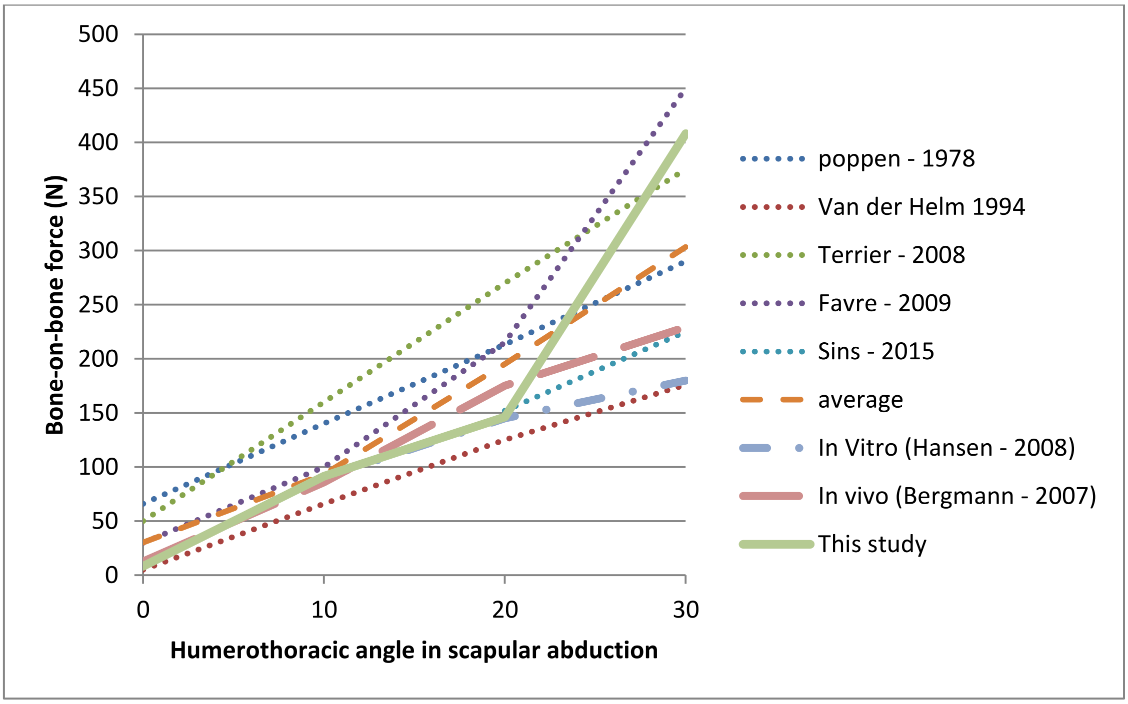

Figure 7-13 The comparison of the magnitude of the bone-on-bone contact forces in each humerothoracic angle of the scapular abduction between this study and literature data

7.4.2 Translations of humeral head relative to glenoid during shoulder abduction

The movement of the humeral head was compared to a recent kinematics study investigating the superior-anterior translation. Matsuki and colleagues reported an average of 1mm humeral superior movement was found in the shoulder scapular abduction from neutral to 30 degrees when measuring *in-vivo* movement of the shoulder of 12 subjects with fluoroscopic imaging and image registration techniques [156]. In our FE simulations, the humeral centre of this study was tracked by the node which was closest to it in the model, namely Node: GH-BONE-LIGAMENTS-1-1.46303. The coordinates of this node in neutral position is (-147.58, -20.66, 71.09); while in 30 degrees scapular abduction is (-150.79, -21.12, 73.11). The Z-axis of this model represented the superior-inferior orientation. Therefore, the coordinate change along the Z-axis 2.02mm was compared with the measurements from this previous study. (See Figure 7-14 and Table 7-4) It was found that although the magnitude of the humeral centre movement was slightly above the range of the measurement data, the general tendency and magnitude range in variation of the humeral centre movement between the two studies were in good agreement.

Table 7-4 Comparison of the humeral centre superior- anterior movement

	This study	**Matsuki et al.**	**Standard deviation**
0 (start)	0.00	0.00	1.05
30 degrees	2.02	0.77	0.98
45 degrees	N/A	1.26	1.03

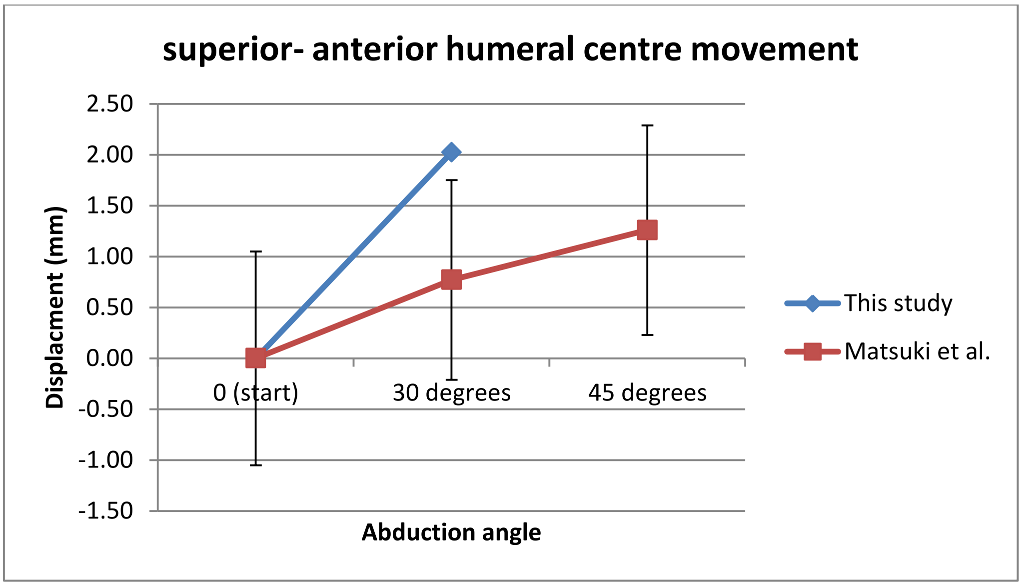

Figure 7-14 The comparison of the relative movement of the humeral centre from 0 (neutral) to 30 degrees scapular abduction between this study and literature data

7.4.3 Stress distribution during shoulder abduction

The distribution of the maximum principal stress in the supraspinatus tendon of this study was compared with previous literature results of an FE study [18]. (See Figure 7-15 and Figure 7-16). Figure 7-16 showed the results in this study in which the range of the principal stress was set to be the same as the range in literature, i.e., 0-15. The overall stress distribution was plotted well (differences in stress distribution were well distinguished) with this setting which indicated that the stress distribution of both studies was in the same range. It can be found that the anterior section of the distribution was quite similar in the articular side where the muscle inserts and wraps around the bone between the two studies. Differences were found in middle section by the supraspinatus wrapping around the humeral head where the literature study did not define this interaction. The posterior section of this study included some portions of the infraspinatus tendon which was not modelled in the literature study. Similar distribution patterns were found on the bursal-side in the posterior section (top left corner of the tendons in view (c) of both figures. However, in fact, the distribution pattern in this study was within the infraspinatus tendon rather than the supraspinatus tendon. This demonstrated that not only the results of this study was comparable to the literature but also further enhanced the investigation with the benefit of the anatomically accurate geometrical representation.

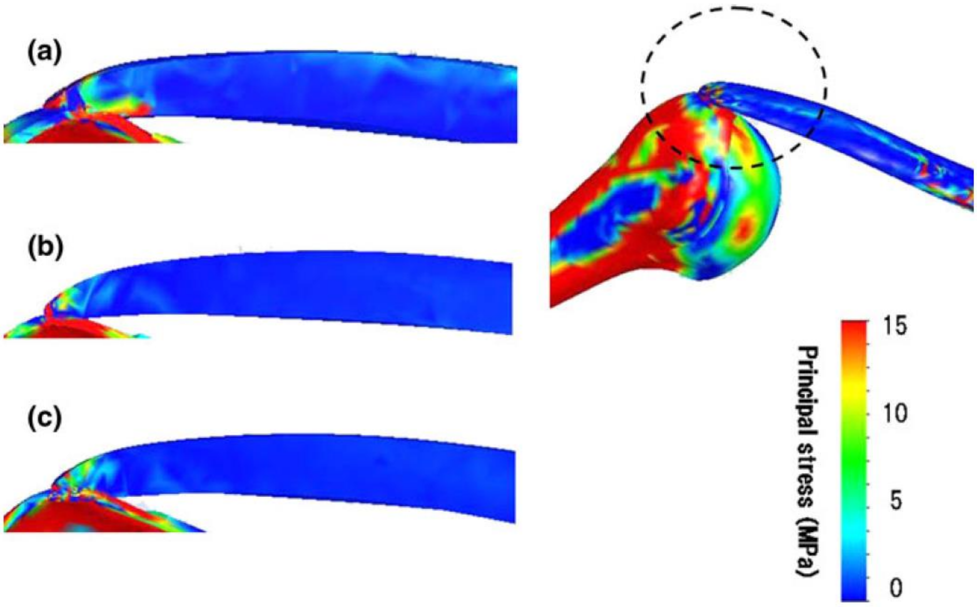

Figure 7-15 Distribution of the tensile stress in the supraspinatus tendon at 45^o abduction in literature. Slice view principal stress maximum in the sagittal plane through the (a) anterior, (b) middle, (c) posterior section of the supraspinatus tendon [18]

7.5 Summary

In this chapter, the constructed FE model was successfully used for the simulation of the scapular abduction. Specifically, the FE models of the other joint angles namely, 10, 20 and 30 degrees humerothoracic abduction were constructed first by reproducing the scapular abduction motion measured in Chapter 3 in the original FE model. Subsequently, the physiological muscle forces calculated in Chapter 4 was implemented via testing by the respective supplement muscle models. The quasi-static FE analysis of the shoulder complex at 0 to 30 degrees scapular abduction was conducted successfully. Material property sensitivity studies were conducted on Young’s modulus of the muscle and tendons. It was found that the bone-on-bone contact and peak stress on the glenoid cartilage were sensitive to Young’s modulus of the muscles while not to the ligament’s.

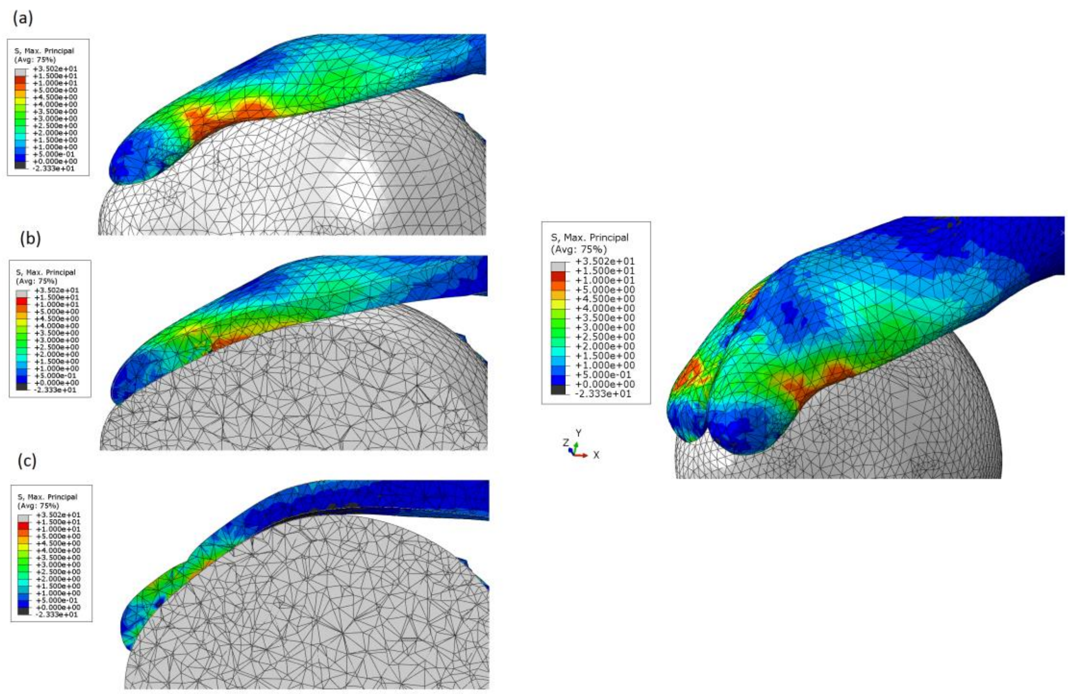

Figure 7-16 Distribution of the tensile stress in the supraspinatus tendon at 30^o abduction in this study. Slice view principal stress maximum in the sagittal plane through the (a) anterior, (b) middle, (c) posterior section of the supraspinatus tendon

The simulation results were validated against *in-vivo* measured bone-on-bone contact force and the humeral head translation relative to the glenoid during shoulder abduction as well as other simulation results in the literature. Both bone-on-bone contact force and the humeral head translation were in good agreement with the *in-vivo* measured results. In addition, the stress distribution of the supraspinatus tendon was found comparable with the literature data. Specifically, it was found that the stress patterns in the posterior section of the supraspinatus tendons were actually on the infraspinatus tendons portion.

This enhanced understanding of the stress distribution in the rotator cuff tendons was achieved by the physiological geometrical representation of this study.

To sum up, the quasi-static FE simulation of the shoulder scapular plane abduction was successfully conducted and validated in the constructed FE models of this study. These FE model would be further used for rotator cuff tear studies in the next chapter. What is more, these models would have the capability to perform numerous shoulder FE studies including but not limited to diagnosing and surgical simulation, prosthetic testing and optimisation, and rehabilitation strategies design etc.

Chapter 8 Finite element analysis of rotator cuff tears propagation

8.1 Introduction

Rotator cuff tear is a common shoulder disorder. Epidemiology studies on the cadavers had reported the incidence of rotator cuff tears to range from 5% to 39% [157, 158]. Especially, it is more common in the elderly population. The incidence of full-thickness rotator cuff tears was reported an approximately 30% prevalence among elderly people [159]. However, the true incidence of rotator cuff tears in living individuals is difficult to report due to the fact that not all rotator cuff tears are symptomatic. The rationale of the rotator cuff tears on the glenohumeral joint stability is still not very clear. Therefore, in this chapter, a biomechanical study on the rotator cuff tears was performed to investigate the influence and mechanism of the rotator cuff tears on the glenohumeral joint stability during the propagation of the tears. The propagation of the tears was defined as initialling from the anterior insertion site on the humeral head of the supraspinatus tendon and propagating posteroinferiorly until full tear on all three rotator tendons i.e. supraspinatus, infraspinatus and teres minor tendons. We hypothesise that the stability of the glenohumeral joint decreases with the increase of the size of the tears. We further hypothesise that small sizes of the rotator cuff tears do not significantly influence the joint stability based on the asymptomatic phenomenon among some rotator cuff tears patient.

In the preceding chapters, the FE model of the human shoulder complex had been successfully constructed and used to simulate the scapular abduction in a sequence of joint angles. The results of the shoulder scapular abduction simulation were validated well with the *in-vivo* and *in-vitro* studies and previous computational studies. The constructed model at 30 degrees scapular abduction, namely Model-30, was used to perform this biomechanical study of the rotator tears. Model-30 was chosen based on an assumption that the consequences of the tears to joint stability are more obvious when magnitude the muscle forces around the joint increase. This assumption was raised based on the fact that the limited range of motion is a common symptom among patients with massive rotator cuff tears, which indicates that the influence of the tears on higher joint abduction angles is more severe than those on lower abduction angles.

To perform this biomechanical study of the rotator cuff tears propagation, a series of static simulations was conducted using FE models with a sequence of increasing tears sizes while keeping all other FE definitions the same in Section 8.2. The simulation results and analysis were presented in Section 8.3. Subsequently, in Section 8.4, the glenohumeral joint stability study was conducted based on the simulation results using a novel integrative stability index quantifying the joint stability defined in this study. Finally, a discussion and conclusion were conducted in Section 8.5.

8.2 Simulation of rotator cuff tears propagation

The simulation of the rotator cuff tear propagation was conducted by performing a series of static FE simulations in Model-30 with a sequence of increasing tear sizes. Specifically, the sequence of tears was created by changing the contact surfaces in the muscle-bone bonding contacts i.e. the firm attachment between the humeral head and supraspinatus, infraspinatus and teres minor tendons. The tears were created from the anterosuperior portion of the supraspinatus insertion site and propagated posteroinferiorly continuously through infraspinatus until a full tear that involved all three rotator cuff tendons. Figure 8-1 and Figure 8-2 showed the constructed FE models with the sequence of increasing tear sizes. The area in red represented the remaining rotator cuff tendons which were defined to be consistent decreasing. Therefore, the eliminated portion represented the cuff tears in an increasing trend. For convenience, the total insertion area of all the three rotator cuff tendons was defined as a number 1 where each rotator cuff tendon insertion site is defined as 1/3. Hence, the intact condition equals tear size 0; tear size 1/6 represents half torn of the supraspinatus tendon; tear size 1/3 represents the complete torn of the supraspinatus tendon; tear size 1/2 represents half torn of the infraspinatus tendon in addition to the complete torn of the supraspinatus tendon and so on till full tear (tear size 1).

Static simulations of all the FE models with the different tear sizes were performed when all the rest of the FE definitions remained consistent with the simulation in Model-30 in the scapular abduction. The simulation already conducted in Chapter 7 was considered as the intact model that represents a healthy shoulder. All simulations converged smoothly. The results and validation can be found in the next section.

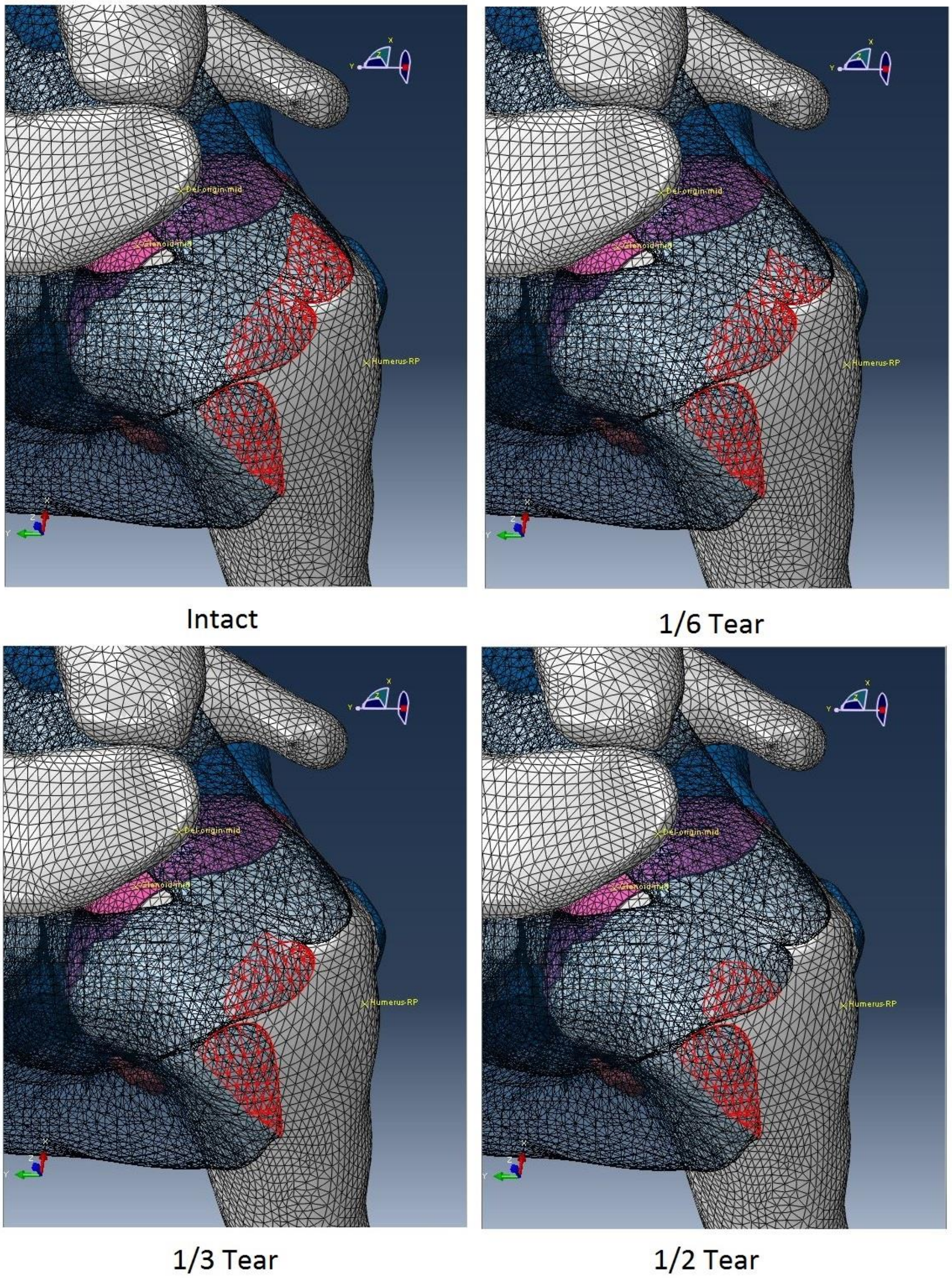

Figure 8-1 Visualisation of the FE models with rotator cuff tears of tear sizes ranging from tear size 0 (intact) to tear size 1/2. The area in red represents the remaining rotator cuff tendons

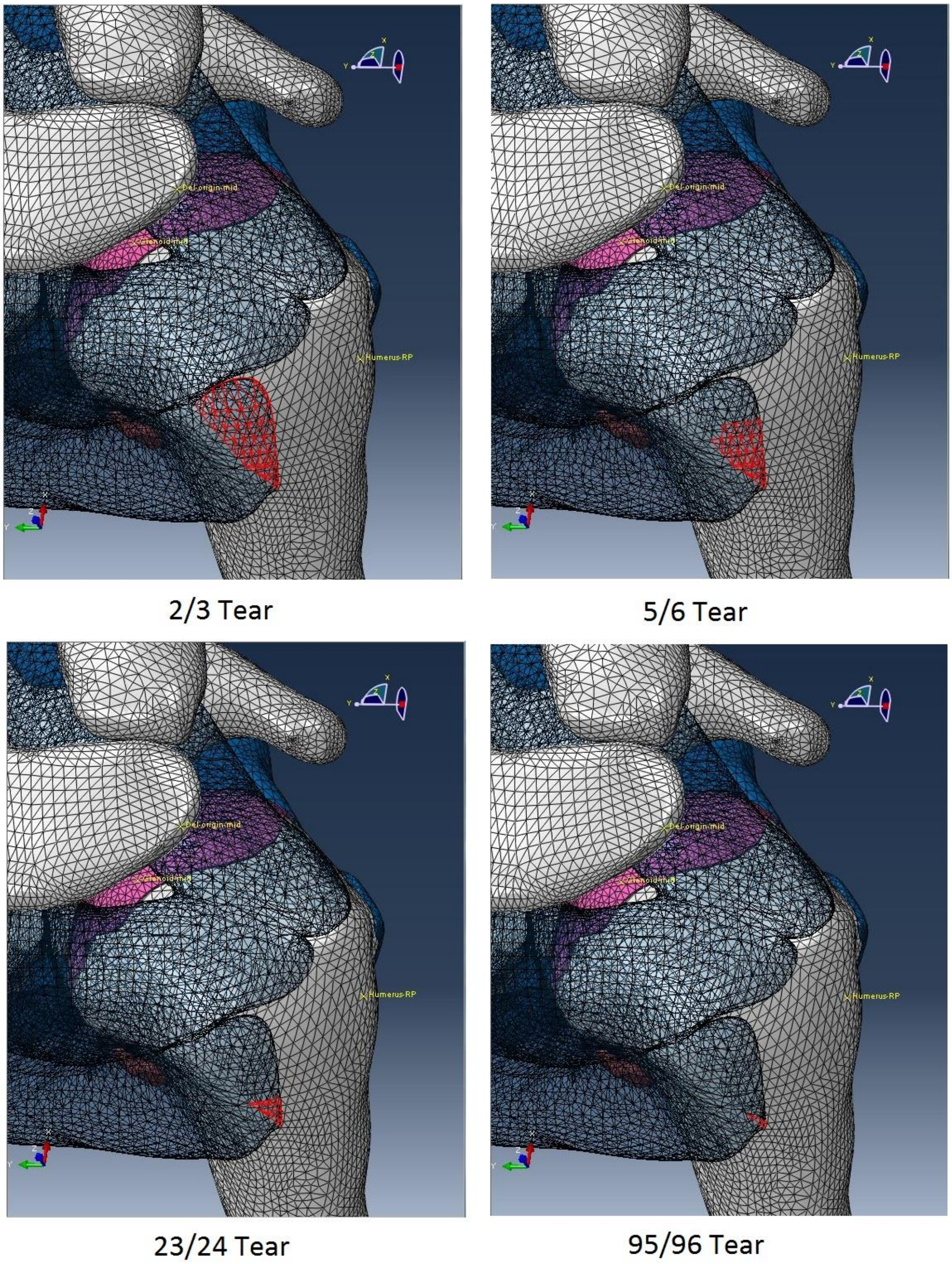

Figure 8-2 Visualisation of the FE models with rotator cuff tears of tear sizes ranging from tear size 2/3 to tear size 95/96. The area in red represents the remaining rotator cuff tendons (Full tear was the figure when no red area remains)

8.3 Results analysis

The results of the displacement/deformation and the Von Mises stress distribution in the glenoid cartilage of the simulation results of FE models of several typical tear sizes can be found from Figure 8-3 to Figure 8-9. The displacement of the humeral bone in lateral view can be found at the top in each of these figures. A continuous superior-anterior translation of the humeral head was found which resulted in the posterior movement of the humerus bone in the distal part where the maximum displacement can be found (the maximum values in the figure legends). This maximum displacement of the humeral bone was found to increase slightly in small tear cases (23.2mm to 24.8mm from intact to tear size 1/3); while it rapidly increased afterward until full tear (24.8mm to 88.8mm from tear size 1/3 to full tear). Simultaneously, the Von Mises stress distribution in the glenoid of the simulation results of each tear case with respect to contact pressure distribution can be found at the bottom in each of these figures. In addition, the detailed view of the contact pressure between the glenohumeral cartilages can be found in Figure 8-10 in the sagittal oblique view on the glenoid cartilage. Continuous superior-anterior movement of the contact pressure area were found in the glenoid cartilages. Similar patterns of small variation at the beginning until the tear size 2/3 when this movement increased rapidly afterwards. The bone-on-bone contact force and the total area in contact of each simulation were summarised in Table 8-1. F_M represents the magnitude of the bone-on-bone force; Fx, Fy and Fz are the force components in the x, y, z-axis directions of the global coordinate. Except a small increase (2.8N) of the bone-on-bone force at the first tears size (1/6), a continuous decrease trend was found for all tear cases. In addition, mild decrease was found in the bone-on-bone force in small tear cases, (408N to 402N from intact to tear size 1/2); while rapidly decrease was found thereafter until tear size 95/96 (402N to 290N) followed by a sudden drop (290N to 114N) in full tear in the end. Similar trend applied to the contact area: generally decreasing trend with a small increase (1.4 mm^2) in early tear cases, followed by rapid decrease and a sudden drop (71.1 mm^2 to 22.15 mm^2) in full tear case in the end.

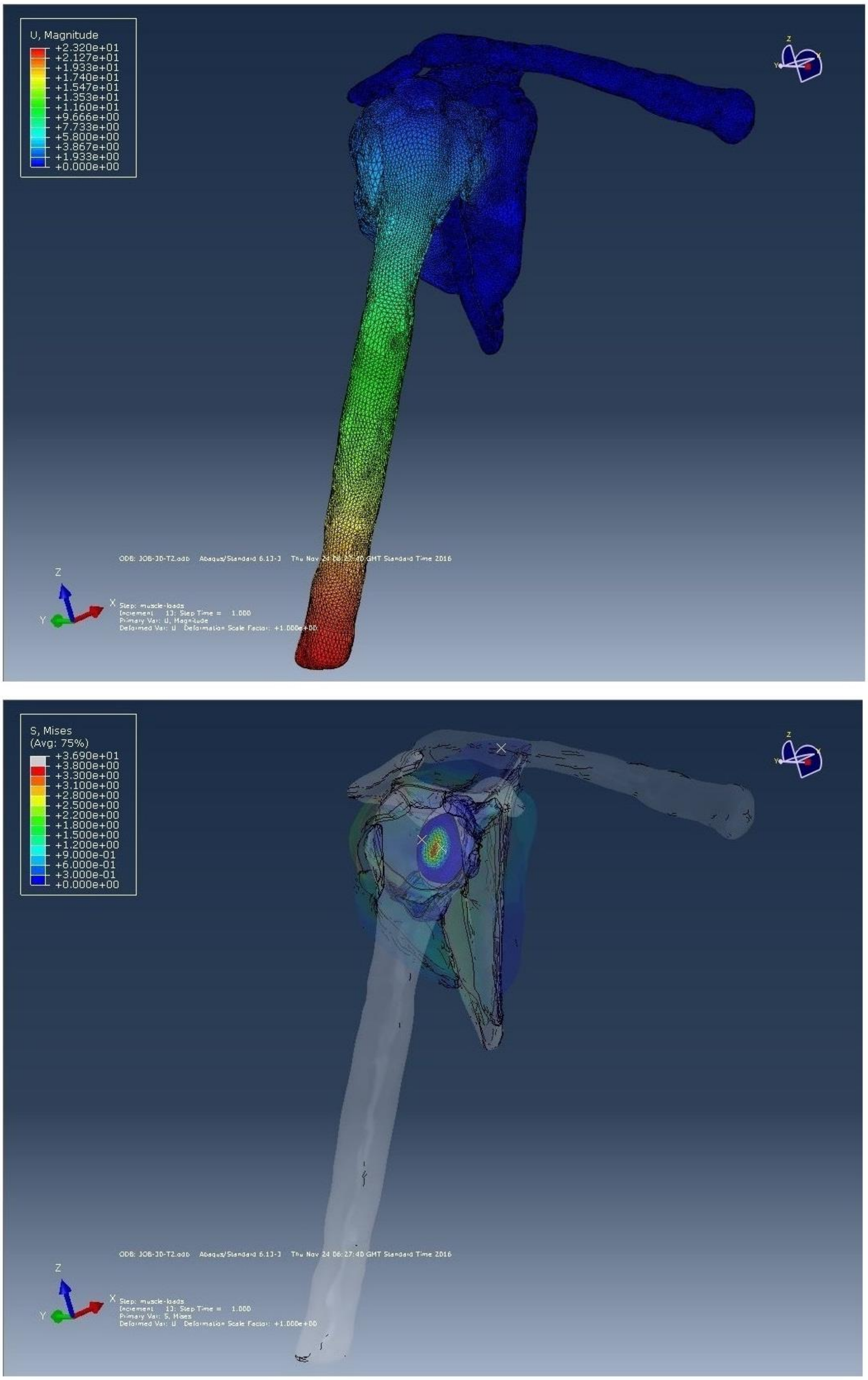

Figure 8-3 The exterior view of the deformation/displacement (top) VERSUS the penetrated view of the Von Mises stress distribution on the glenoid cartilage (bottom) of the simulation results of the FE model with tear size 0 (intact)

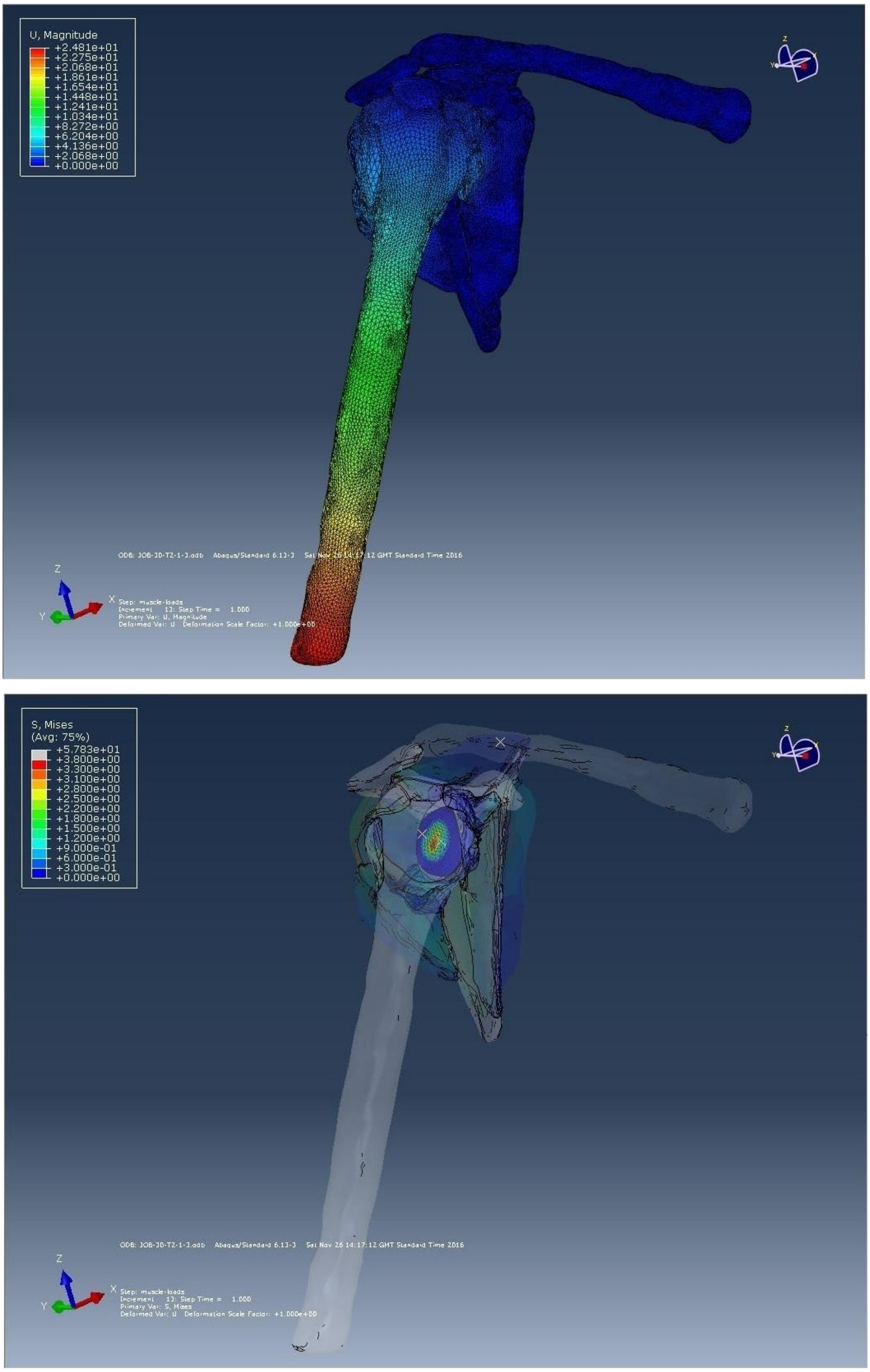

Figure 8-4 The exterior view of the deformation/displacement (top) VERSUS the penetrated view of the Von Mises stress distribution on the glenoid cartilage (bottom) of the simulation results of the FE model with tear size 1/3

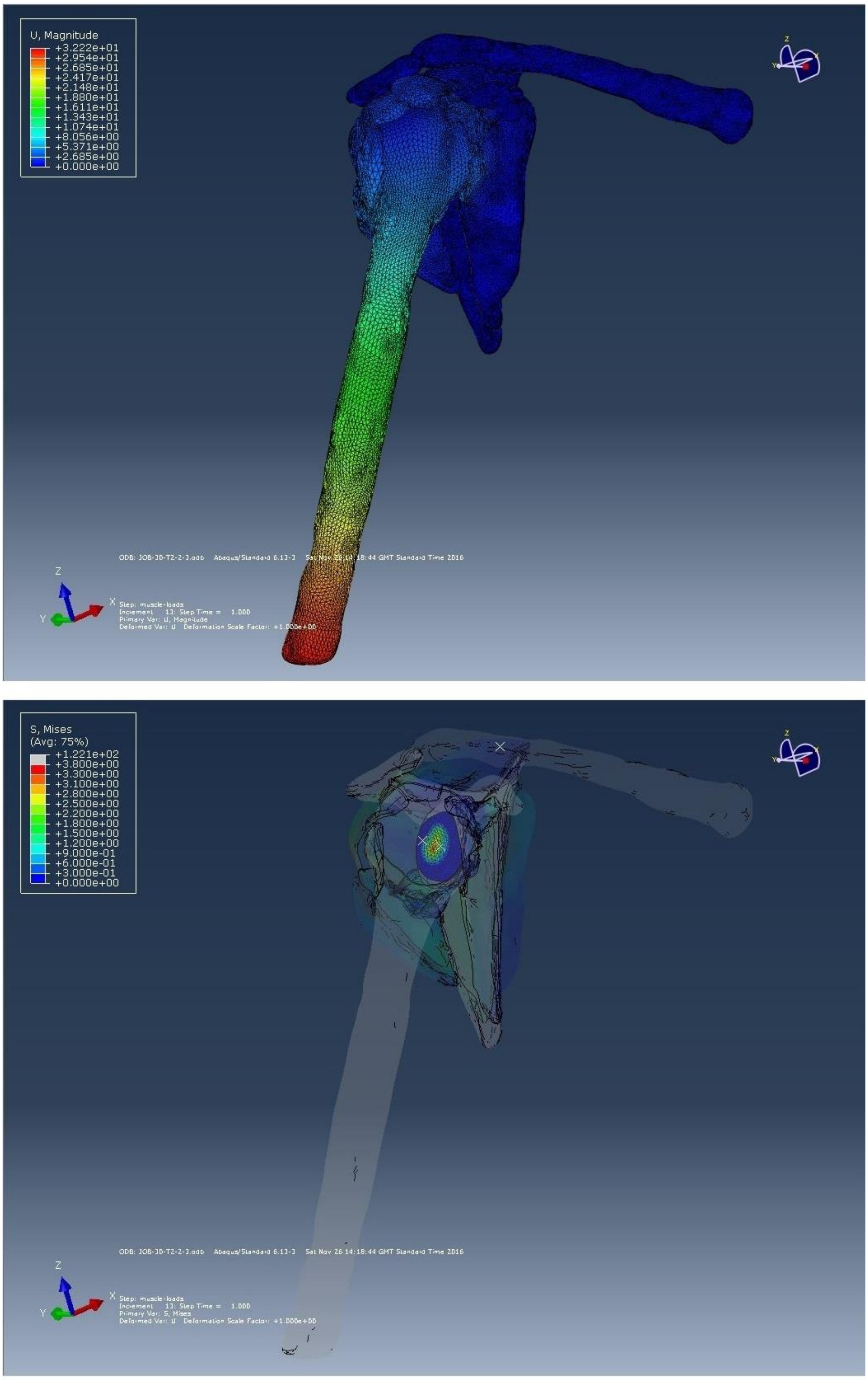

Figure 8-5 The exterior view of the deformation/displacement (top) VERSUS the penetrated view of the Von Mises stress distribution on the glenoid cartilage (bottom) of the simulation results of the FE model with tear size 2/3

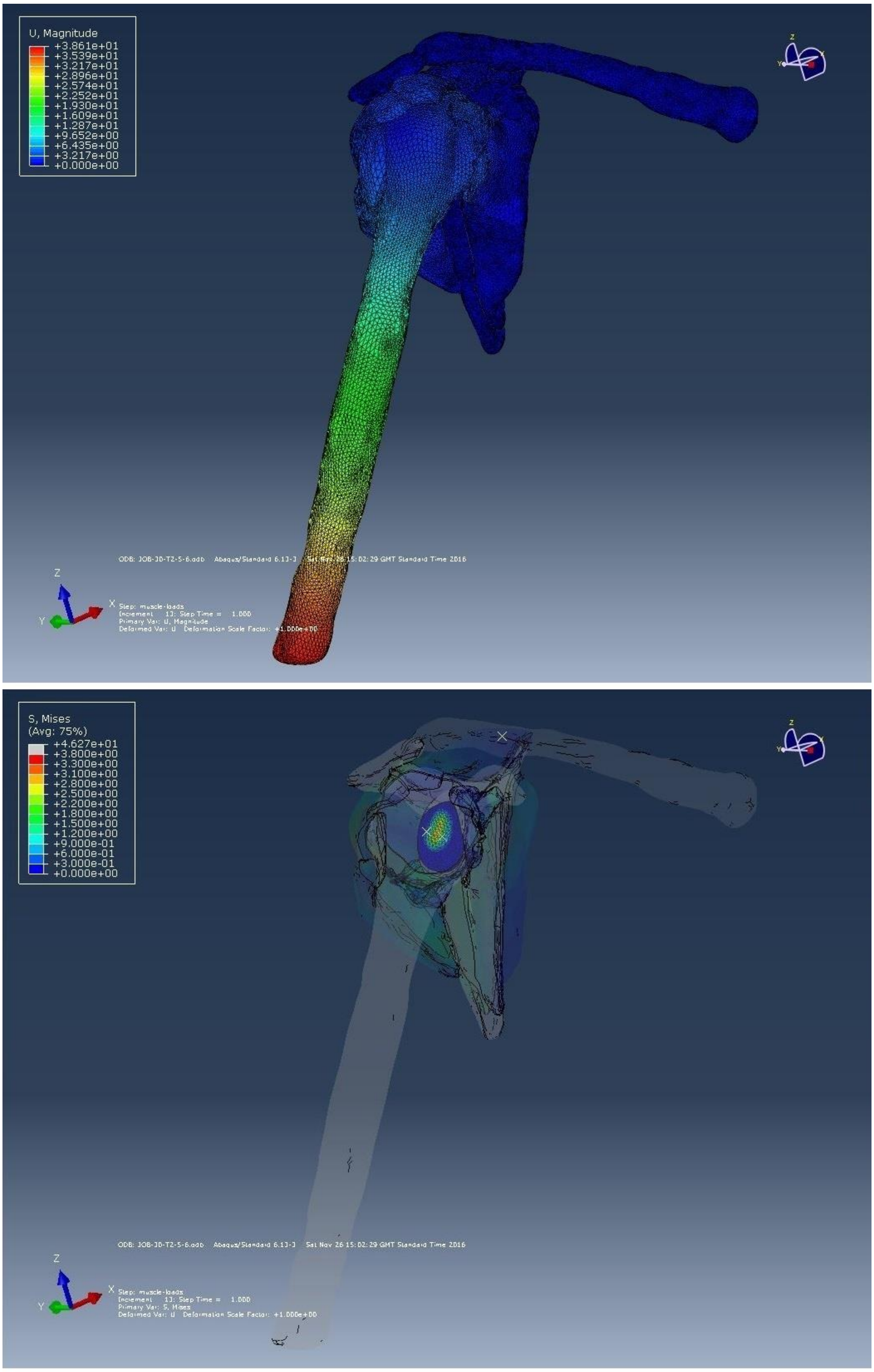

Figure 8-6 The exterior view of the deformation/displacement (top) VERSUS the penetrated view of the Von Mises stress distribution on the glenoid cartilage (bottom) of the simulation results of the FE model with tear size 5/6

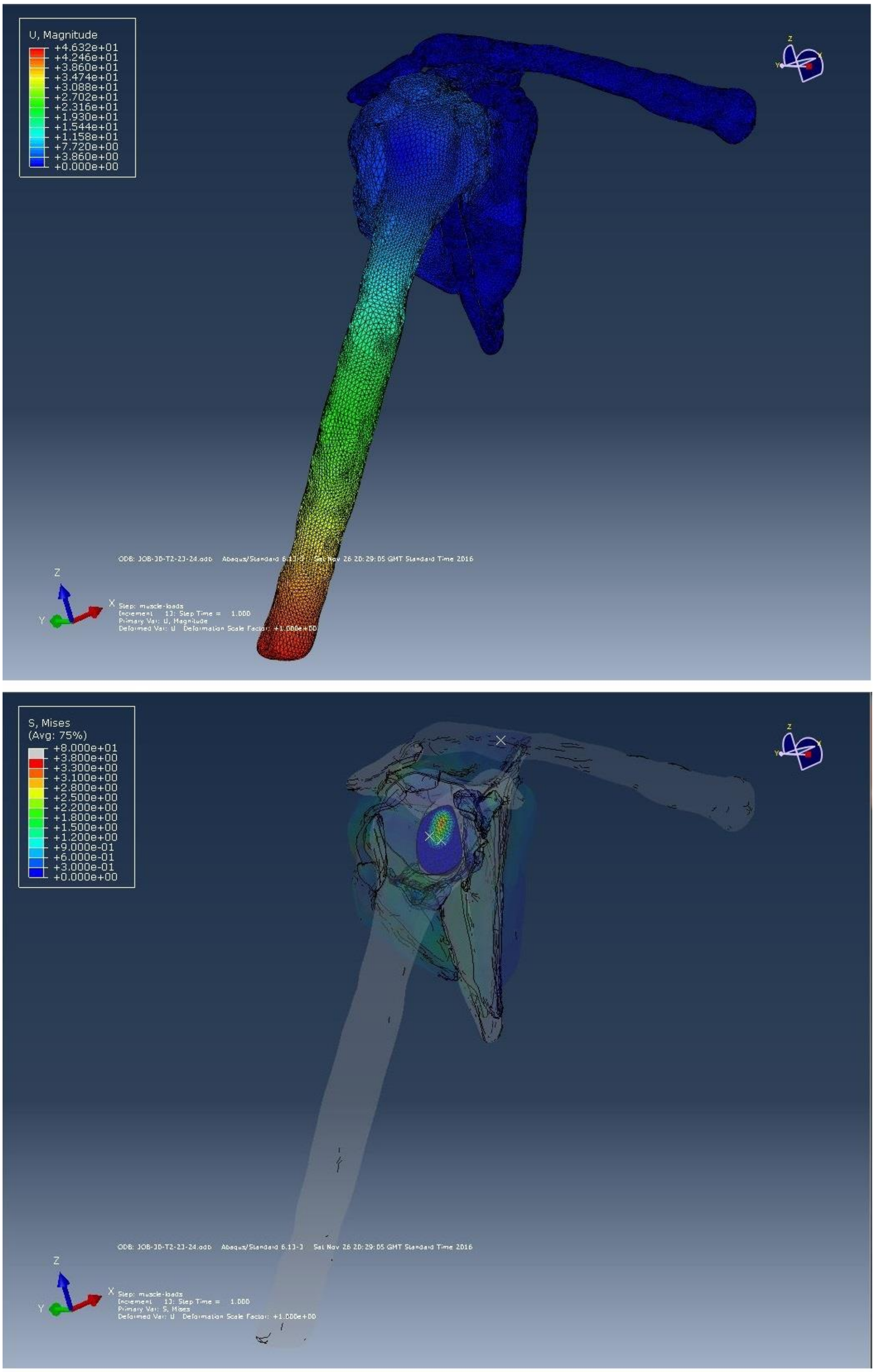

Figure 8-7 The exterior view of the deformation/displacement (top) VERSUS the penetrated view of the Von Mises stress distribution on the glenoid cartilage (bottom) of the simulation results of the FE model with tear size 23/24

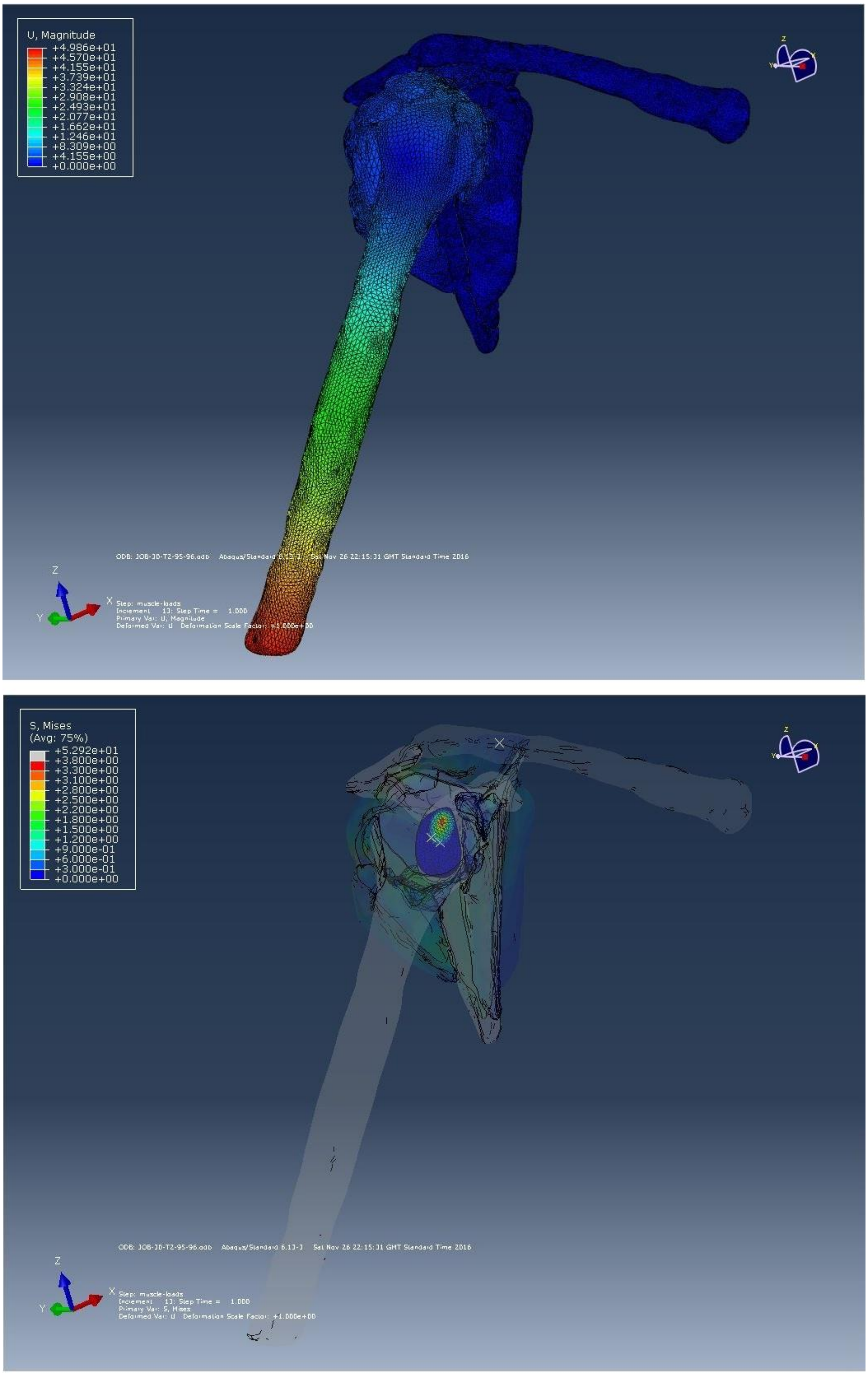

Figure 8-8 The exterior view of the deformation/displacement (top) VERSUS the penetrated view of the Von Mises stress distribution on the glenoid cartilage (bottom) of the simulation results of the FE model with tear size 95/96

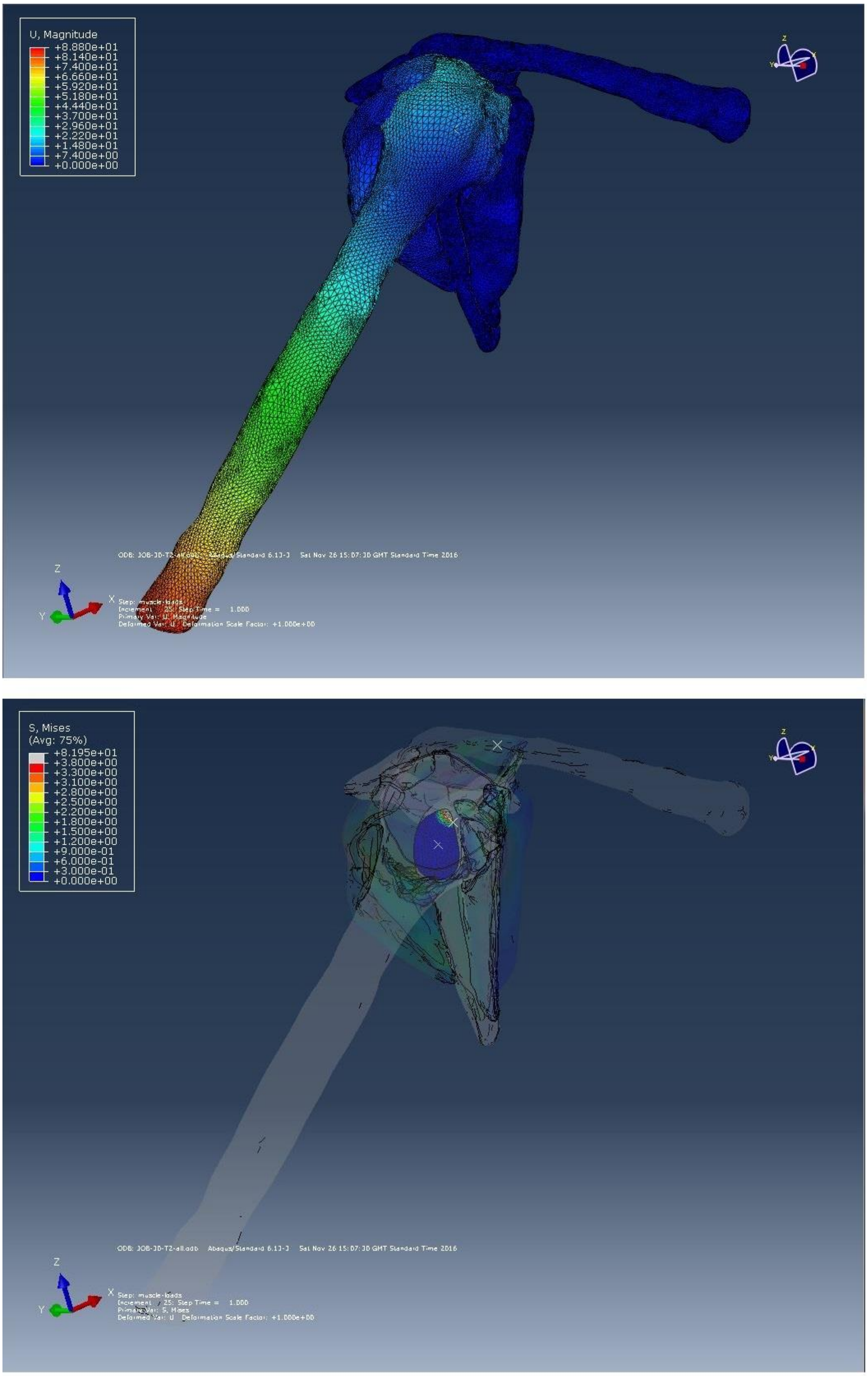

Figure 8-9 The exterior view of the deformation/displacement (top) VERSUS the penetrated view of the Von Mises stress distribution on the glenoid cartilage (bottom) of the simulation results of the FE model with tear size 1 (full tear)

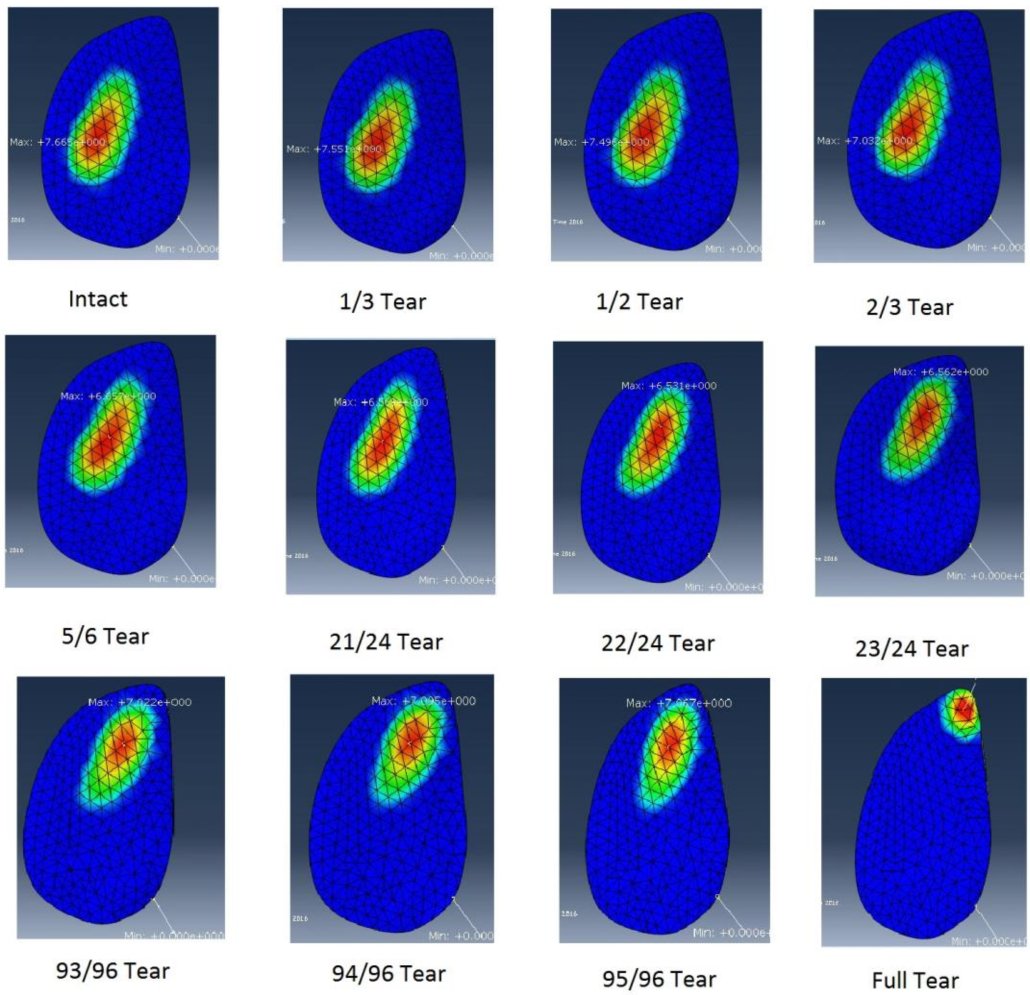

Figure 8-10 Variation of the distribution of the glenohumeral contact pressure on the glenoid cartilage during rotator cuff tear propagation

8.4 Glenohumeral stability analysis

To perform the glenohumeral joint stability analysis, a novel integrative stability index was defined in this study. This stability index was comprised of four ratios that accounted for four independent aspects that influence the stability of the glenohumeral joint. The four ratios were listed as following: (1) S_P: stability ratio quantifying the deviation of the joint contact pressure from the geometrical centroid of the glenoid fossa; (2) S_C: stability ratio quantifying the joint conformity; (3) S_F: stability ratio quantifying

Table 8-1 The bone-on-bone contact forces and total area in contact during the propagation of the rotator cuff tears

Tear size	F_x (N)	F_y (N)	F_z (N)	F_M (N)	Total area in contact (mm^2)
0 (intact)	312.616	260.193	-40.1257	408.704	88.04
1/6	314.857	261.914	-40.1523	411.517	89.2
1/3	312.691	260.062	-39.5506	408.623	89.61
1/2	308.371	256.512	-38.9018	402.995	88.66
2/3	276.165	226.509	-30.091	358.44	84.9
5/6	280.493	221.17	-19.3887	357.727	84.4
21/24	276.129	215.396	-16.0071	350.569	83.5
22/24	272.176	205.339	-7.25471	341.023	84.4
23/24	253.448	185.9	-0.131943	314.3	79.02
93/96	248.795	178.577	4.34983	306.28	75.4
94/96	240.506	169.923	7.57348	294.575	72.6
95/96	237.528	165.549	7.85193	290.782	71.1
1 (full tear)	87.0303	74.0297	0.770311	114.26	22.15

the direction of the bone-on-bone force with respect to the normal direction of the glenoid; (4) S_N: stability ratio quantifying the magnitude of the normal compressive component of the joint bone-on-bone force. Finally, the integrative stability index S can be calculated by the product of the above four ratios i.e., $S = S_P*S_C*S_F*S_N$. The following sections will describe in details the physical meanings of these stability ratios and how to calculate them.

8.4.1 S_P: the influence of the location of the glenohumeral contact pressure to joint stability

The first stability ratio component S_P quantifies the deviation of the contact pressure from the geometrical centroid of the glenoid. The underlying mechanism was that the closer is the pressure centre to the centroid of the glenoid, the better is the stability of the glenohumeral joint.

The centroid of the glenoid can be found in Abaqus through querying the mass property of the glenoid cartilage. Coordinates of this centroid were (-130.80, -4.85, 69.46). (See Figure 8-11)

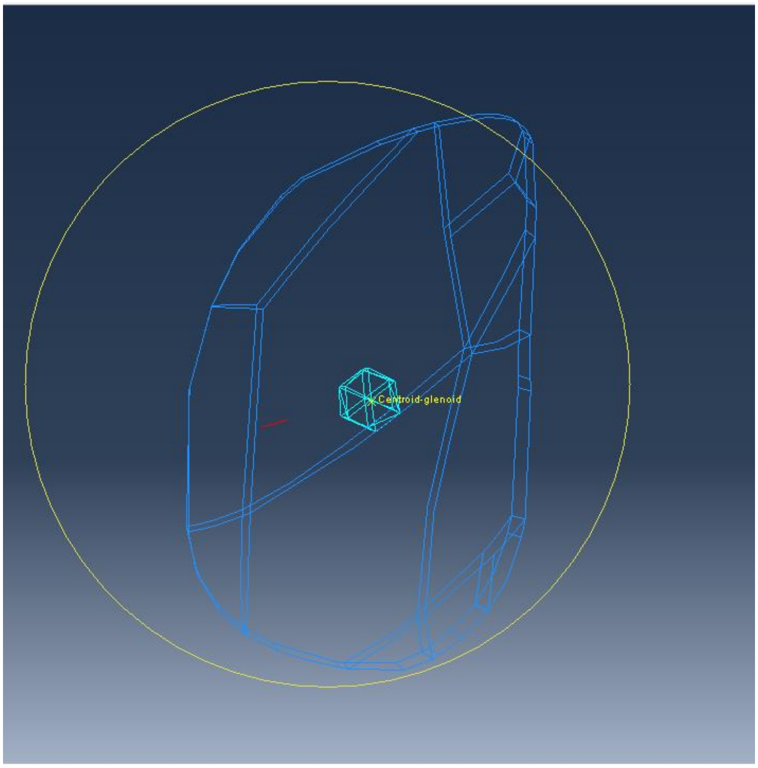

Figure 8-11 Geometrical centroid of the glenoid

The contact pressure area was represented by a pressure centre calculated using the equations below:

$$PC_x = \sum_i P_i x_i \Big/ \sum_i P_i$$

$$PC_y = \sum_i P_i y_i \Big/ \sum_i P_i$$

$$PC_z = \sum_i P_i z_i \Big/ \sum_i P_i$$

Where P_i is the contact pressure at node i; x_i, y_i, z_i are the coordinates of node i in the global coordinate and PC_x PC_y and PC_z are the X, Y, Z coordinates of the contact pressure centre [45]. Figure 8-12 takes the exporting of the contact pressure results in the tear size 0 (intact) as an example. The pressure values of all the nodes on the glenoid cartilage were exported to Excel from Abaqus. (See Figure 8-12) Similarly, the contact pressure results of FE models in each tears size were exported. All the above exported pressure data was further calculated using MATLAB (See Appendix A (4). Pressure centre calculation) The calculated coordinates of the pressure centre can be found in Table 8-2.

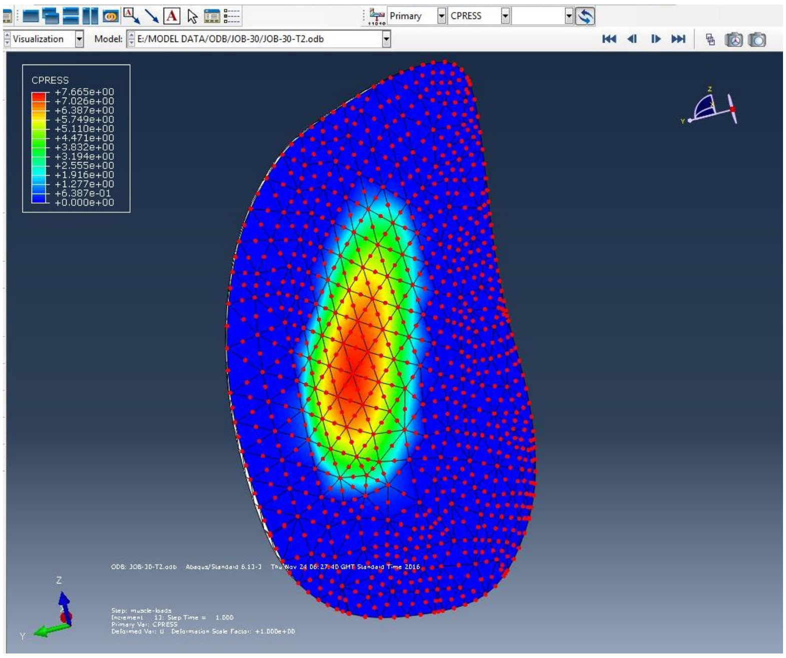

Figure 8-12 Exporting of the contact pressure of all the nodes on the glenoid cartilage

Table 8-2 The position of the contact pressure centre

Tear size	Name of PC_i	X	Y	Z
0 (intact)	PC0	-131.9	-3.31	70.61
1/6	PC1_6	-131.8	-3.35	70.62
1/3	PC1_3	-131.8	-3.397	70.63
1/2	PC1_2	-131.8	-3.405	70.66
2/3	PC2_3	-131.5	-3.63	71.28
5/6	PC5_6	-130.8	-4.455	72.57
21/24	PC21_24	-130.5	-4.746	72.91
22/24	PC22_24	-129.9	-5.534	73.98
23/24	PC23_24	-129.3	-6.261	74.87
93/96	PC93_96	-128.9	-6.821	75.63
94/96	PC94_96	-128.6	-7.262	76.36
95/96	PC95_96	-128.5	-7.374	76.29
1 (full tear)	PC1	-126.1	-11.01	80.75
	Centroid	-130.8	-4.85	69.46

The above-calculated pressure centres were plotted in the glenoid together with the glenoid centroid (See Figure 8-13).

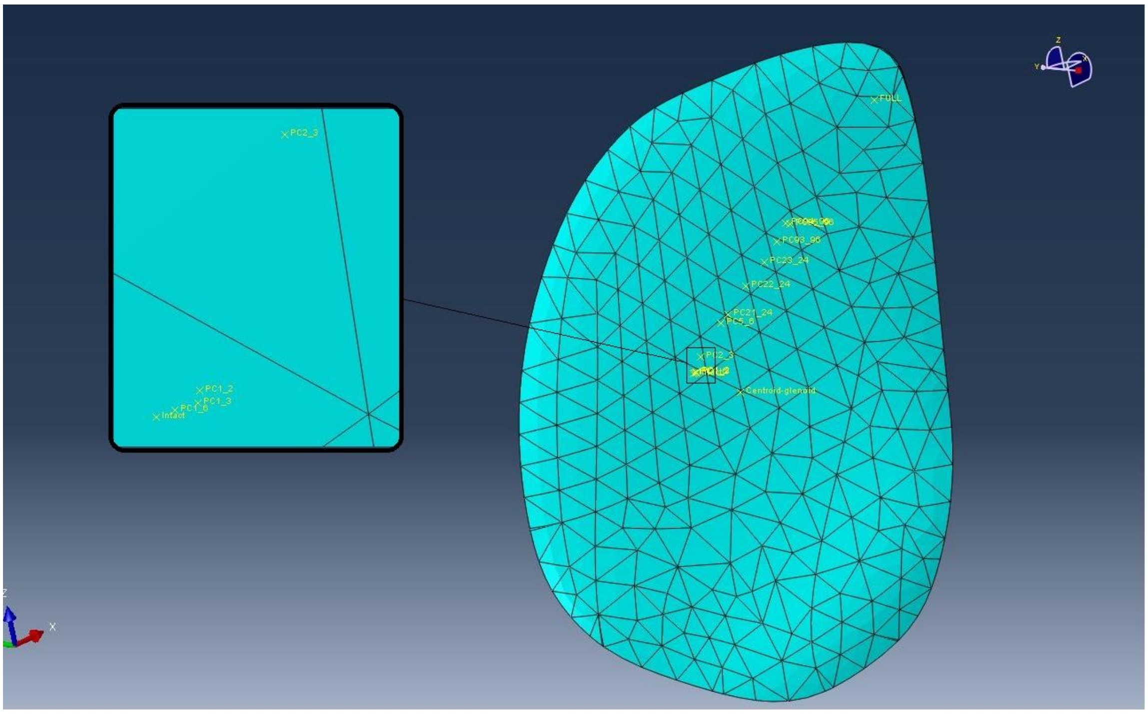

Figure 8-13 The contact pressure centre of each tear size with respective to the glenoid geometrical centroid.

Finally, this stability function was quantified in each tear case by D_i, the distance from the contact pressure centre to the glenoid centroid, where i represents the tears size sequence number. The stability ratio S_P is defined as Di/D_0 where D_0 is the distance from the contact pressure centre to the glenoid centroid in intact condition, i.e. $S_P = (D_i/D_0) * 100\%$. The calculated distance of the contact pressure of each cuff tear size D_i and the relative stability ratio S_{pi} can be found in Table 8-3.

8.4.2 S_C: the influence of the glenohumeral conformity to joint stability

The second stability ratio component S_c quantifies the joint conformity which represents the relative geometrical relationship and the force between the glenoid fossa and the humeral head in the contact region. The underlying mechanism was that the larger are the relative geometrical surfaces, the better is the joint stability; and the larger the contact force during contact, the better is the joint stability.

Table 8-3 The calculated stability ratio component S_p

Tear size	Name of PC_i	Distance to centroid (D_i) (mm)	S_{pi}
0 (intact)	PC0	2.214520264	100.00%
1/6	PC1_6	2.143735058	103.30%
1/3	PC1_3	2.116626798	104.62%
1/2	PC1_2	2.127915647	104.07%
2/3	PC2_3	2.300173906	96.28%
5/6	PC5_6	3.134984051	70.64%
21/24	PC21_24	3.464580205	63.92%
22/24	PC22_24	4.659211951	47.53%
23/24	PC23_24	5.788697695	38.26%
93/96	PC93_96	6.750091925	32.81%
94/96	PC94_96	7.633331121	29.01%
95/96	PC95_96	7.636064169	29.00%
1 (full tear)	PC1	13.69305298	16.17%

This stability function can be quantified by the total contact area in contact of each tear case A_i, where i represents the tears size sequence number. Therefore the stability ratio S_c can be defined as A_i/A_0 where A_0 is the total area in contact of the intact condition, i.e. $S_C = (A_i/A_0) * 100\%$. The calculated stability ratio component S_c in each tear size case can be found in Table 8-4.

8.4.3 S_F: the influence of the direction of the bone-on-bone force to joint stability

The third stability ratio component S_F quantifies the direction of the bone-on-bone force with respect to the normal direction of the glenoid. The underlying mechanism is that the closer is the direction of the bone-on-bone contact force to the glenoid normal direction, the better is the joint stability.

The normal direction of the glenoid was defined as the normal vector which is the vector through the glenoid geometrical centroid and normal to the glenoid surface. The glenoid surface was defined by the mesh surface beneath the centroid as shown in Figure 8-14 (a). Subsequently, the normal vector was determined and normalised as V_N = [0.7581, 0.6418, -0.1157] in the global frame as shown in Figure 8-14 (b).

Table 8-4 The calculated stability ratio component S_c

Tear size	Total area in contact (A_i) (mm^2)	S_{ci}
0 (intact)	88.04	100.00%
1/6	89.2	101.32%
1/3	89.61	101.78%
1/2	88.66	100.70%
2/3	84.9	96.43%
5/6	84.4	95.87%
21/24	83.5	94.84%
22/24	84.4	95.87%
23/24	79.02	89.75%
93/96	75.4	85.64%
94/96	72.6	82.46%
95/96	71.1	80.76%
1 (full tear)	22.15	25.16%

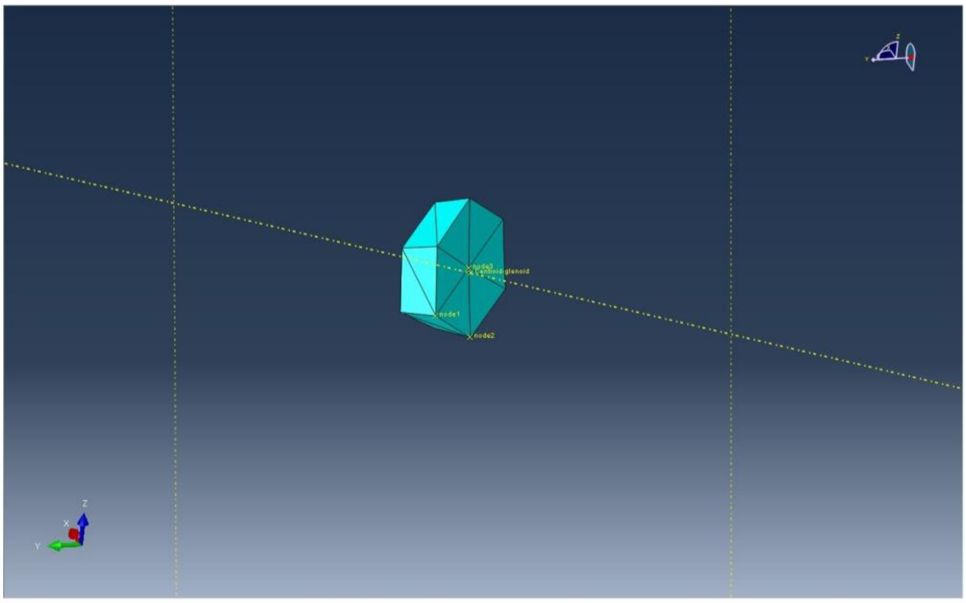

(a)

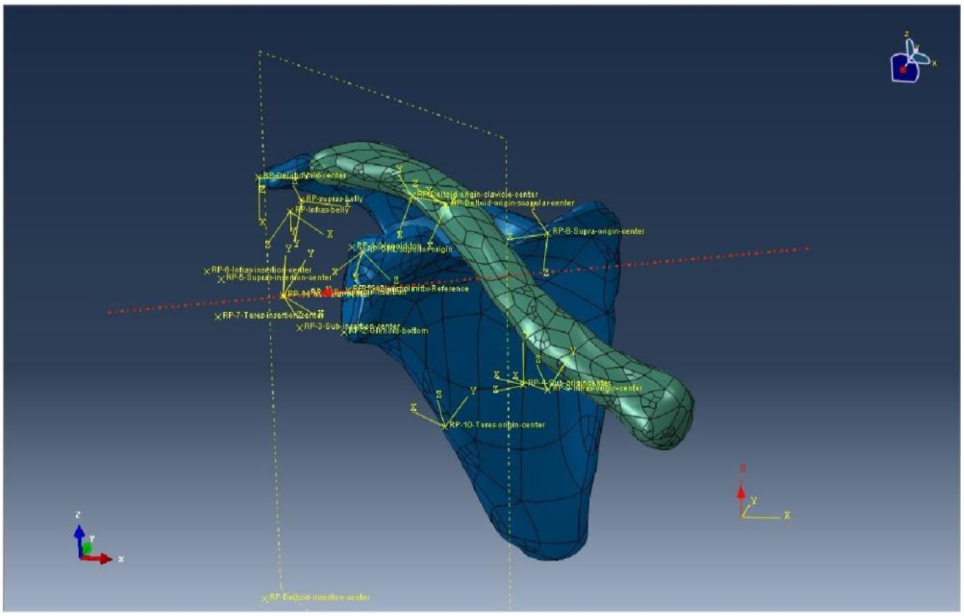

(b)

Figure 8-14 (a) The determination of the glenoid surface and (b) visualisation of the normal vector in the model

Whereas, the direction of the bone-on-bone contact force in each tear case was determined by its force components with respect to each axis in the global frame. (See Table 8-1) Thus their unit force vector V_i can be calculated as shown in Table 8-5. Subsequently, the angle θ_i between the force vector and the glenoid normal vector can be calculated with the equation $\theta_i = \cos^{-1}(V_i V_N / |V_i||V_N|)$.

Table 8-5 Unit force vector along the bone-on-bone force direction and their relative angles with respect to the glenoid normal vector: $\boldsymbol{\theta_i}$

Tear size	**Unit force vector Vi**			$\boldsymbol{\theta_i}$
	x	y	z	
0 (intact)	0.764895241	0.636628923	-0.098177819	1.115401982
1/6	0.765113346	0.636460034	-0.097571471	1.153555558
1/3	0.765232409	0.636436196	-0.096790125	1.196605717
1/2	0.765199352	0.636515159	-0.096531879	1.208202159
2/3	0.770464668	0.631930844	-0.083950002	2.031166662
5/6	0.78409852	0.618265232	-0.054199752	4.055926945
21/24	0.787658642	0.614417612	-0.045660292	4.629684782
22/24	0.798116859	0.602126998	-0.021273391	6.302369225
23/24	0.806347065	0.591442503	-0.000419778	7.724367399
93/96	0.812311486	0.583050898	0.014202122	8.746588638
94/96	0.816451341	0.576841581	0.02570987	9.53221013
95/96	0.820097963	0.571580604	0.027109864	9.796417128
1 (full tear)	0.761688973	0.647907754	0.00674176	7.029010734

Finally, this stability function can be quantified as the compressive component divided by the shear component of the bone-on-bone contact force C_i, where i represents the tears size sequence number. In fact, C_i is equal to the cotangent of the angle θ_i, i.e. $C_i = \cot\theta_i$. (Compressive component = F_M*$\cos\theta_i$ while shear component = F_M*$\sin\theta_i$) Therefore the stability ratio S_F can be defined as C_i/C_0 where C_0 is compressive component divided by the shear component of the bone-on-bone contact force of the intact condition, i.e. $S_F = (C_i/C_0)$*100%. The calculated stability ratio component S_F in each tear size case can be found in Table 8-6.

What is worth mentioning is that the result of S_{F0} is the largest which indicates the direction of bone-on-bone force caused by the intact rotator cuff connection (natural condition) demonstrated the best balanced function.

Table 8-6 The calculated stability ratio component S_F

Tear size	Compressive/Shear (C_i)	S_{Fi}
0 (intact)	51.38739858	100.00%
1/6	49.6873362	96.69%
1/3	47.89924842	93.21%
1/2	47.43937255	92.32%
2/3	28.21080613	54.90%
5/6	14.11000561	27.46%
21/24	12.35508563	24.04%
22/24	9.059083779	17.63%
23/24	7.376328863	14.35%
93/96	6.503026663	12.65%
94/96	5.958273242	11.59%
95/96	5.794537324	11.28%
1 (full tear)	8.114550118	15.79%

8.4.4 S_N: the influence of the magnitude of the compressive component of the bone-on-bone force to joint stability

The last stability ratio component S_N quantifies the magnitude of the normal compressive component of the bone-on-bone force to joint stability. The underlying mechanism was that the larger is the compressive component of the bone-on-bone force, the better is the joint stability.

This stability function can be quantified as the compressive component of the bone-on-bone contact force F_{Ni}, i.e., $F_{Ni} = F_M * \cos\theta_i$, where θ_i is the angle between the force vector and the glenoid normal vector calculated in the previous stability ratio component. Therefore the stability ratio S_N can be defined as F_{Ni}/F_{N0} where F_{N0} is compressive component of the bone-on-bone contact force of the intact condition, i.e. $S_N = (F_{Ni}/F_{N0})*100\%$. The calculated stability ratio component S_N in each tear size case can be found in Table 8-7.

Table 8-7 The calculated stability ratio component S_N

Tear size	Compressive component (F_{Ni}) (N)	S_{Ni}
0 (intact)	408.6265569	100.00%
1/6	411.4335983	100.69%
1/3	408.5338885	99.98%
1/2	402.9054042	98.60%
2/3	358.2147904	87.66%
5/6	356.8310674	87.32%
21/24	349.4251613	85.51%
22/24	338.9619992	82.95%
23/24	311.4480817	76.22%
93/96	302.718137	74.08%
94/96	290.5077029	71.09%
95/96	286.541974	70.12%
1 (full tear)	113.4012582	27.75%

8.4.5 Integrative stability index

The integrative stability index was calculated by multiplying all the above stability ratios. A summary of the above individual stability ratios and the integrative stability index were listed in Table 8-8 and Figure 8-15.

From the results, it can be found that the integrative stability index generally decreases with the increasing of the tear propagating with an exception in 1/6 where there is a small amount of increase in the stability ratio. What's more, the stability ratio decreases slowly before tear size 1/2, but dramatically afterwards. This finding supports our second hypothesis that small tears do not significantly affect the joint stability. In addition, the critical tear size is determined as tear size 1/2 i.e., the tear involved whole supraspinatus tendon and half of the infraspinatus tendon. The integrative stability index was in fact dominated by S_F. This may indicate that the dominant factor in which the rotator cuff tear destabilises the glenohumeral joint is the change of direction of the bone-on-bone force.

Table 8-8 Stability index summary

Tear size	S_P	S_C	S_F	S_N	**S**
0 (intact)	100.00%	100.00%	100.00%	100.00%	100.00%
1/6	103.30%	101.32%	96.69%	100.69%	101.90%
1/3	104.62%	101.78%	93.21%	99.98%	99.24%
1/2	104.07%	100.70%	92.32%	98.60%	95.40%
2/3	96.28%	96.43%	54.90%	87.66%	44.68%
5/6	70.64%	95.87%	27.46%	87.32%	16.24%
21/24	63.92%	94.84%	24.04%	85.51%	12.46%
22/24	47.53%	95.87%	17.63%	82.95%	6.66%
23/24	38.26%	89.75%	14.35%	76.22%	3.76%
93/96	32.81%	85.64%	12.65%	74.08%	2.63%
94/96	29.01%	82.46%	11.59%	71.09%	1.97%
95/96	29.00%	80.76%	11.28%	70.12%	1.85%
1 (full tear)	16.17%	25.16%	15.79%	27.75%	0.18%

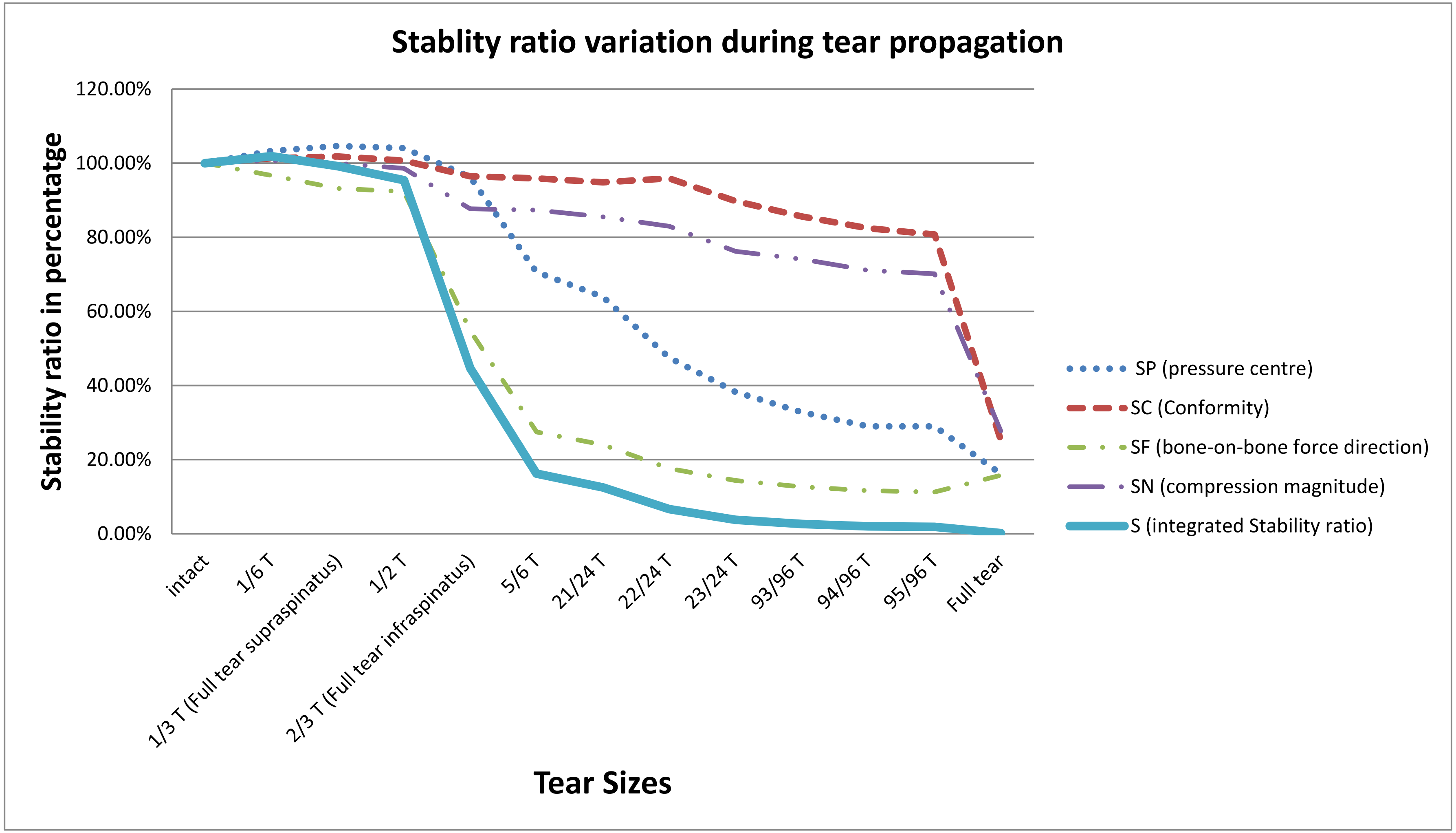

Figure 8-15 The integrative stability index with respect to individual stability ratios during rotator cuff tear propagation

8.5 Discussion

Quantification of the shoulder joint stability

The glenohumeral joint is the most mobile, yet most easily dislocated joint in the human body. Numerous studies had been conducted to perform the joint stability study. A generally accepted concept of the glenohumeral joint stability mechanism was proposed by Lippitt et al. which summarised the stability of the glenohumeral joint in two mechanisms: the concavity compression and scapulohumeral balance mechanisms [160]. Specifically, the concavity compression mechanism described the mechanism as the convex object (humeral head) that is pressed into a concave surface (glenoid fossa); whereas the scapulohumeral balance mechanism indicates that the surrounding soft tissues dynamically positioning glenohumeral joint so that the bone-on-bone contact force is balanced within the glenoid fossa. (See Figure 8-16)

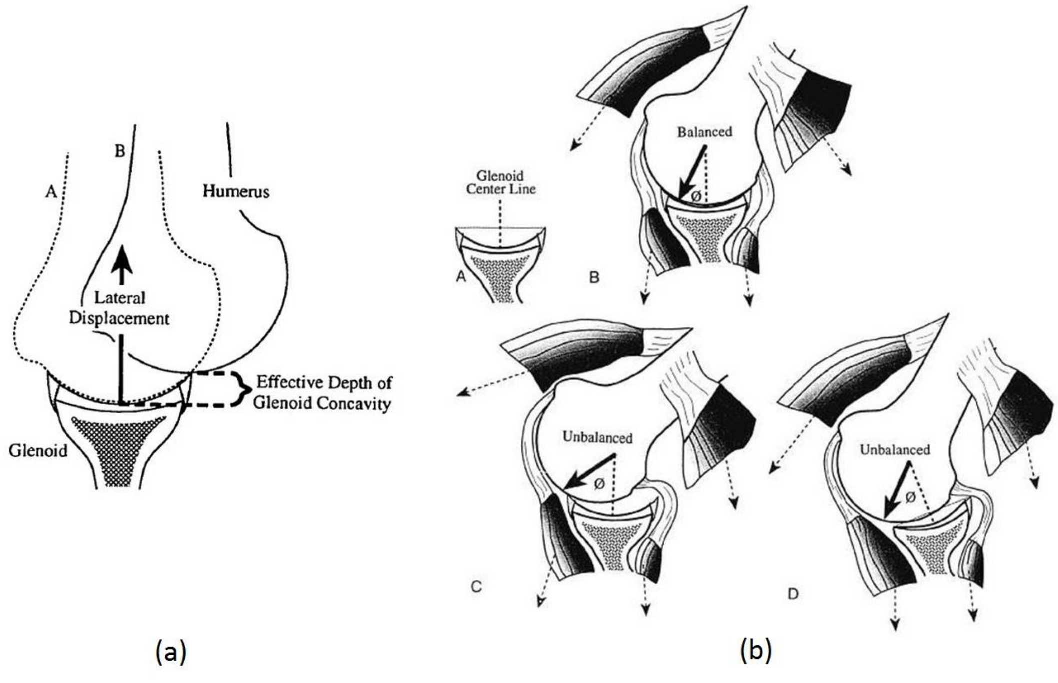

Figure 8-16 (a) The compression concavity mechanism and (b) The scapulohumeral balance mechanism described in literature [160]

However, the quantitative analysis of the combined glenohumeral joint stability from both of the above two mechanisms remained challenging. So far, the most widely used stability ratio is defined as the translational force at dislocation divided by the artificially defined compressive load. Normally, this stability ratio calculation requires the experiment or simulation to be performed in joint dislocation under an artificially defined compressive load e.g. 50N. This index was used to quantify the compression concavity mechanism, which was originally proposed in a cadaveric study [161]. (See Figure 8-17) This ratio has been widely used in cadaveric or simulation studies that investigate the glenohumeral articulating structures especially the influence on joint stability from the changes on the bony geometry due to disorders such as Bankart and Hill-sack lesions [49, 22, 26, 52, 162]. However, limitation of this index is obvious. First of all, the scapulohumeral balanced mechanism from the surrounding soft tissues is neglected. Secondly, the artificially defined compressive load was proposed to simulate the compressive loads from the soft tissues. However, in real cases, this force is actually the bone-on-bone force which varies dynamically rather than static only. In addition, this stability ratio requires experiment or simulation to be performed to GH joint dislocation which can be troublesome and not necessary in some cases. Another joint stability quantifying method was to use the average glenohumeral contact point/area as an indicator [45]. (See Figure 8-18) Although it was a rough description of the joint stability, the rationale was inspiring.

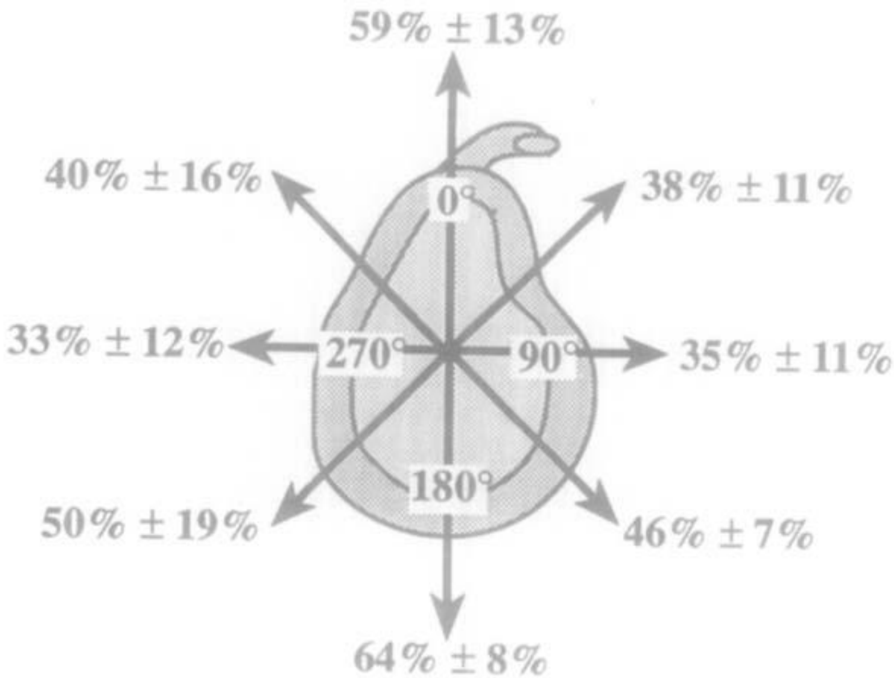

Figure 8-17 The stability ratio definition in literature. Defined as the translating force at dislocation divided by the applied compressive load (50N in this case) [161]

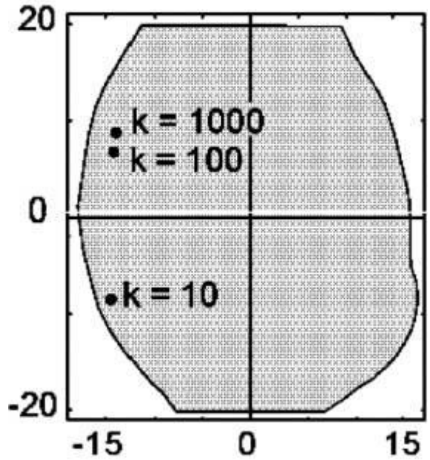

Figure 8-18 The average contact point describing the joint stability [45]

Hence, the integrative stability ratio proposed in this study took account of both of the mechanisms by three combined ratios. Specifically, the combination of the S_P and S_N is, in fact, equivalent to and completely defined the compression concavity mechanism and the S_F quantifies the scapular scapulohumeral balance mechanism. In addition, the joint conformity function was considered which was defined by S_C. What is more importantly, this stability ratio quantification method can be extended to other glenohumeral joint stability studies. For example, the study of the bony Bankart lesion where the geometry of the glenoid fossa was changed, the stability component S_P could be more dominant, rather than S_F in this study. In addition, this stability ratio has the potential capability to examine the fundamental mechanism by which the glenohumeral joint loses its stability in glenohumeral stability analyses, hence, leading to better diagnostic or surgical treatments.

Results comparison with literature findings

Based on a rough observation of the results of the movement of the humerus, a continuous superoanterior translation relative to glenoid was observed. This is a typical symptom for rotator cuff tears confirmed by *in-vivo* studies [163, 164] and cadaveric studies [165, 166]. Especially, the humeral movement results in this study showed good agreement with the *in-vivo* kinematics patterns determined in patients with known massive rotator cuffs [163]. Burkhart and colleagues reported three types of kinematics pattern. Type I, stable fulcrum kinematics with tears of the superior rotator cuff (supraspinatus and a portion of the infraspinatus) (See Figure 8-19). These tear sizes are equivalent to the tear sizes smaller than 1/2 in this study, which according to the stability study was also found stable. Type II, unstable fulcrum kinematics with tears that involved all the superior and posterior rotator cuff. (See Figure 8-20) These tear sizes are equivalent to the tears sizes 21/24 to 1 (full tear) which was determined as unstable based on the stability analysis. Type III were the kinematics patterns that involved subscapularis tears which were not within the scope of this study. Further studies could be done in this type of tears. This agreement in the characterization of shoulder stability supports our findings that tear size 1/2 (the tear involved whole supraspinatus tendon and half of the infraspinatus tendon) is the critical tear size in glenohumeral joint stability.

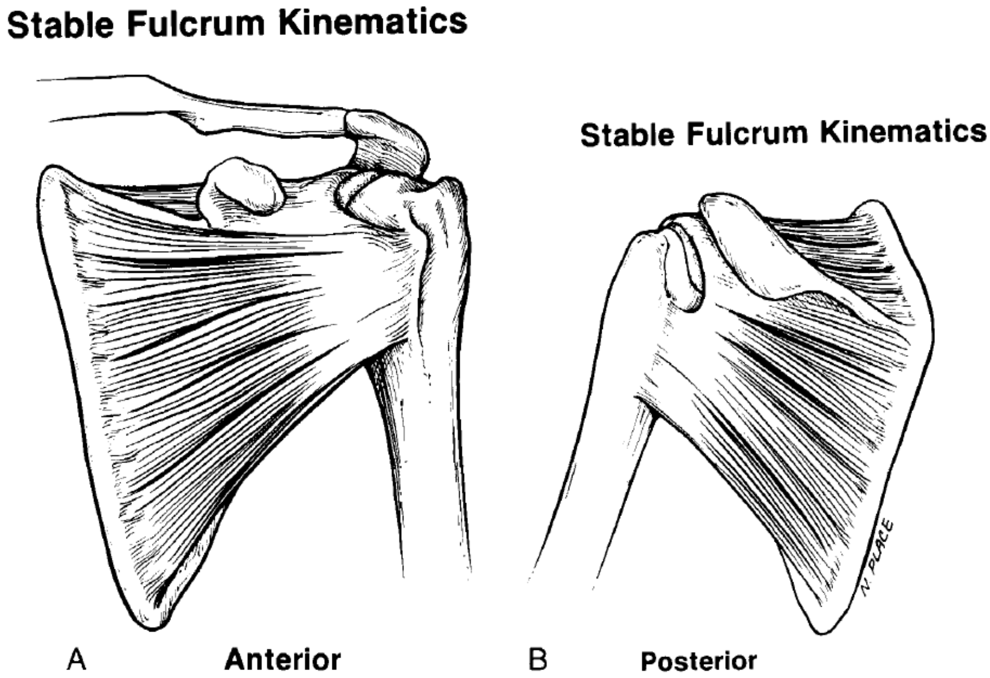

Figure 8-19 Clinically observed stable shoulder with small tears in literature (A) anterior view of a rotator cuff tear with stable fulcrum kinematics (torn supraspinatus and a partial tear of infraspinatus) equivalent to tear sizes 0 to 1/2 in this study. (B) Posterior view of a rotator cuff tear with stable fulcrum kinematics [163]

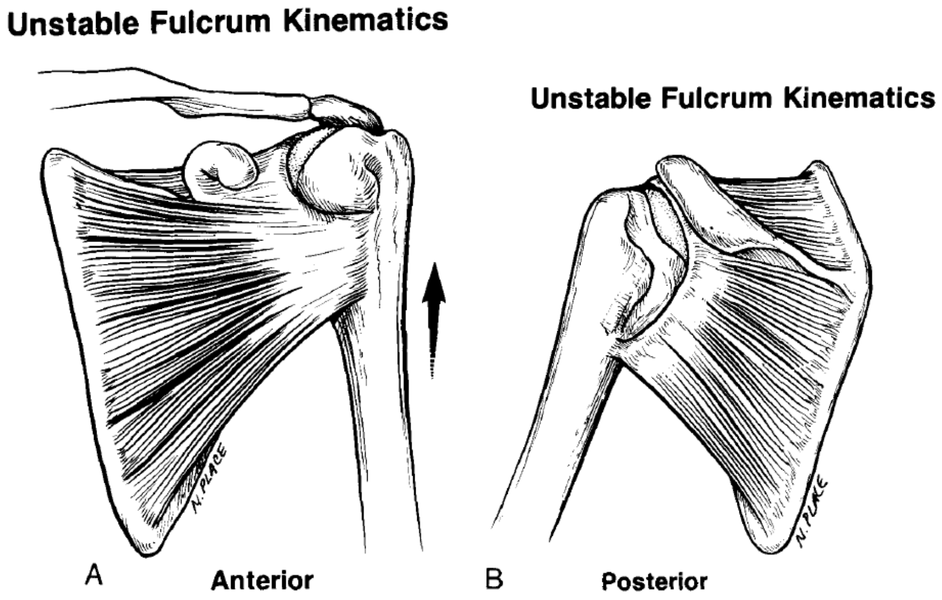

Figure 8-20 Clinically observed unstable shoulder with large tears in literature (A) anterior view of a rotator cuff tear with stable fulcrum kinematics (completely torn supraspinatus and posterior rotator cuff) equivalent to tear sizes 21/24 to 1 (full tear) in this study. (B) Posterior view of a rotator cuff tears with stable fulcrum kinematics [163]

8.6 Summary

A biomechanical study of the influence of the propagation of the rotator cuff tears on the glenohumeral joint stability was conducted on the FE model of the shoulder at 30 degrees scapulothoracic scapular abduction. A novel integrative stability index quantifying the glenohumeral joint stability was proposed and successfully used to quantifying this influence. It was concluded that (1) the stability of the glenohumeral joint generally decreases with the increasing of the tear sizes. However, (2) smaller sizes of tears do not significantly affect the joint stability, in addition, the critical tear size in which the influence of the rotator cuff tears becomes severe was determined as the tear involved whole supraspinatus tendon and half of the infraspinatus tendon. (3) The dominant factor in which the rotator cuff tear destabilises the glenohumeral joint is the change of direction of the bone-on-bone force.

Chapter 9 Conclusions and future work

9.1 Overview of the thesis

The objective of this project was to develop and validate a large-scale subject-specific FE model of the human shoulder musculoskeletal complex aiming to enhance the understanding of fundamental mechanisms underlying shoulder joint mobility and stability nature. The constructing of the FE model had been achieved and further used to simulate the *in-vivo* joint motions and conduct the biomechanical study on the influence and mechanism of the rotator cuff tears on the glenohumeral joint stability. In addition, a systematic quantitative analysis of the shoulder joint stability analysis was proposed using a novel integrative stability index. This index was calculated using all the critical results among the abundant FE simulation results from the tear propagation studies. Both of the validated FE model and the systematic shoulder stability analysis could have extensive clinical applications such as aetiology study of joint pathology, clinical diagnoses advice, computer-aided surgical planning and pre-testing and prosthetic design and optimisations etc.

In Chapter 3, the *in-vivo* 3D subject-specific shoulder motion with simultaneous muscle EMG signals of the subject was measured by advanced stereophotogrammetry and wireless surface EMG system. A detailed experimental protocol was designed to use Vicon infrared cameras and Delsys wireless surface EMG systems based on literature recommendations and practical pre-test for the reflective markers attachment and EMG electrode placement on the human body. The experiment was carefully conducted accordingly. Static motion trials were measured first with the subject remaining still for 5 seconds followed by dynamics trials when the subject performed frontal plane abduction, forward extension, scapular plane abduction and external rotation that aimed to cover normal shoulder motions. All motion trials were performed multiple times to exclude random errors. Some of the raw experimental data were presented subject to pre-processing.

In Chapter 4, a subject-specific multi-body musculoskeletal model was constructed by scaling the generic model using the measured static data from the previous chapter. Firstly, a brief introduction was presented for multi-body musculoskeletal simulation and the OpenSim software. Subsequently, a subject-specific multi-body musculoskeletal model was constructed based on a generic model from literature. The construction was conducted by scaling the generic model using the measured static data of four markers on the thorax and four markers on the humerus during the experiment. The constructed musculoskeletal model contains 3 degrees of freedom in the glenohumeral joint (a general ball-socket joint). A total number of 25 muscles were defined by 29 bundles around the shoulder and elbow joints. The same marker system was used to implement the measured scapular abduction motion trials to drive the model so as to calculate the glenohumeral joint angles during the scapular plane abduction during the motion capture experiment using inverse kinematics method. The predicted joint angles were then used to calculate the joint torques which were further decomposed into individual muscle forces. The predicted muscle forces were validated against literature data. Further, these muscle forces and joint positions were used to define the physiological the loading and boundary conditions in FE simulations in Chapter 6 and 7.

In Chapter 5, the same subject from the motion measurement experiment was selected to perform MR scanning. Several sequences of the MR images were obtained including a sequence of the whole right-side upper body and another two sequences of the detailed view of the glenohumeral joint with high resolution. The images were subsequently used for segmentation and 3D reconstruction to obtain the 3D geometries of all the major shoulder musculoskeletal components. These reconstructed 3D geometries were subjected to further construction such as smoothing and surface generating in Catia V5 for solid model construction. A total of 16 solid tissue structures were constructed, including 3 bones, 2 cartilages, 6 ligaments and 5 muscles.

In Chapter 6, a subject-specific integrated FE model containing all modelling information from Chapter 3 to 5 was constructed. The reconstructed bone, muscle, ligament and cartilage geometries of the subject from Chapter 5 were imported into Abaqus as individual parts before assembly, especially, their relative positions from MR reconstruction were preserved. On the other hand, Chapter 3 and 4 defined the *in-vivo* physiological subject-specific boundary and loading conditions for the FE simulation. Specifically, the measured scapula and clavicle bone kinematic data were defined as the boundary conditions. The calculated muscles forces from Chapter 4 were used to define the muscle loadings that dynamically stabilise the humerus which was left free of any prescribed constraints. Detailed FE model construction process was presented, including assembly, material property, mesh, interaction and loading and boundary conditions. All FE definitions were working as expected in a preliminary simulation. Finally, a mesh size sensitivity study was conducted by a motion simulation independent of the validation.

In Chapter 7, a quasi-static FE analysis of the shoulder scapular plane abduction measured in Chapter 3 was simulated using the constructed subject-specific FE model. FE models at respective joint angles were generated through reproducing the scapular abduction motion. Secondly, the quasi-static analyses of the scapular abduction at respective joint positions were performed using the calculated muscle forces at each relative joint position of the scapular abduction in Chapter 4. The simulation results were validated against *in-vivo* measured bone-on-bone contact forces and the humeral head translation relative to the glenoid during shoulder abduction as well as other simulation results in the literature. Both bone-on-bone contact force and the humeral head translation were in good agreement with the *in-vivo* measured results. In addition, the stress distribution of the supraspinatus tendon was found comparable with the literature data. Furthermore, a material property sensitivity study was conducted on Young's modulus of the muscle and tendons. It was found that the bone-on-bone contact and peak stress on the glenoid cartilage were sensitive to Young's modulus of the muscles while not to the ligament's.

In Chapter 8, the previously constructed and well-validated FE model at 30 degrees scapular plane abduction was further constructed to simulate the rotator cuff tears propagation. The propagation of the tears was defined as initialling from the anterior insertion site on the humeral head of the supraspinatus tendon and propagating posteroinferiorly until full tear on all three rotator cuff tendons i.e. supraspinatus, infraspinatus and teres minor tendons. A series of static simulations was conducted using FE models with a sequence of increasing tears sizes while keeping all other FE definitions the same. All simulations converged successfully and the simulation results were summarised accordingly. To quantitatively study the glenohumeral joint stability using the abundant FE results, a novel integrative stability index quantifying the joint stability was proposed and successfully used to calculate the variation in the glenohumeral joint during the propagation of rotator cuff tears in this study. Through calculation, it was found that (1) the stability of the glenohumeral joint generally decreases with the increasing of the tear sizes. However, (2) smaller sizes of tears do not significantly affect the joint stability, in addition, the critical tear size in which the influence of the rotator cuff tears becomes severe was determined as the tear involved whole supraspinatus tendon and half of the infraspinatus. (3) The dominant factor in which the rotator cuff tears destabilise the glenohumeral joint is the change of direction of the bone-on-bone force. The results showed good agreement with the phenomenon observed during medical practice and scientific reports.

9.2 Original contributions arising from this work

In this thesis, some original and novel contributions have been made to improve our understanding of the biomechanics of shoulder complex.

Firstly, a computational framework combining the two main computational biomechanics methods of the human shoulder complex, i.e. multi-body musculoskeletal method and finite element method has been employed and validated. A large-scale subject-specific human shoulder FE model was successfully constructed based on both the MRI scanning and the *in-vivo* 3D shoulder motion measurements of the same subject. An *in-vivo* quasi-static FE analysis of the shoulder scapular plane abduction defined by the measurement data was conducted and rigorously validated. As far as the author knows, this subject-specific framework has been achieved for the first time in shoulder computational study field.

Secondly, detailed comprehensive 3D geometries of all major hard tissues and soft tissues around the glenohumeral joint were reconstructed based on high-resolution MR images. All possible efforts have been made in every stage of the geometrical reconstruction process intended to get the highest possible accuracy of the model, including multiple scanning, manual segmentation and integrating the state-of-the-art anatomy studies. Furthermore, the reconstructed geometries were confirmed by the medical partners. The 3D geometrical model constructed in this study exceeds most of the previous models in both complexity and accuracy. This makes a step forward towards the realistic representation of the shoulder complex.

Then, several innovative techniques were used in FE modelling. Firstly, all 3D constructed geometrical models were imported to FE environment while carefully preserving their dedicated relative positions. These relative positions were subsequently used to define their physiological contacts. Especially, the three posterior rotator cuff structures were merged to simulate their firmly bonded physiological relationship. Finally, the boundary and loading conditions were completely determined by the *in-vivo* motion measurements and muscle force calculation. Specifically, the clavicle and scapula bone were constrained by measured bone kinematics data, while the humerus was actively positioned and stabilised by the calculated *in-vivo* muscle loadings and passively by the glenoid and the ligament structures without any prescribed artificial control. This model is an accurate reflection of the shoulder joint mobility and stability nature. In addition, the muscle forces implementation for all rotator muscles were defined by predefined stress over the muscle belly portion which is also a realistic representation of the large-scale muscle contraction.

Further, a novel integrative stability index has been proposed to quantify the overall stability of the shoulder joint. This index contains four ratios that quantify four independent physical aspects that influence joint stability. This index has for the first time fully integrated the widely accepted concepts of the glenohumeral joint stability mechanism: the concavity compression and scapulohumeral balance mechanisms. Furthermore, joint conformity mechanism was introduced and included in this integrative index. This integrative stability index has successfully quantified the stability variation in the glenohumeral joint during the propagation of rotator cuff tears. In addition, it can be further used in other glenohumeral joint stability related analysis.

Finally, FE analysis has been conducted to simulate the propagation of the rotator cuff tears for the first time. Using the proposed stability index, the FE simulation results were critically analysed. It was concluded that the stability of the glenohumeral joint generally decreases with increasing tear sizes, and the bone-on-bone force direction was determined as the statically significant mechanism that influences the joint stability due to the rotator cuff tears. In addition, it was proven that smaller sizes of tears do not significantly affect the joint stability and the critical tear size in which the influence of the rotator cuff tears becomes severe was determined for the first time as the tear involved whole supraspinatus tendon and half of the infraspinatus tendon.

9.3 Future work

The outcome of this study is abundant, not limited to the main findings presented. Each part of the work solely can be further used for conducting new research.

Chapter 3 & 4 are the *in-vivo* kinematic study of the dominant shoulder of a normal human. The constructed multi-body model has the potential capabilities for shoulder motion evaluation for physiotherapy, diagnosing and surgical planning for the musculotendinous injuries. A more comprehensive multi-body model is in need which can cover the whole range of motion. Also, EMG data can play more important role in a wider range of motions. In addition, several motions measured in Chapter 3 have not been fully used during this study such as the frontal plane abduction and forward flexion. Further simulations can use these motions to enrich the *in-vivo* shoulder simulations.

Chapter 5 demonstrated the reconstruction of MRI scanning of the same subject. First of all, there were more structures already constructed but have not been imported to the FE model such as the labrum and biceps long head structure and the acromion clavicle ligaments. By adding these structures to the FE model, more integrated shoulder functions can be studied. In addition, the reconstructed MR structures can be exported as STL files for 3D printing.

Chapter 6 is the key outcome of this study. The FE model constructed in this chapter is the state-of-the-art integrated FE model of the human shoulder that could have numerous applications. The motion simulation and biomechanical study conducted in Chapter 7 and 8 are two examples of the application of this model. Similarly, they can be used to conduct other motion simulations or orthopaedic related research.

Reference

1. Linaker CH, Walker-Bone K. Shoulder disorders and occupation. Best Practice & Research Clinical Rheumatology 2015; 29 (3):405-423.

2. Walker-Bone K, Reading I, Coggon D, Cooper C, Palmer KT. The anatomical pattern and determinants of pain in the neck and upper limbs: an epidemiologic study. Pain 2004; 109 (1):45-51.

3. McFarland EG, Garzon-Muvdi J, Jia X, Desai P, Petersen SA. Clinical and diagnostic tests for shoulder disorders: a critical review. British Journal of Sports Medicine 2010; 44 (5):328-332.

4. Veeger H, van der Helm F. Shoulder function: the perfect compromise between mobility and stability. Journal of Biomechanics 2007; 40 (10):2119-2129.

5. Thibbotuwawa N, Gu Y, Oloyede A, Senadeera W, Li T Finite element shoulder models. In: Proceedings of 4th International Conference on Computational Methods (ICCM 2012), 2012.

6. Favre P, Snedeker J, Gerber C. Numerical modelling of the shoulder for clinical applications. Philosophical Transactions of the Royal Society of London A: Mathematical, Physical, and Engineering Sciences 2009; 367 (1895):2095-2118.

7. Wittek A, Grosland NM, Joldes GR, Magnotta V, Miller K. From Finite Element Meshes to Clouds of Points: A Review of Methods for Generation of Computational Biomechanics Models for Patient-Specific Applications. Annals of Biomedical Engineering 2016; 44 (1):3-15.

8. Zheng M, Zou Z, Bartolo PjDs, Peach C, Ren L. Finite element models of the human shoulder complex: a review of their clinical implications and modelling techniques. International Journal for Numerical Methods in Biomedical Engineering 2016; 33 (2):e02777.

9. Bronzino JD. The Biomedical Engineering Handbook, vol 2 Volume Set. Second Edition edn. CRC Press, 1999.

10. Elaine N. Marieb JM. Human Anatomy. Benjamin Cummings, 2001.

11. Netter FH. Atlas of Human Anatomy. Fifth Edition edn. Saunders Elsevier, 2010.

12. Martini FH, Timmons MJ, McKinley MP. Human Anatomy. Prentice Hall 2000.

13. Roy A (2009) Rotator Cuff Disease Clinical Presentation. MedScape

14. Ackland DC, Pandy MG. Lines of action and stabilizing potential of the shoulder musculature. Journal of Anatomy 2009; 215 (2):184-197.

15. Luo ZP, Hsu HC, Grabowski JJ, Morrey BF, An KN. Mechanical environment associated with rotator cuff tears. Journal of Shoulder and Elbow Surgery 1998; 7 (6):616-620.

16. Wakabayashi I, Itoi E, Sano H, Shibuya Y, Sashi R, Minagawa H, Kobayashi M. Mechanical environment of the supraspinatus tendon: a two-dimensional finite element model analysis. Journal of Shoulder and Elbow Surgery 2003; 12 (6):612-617.

17. Sano H, Wakabayashi I, Itoi E. Stress distribution in the supraspinatus tendon with partial-thickness tears: An analysis using two-dimensional finite element model. Journal of Shoulder and Elbow Surgery 2006; 15 (1):100-105.

18. Inoue A, Chosa E, Goto K, Tajima N. Nonlinear stress analysis of the supraspinatus tendon using three-dimensional finite element analysis. Knee Surgery, Sports Traumatology, Arthroscopy 2013; 21 (5):1151-1157.

19. Jahn S, Seror J, Klein J. Lubrication of Articular Cartilage. Annual Review of Biomedical Engineering 2016; 18 (1).

20. Gatti C, Maratt J, Palmer M, Hughes R, Carpenter J. Development and validation of a finite element model of the superior glenoid labrum. Annals of Biomedical Engineering 2010; 38 (12):3766-3776.

21. Bolsterlee B, Veeger DH, Chadwick EK. Clinical applications of musculoskeletal modelling for the shoulder and upper limb. Medical and Biological Engineering and Computing 2013; 51 (9):953-963.

22. Itoi E, Lee SB, Berglund LJ, Berge LL, An KN. The effect of a glenoid defect on anteroinferior stability of the shoulder after Bankart repair: a cadaveric study. Journal of Bone and Joint Surgery - American Volume 2000; 82 (1):35-46.

23. Apreleva M, Parsons IM, Warner JJP, Fu FH, Woo SLY. Experimental investigation of reaction forces at the glenohumeral joint during active abduction. Journal of Shoulder and Elbow Surgery 2000; 9 (5):409-417.

24. Parsons IM, Apreleva M, Fu FH, Woo SLY. The effect of rotator cuff tears on reaction forces at the glenohumeral joint. Journal of Orthopaedic Research 2002; 20 (3):439-446.

25. Ellis BJ, Lujan TJ, Dalton MS, Weiss JA. Medial collateral ligament insertion site and contact forces in the ACL-deficient knee. Journal of Orthopaedic Research 2006; 24 (4):800-810.

26. Kaar SG, Fening SD, Jones MH, Colbrunn RW, Miniaci A. Effect of humeral head defect size on glenohumeral stability: a cadaveric study of simulated Hill-Sachs defects. The American Journal of Sports Medicine 2010; 38 (3):594-599.

27. Dickerson CR, Chaffin DB, Hughes RE. A mathematical musculoskeletal shoulder model for proactive ergonomic analysis. Computer Methods in Biomechanics and Biomedical Engineering 2007; 10 (6):389-400.

28. Garner BA, Pandy MG. Musculoskeletal model of the upper limb based on the visible human male dataset. Computer Methods in Biomechanics and Biomedical Engineering 2001; 4 (2):93-126.

29. Högfors C, Karlsson D, Peterson B. Structure and internal consistency of a shoulder model. Journal of Biomechanics 1995; 28 (7):767-777.

30. Van der Helm FC. A Finite-Element Musculoskeletal Model of the Shoulder Mechanism. Journal of Biomechanics 1994; 27 (5):551-569.

31. Charlton IW, Johnson GR. A model for the prediction of the forces at the glenohumeral joint. Proceedings of the Institution of Mechanical Engineers, Part H: Journal of Engineering in Medicine 2006; 220 (H8):801-812.

32. Nikooyan AA, Veeger HEJ, Chadwick EKJ, Praagman M, van der Helm FCT. Development of a comprehensive musculoskeletal model of the shoulder and elbow. Medical and Biological Engineering and Computing 2011; 49 (12):1425-1435.

33. Prinold JAI, Masjedi M, Johnson GR, Bull AMJ. Musculoskeletal shoulder models: A technical review and proposals for research foci. Proceedings of the Institution of Mechanical Engineers, Part H: Journal of Engineering in Medicine 2013; 227 (10):1041-1057.

34. Stops A, Wilcox R, Jin Z. Computational modelling of the natural hip: a review of finite element and multibody simulations. Computer Methods in Biomechanics and Biomedical Engineering 2012; 15 (9):963-979.

35. Zienkiewicz C. The birth of the finite element method and of computational mechanics. International Journal for Numerical Methods in Engineering 2004; 60 (1):3-10.

36. Zienkiewics O. The finite element method in engineering science. McGraw-Hill, Londres 1971:521.

37. Huiskes R, Hollister SJ. From structure to process, from organ to cell: recent developments of FE-analysis in orthopaedic biomechanics. Journal of Biomechanical Engineering 1993; 115 (4B):520-527.

38. Viceconti M, Olsen S, Nolte LP, Burton K. Extracting clinically relevant data from finite element simulations. Clinical Biomechanics (Bristol, Avon) 2005; 20 (5):451-454.

39. Reilly DT, Burstein AH, Frankel VH. The elastic modulus for bone. Journal of Biomechanics 1974; 7 (3):271-275.

40. Rice JC, Cowin SC, Bowman JA. On the dependence of the elasticity and strength of cancellous bone on apparent density. Journal of Biomechanics 1988; 21 (2):155-168.

41. Veronda DR, Westmann RA. Mechanical Characterization of Skin-Finite Deformations. Journal of Biomechanics 1970; 3 (1):111-124.

42. Pioletti DP, Rakotomanana LR, Benvenuti JF, Leyvraz PF. Viscoelastic constitutive law in large deformations: application to human knee ligaments and tendons. Journal of Biomechanics 1998; 31 (8):753-757.

43. Pioletti DP, Rakotomanana LR, Leyvraz P-F. Strain rate effect on the mechanical behavior of the anterior cruciate ligament–bone complex. Medical Engineering and Physics 1999; 21 (2):95-100.

44. Kempson GE, Tuke MA, Dingle JT, Barrett AJ, Horsfield PH. The effects of proteolytic enzymes on the mechanical properties of adult human articular cartilage. Biochimica et Biophysica Acta 1976; 428 (3):741-760.

45. Büchler P, Ramaniraka N, Rakotomanana L, Iannotti J, Farron A. A finite element model of the shoulder: application to the comparison of normal and osteoarthritic joints. Clinical Biomechanics (Bristol, Avon) 2002; 17 (9-10):630-639.

46. Liu J, Hughes R, Smutz W, Niebur G, Nan-An K. Roles of deltoid and rotator cuff muscles in shoulder elevation. Clinical Biomechanics 1997; 12 (1):32-38.

47. Otis JC, Jiang C-C, Wickiewicz TL, Peterson M, Warren RF, Santner TJ. Changes in the moment arms of the rotator cuff and deltoid muscles with abduction and rotation. Journal of Bone and Joint Surgery 1994; 76 (5):667-676.

48. Terrier A, Reist A, Vogel A, Farron A. Effect of supraspinatus deficiency on humerus translation and glenohumeral contact force during abduction. Clinical Biomechanics (Bristol, Avon) 2007; 22 (6):645-651.

49. Walia P, Miniaci A, Jones MH, Fening SD. Theoretical model of the effect of combined glenohumeral bone defects on anterior shoulder instability: A finite element approach. Journal of Orthopaedic Research 2013; 31 (4):601-607.

50. Nyffeler RW, Sheikh R, Jacob HA, Gerber C. Influence of humeral prosthesis height on biomechanics of glenohumeral abduction. Journal of Bone and Joint Surgery 2004; 86 (3):575-580.

51. Yanagawa T, Goodwin CJ, Shelburne KB, Giphart JE, Torry MR, Pandy MG. Contributions of the individual muscles of the shoulder to glenohumeral joint stability during abduction. Journal of Biomechanical Engineering 2008; 130 (2):21-24.

52. Favre P, Senteler M, Hipp J, Scherrer S, Gerber C, Snedeker JG. An integrated model of active glenohumeral stability. Journal of Biomechanics 2012; 45 (13):2248-2255.

53. Giori NJ, Beaupre GS, Carter DR. Cellular-Shape and Pressure May Mediate Mechanical Control of Tissue Composition in Tendons. Journal of Orthopaedic Research 1993; 11 (4):581-591.

54. Anderson DD, Brown TD, Radin EL. Stress wave effects in a finite element analysis of an impulsively loaded articular joint. Proceedings of the Institution of Mechanical Engineers, Part H: Journal of Engineering in Medicine 1991; 205 (1):27-34.

55. Itoi E, Berglund LJ, Grabowski JJ, Schultz FM, Growney ES, Morrey BF, An KN. Tensile properties of the supraspinatus tendon. Journal of Orthopaedic Research 1995; 13 (4):578-584.

56. Seki N, Itoi E, Shibuya Y, Wakabayashi I, Sano H, Sashi R, Minagawa H, Yamamoto N, Abe H, Kikuchi K, Okada K, Shimada Y. Mechanical environment of the supraspinatus tendon: three-dimensional finite element model analysis. Journal of Orthopaedic Science 2008; 13 (4):348-353.

57. Halloran JP, Easley SK, Petrella AJ, Rullkoetter PJ. Comparison of deformable and elastic foundation finite element simulations for predicting knee replacement mechanics. Journal of Biomechanical Engineering 2005; 127 (5):813-818.

58. Halder A, Zobitz ME, Schultz F, An KN. Mechanical properties of the posterior rotator cuff. Clinical Biomechanics (Bristol, Avon) 2000; 15 (6):456-462.

59. Adams C, Baldwin M, Laz P, Rullkoetter P, Langenderfer J. Effects of rotator cuff tears on muscle moment arms: a computational study. Journal of Biomechanics 2007; 40 (15):3373-3380.

60. Goto K, Tajima N, Chosa E, Totoribe K, Kuroki H, Arizumi Y, Arai T. Mechanical analysis of the lumbar vertebrae in a three-dimensional finite element method model in which intradiscal pressure in the nucleus pulposus was used to establish the model. Journal of Orthopaedic Science 2002; 7 (2):243-246.

61. Nakajima T, Rokuuma N, Hamada K, Tomatsu T, Fukuda H. Histologic and biomechanical characteristics of the supraspinatus tendon: Reference to rotator cuff tearing. Journal of Shoulder and Elbow Surgery 1994; 3 (2):79-87.

62. Van der Helm FC. Analysis of the Kinematic and Dynamic Behavior of the Shoulder Mechanism. Journal of Biomechanics 1994; 27 (5):527-550.

63. Debski R, Weiss J, Newman W, Moore S, McMahon P. Stress and strain in the anterior band of the inferior glenohumeral ligament during a simulated clinical examination. Journal of Shoulder and Elbow Surgery 2005; 14 (1):S24-S31.

64. Moore SM, McMahon PJ, Debski RE. Bi-directional mechanical properties of the axillary pouch of the glenohumeral capsule: implications for modeling and surgical repair. Journal of Biomechanical Engineering 2004; 126 (2):284-288.

65. McMahon PJ, Tibone JE, Cawley PW, Hamilton C, Fechter JD, Elattrache NS, Lee TQ. The anterior band of the inferior glenohumeral ligament: biomechanical properties from tensile testing in the position of apprehension. Journal of Shoulder and Elbow Surgery 1998; 7 (5):467-471.

66. Ellis B, Debski R, Moore S, McMahon P, Weiss J. Methodology and sensitivity studies for finite element modeling of the inferior glenohumeral ligament complex. Journal of Biomechanics 2007; 40 (3):603-612.

67. Simo JC, Vu-Quoc L. On the dynamics in space of rods undergoing large motions—a geometrically exact approach. Computer methods in applied mechanics and engineering 1988; 66 (2):125-161.

68. Moore S, Ellis B, Weiss J, McMahon P, Debski R. The glenohumeral capsule should be evaluated as a sheet of fibrous tissue: a validated finite element model. Annals of Biomedical Engineering 2010; 38 (1):66-76.

69. Ellis B, Drury N, Moore S, McMahon P, Weiss J, Debski R. Finite element modelling of the glenohumeral capsule can help assess the tested region during a clinical exam. Computer Methods in Biomechanics and Biomedical Engineering 2010; 13 (3):413-418.

70. Drury N, Ellis B, Weiss J, McMahon P, Debski R. The impact of glenoid labrum thickness and modulus on labrum and glenohumeral capsule function. Journal of Biomechanical Engineering 2010; 132 (12):121003.

71. DiGiovine NM, Jobe FW, Pink M, Perry J. An electromyographic analysis of the upper extremity in pitching. Journal of Shoulder and Elbow Surgery 1992; 1 (1):15-25.

72. Yeh M-L, Lintner D, Luo Z-P. Stress distribution in the superior labrum during throwing motion. The American Journal of Sports Medicine 2005; 33 (3):395-401.

73. Carey J, Small CF, Pichora DR. In situ compressive properties of the glenoid labrum. Journal of Biomedical Materials Research 2000; 51 (4):711-716.

74. Smith CD, Masouros SD, Hill AM, Wallace AL, Amis AA, Bull AM. Tensile properties of the human glenoid labrum. Journal of Anatomy 2008; 212 (1):49-54.

75. Yao J, Snibbe J, Maloney M, Lerner AL. Stresses and strains in the medial meniscus of an ACL deficient knee under anterior loading: a finite element analysis with image-based experimental validation. Journal of Biomechanical Engineering 2006; 128 (1):135-141.

76. Weiss JA, Gardiner JC, Bonifasi-Lista C. Ligament material behavior is nonlinear, viscoelastic and rate-independent under shear loading. Journal of Biomechanics 2002; 35 (7):943-950.

77. Drury N, Ellis B, Weiss J, McMahon P, Debski R. Finding consistent strain distributions in the glenohumeral capsule between two subjects: implications for development of physical examinations. Journal of Biomechanics 2011; 44 (4):607-613.

78. Büchler P, Farron A. Benefits of an anatomical reconstruction of the humeral head during shoulder arthroplasty: a finite element analysis. Clinical Biomechanics (Bristol, Avon) 2004; 19 (1):16-23.

79. Bigliani LU, Kelkar R, Flatow EL, Pollock RG, Mow VC. Glenohumeral Stability: Biomechanical Properties of Passive and Active Stabilizers. Clinical Orthopaedics and Related Research 1996; 330:13-30.

80. Quental C, Folgado J, Fernandes PR, Monteiro J. Subject-specific bone remodelling of the scapula. Computer Methods in Biomechanics and Biomedical Engineering 2014; 17 (10):1129-1143.

81. Campoli G, Bolsterlee B, van der Helm F, Weinans H, Zadpoor AA. Effects of densitometry, material mapping and load estimation uncertainties on the accuracy of

patient-specific finite-element models of the scapula. Journal of the Royal Society Interface 2014; 11 (93):20131146.

82. Friedman RJ, LaBerge M, Dooley RL, O'Hara AL. Finite element modeling of the glenoid component: effect of design parameters on stress distribution. Journal of Shoulder and Elbow Surgery 1992; 1 (5):261-270.

83. Lacroix D, Murphy LA, Prendergast PJ. Three-dimensional finite element analysis of glenoid replacement prostheses: A comparison of keeled and pegged anchorage systems. Journal of Biomechanical Engineering 2000; 122 (4):430-436.

84. Murphy LA, Prendergast PJ. Acromion-fixation of glenoid components in total shoulder arthroplasty. Journal of Biomechanics 2005; 38 (8):1702-1711.

85. Lacroix D, Prendergast PJ. Stress analysis of glenoid component designs for shoulder arthroplasty. Proceedings of the Institution of Mechanical Engineers, Part H: Journal of Engineering in Medicine 1997; 211 (6):467-474.

86. Terrier A, Buchler P, Farron A. Influence of glenohumeral conformity on glenoid stresses after total shoulder arthroplasty. Journal of Shoulder and Elbow Surgery 2006; 15 (4):515-520.

87. Hopkins AR, Hansen UN, Amis AA, Emery R. The effects of glenoid component alignment variations on cement mantle stresses in total shoulder arthroplasty. Journal of Shoulder and Elbow Surgery 2004; 13 (6):668-675.

88. Stone KD, Grabowski JJ, Cofield RH, Morrey BF, An KN. Stress analyses of glenoid components in total shoulder arthroplasty. Journal of Shoulder and Elbow Surgery 1999; 8 (2):151-158.

89. Quental C, Fernandes P, Monteiro J, Folgado J. Bone remodelling of the scapula after a total shoulder arthroplasty. Biomechanics and Modeling in Mechanobiology 2014; 13 (4):827-838.

90. Terrier A, Buchler P, Farron A. Bone-cement interface of the glenoid component: stress analysis for varying cement thickness. Clinical Biomechanics (Bristol, Avon) 2005; 20 (7):710-717.

91. Gupta S, van der Helm FC, van Keulen F. The possibilities of uncemented glenoid component--a finite element study. Clinical Biomechanics (Bristol, Avon) 2004; 19 (3):292-302.

92. Terrier A, Merlini F, Pioletti DP, Farron A. Comparison of polyethylene wear in anatomical and reversed shoulder prostheses. Journal of Bone and Joint Surgery - British Volume 2009; 91 (7):977-982.

93. Webb JD, Blemker SS, Delp SL. 3D finite element models of shoulder muscles for computing lines of actions and moment arms. Computer Methods in Biomechanics and Biomedical Engineering 2012; 17 (8):829-837.

94. Zou Z, Chávez-Arreola A, Mandal P, Board TN, Alonso-Rasgado T. Optimization of the position of the acetabulum in a ganz periacetabular osteotomy by finite element analysis. Journal of Orthopaedic Research 2013; 31 (3):472-479.

95. Wang J, Qian Z, Ren L, Ren L. A dynamic finite element model of human cervical spine with in vivo kinematic validation. Chinese Science Bulletin 2014; 59 (33):4578-4588.

96. Holzbaur KR, Murray WM, Delp SL. A model of the upper extremity for simulating musculoskeletal surgery and analyzing neuromuscular control. Annals of Biomedical Engineering 2005; 33 (6):829-840.

97. Blemker SS, Pinsky PM, Delp SL. A 3D model of muscle reveals the causes of nonuniform strains in the biceps brachii. Journal of Biomechanics 2005; 38 (4):657-665.

98. Gupta S, van der Helm F. Load transfer across the scapula during humeral abduction. Journal of Biomechanics 2004; 37 (7):1001-1009.

99. Speirs AD, Heller MO, Duda GN, Taylor WR. Physiologically based boundary conditions in finite element modelling. Journal of Biomechanics 2007; 40 (10):2318-2323.

100. Qian ZH, Ren L, Ding Y, Hutchinson JR, Ren LQ. A Dynamic Finite Element Analysis of Human Foot Complex in the Sagittal Plane during Level Walking. Plos One 2013; 8 (11):e79424.

101. Gupta S, Helm FCTvd, Sterk JC, Keulen Fv, Kaptein BL. Development and experimental validation of a three-dimensional finite element model of the human scapula. Proceedings of the Institution of Mechanical Engineers, Part H: Journal of Engineering in Medicine 2004; 218 (2):127-142.

102. Clarke E, Martin J, d'Entremont A, Pandy M, Wilson D, Herbert R. A non-invasive, 3D, dynamic MRI method for measuring muscle moment arms in vivo: Demonstration in the human ankle joint and Achilles tendon. Medical Engineering and Physics 2015; 37 (1):93-99.

103. De Sá Rebelo M, Moreno RA, Gobbi RG, Camanho GL, Ávila LFR, Demange MK, Pecora JR, Gutierrez MA Description of patellar movement by 3D parameters obtained from dynamic CT acquisition. In: SPIE Medical Imaging, 2014. International Society for Optics and Photonics, pp 903538-903538-903539

104. Roriz P, Carvalho L, Frazão O, Santos JL, Simões JA. From conventional sensors to fibre optic sensors for strain and force measurements in biomechanics applications: A review. Journal of Biomechanics 2014; 47 (6):1251-1261.

105. Cook D, Julias M, Nauman E. Biological variability in biomechanical engineering research: Significance and meta-analysis of current modeling practices. Journal of Biomechanics 2014; 47 (6):1241-1250.

106. Anderson AE, Peters CL, Tuttle BD, Weiss JA. Subject-specific finite element model of the pelvis: development, validation and sensitivity studies. Journal of Biomechanical Engineering 2005; 127 (3):364-373.

107. Schileo E, Taddei F, Malandrino A, Cristofolini L, Viceconti M. Subject-specific finite element models can accurately predict strain levels in long bones. Journal of Biomechanics 2007; 40 (13):2982-2989.

108. Hafez M, Chelule K, Seedhom B, Sherman K. Computer-assisted total knee arthroplasty using patient-specific templating. Clinical Orthopaedics and Related Research 2006; 444:184-192.

109. Lombardi Jr AV, Berend KR, Adams JB, White D, Chelule K, Seedhom B. Patient-specific approach in total knee arthroplasty. Orthopedics 2008; 31 (9):927.

110. Ren L, Jones RK, Howard D. Whole body inverse dynamics over a complete gait cycle based only on measured kinematics. Journal of Biomechanics 2008; 41 (12):2750-2759.

111. Ludewig PM, Behrens SA, Meyer SM, Spoden SM, Wilson LA. Three-dimensional clavicular motion during arm elevation: reliability and descriptive data. Journal of Orthopaedic and Sports Physical Therapy 2004; 34 (3):140-149.

112. Warner MB, Chappell PH, Stokes MJ. Measuring scapular kinematics during arm lowering using the acromion marker cluster. Human Movement Science 2012; 31 (2):386-396.

113. Winter DA. Biomechanics and motor control of human movement. John Wiley & Sons, Inc., Hoboken, New Jersey, 2005.

114. Cappozzo A, Della Croce U, Leardini A, Chiari L. Human movement analysis using stereophotogrammetry: Part 1: theoretical background. Gait and Posture 2005; 21 (2):186-196.

115. Wu G, van der Helm FC, Veeger HE, Makhsous M, Van Roy P, Anglin C, Nagels J, Karduna AR, McQuade K, Wang X, Werner FW, Buchholz B. ISB recommendation on definitions of joint coordinate systems of various joints for the reporting of human joint motion--Part II: shoulder, elbow, wrist and hand. Journal of Biomechanics 2005; 38 (5):981-992.

116. Meskers C, Van der Helm FC, Rozendaal L, Rozing P. In vivo estimation of the glenohumeral joint rotation center from scapular bony landmarks by linear regression. Journal of Biomechanics 1997; 31 (1):93-96.

117. Potvin J, Brown S. Less is more: high pass filtering, to remove up to 99% of the surface EMG signal power, improves EMG-based biceps brachii muscle force estimates. Journal of Electromyography and Kinesiology 2004; 14 (3):389-399.

118. Peterson SL, Rayan GM. Shoulder and upper arm muscle architecture. Journal of Hand Surgery 2011; 36 (5):881-889.

119. Ali MA, Sundaraj K, Ahmad RB, Ahamed NU, Islam MA, Sundaraj S. Evaluation of repetitive isometric contractions on the heads of triceps brachii muscle during grip force exercise. Technology and Health Care 2014; 22 (4):617-625.

120. Kelly BT, Kadrmas WR, Speer KP. The Manual Muscle Examination for Rotator Cuff Strength An Electromyographic Investigation. The American Journal of Sports Medicine 1996; 24 (5):581-588.

121. Ha S-m, Cynn H-s, Kwon O-y, Park K-n, Kim G-m. A reliability of electromyographic normalization methods for the infraspinatus muscle in healthy subjects. Journal of Human Kinetics 2013; 36 (1):69-76.

122. Criswell E. Cram's introduction to surface electromyography. Jones & Bartlett Publishers, 2010.

123. Ekstrom RA, Soderberg GL, Donatelli RA. Normalization procedures using maximum voluntary isometric contractions for the serratus anterior and trapezius muscles during surface EMG analysis. Journal of Electromyography and Kinesiology 2005; 15 (4):418-428.

124. Orozco-Levi M, Gea J, Monells J, Aran X, Aguar M, Broquetas J. Activity of latissimus dorsi muscle during inspiratory threshold loads. European Respiratory Journal 1995; 8 (3):441-445.

125. Werner CM, Ruckstuhl T, Müller R, Zanetti M, Gerber C. Influence of psychomotor skills and innervation patterns on results of latissimus dorsi tendon transfer for irreparable rotator cuff tears. Journal of Shoulder and Elbow Surgery 2008; 17 (1):S22-S28.

126. Park HS, Kim JY, Kim JG, Choi SW, Kim Y. A new position measurement system using a motion-capture camera for wind tunnel tests. Sensors 2013; 13 (9):12329-12344.

127. Nigg BM. Biomechanics of the musculo-skeletal system, vol 2. 2nd edition edn., 1999.

128. Anderson FC, Pandy MG. Static and dynamic optimization solutions for gait are practically equivalent. Journal of Biomechanics 2001; 34 (2):153-161.

129. Erdemir A, McLean S, Herzog W, van den Bogert AJ. Model-based estimation of muscle forces exerted during movements. Clinical Biomechanics 2007; 22 (2):131-154.

130. Delp SL, Anderson FC, Arnold AS, Loan P, Habib A, John CT, Guendelman E, Thelen DG. OpenSim: open-source software to create and analyze dynamic simulations of movement. IEEE Transactions on Biomedical Engineering 2007; 54 (11):1940-1950.

131. Seth A, Sherman M, Reinbolt JA, Delp SL. OpenSim: a musculoskeletal modeling and simulation framework for in silico investigations and exchange. Procedia Iutam 2011; 2:212-232.

132. Anderson F, Guendelman E, Habib A, Hamner S, Holzbaur K, John C, Ku J, Liu M, Loan P, Reinbolt J. OpenSim user’s guide. Palo Alto: Stanford University, 2008.

133. Steele KM, Tresch MC, Perreault EJ. The number and choice of muscles impact the results of muscle synergy analyses. Frontiers in Computational Neuroscience 2013; 7:105.

134. Holzbaur KR, Delp SL, Gold GE, Murray WM. Moment-generating capacity of upper limb muscles in healthy adults. Journal of Biomechanics 2007; 40 (11):2442-2449.

135. Gatti CJ, Dickerson CR, Chadwick EK, Mell AG, Hughes RE. Comparison of model-predicted and measured moment arms for the rotator cuff muscles. Clinical Biomechanics 2007; 22 (6):639-644.

136. Inman VT, Abbott LC. Observations on the function of the shoulder joint. Journal of Bone and Joint Surgery - American Volume 1944; 26 (1):1-30.

137. Sins L, Tétreault P, Hagemeister N, Nuño N. Adaptation of the AnyBody™ Musculoskeletal Shoulder Model to the Nonconforming Total Shoulder Arthroplasty Context. Journal of Biomechanical Engineering 2015; 137 (10):101006-101006.

138. Hansen ML, Otis JC, Johnson JS, Cordasco FA, Craig EV, Warren RF. Biomechanics of Massive Rotator Cuff Tears: Implications for Treatment. Journal of Bone and Joint Surgery - American Volume 2008; 90 (2):316-325.

139. Quental C, Folgado J, Ambrósio J, Monteiro J. Critical analysis of musculoskeletal modelling complexity in multibody biomechanical models of the upper limb. Computer Methods in Biomechanics and Biomedical Engineering 2015; 18 (7):749-759.

140. Sun W, Lal P. Recent development on computer aided tissue engineering—a review. Computer Methods and Programs in Biomedicine 2002; 67 (2):85-103.

141. Kröner E, Westenberg J, van der Geest R, Brouwer N, Doornbos J, Kooi M, van der Wall E, Lamb H, Siebelink H. High field carotid vessel wall imaging: A study on reproducibility. European Journal of Radiology 2013; 82 (4):680-685.

142. Krawczyk DC, Boggan AL, McClelland MM, Bartlett JC. The neural organization of perception in chess experts. Neuroscience Letters 2011; 499 (2):64-69.

143. Lumsdaine W, Smith A, Walker RG, Benz D, Mohammed KD, Stewart F. Morphology of the humeral insertion of the supraspinatus and infraspinatus tendons: Application to rotator cuff repair. Clinical Anatomy 2015; 28 (6):767-773.

144. Rao AG, Kim TK, Chronopoulos E, McFarland EG. Anatomical variants in the anterosuperior aspect of the glenoid labrum. Journal of Bone and Joint Surgery - American Volume 2003; 85 (4):653-659.

145. Yeh L, Kwak S, Kim Y-S, Chou DS, Muhle C, Skaf A, Trudell D, Resnick D. Evaluation of articular cartilage thickness of the humeral head and the glenoid fossa by MR arthrography: anatomic correlation in cadavers. Skeletal Radiology 1998; 27 (9):500-504.

146. Simulia AV. 6.13 Documentation. Dassault systemes. 2013.

147. Bucki M, Lobos C, Payan Y. A fast and robust patient specific finite element mesh registration technique: application to 60 clinical cases. Medical Image Analysis 2010; 14 (3):303-317.

148. Gefen A, Megido-Ravid M, Itzchak Y, Arcan M. Biomechanical analysis of the three-dimensional foot structure during gait: a basic tool for clinical applications. Journal of Biomechanical Engineering 2000; 122 (6):630-639.

149. Verim Ö, Taşgetiren S, Er MS, Timur M, Yuran AF. Anatomical comparison and evaluation of human proximal femurs modeling via different devices and FEM analysis. The International Journal of Medical Robotics and Computer Assisted Surgery 2013; 9 (2):e19-e24.

150. Fung Y-c. A first course in continuum mechanics. Englewood Cliffs, NJ, Prentice-Hall, Inc., 1977.

151. Babuska I, Oden JT. Verification and validation in computational engineering and science: basic concepts. Computer methods in applied mechanics and engineering 2004; 193 (36):4057-4066.

152. Terrier A, Aeberhard M, Michellod Y, Mullhaupt P, Gillet D, Farron A, Pioletti DP. A musculoskeletal shoulder model based on pseudo-inverse and null-space optimization. Medical Engineering and Physics 2010; 32 (9):1050-1056.

153. Bergmann G, Graichen F, Bender A, Kääb M, Rohlmann A, Westerhoff P. In vivo glenohumeral contact forces—measurements in the first patient 7 months postoperatively. Journal of Biomechanics 2007; 40 (10):2139-2149.

154. Poppen N, Walker P. Forces at the glenohumeral joint in abduction. Clinical Orthopaedics and Related Research 1978; 135:165-170.

155. Terrier A, Vogel A, Capezzali M, Farron A. An algorithm to allow humerus translation in the indeterminate problem of shoulder abduction. Medical Engineering and Physics 2008; 30 (6):710-716.

156. Matsuki K, Matsuki KO, Yamaguchi S, Ochiai N, Sasho T, Sugaya H, Toyone T, Wada Y, Takahashi K, Banks SA. Dynamic in vivo glenohumeral kinematics during scapular plane abduction in healthy shoulders. Journal of Orthopaedic and Sports Physical Therapy 2012; 42 (2):96-104.

157. Neer CS. Impingement lesions. Clinical Orthopaedics and Related Research 1983; 173:70-77.

158. DePalma A, Callery G, Bennett G. Variational anatomy and degenerative lesions of the shoulder joint. Instructional Course Lectures 1949; 6:255-281.

159. Maffulli N, Furia JP. Rotator Cuff Disorders: Basic Science and Clinical Medicine. JP Medical Ltd, 2012.

160. Lippitt S, Mstsen F. Mechanisms of glenohumeral joint stability. Clinical Orthopaedics and Related Research 1993; 291:20-28.

161. Lippitt SB, Vanderhooft JE, Harris SL, Sidles JA, Harryman DT, Matsen FA. Glenohumeral stability from concavity-compression: a quantitative analysis. Journal of Shoulder and Elbow Surgery 1993; 2 (1):27-35.

162. Halder A, Kuhl S, Zobitz M, Larson D, An K-N. Effects of the glenoid labrum and glenohumeral abduction on stability of the shoulder joint through concavity-compression. Journal of Bone and Joint Surgery - American Volume 2001; 83 (7):1062-1069.

163. Burkhart SS. Fluoroscopic Comparison of Kinematic Patterns in Massive Rotator Cuff Tears: A Suspension Bridge Model. Clinical Orthopaedics and Related Research 1992; 284:144-152.

164. Paletta GA, Warner JJ, Warren RF, Deutsch A, Altchek DW. Shoulder kinematics with two-plane x-ray evaluation in patients with anterior instability or rotator cuff tearing. Journal of Shoulder and Elbow Surgery 1997; 6 (6):516-527.

165. Sharkey NA, Marder RA. The rotator cuff opposes superior translation of the humeral head. The American Journal of Sports Medicine 1995; 23 (3):270-275.

166. Thompson WO, Debski RE, Boardman ND, Taskiran E, Warner JJ, Fu FH, Woo SL-Y. A biomechanical analysis of rotator cuff deficiency in a cadaveric model. The American Journal of Sports Medicine 1996; 24 (3):286-292.

Appendices

Appendix A: MATLAB coding

(1) Raw experiment data coordinates transformation and smoothing

```
clear;
t=[-1,0,0;0,0,1;0,1,0];
b12=cell(1,8);
b13=cell(1,8);
b14=cell(1,8);
b15=cell(1,8);
b18=cell(1,8);
b19=cell(1,8);
b20=cell(1,8);
data12=xlsread('C:\Users\mbgnjmz8\Dropbox\Research\Matlab calculation\scaption 8 markers\Scaption RAW data','Scaption_12','B10:Y1209');
data13=xlsread('C:\Users\mbgnjmz8\Dropbox\Research\Matlab calculation\scaption 8 markers\Scaption RAW data','Scaption_13','B10:Y1209');
data14=xlsread('C:\Users\mbgnjmz8\Dropbox\Research\Matlab calculation\scaption 8 markers\Scaption RAW data','Scaption_14','B10:Y1209');
data15=xlsread('C:\Users\mbgnjmz8\Dropbox\Research\Matlab calculation\scaption 8 markers\Scaption RAW data','Scaption_15','B10:Y1209');
data18=xlsread('C:\Users\mbgnjmz8\Dropbox\Research\Matlab calculation\scaption 8 markers\Scaption RAW data','Scaption_18','B10:Y1209');
data19=xlsread('C:\Users\mbgnjmz8\Dropbox\Research\Matlab calculation\scaption 8 markers\Scaption RAW data','Scaption_19','B10:Y1209');
data20=xlsread('C:\Users\mbgnjmz8\Dropbox\Research\Matlab calculation\scaption 8 markers\Scaption RAW data','Scaption_20','B10:Y1209');
for i=1:8
b12(i)=[data12(:,(3*i-2)),data12(:,(3*i-1)),data12(:,(3*i))]*t;
end
S12=cell2mat(b12);
for i=1:8
b13(i)=[data13(:,(3*i-2)),data13(:,(3*i-1)),data13(:,(3*i))]*t;
end
S13=cell2mat(b13);
for i=1:8
```

```
b14(i)=[data14(:,(3*i-2)),data14(:,(3*i-1)),data14(:,(3*i))]*t;
end
S14=cell2mat(b14);
for i=1:8
b15(i)=[data15(:,(3*i-2)),data15(:,(3*i-1)),data15(:,(3*i))]*t;
end
S15=cell2mat(b15);
for i=1:8
b18(i)=[data18(:,(3*i-2)),data18(:,(3*i-1)),data18(:,(3*i))]*t;
end
S18=cell2mat(b18);
for i=1:8
b19(i)=[data19(:,(3*i-2)),data19(:,(3*i-1)),data19(:,(3*i))]*t;
end
S19=cell2mat(b19);
for i=1:8
b20(i)=[data20(:,(3*i-2)),data20(:,(3*i-1)),data20(:,(3*i))]*t;
end
S20=cell2mat(b20);
%xlswrite('C:\Users\mbgnjmz8\Dropbox\Research\Matlab calculation\scaption 8 markers\results_coordinates_transformation.xlsx',S12,'Scaption_12','B10:Y1209');
%xlswrite('C:\Users\mbgnjmz8\Dropbox\Research\Matlab calculation\scaption 8 markers\results_coordinates_transformation.xlsx',S13,'Scaption_13','B10:Y1209');
%xlswrite('C:\Users\mbgnjmz8\Dropbox\Research\Matlab calculation\scaption 8 markers\results_coordinates_transformation.xlsx',S14,'Scaption_14','B10:Y1209');
%xlswrite('C:\Users\mbgnjmz8\Dropbox\Research\Matlab calculation\scaption 8 markers\results_coordinates_transformation.xlsx',S15,'Scaption_15','B10:Y1209');
%xlswrite('C:\Users\mbgnjmz8\Dropbox\Research\Matlab calculation\scaption 8 markers\results_coordinates_transformation.xlsx',S18,'Scaption_18','B10:Y1209');
%xlswrite('C:\Users\mbgnjmz8\Dropbox\Research\Matlab calculation\scaption 8 markers\results_coordinates_transformation.xlsx',S19,'Scaption_19','B10:Y1209');
%xlswrite('C:\Users\mbgnjmz8\Dropbox\Research\Matlab calculation\scaption 8 markers\results_coordinates_transformation.xlsx',S20,'Scaption_20','B10:Y1209');
[b,a]=butter(4,0.03);%Wn=3(from paper)/(200(sampling frequency)/2)
Scaption12=filtfilt(b,a,S12);
Scaption13=filtfilt(b,a,S13);
Scaption14=filtfilt(b,a,S14);
```

```
Scaption15=filtfilt(b,a,S15);
Scaption18=filtfilt(b,a,S18);
Scaption19=filtfilt(b,a,S19);
Scaption20=filtfilt(b,a,S20);
%xlswrite('C:\Users\mbgnjmz8\Dropbox\Research\Matlab calculation\scaption 8 markers\results_filtered.xlsx',Scaption12,'Scaption_12','B10:Y1209');
%xlswrite('C:\Users\mbgnjmz8\Dropbox\Research\Matlab calculation\scaption 8 markers\results_filtered.xlsx',Scaption13,'Scaption_13','B10:Y1209');
%xlswrite('C:\Users\mbgnjmz8\Dropbox\Research\Matlab calculation\scaption 8 markers\results_filtered.xlsx',Scaption14,'Scaption_14','B10:Y1209');
%xlswrite('C:\Users\mbgnjmz8\Dropbox\Research\Matlab calculation\scaption 8 markers\results_filtered.xlsx',Scaption15,'Scaption_15','B10:Y1209');
%xlswrite('C:\Users\mbgnjmz8\Dropbox\Research\Matlab calculation\scaption 8 markers\results_filtered.xlsx',Scaption18,'Scaption_18','B10:Y1209');
%xlswrite('C:\Users\mbgnjmz8\Dropbox\Research\Matlab calculation\scaption 8 markers\results_filtered.xlsx',Scaption19,'Scaption_19','B10:Y1209');
%xlswrite('C:\Users\mbgnjmz8\Dropbox\Research\Matlab calculation\scaption 8 markers\results_filtered.xlsx',Scaption20,'Scaption_20','B10:Y1209');

xlswrite('C:\Users\mbgnjmz8\Dropbox\Research\Matlab calculation\scaption 8 markers\OpeSim_format.xlsx',Scaption12,'Scaption_12','C7:Z1206');
xlswrite('C:\Users\mbgnjmz8\Dropbox\Research\Matlab calculation\scaption 8 markers\OpeSim_format.xlsx',Scaption13,'Scaption_13','C7:Z1206');
xlswrite('C:\Users\mbgnjmz8\Dropbox\Research\Matlab calculation\scaption 8 markers\OpeSim_format.xlsx',Scaption14,'Scaption_14','C7:Z1206');
xlswrite('C:\Users\mbgnjmz8\Dropbox\Research\Matlab calculation\scaption 8 markers\OpeSim_format.xlsx',Scaption15,'Scaption_15','C7:Z1206');
xlswrite('C:\Users\mbgnjmz8\Dropbox\Research\Matlab calculation\scaption 8 markers\OpeSim_format.xlsx',Scaption18,'Scaption_18','C7:Z1206');
xlswrite('C:\Users\mbgnjmz8\Dropbox\Research\Matlab calculation\scaption 8 markers\OpeSim_format.xlsx',Scaption19,'Scaption_19','C7:Z1206');
xlswrite('C:\Users\mbgnjmz8\Dropbox\Research\Matlab calculation\scaption 8 markers\OpeSim_format.xlsx',Scaption20,'Scaption_20','C7:Z1206');
```

(2) Muscle forces normalisation

```
% cubic spline interpolation
clear;
clc;
```

```
x12=xlsread('C:\Users\mbgnjmz8\Dropbox\Research\Matlab calculation\Normalisation\muscle force','IK_MF_12','A3:A136');
y12DEL1=xlsread('C:\Users\mbgnjmz8\Dropbox\Research\Matlab calculation\Normalisation\muscle force','IK_MF_12','H3:H136');
y12DEL2=xlsread('C:\Users\mbgnjmz8\Dropbox\Research\Matlab calculation\Normalisation\muscle force','IK_MF_12','I3:I136');
y12DEL3=xlsread('C:\Users\mbgnjmz8\Dropbox\Research\Matlab calculation\Normalisation\muscle force','IK_MF_12','J3:J136');
y12SUP=xlsread('C:\Users\mbgnjmz8\Dropbox\Research\Matlab calculation\Normalisation\muscle force','IK_MF_12','K3:K136');
y12INF=xlsread('C:\Users\mbgnjmz8\Dropbox\Research\Matlab calculation\Normalisation\muscle force','IK_MF_12','L3:L136');
y12SUB=xlsread('C:\Users\mbgnjmz8\Dropbox\Research\Matlab calculation\Normalisation\muscle force','IK_MF_12','M3:M136');
y12TM=xlsread('C:\Users\mbgnjmz8\Dropbox\Research\Matlab calculation\Normalisation\muscle force','IK_MF_12','N3:N136');

xx=0:30;
F12DEL1=spline(x12,y12DEL1);
N12DEL1=ppval(F12DEL1,xx);
F12DEL2=spline(x12,y12DEL2);
N12DEL2=ppval(F12DEL2,xx);
F12DEL3=spline(x12,y12DEL3);
N12DEL3=ppval(F12DEL3,xx);
F12SUP=spline(x12,y12SUP);
N12SUP=ppval(F12SUP,xx);
F12INF=spline(x12,y12INF);
N12INF=ppval(F12INF,xx);
F12SUB=spline(x12,y12SUB);
N12SUB=ppval(F12SUB,xx);
F12TM=spline(x12,y12TM);
N12TM=ppval(F12TM,xx);

%plot(xx,N12DEL1);
%hold all;
%plot(xx,N12DEL2);
%hold all;
```

```
%plot(xx,N12DEL3);
%hold all;
%plot(xx,N12SUP);
%hold all;
%plot(xx,N12INF);
%hold all;
%plot(xx,N12SUB);
%hold all;
%plot(xx,N12TM);
%hold all;

x13=xlsread('C:\Users\mbgnjmz8\Dropbox\Research\Matlab calculation\Normalisation\muscle force','IK_MF_13','A3:A151');
y13DEL1=xlsread('C:\Users\mbgnjmz8\Dropbox\Research\Matlab calculation\Normalisation\muscle force','IK_MF_13','H3:H151');
y13DEL2=xlsread('C:\Users\mbgnjmz8\Dropbox\Research\Matlab calculation\Normalisation\muscle force','IK_MF_13','I3:I151');
y13DEL3=xlsread('C:\Users\mbgnjmz8\Dropbox\Research\Matlab calculation\Normalisation\muscle force','IK_MF_13','J3:J151');
y13SUP=xlsread('C:\Users\mbgnjmz8\Dropbox\Research\Matlab calculation\Normalisation\muscle force','IK_MF_13','K3:K151');
y13INF=xlsread('C:\Users\mbgnjmz8\Dropbox\Research\Matlab calculation\Normalisation\muscle force','IK_MF_13','L3:L151');
y13SUB=xlsread('C:\Users\mbgnjmz8\Dropbox\Research\Matlab calculation\Normalisation\muscle force','IK_MF_13','M3:M151');
y13TM=xlsread('C:\Users\mbgnjmz8\Dropbox\Research\Matlab calculation\Normalisation\muscle force','IK_MF_13','N3:N151');

xx=0:30;
F13DEL1=spline(x13,y13DEL1);
N13DEL1=ppval(F13DEL1,xx);
F13DEL2=spline(x13,y13DEL2);
N13DEL2=ppval(F13DEL2,xx);
F13DEL3=spline(x13,y13DEL3);
N13DEL3=ppval(F13DEL3,xx);
F13SUP=spline(x13,y13SUP);
N13SUP=ppval(F13SUP,xx);
```

```
F13INF=spline(x13,y13INF);
N13INF=ppval(F13INF,xx);
F13SUB=spline(x13,y13SUB);
N13SUB=ppval(F13SUB,xx);
F13TM=spline(x13,y13TM);
N13TM=ppval(F13TM,xx);

%plot(xx,N13DEL1);
%hold all;
%plot(xx,N13DEL2);
%hold all;
%plot(xx,N13DEL3);
%hold all;
%plot(xx,N13SUP);
%hold all;
%plot(xx,N13INF);
%hold all;
%plot(xx,N13SUB);
%hold all;
%plot(xx,N13TM);
%hold all;

x14=xlsread('C:\Users\mbgnjmz8\Dropbox\Research\Matlab calculation\Normalisation\muscle force','IK_MF_14','A3:A147');
y14DEL1=xlsread('C:\Users\mbgnjmz8\Dropbox\Research\Matlab calculation\Normalisation\muscle force','IK_MF_14','H3:H147');
y14DEL2=xlsread('C:\Users\mbgnjmz8\Dropbox\Research\Matlab calculation\Normalisation\muscle force','IK_MF_14','I3:I147');
y14DEL3=xlsread('C:\Users\mbgnjmz8\Dropbox\Research\Matlab calculation\Normalisation\muscle force','IK_MF_14','J3:J147');
y14SUP=xlsread('C:\Users\mbgnjmz8\Dropbox\Research\Matlab calculation\Normalisation\muscle force','IK_MF_14','K3:K147');
y14INF=xlsread('C:\Users\mbgnjmz8\Dropbox\Research\Matlab calculation\Normalisation\muscle force','IK_MF_14','L3:L147');
y14SUB=xlsread('C:\Users\mbgnjmz8\Dropbox\Research\Matlab calculation\Normalisation\muscle force','IK_MF_14','M3:M147');
```

```
y14TM=xlsread('C:\Users\mbgnjmz8\Dropbox\Research\Matlab calculation\Normalisation\muscle force','IK_MF_14','N3:N147');

xx=0:30;
F14DEL1=spline(x14,y14DEL1);
N14DEL1=ppval(F14DEL1,xx);
F14DEL2=spline(x14,y14DEL2);
N14DEL2=ppval(F14DEL2,xx);
F14DEL3=spline(x14,y14DEL3);
N14DEL3=ppval(F14DEL3,xx);
F14SUP=spline(x14,y14SUP);
N14SUP=ppval(F14SUP,xx);
F14INF=spline(x14,y14INF);
N14INF=ppval(F14INF,xx);
F14SUB=spline(x14,y14SUB);
N14SUB=ppval(F14SUB,xx);
F14TM=spline(x14,y14TM);
N14TM=ppval(F14TM,xx);

%plot(xx,N14DEL1);
%hold all;
%plot(xx,N14DEL2);
%hold all;
%plot(xx,N14DEL3);
%hold all;
%plot(xx,N14SUP);
%hold all;
%plot(xx,N14INF);
%hold all;
%plot(xx,N14SUB);
%hold all;
%plot(xx,N14TM);
%hold all;

x15=xlsread('C:\Users\mbgnjmz8\Dropbox\Research\Matlab calculation\Normalisation\muscle force','IK_MF_15','A3:A161');
```

```
y15DEL1=xlsread('C:\Users\mbgnjmz8\Dropbox\Research\Matlab calculation\Normalisation\muscle force','IK_MF_15','H3:H161');
y15DEL2=xlsread('C:\Users\mbgnjmz8\Dropbox\Research\Matlab calculation\Normalisation\muscle force','IK_MF_15','I3:I161');
y15DEL3=xlsread('C:\Users\mbgnjmz8\Dropbox\Research\Matlab calculation\Normalisation\muscle force','IK_MF_15','J3:J161');
y15SUP=xlsread('C:\Users\mbgnjmz8\Dropbox\Research\Matlab calculation\Normalisation\muscle force','IK_MF_15','K3:K161');
y15INF=xlsread('C:\Users\mbgnjmz8\Dropbox\Research\Matlab calculation\Normalisation\muscle force','IK_MF_15','L3:L161');
y15SUB=xlsread('C:\Users\mbgnjmz8\Dropbox\Research\Matlab calculation\Normalisation\muscle force','IK_MF_15','M3:M161');
y15TM=xlsread('C:\Users\mbgnjmz8\Dropbox\Research\Matlab calculation\Normalisation\muscle force','IK_MF_15','N3:N161');

xx=0:30;
F15DEL1=spline(x15,y15DEL1);
N15DEL1=ppval(F15DEL1,xx);
F15DEL2=spline(x15,y15DEL2);
N15DEL2=ppval(F15DEL2,xx);
F15DEL3=spline(x15,y15DEL3);
N15DEL3=ppval(F15DEL3,xx);
F15SUP=spline(x15,y15SUP);
N15SUP=ppval(F15SUP,xx);
F15INF=spline(x15,y15INF);
N15INF=ppval(F15INF,xx);
F15SUB=spline(x15,y15SUB);
N15SUB=ppval(F15SUB,xx);
F15TM=spline(x15,y15TM);
N15TM=ppval(F15TM,xx);

%plot(xx,N15DEL1);
%hold all;
%plot(xx,N15DEL2);
%hold all;
%plot(xx,N15DEL3);
%hold all;
```

```
%plot(xx,N15SUP);
%hold all;
%plot(xx,N15INF);
%hold all;
%plot(xx,N15SUB);
%hold all;
%plot(xx,N15TM);
%hold all;

x18=xlsread('C:\Users\mbgnjmz8\Dropbox\Research\Matlab calculation\Normalisation\muscle force','IK_MF_18','A3:A179');
y18DEL1=xlsread('C:\Users\mbgnjmz8\Dropbox\Research\Matlab calculation\Normalisation\muscle force','IK_MF_18','H3:H179');
y18DEL2=xlsread('C:\Users\mbgnjmz8\Dropbox\Research\Matlab calculation\Normalisation\muscle force','IK_MF_18','I3:I179');
y18DEL3=xlsread('C:\Users\mbgnjmz8\Dropbox\Research\Matlab calculation\Normalisation\muscle force','IK_MF_18','J3:J179');
y18SUP=xlsread('C:\Users\mbgnjmz8\Dropbox\Research\Matlab calculation\Normalisation\muscle force','IK_MF_18','K3:K179');
y18INF=xlsread('C:\Users\mbgnjmz8\Dropbox\Research\Matlab calculation\Normalisation\muscle force','IK_MF_18','L3:L179');
y18SUB=xlsread('C:\Users\mbgnjmz8\Dropbox\Research\Matlab calculation\Normalisation\muscle force','IK_MF_18','M3:M179');
y18TM=xlsread('C:\Users\mbgnjmz8\Dropbox\Research\Matlab calculation\Normalisation\muscle force','IK_MF_18','N3:N179');

xx=0:30;
F18DEL1=spline(x18,y18DEL1);
N18DEL1=ppval(F18DEL1,xx);
F18DEL2=spline(x18,y18DEL2);
N18DEL2=ppval(F18DEL2,xx);
F18DEL3=spline(x18,y18DEL3);
N18DEL3=ppval(F18DEL3,xx);
F18SUP=spline(x18,y18SUP);
N18SUP=ppval(F18SUP,xx);
F18INF=spline(x18,y18INF);
N18INF=ppval(F18INF,xx);
```

```
F18SUB=spline(x18,y18SUB);
N18SUB=ppval(F18SUB,xx);
F18TM=spline(x18,y18TM);
N18TM=ppval(F18TM,xx);

%plot(xx,N18DEL1);
%hold all;
%plot(xx,N18DEL2);
%hold all;
%plot(xx,N18DEL3);
%hold all;
%plot(xx,N18SUP);
%hold all;
%plot(xx,N18INF);
%hold all;
%plot(xx,N18SUB);
%hold all;
%plot(xx,N18TM);
%hold all;

x19=xlsread('C:\Users\mbgnjmz8\Dropbox\Research\Matlab calculation\Normalisation\muscle force','IK_MF_19','A3:A152');
y19DEL1=xlsread('C:\Users\mbgnjmz8\Dropbox\Research\Matlab calculation\Normalisation\muscle force','IK_MF_19','H3:H152');
y19DEL2=xlsread('C:\Users\mbgnjmz8\Dropbox\Research\Matlab calculation\Normalisation\muscle force','IK_MF_19','I3:I152');
y19DEL3=xlsread('C:\Users\mbgnjmz8\Dropbox\Research\Matlab calculation\Normalisation\muscle force','IK_MF_19','J3:J152');
y19SUP=xlsread('C:\Users\mbgnjmz8\Dropbox\Research\Matlab calculation\Normalisation\muscle force','IK_MF_19','K3:K152');
y19INF=xlsread('C:\Users\mbgnjmz8\Dropbox\Research\Matlab calculation\Normalisation\muscle force','IK_MF_19','L3:L152');
y19SUB=xlsread('C:\Users\mbgnjmz8\Dropbox\Research\Matlab calculation\Normalisation\muscle force','IK_MF_19','M3:M152');
y19TM=xlsread('C:\Users\mbgnjmz8\Dropbox\Research\Matlab calculation\Normalisation\muscle force','IK_MF_19','N3:N152');
```

```
xx=0:30;
F19DEL1=spline(x19,y19DEL1);
N19DEL1=ppval(F19DEL1,xx);
F19DEL2=spline(x19,y19DEL2);
N19DEL2=ppval(F19DEL2,xx);
F19DEL3=spline(x19,y19DEL3);
N19DEL3=ppval(F19DEL3,xx);
F19SUP=spline(x19,y19SUP);
N19SUP=ppval(F19SUP,xx);
F19INF=spline(x19,y19INF);
N19INF=ppval(F19INF,xx);
F19SUB=spline(x19,y19SUB);
N19SUB=ppval(F19SUB,xx);
F19TM=spline(x19,y19TM);
N19TM=ppval(F19TM,xx);

%plot(xx,N19DEL1);
%hold all;
%plot(xx,N19DEL2);
%hold all;
%plot(xx,N19DEL3);
%hold all;
%plot(xx,N19SUP);
%hold all;
%plot(xx,N19INF);
%hold all;
%plot(xx,N19SUB);
%hold all;
%plot(xx,N19TM);
%hold all;

x20=xlsread('C:\Users\mbgnjmz8\Dropbox\Research\Matlab calculation\Normalisation\muscle force','IK_MF_20','A3:A220');
y20DEL1=xlsread('C:\Users\mbgnjmz8\Dropbox\Research\Matlab calculation\Normalisation\muscle force','IK_MF_20','H3:H220');
```

```
y20DEL2=xlsread('C:\Users\mbgnjmz8\Dropbox\Research\Matlab calculation\Normalisation\muscle force','IK_MF_20','I3:I220');
y20DEL3=xlsread('C:\Users\mbgnjmz8\Dropbox\Research\Matlab calculation\Normalisation\muscle force','IK_MF_20','J3:J220');
y20SUP=xlsread('C:\Users\mbgnjmz8\Dropbox\Research\Matlab calculation\Normalisation\muscle force','IK_MF_20','K3:K220');
y20INF=xlsread('C:\Users\mbgnjmz8\Dropbox\Research\Matlab calculation\Normalisation\muscle force','IK_MF_20','L3:L220');
y20SUB=xlsread('C:\Users\mbgnjmz8\Dropbox\Research\Matlab calculation\Normalisation\muscle force','IK_MF_20','M3:M220');
y20TM=xlsread('C:\Users\mbgnjmz8\Dropbox\Research\Matlab calculation\Normalisation\muscle force','IK_MF_20','N3:N220');

xx=0:30;
F20DEL1=spline(x20,y20DEL1);
N20DEL1=ppval(F20DEL1,xx);
F20DEL2=spline(x20,y20DEL2);
N20DEL2=ppval(F20DEL2,xx);
F20DEL3=spline(x20,y20DEL3);
N20DEL3=ppval(F20DEL3,xx);
F20SUP=spline(x20,y20SUP);
N20SUP=ppval(F20SUP,xx);
F20INF=spline(x20,y20INF);
N20INF=ppval(F20INF,xx);
F20SUB=spline(x20,y20SUB);
N20SUB=ppval(F20SUB,xx);
F20TM=spline(x20,y20TM);
N20TM=ppval(F20TM,xx);

%plot(xx,N20DEL1);
%hold all;
%plot(xx,N20DEL2);
%hold all;
%plot(xx,N20DEL3);
%hold all;
%plot(xx,N20SUP);
%hold all;
```

```
%plot(xx,N20INF);
%hold all;
%plot(xx,N20SUB);
%hold all;
%plot(xx,N20TM);
%hold all;

%MDEL1=(N12DEL1+N13DEL1+N14DEL1+N15DEL1+N18DEL1+N19DEL1+N20DEL1)/7;
%MDEL2=(N12DEL2+N13DEL2+N14DEL2+N15DEL2+N18DEL2+N19DEL2+N20DEL2)/7;
%MDEL3=(N12DEL3+N13DEL3+N14DEL3+N15DEL3+N18DEL3+N19DEL3+N20DEL3)/7;
%MSUP=(N12SUP+N13SUP+N14SUP+N15SUP+N18SUP+N19SUP+N20SUP)/7;
%MINF=(N12INF+N13INF+N14INF+N15INF+N18INF+N19INF+N20INF)/7;
%MSUB=(N12SUB+N13SUB+N14SUB+N15SUB+N18SUB+N19SUB+N20SUB)/7;
%MTM=(N12TM+N13TM+N14TM+N15TM+N18TM+N19TM+N20TM)/7;

MDEL1=(N13DEL1+N14DEL1+N15DEL1+N18DEL1+N19DEL1+N20DEL1)/6;
MDEL2=(N13DEL2+N14DEL2+N15DEL2+N18DEL2+N19DEL2+N20DEL2)/6;
MDEL3=(N13DEL3+N14DEL3+N15DEL3+N18DEL3+N19DEL3+N20DEL3)/6;
MSUP=(N13SUP+N14SUP+N15SUP+N18SUP+N19SUP+N20SUP)/6;
MINF=(N13INF+N14INF+N15INF+N18INF+N19INF+N20INF)/6;
MSUB=(N13SUB+N14SUB+N15SUB+N18SUB+N19SUB+N20SUB)/6;
MTM=(N13TM+N14TM+N15TM+N18TM+N19TM+N20TM)/6;

%xlswrite('C:\Users\mbgnjmz8\Dropbox\Research\Matlab
calculation\Normalisation\results.xlsx',MDEL1','average','C3:C33');
%xlswrite('C:\Users\mbgnjmz8\Dropbox\Research\Matlab
calculation\Normalisation\results.xlsx',MDEL2','average','D3:D33');
%xlswrite('C:\Users\mbgnjmz8\Dropbox\Research\Matlab
calculation\Normalisation\results.xlsx',MDEL3','average','E3:E33');
%xlswrite('C:\Users\mbgnjmz8\Dropbox\Research\Matlab
calculation\Normalisation\results.xlsx',MSUP','average','F3:F33');
%xlswrite('C:\Users\mbgnjmz8\Dropbox\Research\Matlab
calculation\Normalisation\results.xlsx',MINF','average','G3:G33');
%xlswrite('C:\Users\mbgnjmz8\Dropbox\Research\Matlab
calculation\Normalisation\results.xlsx',MSUB','average','H3:H33');
%xlswrite('C:\Users\mbgnjmz8\Dropbox\Research\Matlab
calculation\Normalisation\results.xlsx',MTM','average','I3:I33');
```

```
%Standard deviation
XDEL1=[N13DEL1;N14DEL1;N15DEL1;N18DEL1;N19DEL1;N20DEL1];
XDEL2=[N13DEL2;N14DEL2;N15DEL2;N18DEL2;N19DEL2;N20DEL2];
XDEL3=[N13DEL3;N14DEL3;N15DEL3;N18DEL3;N19DEL3;N20DEL3];
XSUP=[N13SUP;N14SUP;N15SUP;N18SUP;N19SUP;N20SUP];
XINF=[N13INF;N14INF;N15INF;N18INF;N19INF;N20INF];
XSUB=[N13SUB;N14SUB;N15SUB;N18SUB;N19SUB;N20SUB];
XTM=[N13TM;N14TM;N15TM;N18TM;N19TM;N20TM];
SDDEL1=std(XDEL1);
SDDEL2=std(XDEL2);
SDDEL3=std(XDEL3);
SDSUP=std(XSUP);
SDINF=std(XINF);
SDSUB=std(XSUB);
SDTM=std(XTM);
```

(3) Humeral centre estimation

The 4 points' coordinates in global coordinates were read off the model as shown in the table below.

	X	Y	Z
Point 1	-146.246574	-36.541317	90.53365
Point 2	-140.630635	-14.814765	93.880432
Point 3	-152.363161	-3.88294	87.120752
Point 4	-127.618991	-10.809304	74.494313

```
syms x y z r
S=solve('(x--146)^2+(y--36)^2+(z-90)^2==r^2','(x--140)^2+(y--14)^2+(z-93)^2==r^2','(x--152)^2+(y--3)^2+(z-87)^2==r^2','(x--127)^2+(y--10)^2+(z-74)^2==r^2','x','y','z','r');
x=S.x;
y=S.y;
z=S.z;
r=S.r;
x=vpa(x,4)
```

```
y=vpa(y,4)
z=vpa(z,4)
r=vpa(r,4)
```

(4) Pressure centre calculation

```
clear;
C0=xlsread('C:\Users\mbgnjmz8\Dropbox\Research\Matlab calculation\pressure center\glenoid-pressure','intact','P18:R952');
P0=xlsread('C:\Users\mbgnjmz8\Dropbox\Research\Matlab calculation\pressure center\glenoid-pressure','intact','V18:V952');
C1_6=xlsread('C:\Users\mbgnjmz8\Dropbox\Research\Matlab calculation\pressure center\glenoid-pressure','1_6','P18:R952');
P1_6=xlsread('C:\Users\mbgnjmz8\Dropbox\Research\Matlab calculation\pressure center\glenoid-pressure','1_6','V18:V952');
C1_3=xlsread('C:\Users\mbgnjmz8\Dropbox\Research\Matlab calculation\pressure center\glenoid-pressure','1_3','P18:R952');
P1_3=xlsread('C:\Users\mbgnjmz8\Dropbox\Research\Matlab calculation\pressure center\glenoid-pressure','1_3','V18:V952');
C1_2=xlsread('C:\Users\mbgnjmz8\Dropbox\Research\Matlab calculation\pressure center\glenoid-pressure','1_2','P18:R952');
P1_2=xlsread('C:\Users\mbgnjmz8\Dropbox\Research\Matlab calculation\pressure center\glenoid-pressure','1_2','V18:V952');
C2_3=xlsread('C:\Users\mbgnjmz8\Dropbox\Research\Matlab calculation\pressure center\glenoid-pressure','2_3','P18:R952');
P2_3=xlsread('C:\Users\mbgnjmz8\Dropbox\Research\Matlab calculation\pressure center\glenoid-pressure','2_3','V18:V952');
C5_6=xlsread('C:\Users\mbgnjmz8\Dropbox\Research\Matlab calculation\pressure center\glenoid-pressure','5_6','P18:R952');
P5_6=xlsread('C:\Users\mbgnjmz8\Dropbox\Research\Matlab calculation\pressure center\glenoid-pressure','5_6','V18:V952');
C21_24=xlsread('C:\Users\mbgnjmz8\Dropbox\Research\Matlab calculation\pressure center\glenoid-pressure','21_24','P18:R952');
P21_24=xlsread('C:\Users\mbgnjmz8\Dropbox\Research\Matlab calculation\pressure center\glenoid-pressure','21_24','V18:V952');
C22_24=xlsread('C:\Users\mbgnjmz8\Dropbox\Research\Matlab calculation\pressure center\glenoid-pressure','22_24','P18:R952');
```

P22_24=xlsread('C:\Users\mbgnjmz8\Dropbox\Research\Matlab calculation\pressure center\glenoid-pressure','22_24','V18:V952');

C23_24=xlsread('C:\Users\mbgnjmz8\Dropbox\Research\Matlab calculation\pressure center\glenoid-pressure','23_24','P18:R952');

P23_24=xlsread('C:\Users\mbgnjmz8\Dropbox\Research\Matlab calculation\pressure center\glenoid-pressure','23_24','V18:V952');

C93_96=xlsread('C:\Users\mbgnjmz8\Dropbox\Research\Matlab calculation\pressure center\glenoid-pressure','93_96','P18:R952');

P93_96=xlsread('C:\Users\mbgnjmz8\Dropbox\Research\Matlab calculation\pressure center\glenoid-pressure','93_96','V18:V952');

C94_96=xlsread('C:\Users\mbgnjmz8\Dropbox\Research\Matlab calculation\pressure center\glenoid-pressure','94_96','P18:R952');

P94_96=xlsread('C:\Users\mbgnjmz8\Dropbox\Research\Matlab calculation\pressure center\glenoid-pressure','94_96','V18:V952');

C95_96=xlsread('C:\Users\mbgnjmz8\Dropbox\Research\Matlab calculation\pressure center\glenoid-pressure','95_96','P18:R952');

P95_96=xlsread('C:\Users\mbgnjmz8\Dropbox\Research\Matlab calculation\pressure center\glenoid-pressure','95_96','V18:V952');

C1=xlsread('C:\Users\mbgnjmz8\Dropbox\Research\Matlab calculation\pressure center\glenoid-pressure','full','P18:R952');

P1=xlsread('C:\Users\mbgnjmz8\Dropbox\Research\Matlab calculation\pressure center\glenoid-pressure','full','V18:V952');

PC0=[sum(C0(:,1)'*P0),sum(C0(:,2)'*P0),sum(C0(:,3)'*P0)]/sum(P0);

PC1_6=[sum(C1_6(:,1)'*P1_6),sum(C1_6(:,2)'*P1_6),sum(C1_6(:,3)'*P1_6)]/sum(P1_6);

PC1_3=[sum(C1_3(:,1)'*P1_3),sum(C1_3(:,2)'*P1_3),sum(C1_3(:,3)'*P1_3)]/sum(P1_3);

PC1_2=[sum(C1_2(:,1)'*P1_2),sum(C1_2(:,2)'*P1_2),sum(C1_2(:,3)'*P1_2)]/sum(P1_2);

PC2_3=[sum(C2_3(:,1)'*P2_3),sum(C2_3(:,2)'*P2_3),sum(C2_3(:,3)'*P2_3)]/sum(P2_3);

PC5_6=[sum(C5_6(:,1)'*P5_6),sum(C5_6(:,2)'*P5_6),sum(C5_6(:,3)'*P5_6)]/sum(P5_6);

PC21_24=[sum(C21_24(:,1)'*P21_24),sum(C21_24(:,2)'*P21_24),sum(C21_24(:,3)'*P21_24)]/sum(P21_24);

PC22_24=[sum(C22_24(:,1)'*P22_24),sum(C22_24(:,2)'*P22_24),sum(C22_24(:,3)'*P22_24)]/sum(P22_24);

PC23_24=[sum(C23_24(:,1)'*P23_24),sum(C23_24(:,2)'*P23_24),sum(C23_24(:,3)'*P23_24)]/sum(P23_24);

PC93_96=[sum(C93_96(:,1)'*P93_96),sum(C93_96(:,2)'*P93_96),sum(C93_96(:,3)'*P93_96)]/sum(P93_96);

PC94_96=[sum(C94_96(:,1)'*P94_96),sum(C94_96(:,2)'*P94_96),sum(C94_96(:,3)'*P94_96)]/sum(P94_96);

```
PC95_96=[sum(C95_96(:,1)'*P95_96),sum(C95_96(:,2)'*P95_96),sum(C95_96(:,3)'*P95_96)]/sum(P95_96);
PC1=[sum(C1(:,1)'*P1),sum(C1(:,2)'*P1),sum(C1(:,3)'*P1)]/sum(P1);
```

Appendix B: Reprint of the published paper in Section 2.3: Review of finite element models of the human shoulder complex.

The main body of Section 2.3 consists of the attached publication:

Zheng M, Zou Z, Peach C, Ren L. Finite element models of the human shoulder complex: a review of their clinical implications and modelling techniques. International journal for numerical methods in biomedical engineering 2016;

The reprint of this paper is attached in the following pages.

INTERNATIONAL JOURNAL FOR NUMERICAL METHODS IN BIOMEDICAL ENGINEERING
Int. J. Numer. Meth. Biomed. Engng. (2016); e02777
Published online in Wiley Online Library (wileyonlinelibrary.com). DOI: 10.1002/cnm.2777

Finite element models of the human shoulder complex: a review of their clinical implications and modelling techniques

Manxu Zheng[1], Zhenmin Zou[1], Paulo jorge Da silva Bartolo[1], Chris Peach[1,2] and Lei Ren[1,*,†]

[1]*School of Mechanical, Aerospace and Civil Engineering, University of Manchester, Manchester M13 9PL, UK*
[2]*The University Hospital of South Manchester NHS Foundation Trust, Southmoor Road, Wythenshawe, Manchester M23 9LT, UK*

SUMMARY

The human shoulder is a complicated musculoskeletal structure and is a perfect compromise between mobility and stability. The objective of this paper is to provide a thorough review of previous finite element (FE) studies in biomechanics of the human shoulder complex. Those FE studies to investigate shoulder biomechanics have been reviewed according to the physiological and clinical problems addressed: glenohumeral joint stability, rotator cuff tears, joint capsular and labral defects and shoulder arthroplasty. The major findings, limitations, potential clinical applications and modelling techniques of those FE studies are critically discussed. The main challenges faced in order to accurately represent the realistic physiological functions of the shoulder mechanism in FE simulations involve (1) subject-specific representation of the anisotropic nonhomogeneous material properties of the shoulder tissues in both healthy and pathological conditions; (2) definition of boundary and loading conditions based on individualised physiological data; (3) more comprehensive modelling describing the whole shoulder complex including appropriate three-dimensional (3D) representation of all major shoulder hard tissues and soft tissues and their delicate interactions; (4) rigorous in vivo experimental validation of FE simulation results. Fully validated shoulder FE models would greatly enhance our understanding of the aetiology of shoulder disorders, and hence facilitate the development of more efficient clinical diagnoses, non-surgical and surgical treatments, as well as shoulder orthotics and prosthetics. © 2016 The Authors. *International Journal for Numerical Methods in Biomedical Engineering* published by John Wiley & Sons Ltd.

Received 30 July 2015; Revised 11 February 2016; Accepted 12 February 2016

KEY WORDS: human shoulder complex; biomechanics; finite element; glenohumeral joint; computational modelling; arthroplasty

1. INTRODUCTION

The human shoulder is a complicated musculoskeletal structure considered as a perfect compromise between mobility and stability [1]. As the major joint in the shoulder complex, the glenohumeral joint permits the greatest range of motion of any joint in the human body. Stability is mainly provided by active muscle actions with a minor contribution from the passive stabilisers, such as glenohumeral capsule, labrum and ligaments etc. The articular surface of the glenoid is considerably smaller than that of the humerus, which facilitates the large range of movement of the joint (see Figure 1 for the typical range of motion of the shoulder joint) [2, 3]. In combination with the motion of the scapulothoracic joint, the range of motion of the human upper extremity covers about 65% of a sphere [4]. However, on the other hand, the poor congruency of the glenohumeral articular surface challenges joint stability. Translational forces parallel to the articular surface exceeding the

*Correspondence to: Lei Ren, School of Mechanical, Aerospace and Civil Engineering, University of Manchester, Manchester M13 9PL, UK.
†E-mail: lei.ren@manchester.ac.uk

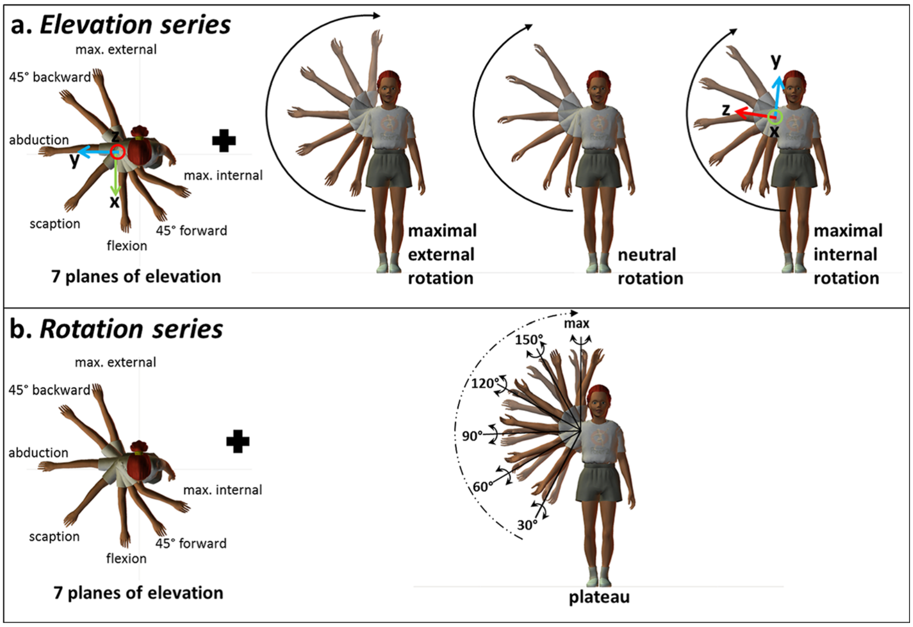

Figure 1. The typical range of motion of the shoulder joint [2].

stabilising capacity of the joint are the biomechanical reason of joint dislocations. Similar to the other synovial joints, such as the hip, knee or elbow joint, in the glenohumeral joint, those forces have to be counteracted by muscles, ligaments and the joint capsule, which orient the joint contact force towards the articular surface, as the poor articular congruency provides very little additional stability (see the forces of shoulder joint at 90° abduction in Figure 2) [5]. This characteristic joint configuration results in high incidences of glenohumeral joint dislocations and most probably predisposes the patient to other painful soft tissue shoulder conditions. However, our understanding of the in vivo biomechanical functioning of the shoulder complex is still very limited. Little is known about the individual contribution of each component of the shoulder musculoskeletal structure to joint stability and mobility and their relationship with each other.

Traditional biomechanical measurements are limited by the existing measuring techniques and ethical issues, and the in vivo internal loading condition of the shoulder musculoskeletal complex

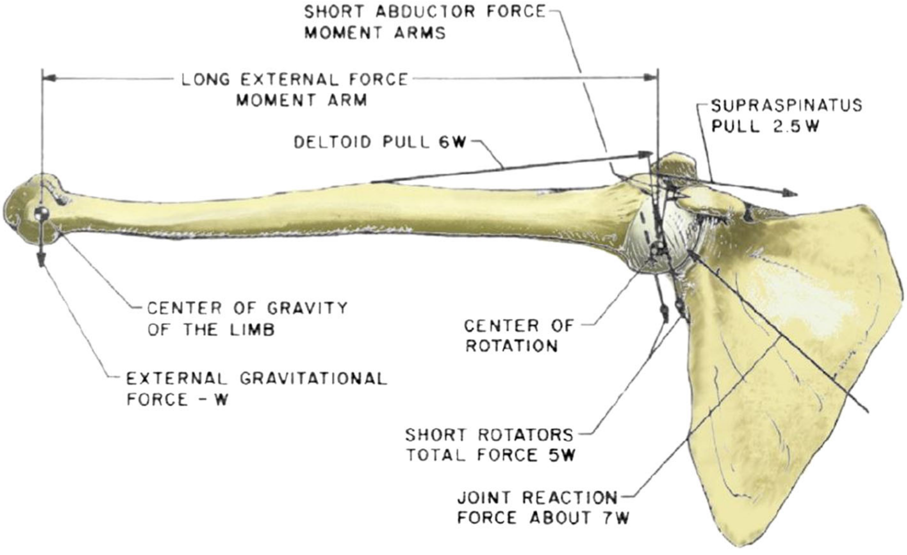

Figure 2. The forces acting at the glenohumeral joint at 90° abduction [5].

DOI: 10.1002/cnm

is almost unmeasurable [6]. Most of the experimental studies to investigate the load transfer in the shoulder structure were limited to in vitro conditions [7–11]. In this scenario, a computational method based on musculoskeletal models provides a valuable tool to estimate the biomechanical behaviour of the shoulder complex under different loading conditions. Computational shoulder models can be roughly classified as two major categories: multi-body models based on rigid body dynamics and finite element (FE) models based on continuum mechanics. In multi-body models, the body segments are assumed to be rigid bodies without deformations and muscles are simplified as single line actuators without 3D volume. In combination with muscle wrapping and muscle force estimation methods (optimisation-based or EMG-driven), these kinds of models are typically used for determining muscle forces in vivo [12–17]. Through dynamic simulation analysis, multi-body models have the potential to investigate neuromuscular control strategies, musculoskeletal dynamics and simulated surgical interventions [18]. However, because of the major model simplification, the sophisticated deformations, stress distributions and interactions of different components of the shoulder musculoskeletal structure cannot be simulated by using multi-body models. Those are critical contributors to the in vivo biomechanical and physiological functioning of the shoulder complex and therefore make it difficult to make any clinically useful conclusions from data provided by these methods. Moreover, measurement data used for driving multi-body models normally suffers from skin artefacts because of skin mounted markers used in motion analysis. Despite those limitations, multi-body models provide a valuable tool to improve our understanding of the in vivo biomechanical functioning of the musculoskeletal system [19].

On the other hand, continuum mechanics models based on a FE method offer a powerful tool to assess the internal loading conditions of the shoulder musculoskeletal structure [20]. They can provide valuable estimates of stress and strain distributions in the bones and soft tissues, which are usually not measurable in vivo. The FE method was first developed to solve elasticity and structural analysis problems in 1940s [21]. Its basic concept is the discretisation (division) of complex mechanical structures into finite numbers of separate components with simple geometry called elements. In this way, complex nonlinear problems become solvable numerically. Nowadays, the FE method has been widely used in different engineering fields for system design and analysis [22]. Over the past decades, the FE method has also been increasingly used for investigating a large range of problems in biomechanics and orthopaedics [23]. According to a recent study, the number of articles using FE analysis in biomechanics appears to be increasing geometrically based on the PubMed database [24]. In FE shoulder modelling, the biggest challenge is how to properly represent the complicated structures and materials of the shoulder musculoskeletal system. This paper provides a critical review of the previous studies using FE models to investigate shoulder biomechanics, which are roughly categorised according to the physiological and clinical problems addressed: glenohumeral joint stability, rotator cuff tears, joint capsular and labral defects, and shoulder arthroplasty. The key modelling techniques used in each of those studies are listed in Table I. The articles reviewed in this study were found based on the Web of Science and PubMed databases by using the keywords of ‘FE’, ‘numerical simulation’, ‘glenohumeral joint’ and ‘shoulder joint’.

2. FE MODELLING OF SHOULDER COMPLEX

2.1. FE models of glenohumeral joint stability

The low congruity of the articular joint surfaces in the shoulder affords its large range of motion; however, it predisposes it to being the most commonly dislocated joint of the body. A number of studies have been conducted to investigate instability of the glenohumeral joint by using FE models considering the major components of the shoulder complex.

Buchler et al. [31] used a FE glenohumeral joint model, consisting of the major rotator cuff muscles and bones, to investigate the changes in joint contact stresses because of the changes of the shape of the humeral head and the glenoid contact shape and orientation in both healthy and pathological conditions. It was found that the changes in shape of the humeral head because of joint disorders (e.g. osteoarthritis) may reduce joint stability. However, one of the drawbacks of this study is

DOI: 10.1002/cnm

Table I. Key modelling techniques and parameters used in the FE shoulder studies reviewed in this paper.

Clinical issue	Dimension	Geometric acquisition		Model components	Material properties		Boundary conditions	Loading conditions	Validation	Reference
		Bones	Soft tissues		Bones	Soft tissues				
Joint instability	3D	In vitro CT scans	In vitro measurement for muscle insertions; Cartilages filling the space between bones	Scapula and humerus;major abduction muscles: deltoid, supraspinatus, infraspinatus, subscapularis	Humerus is rigid; Scapula bone is linear elastic, nonhomogeneous material. $E(\rho) = E_0 (\rho/\rho_0)^2$, $\nu = \nu_0$,where $E_0 = 15\,000$, $\nu_0 = 0.3 \rho_0 = 1800$.[25, 26]	Muscles were assumed exponential hyperelastic, incompressible $W = \alpha \exp(\beta(I_1 - 3)) - \alpha\beta/2 (I_2 - 3)$ Where $\alpha = 0.12$MPa, $\beta = 1.0$; [27–29] Cartilage was defined based on the Neo-Hookean incompressible constitutive law. $W = C_{10} (I_1 - 3)$ with $C_{10} = E/4(1 + \nu)$ where $C_{10} = 1.79$ ($E = 10$, $\nu = 0.3$). [30]	Humerus fixed in transverse plane, vertical translation supported by a spring; Scapula limited by spring elements fixed at spine; Muscles attached fixed with scapula	Initial pre-stress 1.5 kPa on all muscles; Artificial gradual displacement on infraspinatus (external rotation) and subscapularis (internal rotation)	NO	Büchler P, et al.[31] (2002)
	3D	Same as [31]	Same as [31]	Scapula and humerus;major abduction muscles and deltoid	Rigid	Cartilage was defined based on the Neo-Hookean incompressible constitutive law by $W = 1.8(I_1 - 3)$; Muscle was modelled using parallel stiff fibres embedded along the principal direction of the muscle volume, which was described by a soft Neo-Hookean material with $W = 0.5(I_1 - 3)$.	Estimated muscle forces based on literature data	Artificial rotation of scapula and humerus; A humerus weight of 37.5 N applied on mass centre	Validate against literature [32] and in vitro study[33, 34]	Terrier A, et al.[35] (2007)
	3D	Literature data		Humerus and scapula;ligaments	Rigid	Cartilages defined as Neo-Hookean hyperelastic, incompressible material. $C_{10} = E/4(1 + \nu)$ $D_{10} = E/6(1 - 2\nu)$ Where $E = 10$, $\nu = 0.4$ [30, 31]	Humerus fixed in sagittal plane, unconstrained laterally	Humerus moved 1.2 mm to contact glenoid surface; 50 N compressive load applied on humeral head laterally; [7, 11] Move humerus in anteroinferior direction about 17 mm	Validated againstcadaver studies[7, 11]	Walia P, et al. [36] (2013)

(*Continues*)

DOI: 10.1002/cnm

Table I. (Continued)

Clinical issue	Dimension	Geometric acquisition		Model components	Material properties		Boundary conditions	Loading conditions	Validation	Reference
		Bones	Soft tissues		Bones	Soft tissues				
Clinical issue	Dimension	Geometric acquisition		Model components	Material properties		Boundary conditions	Loading conditions	Validation	Reference
		Bones	Soft tissues		Bones	Soft tissues				
	3D	In vitro CT scans for scapulaLiterature data for humerus	Published anatomical data (cartilage and labrum)	Humerus and glenoid;cartilage and labrum	Isotropic linear-elastic(E = 18 000, ν = 0.35)	Cartilage and labrum are defined same as [31] Cartilage: C_{10} = 1.79 (E = 10, ν = 0.4) and Labrum: C_{10} = 12.5 (E = 70, ν = 0.4).	Estimated active muscle forces from multi-body model; Artificial glenohumeral elevation in scapular plane from 0° to 80° with arm weight 35 N applied at arm centre of mass		Validated againstin vitro[33, 37] and in vivo (EMG)[15, 38] studies	Favre P, et al. [39] (2012)
Rotator cuff tears	2D	In vitro MRI scans		Humerus and glenoid; supraspinatus, supraspinatus tendon	Rigid	Supraspinatus tendon was defined as biphasic, linear, fibre reinforced composite with longitudinally arranged collagen fibres (E = 800) acting with an extrafibrillar matrix (plain stress element with E = 8, ν = 0.497).[40]	Humeral head fixed	Estimated theoretical load and angle on supraspinatus	No	Luo ZP, et al. [41] (1998)
	2D	In vivo MRI (humeral head)	In vivo MRI for supraspinatusIn vitro measurement for cartilages	Humeral head; supraspinatus tendon and cartilages	Humeral head was divided to three regions: cortical bone (E = 13 800, ν = 0.3); subchondral bone (E = 2780, ν = 0.3); cancellous bone (E = 1380, ν = 0.3)[42]	Supraspinatus tendon: E = 168, ν = 0.497.Articular cartilage: E = 35, ν = 0.450.[40, 43]Medium values between the tendon and the cancellous bone were defined for calcified fibrocartilage (E = 976, ν = 0.366) and noncalcified fibrocartilage (E = 572, ν = 0.432).	Humeral head fixed	Estimated theoretical load and angle on supraspinatus	Validated against literature data[41]	Wakabayashi I, et al.[32] (2003)
	2D	Same as [32]	Same as [32]	Humeral head; supraspinatus tendon and cartilages	Same as [32]	Same as [32]	Humeral head fixed	Estimated theoretical load and angle on supraspinatus	Validated against literature data[41]	Sano H, et al. [44] (2006)
	3D	In vivo CT scans for humeral head	In vivo MRI for tendon;In vitro measurements for calcified and noncalcified cartilages	Humerus head; supraspinatus tendon and cartilages	Same as [32]	Same as [32]	Humeral head fixed	Estimated theoretical load and angle on supraspinatus	No	Seki N, et al. [45] (2008)

(*Continues*)

DOI: 10.1002/cnm

Table I. (Continued)

Clinical issue	Dimension	Geometric acquisition		Model components	Material properties		Boundary conditions	Loading conditions	Validation	Reference
		Bones	Soft tissues		Bones	Soft tissues				
Clinical issue	Dimension	Geometric acquisition		Model components	Material properties		Boundary conditions	Loading conditions	Validation	Reference
		Bones	Soft tissues		Bones	Soft tissues				
Rotator cuff tears	3D	In vitro CT scans for scapula and humerus	Cryosection photos for glenoid, humeral cartilages and rotator cuff tendons	Scapula and humerus;humeral articular cartilage and rotator cuff tendons	Rigid	Cartilage was modelled as a rigid body with a pressure–overclosure relationship;[46]Tendons were represented with a linear elastic orthotropic material model (E = 140 ν = 0.497).[41, 47]	Scapula fixed;Pre-defined kinematic boundary for humerus	Artificial rotation from 45° internal to 45° external about an axis parallel to the humeral shaft;	Validated againstin vitro study	Adams C, et al.[48] (2007)
	3D	In vivo CT scans		Scapula and humerus;rotator cuff tendons and deltoid muscle	SolidE = 15 000, ν = 0.3.[35, 48]	Muscle and tendons were defined as non-linear elastic material;Articular cartilage linear elastic E = 15, ν = 0.45.[49, 50]	Scapula fixed	Pre-defined loads on tendons based on cadaver studies[8, 9, 51]	Validated againstin vitro study[50]	Inoue A, et al. [52] (2013)
Capsule and labrum defects	3D	In vitro CT scans		Scapula and humerus;anterior band of IGHL	Rigid	Anterior band of IGHL was represented using fibre-reinforced composites. (average material properties from literature)	Measured bone kinematics from the cadaver study		No	Debski R, et al.[53] (2005)
	3D	In vitro CT scans		Scapula and humerus;joint capsule androtator cuff tendon	Rigid	IGHL was defined as isotropic hypoelastic.(E = 10.1, ν = 0.4)[54]	Measured bone kinematics from the cadaver study[10]		Validated againstin vitro study[54, 55]	Ellis B, et al. [56] (2007)
	3D	In vitro CT scans		Scapula and humerus;capsule, ligaments and cartilages	Rigid	Capsular regions have the same ν = 0.4995 but individual E:Anterior band of IGHL E = 2.05Posterior band of IGHL E = 3.73Anterosuperior E = 2.12Axillary pouch E = 4.92Posterior E = 2.05	Measured bone kinematics from the cadaver study[57]		Validated againstin vitro study	Moore S, et al. [58] (2008)
	3D	Same as [58]		Scapula and humerus;capsule and cartilage	Same as [58]	Same as [58]	Measured bone kinematics from the cadaver study		Validated againstin vitro study	Ellis B, et al. [59] (2010)

(*Continues*)

Table I. (Continued)

Clinical issue	Dimension	Geometric acquisition: Bones	Geometric acquisition: Soft tissues	Model components	Material properties: Bones	Material properties: Soft tissues	Boundary conditions	Loading conditions	Validation	Reference
	3D	In vitro CT scans		Scapula and humerus;capsule, humeral head cartilage	Rigid	Capsule tissues were represented using an isotropic hyperelastic constitutive model.	Measured bone kinematics from the cadaver study		Validated against specimen-specificin vitro study	Drury N, et al. [60] (2011)
Clinical issue	Dimension	Geometric acquisition: Bones	Geometric acquisition: Soft tissues	Model components	Material properties: Bones	Material properties: Soft tissues	Boundary conditions	Loading conditions	Validation	Reference
Capsule and labrum defects	3D	In vitro measurements		Glenoidlabrum and biceps long head tendon	Glenoid defined as elastic isotropic material (E = 1400)	Labrum and biceps defined as elastic isotropic material (E = 241)	Glenoid fixed	Pre-defined loads on LHBT from muscle activities from literature[61]	No	Yeh ML, et al. [62] (2005)
	3D	In vitro CT scans		Glenoid;labrum, cartilages of humeral head and glenoid	Rigid	The humeral cartilage was assumed rigid;Glenoid cartilage was isotropic with properties of$E = 1.7$, $\nu = 0.018$, $\phi_s = 0.25$,$\rho = 1075$; Labrum was transverse isotropic with properties of$E_p = 0.24$, $E_\theta = 22.8$, $_p = 0.33$, $_{\theta p} = 0.10$, $G_{\theta p} = 2\phi_s = 0.75$, $\rho = 1225$Subscripts define the transverse plane (p) and the circumferential direction (θ) of the labrum.[63–65]	Glenoid fixedHumeral cartilages constrained from all rotations and displacement along X-axis direction (anteroposterior oblique direction).	Move the humeral cartilage 1, 2 and 3 mm in +Y direction (superiorly)50 N applied in −Z direction (medial oblique direction)	Validated againstin vitro study	Gatti C, et al. [66] (2010)
	3D	In vitro CT scans		Glenoid, glenoid labrum, humeral head and glenoid cartilage.	Rigid	Estimated material coefficients of capsule.[53, 67]	Measured humerus motion from in vitro experiment	25 N anterior load applied at 60° of glenohumeral abduction and 0°, 30° and 60° of external rotation	Validated againstin vitro study	Drury N, et al. [68] (2011)

E: Young's modulus (MPa); ν: Poison's ratio; ρ: density (kg m^{-3}); I_1: first invariants of the Cauchy–Green tensor; G: shear modulus (MPa); ϕ_s: solid volume fraction; W: strain energy density function; C_{10}, D_{10}: material property constants.

DOI: 10.1002/cnm

lack of validation. This FE glenohumeral joint model was also used for analysing the biomechanical effect of the shapes of prosthetic humeral heads after shoulder arthroplasty [69]. Two prosthetic designs were examined against an intact shoulder: the second-generation (Neer II) and a patient-specific anatomical implant. Similar to the previous FE simulation, joint contact stresses (location and magnitude) were calculated and compared in three cases: intact shoulder, Neer II and patient-specific condition. The result showed that the patient-specific implant produced closer biomechanical conditions in both stress location and magnitude to the intact shoulder than the second generation implant. The Neer II implant moved the joint contact area eccentrically and led to bone contact stresses being up to 8 times higher than in the intact shoulder.

Terrier et al. [35] used a 3D FE model of the shoulder to investigate the biomechanical consequence of supraspinatus deficiency with a major focus on the reduction in glenohumeral joint stability that could lead to secondary osteoarthritis. The effect of supraspinatus deficiency was examined by FE model analyses in both healthy and pathological conditions (considered as a full supraspinatus tear). The result suggested that supraspinatus deficiency increases the upward migration of the humeral head resulting in increased eccentric loading, and thus decreases glenohumeral joint stability. A similar FE shoulder model was used for investigating the effect of combined defects of the humeral head (Hill–Sachs) and of the glenoid (bony Bankart lesion) by Walia et al. (see Figure 3) [36]. It was found that the glenohumeral joint stability (defined as the ratio of shear force to compressive force) was decreased from 43% to 0% for the combined presence of both lesions compared to the normal healthy shoulder.

A recent FE model of the glenohumeral joint used estimated muscle forces as the loading condition, and the humerus was allowed to move freely with six degrees of freedom [39]. These loading and boundary conditions enable the FE analyses to simulate motions of the shoulder complex closer to its realistic physiological condition than those with pre-described or artificially defined constraints. The FE analyses used tissue deformations, contact areas and contact pressures to evaluate glenohumeral joint stability. This study provides a useful framework for future FE studies of the shoulder complex. The major limitation of the study is that only the scapula and the humerus bones were considered, and the 3D geometry and structure of muscles and other soft tissues were neglected in the model. Their interactions with the bones and other musculoskeletal components could not be examined in the FE analyses.

In the studies discussed, different methods were used for quantifying glenohumeral joint stability. Buchler et al. [31] used an average of the contact area between the humeral head and the glenoid. Similarly, Terrier et al. [35] calculated the contact point on the glenoid to measure joint stability. Walia et al. [7] used a stability ratio (shear force over compressive force) defined in a cadaveric study. In a recent study by Favre et al. [39], glenohumeral joint stability was defined as the shear force required to dislocate the joint under a 50-N compressive load. The common feature of these methods is that glenohumeral joint stability is measured as the ability of the joint to keep the humeral head in the centre of the glenoid either through relative displacements or shear and compressive stresses. However, little is known about the relationships between those different methods. There is a lack of comparative studies as well a need to standardise how to quantify and report shoulder joint stability. Moreover, for simplification, most of the previous modelling studies

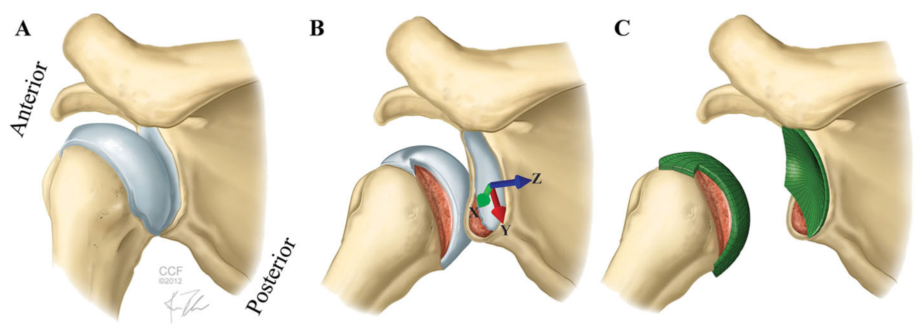

Figure 3. (A) Intact shoulder at 0° abduction; (B) combination of Hill–Sachs and bony Bankart lesion at 90° abduction; (C) FE mesh in combined case [36].

DOI: 10.1002/cnm

considered only part of the shoulder musculoskeletal complex by neglecting some important factors that may have considerable effect on joint stability, e.g. muscle to muscle and/or muscle to bone contact forces. This leads to a poor understanding of the individual contribution of musculoskeletal components to shoulder stability. Joint stability is an overall performance that requires effective functioning of each part of the musculoskeletal structure [70]. Therefore, systematic investigations based on more comprehensive modelling with exchangeable evaluation results are needed for future studies.

2.2. *FE models of rotator cuff tears*

The shoulder complex is actively stabilised by contractions of the rotator cuff muscles. Rotator cuff tendon tears are one of the most common pathologies in the shoulder and the supraspinatus tendon is the most frequently affected. Tears can cause chronic shoulder pain, and may lead to secondary degenerative changes in the shoulder (e.g. cuff tear arthropathy). The aetiology of a rotator cuff tear is multi-factorial with genetic and environmental factors playing an important role. However, so far, the fundamental mechanism that initiates rotator cuff tears remains unclear. A number of studies have been conducted to explore the underlying biomechanical mechanisms which might cause rotator cuff tears using FE shoulder models.

In 1998, Luo et al. [41] used a simplified 2D FE shoulder model for the first time to investigate the initialisation mechanism of rotator cuff tears by analysing the stress environment in the supraspinatus tendon. The stress distribution was evaluated at the humeroscapular elevation angle of 0°, 30° and 60° respectively and also under two different acromial conditions (with and without subacromial impingement). It was found that the high stress concentration generated by subacromial impingement could initiate a tear. Moreover, the results showed that this tear may occur on the bursal side, the articular side or within the tendon rather than only on the bursal side as the traditional mechanical models suggest. Two further studies based on improved Luo's model were conducted. Wakabayashi et al. [32] applied histological differences at the tendon insertion in their FE model to analyse the stress environment of the supraspinatus tendon. This study showed slightly different result from Luo's study and found that the maximum principle stress of the tendon occurs at the region in contact with the humeral head rather than at the insertion point. Whereas Sano et al. [44] examined the stress distribution in the pathological rotator cuff tendon and revealed potential partial thickness tears at three different locations: on the articular surface, on the bursal surface and in the mid-substance close to the insertion. It was found that high stress concentration occurs at the articular side of the insertion and the site of tear. The two studies used same modelling method and conditions as Luo's original model, but employed different histological parameters to simulate pathological conditions. Although those studies have improved our understanding of the initiation mechanism of rotator cuff tears, they were limited to 2D condition and lacked experimental validations.

The first 3D FE model of rotator cuff tears was reported by Seki et al. [45] in 2008 to analyse the 3D stress distribution in the supraspinatus tendon. It was found that the maximum stress occurs in the anterior portion of the articular side of the tendon insertion rather than at the tendon contact point with the humeral head as suggested by 2D analyses. This explains the frequent occurrence of rotator cuff tears at this site. This improvement was achieved because of the advantage of the 3D model analysis where the anteroposterior direction was investigated showing that the anterior part of the rotator cuff is not in contact with the superior surface of the humeral head. However, this study only analysed part of the shoulder complex at 0° abduction without experimental validation.

Adams et al. [48] used a 3D FE model of the glenohumeral joint to investigate the effect of morphological changes in the rotator cuff tendons following a tear. The result showed that the moment arms of infraspinatus and teres minor muscles were generally decreased. Consequently, the muscles attached to the torn tendons are required to generate more forces for the same motions, and the overall strength of the shoulder is decreased. This study revealed a potential relationship between shoulder strength reduction and sizes and locations of the rotator cuff tears. The magnitudes and general trends of the calculated moment arms were found in reasonably good agreements with the measured data. A limitation of this study is that tendons were divided along the force bearing direction, which

DOI: 10.1002/cnm

only happens in massive cuff tears transverse to tendon collagen fibrils. Cuff tears along tendon collagen fibrils were neglected in the model analysis.

A most recent FE study of rotator cuff tears was conducted by Inoue et al. [52] A 3D FE model including the rotator cuff muscles and the middle fibres of the deltoid muscle was used for investigating the biomechanical mechanism of rotator cuff tears. Different stresses were found in the articular and bursal sides of the supraspinatus tendon resulting in shearing between the two layers, which was believed to initiate partial-thickness tears (see Figure 4). The limitation of this study is that the muscles and bones were reconstructed based on CT images, which are not very suitable for segmentation of soft tissues. Moreover, the simulated movement was limited to shoulder abduction, and only three rotator cuff muscles and middle fibres of the deltoid were considered in the model.

Those modelling studies investigated the aetiology of rotator cuff tears based on the hypothesis that mechanical stress concentration initiates tendon tissue tear. Although recent studies demonstrated some promising results, the underlying mechanism triggering the pathological process still remains unclear [52]. As the shoulder joint is actively stabilised by the rotator cuff muscles, the loading condition at the rotator cuff tendon may have a major effect on the simulation results. However, existing FE models either used in vitro data or were based on roughly estimated tendon force data. Therefore, more accurate in vivo muscle force data is needed in order to provide more convincing results to reveal the fundamental mechanism underlying rotator cuff tears.

2.3. *FE models of capsular and labral defects*

The shoulder articular capsule and labrum are the major passive stabilisers of the glenohumeral joint. The capsule is a thin and loose structure reinforced by surrounding ligaments such as the inferior glenohumeral ligament (IGHL). The labrum is an integral component of the glenoid insertion of the IGHL, which increases the depth and concavity to the glenoid fossa to resist the humeral head translation [60]. Injuries, such as a Bankart lesion or HAGL lesion (humeral avulsion of the glenohumeral ligament), are common after an anterior shoulder dislocation. A number of FE studies have been conducted to understand the pathomechanics of the shoulder capsule and labrum. This may lead to new biomechanically oriented strategies to improve clinical diagnosis and surgical interventions to address capsular and labral defects [59].

The first FE study of the capsule was conducted by Debski et al. [53] in 2005, where a FE model of the glenohumeral joint with the anterior band of the IGHL was used for analysing the stress and

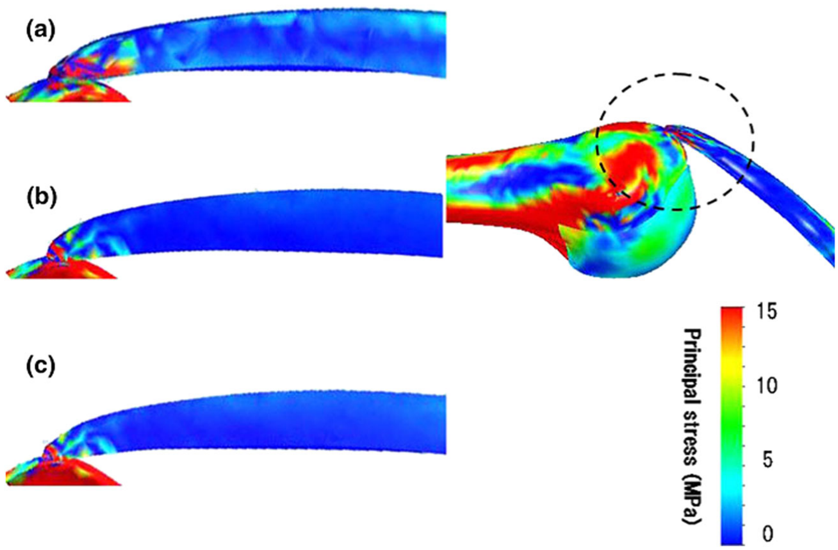

Figure 4. Distributions of tensile stress in the supraspinatus tendon at 90°. View (a), (b) and (c) are anterior, middle and posterior section of the supraspinatus tendon in the sagittal plane respectively [52].

DOI: 10.1002/cnm

strain distribution in the IGHL. Although the study revealed the continuous nature of the glenohumeral capsule, the FE model was limited by the fact that only the anterior band of the IGHL was considered and experimental validation was absent. Another FE model of the IGHL was constructed later to examine the strains and forces in the IGHL complex by Ellis et al. [56] It was found through a sensitivity analysis that the predicted strains were highly sensitive to the changes in the ratio of bulk to shear modulus of the IGHL complex. A further study suggested that it is more appropriate to consider the glenohumeral capsule as a sheet of fibrous tissue. This provides useful suggestions on better representation of ligaments in FE modelling [58].

Recently, Ellis et al. [59] constructed two subject-specific FE models of the IGHL to analyse the glenohumeral joint positions in clinical examinations by evaluating the strain distribution (see Figure 5). It was suggested that the isolated discrete capsule regions should not be used in analysing the function of the glenohumeral capsule. The study concluded that the positions of 30° and 60° of external rotation can be used for testing the glenoid side of the IGHL during clinical examinations, but are not useful for assessing the humeral side of the IGHL [59]. This provides useful suggestions to improvements in clinical evaluation of shoulder instability. The most recent FE study of the glenohumeral capsule was conducted by Drury et al. [68] with a more detailed model construction. The result showed that the glenoid side of the capsule undergoes the greatest deformation at the joint position under 60° abduction and at a mid-range ($20° - 40°$) of external rotation. This suggested that standard glenohumeral joint positions could be used for the examination of pathology in the anterior inferior capsule caused by dislocations. FE studies have also been conducted to investigate defects of glenohumeral labrum, such as superior labrum anterior posterior (SLAP) tears, which are normally found among athletes involved in overhead sports [62]. Yeh et al. constructed 3D FE models of the superolabral complex with different biceps origins at four orientations during throwing, and the change of peak stress was examined. The maximum stress about 160 Mpa was found in the deceleration phase of throwing, two times of that in the late cocking phase. This high stress in the deceleration phase may lead to tears at the superior glenohumeral labrum. However, no experimental validation was conducted in this study. A later FE study revealed that the superior humeral translation resulting in a shear force to the labrum could be a possible mechanism to the development of SLAP lesions [66].

Recent studies have attempted to consider both the capsule and labrum in FE glenohumeral joint models. Drury et al. [60] constructed a subject-specific FE model of the glenohumeral joint with the capsule and labrum components to investigate the effect of degenerating tissues on strains in the glenohumeral labrum and capsule by simulating varied labrum thickness and modulus. The results showed that decreasing the thickness of the labrum because of degeneration increases the average and peak strains in the labrum. This increase in strain provides a possible biomechanical mechanism by which the tissue degeneration results in glenohumeral labrum pathology with ageing and also confirms the important, however minor static contribution of the labrum to shoulder stability.

In comparison to the rotator cuff muscles, the capsule and labrum are major passive stabilisers of the shoulder joint. They function to assist with stability when the shoulder joint reaches or exceeds the limit of the joint range of motion. In this scenario, material property might be more important than in vivo loading for investigations of capsule and labrum defects. Although material property studies have been conducted for the capsule ligaments based on specimen-specific experiments [56, 58], more detailed studies are needed to quantify the complex material behaviour of the capsule and labrum in vivo. Moreover, further studies may need to pay more attention to accurate representation of the glenoid insertion site which varies significantly between subjects [60].

2.4. FE models for shoulder arthroplasty

A total shoulder replacement includes the replacement of the humeral head and the glenoid with prostheses that perform as a new joint. Therefore, the prosthesis design is fundamental in shoulder arthroplasty. FE analysis has been widely used in the design of prosthesis especially in investigating the clinically important issue of glenoid component aseptic loosening. The FE studies conducted for shoulder arthroplasty assessment are critically reviewed in this section, and key design parameters and major findings of each study are detailed in Table II.

DOI: 10.1002/cnm

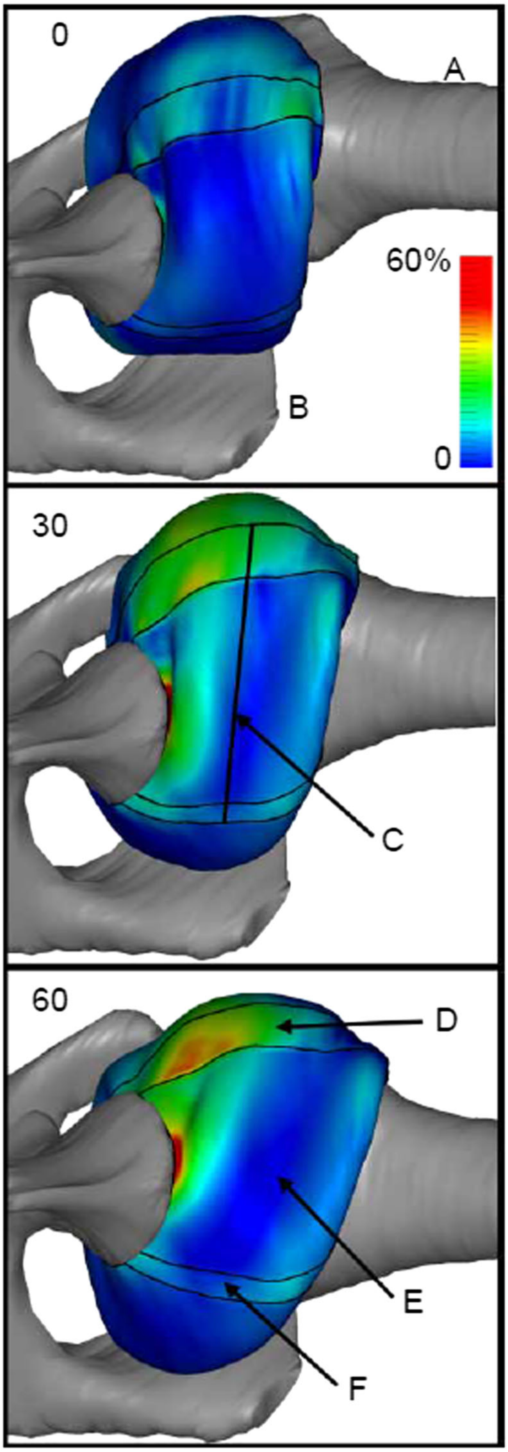

Figure 5. Inferior view of the first principal strain distribution in the left shoulder under 60° of abduction at 0°, 30° and 60° of external rotation. A, Humerus; B, glenoid; C, IGHL mid-line; D, anterior band of IGHL; E, axillary pouch and F, posterior of IGHL [59].

The scapula is connected to the axial skeleton via the clavicle. It provides a mobile yet stable base for humeral movement. The scapula also provides the insertion for a number of shoulder muscles and ligaments. Several studies have been conducted to investigate the biomechanics of the scapula because bone remodelling of the scapula is considered as the first step towards the study of

DOI: 10.1002/cnm

Table II. The fundamental information and major findings of the FE shoulder arthroplasty studies reviewed in this paper.

Implant geometry	Orientation and position	Cement	Prosthesis material	Glenohumeral conformity	Findings	Reference
Keel, stair-stepped, wedge and screw	N/A	Cemented	Cobalt–chromium metal for backingand polyethylene	N/A	1. An all-polyethylene implant could provide a more physiological stress distribution for nonaxial loads; 2. A soft tissue layer results in higher stresses; 3. Stair-stepped and wedge designs demonstrated a more natural stress distribution compared to keel design; 4. Screw orientation does not make much difference.	Friedman RJ, et al.[71] (1992)
Triangular keel	N/A	Cemented	Cobalt–chromium metal for backingand polyethylene	High and low conformity achieved by varying load distribution over contact area	Fatigue failure could originate from the high stresses in cement.	Lacroix D and Prendergast PJ.[72] (1997)
Keel	N/A	Cemented all-polyethylene componentUncemented metal-backed component		N/A	1. Cemented all-polyethylene design produced more natural stress overall.2. Extremely high stress were found in the polyethylene in contact with metal surface	Stone KD, et al.[73] (1999)
Peg and Keel(DD 1134-96 and DD 1134-85DePuy Inc.)	N/A	Cemented	All-polyethylene	N/A	A ‘pegged’ anchorage system is superior for normal bone, whereas a ‘keeled’ anchorage system is suitable for rheumatoid arthritis bone.	Lacroix D, et al.[74] (2000)
Keel	N/A	Cemented and uncemented glenoid component	Polyethylene cup with a metal-backing	N/A	Uncemented design is a reasonable alternative to fixation with cement.	Gupta S, et al.[75] (2004)
Peg(Anatomica glenoid component Centerpulse Ltd.)	five component alignments: central, anteverted, retroverted, inferiorly inclined and superiorly inclined.	Cemented	Ultra-high molecular-weight polyethylene	N/A	Central alignment is the correct position. Misalignment of the glenoid prosthesis can lead to loosening.Joint replacement depends much on bone stiffness.	Hopkins, AR, et al.[76] (2004)

(*Continues*)

DOI: 10.1002/cnm

Table II. (Continued)

Implant geometry	Orientation and position	Cement	Prosthesis material	Glenohumeral conformity	Findings	Reference
Acromion-fixation	N/A	Cemented	Polyethylene	N/A	High stresses were found in the part of prosthesis that attached to the acromion. The acromion-fixation design is not a good alternative.	Murphy LA and Prendergast J.[77] (2005)
Keel	N/A	Cement mantle thickness were examined from0. 5–2 mm	All-polyethylene	N/A	The cement thinning weakens the cement, whereas the cement thickening makes the implant rigid, consequently increases the stress on bone cement interface.Optimal cement thickness is found to be between 1.0 and 1.5 mm.	Terrier A, et al.[78] (2005)
Keel	Humeral and glenoid components were implanted based on the manufacturer's recommendation	Cemented	All-polyethylene	Different values of conformity were tested (1–15 mm of radial mismatch)	Conformity had no influence at 0° of retroversion, whereas, at 15° of retroversion, the contact pressure, cement stress, shear stress and micro motions at bone–cement interface increased by more than 200% and exceeded critical values above 10 mm.	Terrier A, et al.[79] (2006)
Reversed and anatomical (Aequalis prosthesis, Tornier Inc)	N/A	N/A	All-polyethylene	N/A	Volumetric wear for the anatomical prosthesis and reversed version were 8.4 mm and 44.6 mm respectively.Contact pressure for the anatomical prosthesis was about 20 times lower than that of the reversed. Anatomical prosthesis showed the consistency with the biomechanical and clinical data.	Terrier A, et al.[80] (2009)

(*Continues*)

Table II. (Continued)

Implant geometry	Orientation and position	Cement	Prosthesis material	Glenohumeral conformity	Findings	Reference
Four anatomical and one reversed	N/A	Three anatomical models were CementedOne anatomical was Cementless	Three cemented anatomical model were all-polyethylene;One cementless anatomical model was metal-back; Reversed model was all metal	N/A	Cementless, metal-back components are more likely to have stress shielding than cemented all-polyethylene components regardless of bone quality. The all-polyethylene components are better in treatment of the shoulder joint.	Quental C, et al.[81] (2014)

DOI: 10.1002/cnm

complications of shoulder arthroplasty [82]. According to a recent study, A typical bone modelling procedure for creating a patient-specific FE model involves four steps: (1) geometry acquisition using medical images (CT/MR); (2) segmentation of those images and creating FE meshes; (3) definition of patient-specific material properties and (4) application of patient-specific multi-body loading and boundary conditions. The authors also examined the effect of three major modelling uncertainties, including bone density, musculoskeletal loads and material mapping relationship, on the predicted strain distribution. It was found that the number of uncertain components and the level of uncertainties determine the uncertainty of the results. The limitation of this study is that the material mapping relationship was determined based on cadaveric experiments conducted in vitro rather than from data measured in vivo [83].

Glenoid component loosening is a critical clinical issue in total shoulder arthroplasty. Most of the FE studies of shoulder arthroplasty were designed to investigate this problem. Through FE simulation analyses, the biomechanical effects of different key design parameters, such as implant shape, positioning and orientation, prosthesis material, use of bone cement and articular conformity, were examined. A large number of those studies investigated the effect of the shape of the glenoid component. Different glenoid shapes: keel, stair-stepped, wedge and screw, were compared in an early study [71]. It suggested that the stair-stepped and wedge designs provided a more natural stress distribution compared to the keel design. However, this study was only limited to 2D condition. A later FE study found that the peg design is superior for normal bones, whereas the keel design is more suitable for rheumatoid bone [74]. Based on a failure model, the FE simulation predicted 94% and 86% of bone cement survival probability for the peg design for normal bone and rheumatoid bone conditions respectively. Whereas, the survival probabilities for the keel design are 68% and 99% respectively. Another study has concluded that a novel design with acromial fixation point for the glenoid component is unsuitable for shoulder arthroplasty because of the high stress resulted in the part of prosthesis attached to the acromion [77].

The conformity of the glenoid component with the humerus component has been investigated using FE analyses as well. It was found that a higher conformity has the advantage of moderating cement stress [72], and the effect of conformity is sensitive to the shoulder joint position [79]. For example, for the same conformity, the contact pressure, cement stress, shear stress and micromotions at the bone–cement interface were increased by more than 200% at 15° of retroversion compared to those at 0° of retroversion. Another FE study showed that the central alignment with the humerus component is the correct position for the glenoid component, and misalignment may lead to glenoid loosening [76].

Studies looking at the choice of prosthetic components did suggest that metal backed glenoid component might be best [71–73]. However, a recent study has shown that all-polyethylene cemented glenoid components are likely to be more resilient to aseptic loosening (see Figure 6) [81]. The use of bone cement is a controversial element to glenoid component implantation. A number of studies have been conducted to investigate this issue. An early 2D FE study analysed local stresses at the bone implant interface between two glenoid designs. This showed that the cemented all-polyethylene design produced more natural stress overall although extremely high stresses were found in the interface between the polyethylene and the metal [73]. A recent FE study using an integrated model suggested that the cementless, metal-back components are more likely to have stress shielding than the cemented all-polyethylene components regardless of bone quality [81]. Another study investigating the effect of cement thickness concluded that although a thin cement mantle weakens the cement, a thick mantle makes the implant rigid and consequently increases the stress in the bone–cement interface [78]. The optimal cement thickness was found to be between 1.0 and 1.5 mm [78].

The previous studies of total shoulder arthroplasty using FE simulation analyses have greatly improved our understanding of the biomechanical effects of the key design parameters of shoulder implants, e.g. 3D shape, position and orientation, material and articular conformity etc. Future work should involve investigations of some unsolved problems, e.g. the mechanical degradation of the interfaces in cemented components [81], and bone loss in aseptic in both cemented and cementless components [81] as well as glenoid notching in reverse total shoulder arthroplasty. However, similar to the studies investigating shoulder joint instability, the major limitation here is still lack of

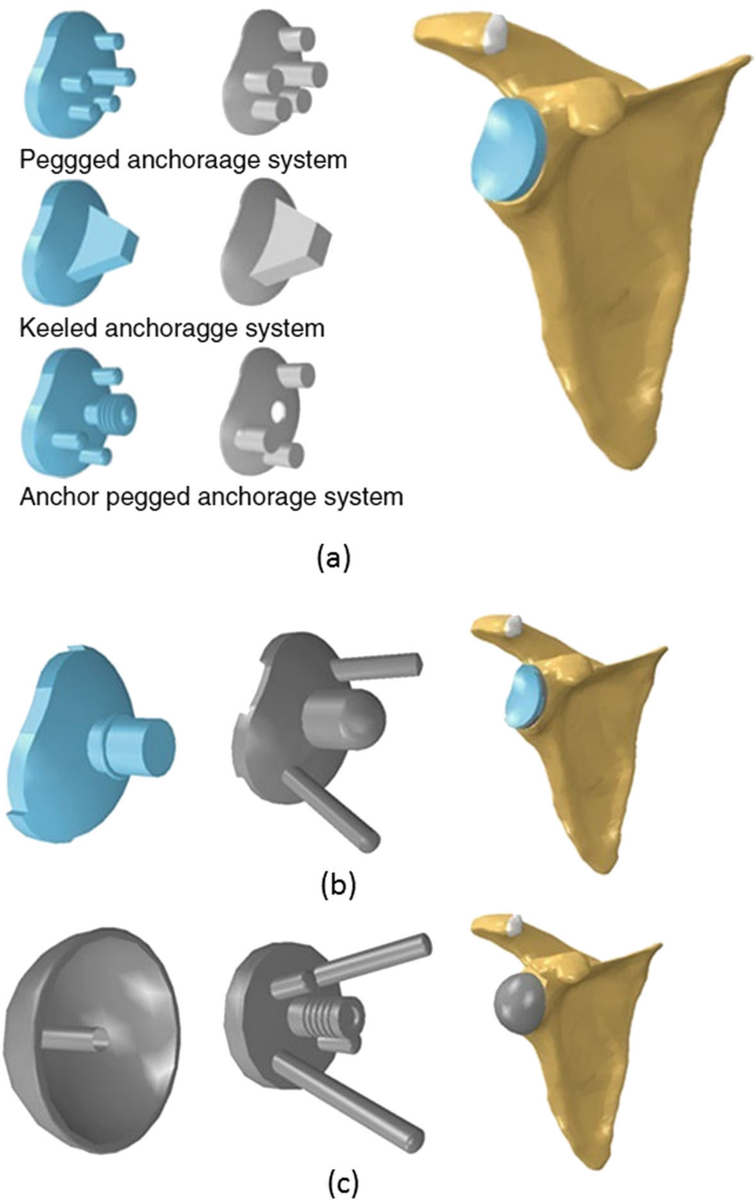

Figure 6. (a) Three anatomical models of the cemented glenoid components (on the left) and their corresponding cement mantles (in the middle); (b) the cementless anatomical model of glenoid component; (c) the reversed glenoid component [81].

detailed representation of all major shoulder musculoskeletal components and also physiologically realistic in vivo loading and boundary conditions.

3. FE SHOULDER MODELLING TECHNIQUES

For the FE studies reviewed in the preceding section, the key modelling techniques used in each shoulder FE model were listed in Table I. To reduce the computational load, most of those FE models only considered part of the shoulder structure rather than modelling the whole shoulder complex. Therefore, major model simplifications and assumptions were normally involved in the modelling processes. Those simplifications and assumptions could greatly facilitate the computations when representing a complex musculoskeletal structure such as the human shoulder complex. However, this will inevitably lead to discrepancies between the simulated results and the realistic

DOI: 10.1002/cnm

physiological functions. The limitations of those FE models are discussed in this section in terms of the key modelling techniques used: geometric data acquisition, material property representation, boundary and loading condition definition and experimental validation.

Normally, the first step in FE shoulder modelling is to reconstruct the 2D or 3D geometry of hard tissues and soft tissues of the musculoskeletal structure. Different approaches have been used for acquiring the dataset for the geometric construction varying from using literature data [71], average measured data [36] to subject-specific medical imaging data [31, 32, 39, 41, 44, 45, 48, 52, 53, 56, 58–60,62, 66, 68, 84]. For geometric construction of bones, the most widely used approach is based on computed tomography (CT) imaging data, for example, the CT image databases for the modelling of the cervical spine and hip joint in our previous studies [85, 86]. While in some studies the bone geometry was measured directly in cadaveric dissections or used the datasets from literature [32, 39, 48, 56]. For geometric modelling of soft tissues, such as musculotendinous units and ligaments, datasets obtained from magnetic resonance (MR) imaging or colour cryosections were normally used [32, 41, 44, 45, 48]. However, the geometric reconstruction of articular cartilages still remains challenging. Assumptions are normally used for defining the geometry of articular cartilage, for example using the estimated average thickness for the whole bone surface [82] or filling the space between the humerus and the scapula with hyaline cartilage [31]. Some recent studies used the published anatomical datasets to determine the cartilage geometry [36, 39]. Subject-specific accurate geometric modelling of cartilage will assist a better understanding of the in vivo cartilage mechanics in the glenohumeral joint. In many studies, the geometric data was obtained in vitro. However, to investigate the in vivo functioning of the shoulder complex, the geometric data of the shoulder tissues is acquired preferentially in vivo under unloaded conditions.

Because of the great complexity in the mechanical behaviours of biological materials, it has been proven very challenging to represent the realistic material properties of the shoulder tissues in FE modelling. Major assumptions were typically used in most of the FE shoulder studies. In most cases, bones were assumed to be rigid or isotropic linear elastic material with relatively large Young’s modulus, because the deformation of bones is almost negligible compared to that of soft tissues. Muscles and tendons were modelled as isotropic linear elastic materials in many early studies [32, 35, 41, 44, 45, 48]. Some later FE studies considered the non-linearity in the material properties of muscles and tendons which is more accurate and closer to in vivo condition [52]. However, only the passive behaviour of the musculotendinous units was represented in the modelling. A most recent shoulder FE study described the material property of muscles by using a constitutive relationship representing both the active and passive behaviour of muscles along the direction of muscle fibres [84, 87]. Conversely, tendons were modelled using different parameters to describe their along-fibre and cross-fibre properties [84]. These detailed properties have been shown to agree with in vivo measurement of the biceps brachii [88]. In most cases, joint capsules were modelled as isotropic hyperelastic material [53, 56], and detailed parameters for each region were assigned in some studies which was validated through experimental strain measurements [58]. The labrum was normally assumed to be an isotropic material [62]. Lately, detailed transverse isotropic material properties were applied in some recent studies which compared well to the experiment measurements [66]. For articular cartilages, they were modelled as homogeneous linear elastic material in most of the studies [32, 35, 44, 45, 52, 82]. However, in some cases, they were considered to be rigid same as bones by assuming that the material properties of cartilages do not have significant effect on simulation results [48, 66]. Biological materials normally have complicated mechanical property, which is anisotropic and nonhomogeneous in nature with nonlinear and viscoelastic behaviours. However, depending on the research problem to be addressed, this material property might be simplified in some cases without compromising the quality of the analysis results. More sensitivity analysis studies are needed in the future to better understand the effect of different material properties [24].

The definition of boundary and loading conditions in previous shoulder FE studies varies dramatically because of the complexity in the joint motions and musculoskeletal loads of the shoulder complex. Many studies only considered part of the complex, and modelled the neglected parts using artificially imposed boundary or loading conditions [31, 32, 41, 44, 45, 62]. A number of studies defined their boundary and loading conditions according to the apparatus settings in the cadaveric

DOI: 10.1002/cnm

experiments to facilitate model validations [39, 48, 52, 53, 58, 66, 68, 89]. Whereas, in some other studies, boundary conditions were defined by imposing artificially prescribed displacements or rotations of certain muscles or bones [56, 59, 60, 84]. However, none of the previously stated boundary and loading conditions are capable of describing the realistic physiological conditions of the shoulder complex where significant muscle activations are involved. Some studies have addressed this and have attempted to use previously determined muscle forces from multi-body models as boundary and loading conditions [35, 78, 82]. But, they either considered the scapula in isolation [78, 82] or performed a 2D analysis only [35]. The most appropriate implementation of boundary and loading conditions in shoulder FE modelling is to describe the natural shoulder joint and bone motions driven by physiologically realistic muscle forces without any artificial constraints imposed [39]. This kind of physiological boundary condition has been proven to be beneficial in FE modelling of the femur [90]. In addition, the FE simulation analyses in most of the studies were only limited to the static or quasi-static condition. We have applied dynamic FE simulation analysis to study cervical spine and foot biomechanics [86, 91], and have an ongoing study to use dynamic FE analysis to investigate the in vivo functioning of the shoulder complex. Physiologically more realistic loading and boundary conditions are likely to provide the best way to predict the tissue stress environment in vivo.

Experimental validation of FE models is essential because model simplifications and assumptions are normally employed in shoulder FE studies. Unfortunately, some of the studies were not validated or only simply compared to previously published results [32, 41, 44, 45, 71]. For in vitro measurement based studies, it is straightforward to validate the models against the specimen-specific experimental data [36, 48, 52, 58, 66], for example strain gauge data for surface strain [75, 89, 92]. However, those validations were conducted based on the data collected in vitro, rather than in vivo data describing the physiological functioning of the shoulder complex. In vivo validations are challenging because of the limitation of current measuring techniques. Theoretically, FE simulation results could be validated in vivo against measured translational/rotational displacement data, strain/deformation data and stress/pressure data. The positions and orientations of bones or joints captured from motion analysis systems or X-ray systems could provide useful datasets to validate FE simulations in vivo. Recently, we have successfully used this method to validate a FE model of cervical spine [86]. Advances in medical imaging domains (e.g. dynamic MR/CT scanning or ultrasound) [93, 94] and force and pressure sensing techniques [95, 96] provide promising methods to validate FE simulation results in vivo against tissue deformation and contact pressure data.

It is evident that more comprehensive musculoskeletal FE modelling with physiologically realistic loading and boundary conditions is needed to further improve our understanding of the in vivo functioning of the shoulder complex. To further this, subject-specific modelling is the most promising simulation solution. In musculoskeletal modelling, there are normally a large number of uncertainties involved in different components of the system, which is further confounded by inter-subject variations [24, 97]. To rigorously validate the modelling results in vivo, personalised datasets and parameters are desirable. Subject-specific modelling studies have been successfully applied to other musculoskeletal complexes, such as pelvis [98] and femur [99], but very few to the shoulder joint. Future orthopaedic interventions and surgeries are likely to benefit from patient-specific biomechanical analyses and assessments before and/or after treatments. This approach has been successfully demonstrated in the total knee arthroplasty [100, 101] and periacetabular osteotomy surgery [85].

4. CONCLUSION

Previous FE studies to investigate shoulder biomechanics have been critically reviewed according to the clinical issues addressed. This confirms that FE modelling is a valuable tool to examine both physiological functions and clinical problems of the shoulder complex. Most of those modelling studies have improved our understanding of the biomechanical functioning of the shoulder joint. Specifically, they normally have one or more research focuses: biomechanical mechanism underlying joint motion, aetiology of joint pathology, clinical diagnoses of joint diseases and shoulder prosthetics design. It may be difficult to say which is the best model, but the most recent models using

DOI: 10.1002/cnm

latest techniques tend to have more complicated configurations and provide more detailed databases than the models before. It is noticeable that more comprehensive model is needed to better understand the in vivo functioning and also the interaction of different components of the shoulder joint. Recently there has been a tendency in shoulder FE studies to construct subject-specific or patient-specific FE models informed by muscle force and/or bone motion data from measurement based multi-body modelling. Despite the aforementioned limitations of multi-body modelling, this integration offers some promising solutions by providing more accurate boundary and loading conditions.

Fully validated shoulder FE models will greatly enhance our understanding of the fundamental mechanisms underlying shoulder mobility and stability, and the aetiology of shoulder disorders, and hence facilitate the development of more efficient clinical examinations and diagnoses, non-surgical and surgical interventions and treatments including prostheses. In author's opinion, the model validation may need to be conducted by interactively working with clinicians. First, FE models could be carefully validated for healthy people by using the latest medical imaging and sensing techniques. Then, with some confidences built up, the models could be applied to individual clinical case by using the patient-specific database provided by clinicians. The models could be further improved based on prediction results and also feedbacks of doctors. Indeed, we still face many challenging problems before the realistic physiological functions of the shoulder mechanism can be accurately represented and analysed in FE simulations.

Future works and challenges involve:

1. Subject-specific representation of the non-linear anisotropic nonhomogeneous material properties of the shoulder tissues in both healthy and pathological conditions, and also definition of boundary and loading conditions based on individualised physiological data. Special attention should be paid to the consistency between the FE models and the multi-body models used for muscle force estimation.
2. More comprehensive models describing the whole shoulder complex including appropriate 3D representations of all major shoulder hard tissues and soft tissues and their delicate interactions, are highly demanded to better understand the biomechanical functioning of the shoulder mechanism.
3. Dynamic FE simulations based on physiologically realistic boundary and loading conditions to better understand the in vivo biomechanical functioning of the shoulder joint during our daily activities.
4. Advanced medical imaging, sensing techniques to quantify in vivo strain and stress distributions of soft and hard tissues in both normal and pathological conditions so as to validate FE models more rigorously.

ACKNOWLEDGEMENTS

This study has been partly supported by the UK Engineering Physical Science Research Council (EPSRC) from grant number EP/I033602/1 and EP/K019759/1.

REFERENCES

1. Veeger H, van der Helm F. Shoulder function: the perfect compromise between mobility and stability. *Journal of Biomechanics* 2007; **40**(10):2119–2129. doi:http://dx.doi.org/10.1016/j.jbiomech.2006.10.016.
2. Haering D, Raison M, Begon M. Measurement and description of three-dimensional shoulder range of motion with degrees of freedom interactions. *Journal of Biomechanical Engineering* 2014; **136**(8):084502. doi:http://dx.doi.org/10.1115/1.4027665.
3. Martini FH, Timmons MJ, McKinley MP. *Human Anatomy*. Prentice Hall: Upper Saddle River, New Jersey, USA, 2000; 223.
4. Engin AE, Chen SM. Statistical data base for the biomechanical properties of the human shoulder complex—I: Kinematics of the shoulder complex. *Journal of Biomechanical Engineering-T Asme* 1986; **108**(3):215–221. doi:http://dx.doi.org/10.1115/1.3138605.
5. Buechel FF, Pappas MJ. *Principles of Human Joint Replacement*. Springer: Berlin, Germany, 2015; 385.

6. Bolsterlee B, Veeger DH, Chadwick EK. Clinical applications of musculoskeletal modelling for the shoulder and upper limb. *Medical and Biological Engineering and Computing* 2013; **51**(9):953–963. doi:http://dx.doi.org/10.1007/s11517-013-1099-5.
7. Itoi E, Lee SB, Berglund LJ, Berge LL, An KN. The effect of a glenoid defect on anteroinferior stability of the shoulder after Bankart repair: a cadaveric study. *Journal of Bone and Joint Surgery (American)* 2000; **82**(1):35–46.
8. Apreleva M, Parsons IM, Warner JJP, Fu FH, Woo SLY. Experimental investigation of reaction forces at the glenohumeral joint during active abduction. *Journal of Shoulder and Elbow Surgery* 2000; **9**(5):409–417. doi:http://dx.doi.org/10.1067/mse.2000.106321.
9. Parsons IM, Apreleva M, Fu FH, Woo SLY. The effect of rotator cuff tears on reaction forces at the glenohumeral joint. *Journal of Orthopaedic Research* 2002; **20**(3):439–446. doi:http://dx.doi.org/10.1016/S0736-0266(01)00137-1.
10. Ellis BJ, Lujan TJ, Dalton MS, Weiss JA. Medial collateral ligament insertion site and contact forces in the ACL-deficient knee. *Journal of Orthopaedic Research* 2006; **24**(4):800–810. doi:http://dx.doi.org/10.1002/jor.20102.
11. Kaar SG, Fening SD, Jones MH, Colbrunn RW, Miniaci A. Effect of humeral head defect size on glenohumeral stability: a cadaveric study of simulated Hill-Sachs defects. *American Journal of Sports Medicine* 2010; **38**(3):594–599. doi:http://dx.doi.org/10.1177/0363546509350295.
12. Dickerson CR, Chaffin DB, Hughes RE. A mathematical musculoskeletal shoulder model for proactive ergonomic analysis. *Computer Methods in Biomechanics and Biomedical Engineering* 2007; **10**(6):389–400. doi:http://dx.doi.org/10.1080/10255840701592727.
13. Garner BA, Pandy MG. Musculoskeletal model of the upper limb based on the visible human male dataset. *Computer Methods in Biomechanics and Biomedical Engineering* 2001; **4**(2):93–126. doi:http://dx.doi.org/10.1080/10255840008908000.
14. Högfors C, Karlsson D, Peterson B. Structure and internal consistency of a shoulder model. *Journal of Biomechanics* 1995; **28**(7):767–777. doi:http://dx.doi.org/10.1016/0021-9290(94)00134-P.
15. Van der Helm FC. A finite-element musculoskeletal model of the shoulder mechanism. *Journal of Biomechanics* 1994; **27**(5):551–569. doi:http://dx.doi.org/10.1016/0021-9290(94)90065-5.
16. Charlton IW, Johnson GR. A model for the prediction of the forces at the glenohumeral joint. *Proceedings of the Institution of Mechanical Engineers. Part H* 2006; **220**(H8):801–812. doi:http://dx.doi.org/10.1243/09544119jeim147.
17. Nikooyan AA, Veeger HEJ, Chadwick EKJ, Praagman M, van der Helm FCT. Development of a comprehensive musculoskeletal model of the shoulder and elbow. *Medical and Biological Engineering and Computing* 2011; **49**(12):1425–1435. doi:http://dx.doi.org/10.1007/s11517-011-0839-7.
18. Prinold JAI, Masjedi M, Johnson GR, Bull AMJ. Musculoskeletal shoulder models: a technical review and proposals for research foci. *Proceedings of the Institution of Mechanical Engineers. Part H* 2013; **227**(10):1041–1057. doi:http://dx.doi.org/10.1177/0954411913492303.
19. Stops A, Wilcox R, Jin Z. Computational modelling of the natural hip: a review of finite element and multibody simulations. *Computer Methods in Biomechanics and Biomedical Engineering* 2012; **15**(9):963–979.
20. Favre P, Snedeker J, Gerber C. Numerical modelling of the shoulder for clinical applications. *Philosophical Transactions of the Royal Society A: Mathematical, Physical and Engineering Sciences* 1895; **2009**(367):2095–2118. doi:http://dx.doi.org/10.1098/rsta.2008.0282.
21. Zienkiewicz C. The birth of the finite element method and of computational mechanics. *International Journal for Numerical Methods in Engineering* 2004; **60**(1):3–10. doi:http://dx.doi.org/10.1002/Nme.951.
22. Zienkiewics O. *The Finite Element Method in Engineering Science*. McGraw-Hill: Londres, 1971; 521.
23. Huiskes R, Hollister SJ. From structure to process, from organ to cell: recent developments of FE-analysis in orthopaedic biomechanics. *Journal of Biomechanical Engineering-T Asme* 1993; **115**(4B):520–527. doi:http://dx.doi.org/10.1115/1.2895534.
24. Viceconti M, Olsen S, Nolte LP, Burton K. Extracting clinically relevant data from finite element simulations. *Clinical Biomechanics (Bristol, Avon)* 2005; **20**(5):451–454. doi:http://dx.doi.org/10.1016/j.clinbiomech.2005.01.010.
25. Reilly DT, Burstein AH, Frankel VH. The elastic modulus for bone. *Journal of Biomechanics* 1974; **7**(3):271–275. doi:http://dx.doi.org/10.1016/0021-9290(74)90018-9.
26. Rice JC, Cowin SC, Bowman JA. On the dependence of the elasticity and strength of cancellous bone on apparent density. *Journal of Biomechanics* 1988; **21**(2):155–168. doi:http://dx.doi.org/10.1016/0021-9290(88)90008-5.
27. Veronda DR, Westmann RA. Mechanical characterization of skin-finite deformations. *Journal of Biomechanics* 1970; **3**(1):111–124. doi:http://dx.doi.org/10.1016/0021-9290(70)90055-2.
28. Pioletti DP, Rakotomanana LR, Benvenuti JF, Leyvraz PF. Viscoelastic constitutive law in large deformations: application to human knee ligaments and tendons. *Journal of Biomechanics* 1998; **31**(8):753–757. doi:http://dx.doi.org/10.1016/S0021-9290(98)00077-3.
29. Pioletti DP, Rakotomanana LR, Leyvraz P-F. Strain rate effect on the mechanical behavior of the anterior cruciate ligament–bone complex. *Medical Engineering and Physics* 1999; **21**(2):95–100. doi:http://dx.doi.org/10.1016/S1350-4533(99)00028-4.
30. Kempson GE, Tuke MA, Dingle JT, Barrett AJ, Horsfield PH. The effects of proteolytic enzymes on the mechanical properties of adult human articular cartilage. *Biochimica Et Biophysica Acta* 1976; **428**(3):741–760. doi:http://dx.doi.org/10.1016/0304-4165(76)90205-1.
31. Büchler P, Ramaniraka N, Rakotomanana L, Iannotti J, Farron A. A finite element model of the shoulder: application to the comparison of normal and osteoarthritic joints. *Clinical Biomechanics (Bristol, Avon)* 2002; **17**(9-10):630–639. doi:http://dx.doi.org/10.1016/S0268-0033(02)00106-7.

32. Wakabayashi I, Itoi E, Sano H, Shibuya Y, Sashi R, Minagawa H, Kobayashi M. Mechanical environment of the supraspinatus tendon: a two-dimensional finite element model analysis. *Journal of Shoulder and Elbow Surgery* 2003; **12**(6):612–617. doi:http://dx.doi.org/10.1016/s1058274603002143.
33. Liu J, Hughes R, Smutz W, Niebur G, Nan-An K. Roles of deltoid and rotator cuff muscles in shoulder elevation. *Clinical Biomechanics* 1997; **12**(1):32–38. doi:http://dx.doi.org/10.1016/S0268-0033(96)00047-2.
34. Otis JC, Jiang C-C, Wickiewicz TL, Peterson M, Warren RF, Santner TJ. Changes in the moment arms of the rotator cuff and deltoid muscles with abduction and rotation. *Journal of Bone and Joint Surgery* 1994; **76**(5):667–676.
35. Terrier A, Reist A, Vogel A, Farron A. Effect of supraspinatus deficiency on humerus translation and glenohumeral contact force during abduction. *Clinical Biomechanics (Bristol, Avon)* 2007; **22**(6):645–651. doi:http://dx.doi.org/10.1016/j.clinbiomech.2007.01.015.
36. Walia P, Miniaci A, Jones MH, Fening SD. Theoretical model of the effect of combined glenohumeral bone defects on anterior shoulder instability: a finite element approach. *Journal of Orthopaedic Research* 2013; **31**(4):601–607. doi:http://dx.doi.org/10.1002/jor.22267.
37. Nyffeler RW, Sheikh R, Jacob HA, Gerber C. Influence of humeral prosthesis height on biomechanics of glenohumeral abduction. *Journal of Bone and Joint Surgery* 2004; **86**(3):575–580.
38. Yanagawa T, Goodwin CJ, Shelburne KB, Giphart JE, Torry MR, Pandy MG. Contributions of the individual muscles of the shoulder to glenohumeral joint stability during abduction. *Journal of Biomechanical Engineering-T Asme* 2008; **130**(2):21–24. doi:http://dx.doi.org/10.1115/1.2903422.
39. Favre P, Senteler M, Hipp J, Scherrer S, Gerber C, Snedeker JG. An integrated model of active glenohumeral stability. *Journal of Biomechanics* 2012; **45**(13):2248–2255. doi:http://dx.doi.org/10.1016/j.jbiomech.2012.06.010.
40. Giori NJ, Beaupre GS, Carter DR. Cellular-shape and pressure may mediate mechanical control of tissue composition in tendons. *Journal of Orthopaedic Research* 1993; **11**(4):581–591. doi:http://dx.doi.org/10.1002/jor.1100110413.
41. Luo ZP, Hsu HC, Grabowski JJ, Morrey BF, An KN. Mechanical environment associated with rotator cuff tears. *Journal of Shoulder and Elbow Surgery* 1998; **7**(6):616–620. doi:http://dx.doi.org/10.1016/S1058-2746(98)90010-6.
42. Anderson DD, Brown TD, Radin EL. Stress wave effects in a finite element analysis of an impulsively loaded articular joint. *Proceedings of the Institution of Mechanical Engineers. Part H* 1991; **205**(1):27–34. doi:http://dx.doi.org/10.1243/PIME_PROC_1991_205_258_02.
43. Itoi E, Berglund LJ, Grabowski JJ, Schultz FM, Growney ES, Morrey BF, An KN. Tensile properties of the supraspinatus tendon. *Journal of Orthopaedic Research* 1995; **13**(4):578–584. doi:http://dx.doi.org/10.1002/jor.1100130413.
44. Sano H, Wakabayashi I, Itoi E. Stress distribution in the supraspinatus tendon with partial-thickness tears: an analysis using two-dimensional finite element model. *Journal of Shoulder and Elbow Surgery* 2006; **15**(1):100–105. doi:http://dx.doi.org/10.1016/j.jse.2005.04.003.
45. Seki N, Itoi E, Shibuya Y, Wakabayashi I, Sano H, Sashi R, Minagawa H, Yamamoto N, Abe H, Kikuchi K, Okada K, Shimada Y. Mechanical environment of the supraspinatus tendon: three-dimensional finite element model analysis. *Journal of Orthopaedic Science* 2008; **13**(4):348–353. doi:http://dx.doi.org/10.1007/s00776-008-1240-8.
46. Halloran JP, Easley SK, Petrella AJ, Rullkoetter PJ. Comparison of deformable and elastic foundation finite element simulations for predicting knee replacement mechanics. *Journal of Biomechanical Engineering-T Asme* 2005; **127**(5):813–818. doi:http://dx.doi.org/10.1115/1.1992522.
47. Halder A, Zobitz ME, Schultz F, An KN. Mechanical properties of the posterior rotator cuff. *Clinical Biomechanics (Bristol, Avon)* 2000; **15**(6):456–462. doi:http://dx.doi.org/10.1016/S0268-0033(99)00095-9.
48. Adams C, Baldwin M, Laz P, Rullkoetter P, Langenderfer J. Effects of rotator cuff tears on muscle moment arms: a computational study. *Journal of Biomechanics* 2007; **40**(15):3373–3380. doi:http://dx.doi.org/10.1016/j.jbiomech.2007.05.017.
49. Goto K, Tajima N, Chosa E, Totoribe K, Kuroki H, Arizumi Y, Arai T. Mechanical analysis of the lumbar vertebrae in a three-dimensional finite element method model in which intradiscal pressure in the nucleus pulposus was used to establish the model. *Journal of Orthopaedic Science* 2002; **7**(2):243–246. doi:http://dx.doi.org/10.1007/s007760200040.
50. Nakajima T, Rokuuma N, Hamada K, Tomatsu T, Fukuda H. Histologic and biomechanical characteristics of the supraspinatus tendon: reference to rotator cuff tearing. *Journal of Shoulder and Elbow Surgery* 1994; **3**(2):79–87. doi:http://dx.doi.org/10.1016/S1058-2746(09)80114-6.
51. Van der Helm FC. Analysis of the kinematic and dynamic behavior of the shoulder mechanism. *Journal of Biomechanics* 1994; **27**(5):527–550. doi:http://dx.doi.org/10.1016/0021-9290(94)90064-7.
52. Inoue A, Chosa E, Goto K, Tajima N. Nonlinear stress analysis of the supraspinatus tendon using three-dimensional finite element analysis. *Knee Surgery, Sports Traumatology, Arthroscopy* 2013; **21**(5):1151–1157. doi:http://dx.doi.org/10.1007/s00167-012-2008-4.
53. Debski R, Weiss J, Newman W, Moore S, McMahon P. Stress and strain in the anterior band of the inferior glenohumeral ligament during a simulated clinical examination. *Journal of Shoulder and Elbow Surgery* 2005; **14**(1):S24–S31. doi:http://dx.doi.org/10.1016/j.jse.2004.10.003.
54. Moore SM, McMahon PJ, Debski RE. Bi-directional mechanical properties of the axillary pouch of the glenohumeral capsule: implications for modeling and surgical repair. *Journal of Biomechanical Engineering-T Asme* 2004; **126**(2):284–288. doi:http://dx.doi.org/10.1115/1.1695574.

55. McMahon PJ, Tibone JE, Cawley PW, Hamilton C, Fechter JD, Elattrache NS, Lee TQ. The anterior band of the inferior glenohumeral ligament: biomechanical properties from tensile testing in the position of apprehension. *Journal of Shoulder and Elbow Surgery* 1998; **7**(5):467–471. doi:http://dx.doi.org/10.1016/S1058-2746(98)90196-3.
56. Ellis B, Debski R, Moore S, McMahon P, Weiss J. Methodology and sensitivity studies for finite element modeling of the inferior glenohumeral ligament complex. *Journal of Biomechanics* 2007; **40**(3):603–612. doi:http://dx.doi.org/10.1016/j.jbiomech.2006.01.024.
57. Simo JC, Vu-Quoc L. On the dynamics in space of rods undergoing large motions—a geometrically exact approach. *Computer Methods in Applied Mechanics and Engineering* 1988; **66**(2):125–161. doi:http://dx.doi.org/10.1016/0045-7825(88)90073-4.
58. Moore S, Ellis B, Weiss J, McMahon P, Debski R. The glenohumeral capsule should be evaluated as a sheet of fibrous tissue: a validated finite element model. *Annals of Biomedical Engineering* 2010; **38**(1):66–76. doi:http://dx.doi.org/10.1007/s10439-009-9834-7.
59. Ellis B, Drury N, Moore S, McMahon P, Weiss J, Debski R. Finite element modelling of the glenohumeral capsule can help assess the tested region during a clinical exam. *Computer Methods in Biomechanics and Biomedical Engineering* 2010; **13**(3):413–418. doi:http://dx.doi.org/10.1080/10255840903317378.
60. Drury N, Ellis B, Weiss J, McMahon P, Debski R. The impact of glenoid labrum thickness and modulus on labrum and glenohumeral capsule function. *Journal of Biomechanical Engineering-T Asme* 2010; **132**(12):121003. doi:http://dx.doi.org/10.1115/1.4002622.
61. DiGiovine NM, Jobe FW, Pink M, Perry J. An electromyographic analysis of the upper extremity in pitching. *Journal of Shoulder and Elbow Surgery* 1992; **1**(1):15–25. doi:http://dx.doi.org/10.1016/S1058-2746(09)80011-6.
62. Yeh M-L, Lintner D, Luo Z-P. Stress distribution in the superior labrum during throwing motion. *American Journal of Sports Medicine* 2005; **33**(3):395–401. doi:http://dx.doi.org/10.1177/0363546504268404.
63. Carey J, Small CF, Pichora DR. In situ compressive properties of the glenoid labrum. *Journal of Biomedical Materials Research* 2000; **51**(4):711–716. doi:http://dx.doi.org/10.1002/1097-4636(20000915)51:43.0.CO;2-Z.
64. Smith CD, Masouros SD, Hill AM, Wallace AL, Amis AA, Bull AM. Tensile properties of the human glenoid labrum. *Journal of Anatomy* 2008; **212**(1):49–54. doi:http://dx.doi.org/10.1111/j.1469-7580.2007.00832.x.
65. Yao J, Snibbe J, Maloney M, Lerner AL. Stresses and strains in the medial meniscus of an ACL deficient knee under anterior loading: a finite element analysis with image-based experimental validation. *Journal of Biomechanical Engineering-T Asme* 2006; **128**(1):135–141. doi:http://dx.doi.org/10.1115/1.2132373.
66. Gatti C, Maratt J, Palmer M, Hughes R, Carpenter J. Development and validation of a finite element model of the superior glenoid labrum. *Annals of Biomedical Engineering* 2010; **38**(12):3766–3776. doi:http://dx.doi.org/10.1007/s10439-010-0105-4.
67. Weiss JA, Gardiner JC, Bonifasi-Lista C. Ligament material behavior is nonlinear, viscoelastic and rate-independent under shear loading. *Journal of Biomechanics* 2002; **35**(7):943–950. doi:http://dx.doi.org/10.1016/S0021-9290(02)00041-6.
68. Drury N, Ellis B, Weiss J, McMahon P, Debski R. Finding consistent strain distributions in the glenohumeral capsule between two subjects: implications for development of physical examinations. *Journal of Biomechanics* 2011; **44**(4):607–613. doi:http://dx.doi.org/10.1016/j.jbiomech.2010.11.018.
69. Büchler P, Farron A. Benefits of an anatomical reconstruction of the humeral head during shoulder arthroplasty: a finite element analysis. *Clinical Biomechanics (Bristol, Avon)* 2004; **19**(1):16–23. doi:http://dx.doi.org/10.1016/j.clinbiomech.2003.09.009.
70. Bigliani LU, Kelkar R, Flatow EL, Pollock RG, Mow VC. Glenohumeral stability: biomechanical properties of passive and active stabilizers. *Clinical Orthopaedics and Related Research* 1996; **330**:13–30.
71. Friedman RJ, LaBerge M, Dooley RL, O'Hara AL. Finite element modeling of the glenoid component: effect of design parameters on stress distribution. *Journal of Shoulder and Elbow Surgery* 1992; **1**(5):261–270. doi:http://dx.doi.org/10.1016/S1058-2746(09)80068-2.
72. Lacroix D, Prendergast PJ. Stress analysis of glenoid component designs for shoulder arthroplasty. *Proceedings of the Institution of Mechanical Engineers. Part H* 1997; **211**(6):467–474. doi:http://dx.doi.org/10.1243/0954411981534583.
73. Stone KD, Grabowski JJ, Cofield RH, Morrey BF, An KN. Stress analyses of glenoid components in total shoulder arthroplasty. *Journal of Shoulder and Elbow Surgery* 1999; **8**(2):151–158. doi:http://dx.doi.org/10.1016/S1058-2746(99)90009-5.
74. Lacroix D, Murphy LA, Prendergast PJ. Three-dimensional finite element analysis of glenoid replacement prostheses: a comparison of keeled and pegged anchorage systems. *Journal of Biomechanical Engineering-T Asme* 2000; **122**(4):430–436. doi:http://dx.doi.org/10.1115/1.1286318.
75. Gupta S, van der Helm FC, van Keulen F. The possibilities of uncemented glenoid component—a finite element study. *Clinical Biomechanics (Bristol, Avon)* 2004; **19**(3):292–302. doi:http://dx.doi.org/10.1016/j.clinbiomech.2003.12.002.
76. Hopkins AR, Hansen UN, Amis AA, Emery R. The effects of glenoid component alignment variations on cement mantle stresses in total shoulder arthroplasty. *Journal of Shoulder and Elbow Surgery* 2004; **13**(6):668–675. doi:http://dx.doi.org/10.1016/S1058274604001399.
77. Murphy LA, Prendergast PJ. Acromion-fixation of glenoid components in total shoulder arthroplasty. *Journal of Biomechanics* 2005; **38**(8):1702–1711. doi:http://dx.doi.org/10.1016/j.jbiomech.2004.06.030.

78. Terrier A, Buchler P, Farron A. Bone–cement interface of the glenoid component: stress analysis for varying cement thickness. *Clinical Biomechanics (Bristol, Avon)* 2005; **20**(7):710–717. doi:http://dx.doi.org/10.1016/j.clinbiomech.2005.03.010.
79. Terrier A, Buchler P, Farron A. Influence of glenohumeral conformity on glenoid stresses after total shoulder arthroplasty. *Journal of Shoulder and Elbow Surgery* 2006; **15**(4):515–520. doi:http://dx.doi.org/10.1016/j.jse.2005.09.021.
80. Terrier A, Merlini F, Pioletti DP, Farron A. Comparison of polyethylene wear in anatomical and reversed shoulder prostheses. *Journal of Bone and Joint Surgery (British)* 2009; **91**(7):977–982. doi:http://dx.doi.org/10.1302/0301-620X.91B7.21999.
81. Quental C, Fernandes P, Monteiro J, Folgado J. Bone remodelling of the scapula after a total shoulder arthroplasty. *Biomechanics and Modeling in Mechanobiology* 2014; **13**(4):827–838. doi:http://dx.doi.org/10.1007/s10237-013-0537-5.
82. Quental C, Folgado J, Fernandes PR, Monteiro J. Subject-specific bone remodelling of the scapula. *Computer Methods in Biomechanics and Biomedical Engineering* 2014; **17**(10):1129–1143. doi:http://dx.doi.org/10.1080/10255842.2012.738198.
83. Campoli G, Bolsterlee B, van der Helm F, Weinans H, Zadpoor AA. Effects of densitometry, material mapping and load estimation uncertainties on the accuracy of patient-specific finite-element models of the scapula. *Journal of the Royal Society Interface* 2014; **11**(93: 20131146). doi:http://dx.doi.org/10.1098/rsif.2013.1146.
84. Webb JD, Blemker SS, Delp SL. 3D finite element models of shoulder muscles for computing lines of actions and moment arms. *Computer Methods in Biomechanics and Biomedical Engineering* 2012; **17**(8):829–837. doi:http://dx.doi.org/10.1080/10255842.2012.719605.
85. Zou Z, Chávez-Arreola A, Mandal P, Board TN, Alonso-Rasgado T. Optimization of the position of the acetabulum in a ganz periacetabular osteotomy by finite element analysis. *Journal of Orthopaedic Research* 2013; **31**(3):472–479.
86. Wang J, Qian Z, Ren L, Ren L. A dynamic finite element model of human cervical spine with in vivo kinematic validation. *Chinese Science Bulletin* 2014; **59**(33):4578–4588.
87. Holzbaur KR, Murray WM, Delp SL. A model of the upper extremity for simulating musculoskeletal surgery and analyzing neuromuscular control. *Annals of Biomedical Engineering* 2005; **33**(6):829–840. doi:http://dx.doi.org/10.1007/s10439-005-3320-7.
88. Blemker SS, Pinsky PM, Delp SL. A 3D model of muscle reveals the causes of nonuniform strains in the biceps brachii. *Journal of Biomechanics* 2005; **38**(4):657–665. doi:http://dx.doi.org/10.1016/j.jbiomech.2004.04.009.
89. Gupta S, van der Helm F. Load transfer across the scapula during humeral abduction. *Journal of Biomechanics* 2004; **37**(7):1001–1009. doi:http://dx.doi.org/10.1016/j.jbiomech.2003.11.025.
90. Speirs AD, Heller MO, Duda GN, Taylor WR. Physiologically based boundary conditions in finite element modelling. *Journal of Biomechanics* 2007; **40**(10):2318–2323. doi:http://dx.doi.org/10.1016/j.jbiomech.2006.10.038.
91. Qian ZH, Ren L, Ding Y, Hutchinson JR, Ren LQ. A dynamic finite element analysis of human foot complex in the sagittal plane during level walking. *Plos One* 2013; **8**(11: e79424). doi:http://dx.doi.org/10.1371/journal.pone.0079424.
92. Gupta S, Helm FCT, Sterk JC, Keulen F, Kaptein BL. Development and experimental validation of a three-dimensional finite element model of the human scapula. *Proceedings of the Institution of Mechanical Engineers. Part H* 2004; **218**(2):127–142. doi:http://dx.doi.org/10.1243/095441104322984022.
93. Clarke E, Martin J, d'Entremont A, Pandy M, Wilson D, Herbert R. A non-invasive, 3D, dynamic MRI method for measuring muscle moment arms in vivo: demonstration in the human ankle joint and Achilles tendon. *Medical Engineering and Physics* 2015; **37**(1):93–99. doi:http://dx.doi.org/10.1016/j.medengphy.2014.11.003.
94. De Sá Rebelo M, Moreno RA, Gobbi RG, Camanho GL, Ávila LFR, Demange MK, Pecora JR, Gutierrez MA Description of patellar movement by 3D parameters obtained from dynamic CT acquisition. In: SPIE Medical Imaging, 2014. International Society for Optics and Photonics, pp 903538-903538-903539
95. Roriz P, Carvalho L, Frazão O, Santos JL, Simões JA. From conventional sensors to fibre optic sensors for strain and force measurements in biomechanics applications: a review. *Journal of Biomechanics* 2014; **47**(6):1251–1261. doi:http://dx.doi.org/10.1016/j.jbiomech.2014.01.054.
96. Tao K, Wang D, Wang C, Wang X, Liu A, Nester CJ, Howard D. An in vivo experimental validation of a computational model of human foot. *Journal of Bionic Engineering* 2009; **6**(4):387–397.
97. Cook D, Julias M, Nauman E. Biological variability in biomechanical engineering research: significance and meta-analysis of current modeling practices. *Journal of Biomechanics* 2014; **47**(6):1241–1250. doi:http://dx.doi.org/10.1016/j.jbiomech.2014.01.040.
98. Anderson AE, Peters CL, Tuttle BD, Weiss JA. Subject-specific finite element model of the pelvis: development, validation and sensitivity studies. *Journal of Biomechanical Engineering-T Asme* 2005; **127**(3):364–373. doi:http://dx.doi.org/10.1115/1.1894148.
99. Schileo E, Taddei F, Malandrino A, Cristofolini L, Viceconti M. Subject-specific finite element models can accurately predict strain levels in long bones. *Journal of Biomechanics* 2007; **40**(13):2982–2989. doi:http://dx.doi.org/10.1016/j.jbiomech.2007.02.010.
100. Hafez M, Chelule K, Seedhom B, Sherman K. Computer-assisted total knee arthroplasty using patient-specific templating. *Clinical Orthopaedics and Related Research* 2006; **444**:184–192. doi:http://dx.doi.org/10.1097/01.blo.0000201148.06454.ef.
101. Lombardi AV Jr, Berend KR, Adams JB, White D, Chelule K, Seedhom B. Patient-specific approach in total knee arthroplasty. *Orthopedics* 2008; **31**(9):927. doi:http://dx.doi.org/10.3928/01477447-20080901-21.